

SEISMIC BEHAVIOUR INVESTIGATION OF A CABLE-
STAYED BRIDGE WITH HYBRID PASSIVE CONTROL
SYSTEM

AHAD JAVANMARDI

FACULTY OF ENGINEERING
UNIVERSITY OF MALAYA
KUALA LUMPUR

2019

**SEISMIC BEHAVIOUR INVESTIGATION OF A
CABLE-STAYED BRIDGE WITH HYBRID PASSIVE
CONTROL SYSTEM**

AHAD JAVANMARDI

**THESIS SUBMITTED IN FULFILMENT OF THE
REQUIREMENTS FOR THE DEGREE OF DOCTOR OF
PHILOSOPHY**

**FACULTY OF ENGINEERING
UNIVERSITY OF MALAYA
KUALA LUMPUR**

2019

UNIVERSITY OF MALAYA
ORIGINAL LITERARY WORK DECLARATION

Name of Candidate: **Ahad Javanmardi**

Matric No: **KHA140026**

Name of Degree: **Doctor of Philosophy**

Title of Project Thesis: **Seismic Behaviour Investigation of a Cable-Stayed Bridge with Hybrid Passive Control System**

Field of Study: **Structural Engineering and Materials**

I do solemnly and sincerely declare that:

- (1) I am the sole author/writer of this Work;
- (2) This Work is original;
- (3) Any use of any work in which copyright exists was done by way of fair dealing and for permitted purposes and any excerpt or extract from, or reference to or reproduction of any copyright work has been disclosed expressly and sufficiently and the title of the Work and its authorship have been acknowledged in this Work;
- (4) I do not have any actual knowledge nor do I ought reasonably to know that the making of this work constitutes an infringement of any copyright work;
- (5) I hereby assign all and every rights in the copyright to this Work to the University of Malaya ("UM"), who henceforth shall be owner of the copyright in this Work and that any reproduction or use in any form or by any means whatsoever is prohibited without the written consent of UM having been first had and obtained;
- (6) I am fully aware that if in the course of making this Work I have infringed any copyright whether intentionally or otherwise, I may be subject to legal action or any other action as may be determined by UM.

Candidate's Signature

Date:

Subscribed and solemnly declared before,

Witness's Signature

Date:

Name:

Designation:

SEISMIC BEHAVIOUR INVESTIGATION OF A CABLE-STAYED BRIDGE WITH HYBRID PASSIVE CONTROL SYSTEM

ABSTRACT

The construction of cable-stayed bridges has been increasing worldwide owing to their characteristics, such as appealing aesthetics, longer span length and lightweight that have high logistic and economic value. However, cable-stayed bridges are also associated with low structural damping and longer fundamental periods, which make them highly vulnerable to large amplitude oscillation during seismic events. Consequently, studying the seismic response and protection of cable-stayed bridges from seismic loading is essential. This research studies the seismic behavior and protection of an existing steel cable-stayed bridge located in a high-risk seismic zone in Canada. This bridge was chosen based on the availability of detailing data and experimental results. For instance, earthquake-induced pounding caused structural damages and also one anchorage plate in the bridge support failed due to the Saguenay earthquake in 1988. The main objective of this research is thus to enhance the seismic performance of the cable-stayed bridge by means of a hybrid passive control system, which is a combination of seismic isolator and a novel metallic damper to minimize future damage that may be induced by earthquakes. Initially, the cable-stayed bridge is rigorously modeled in three dimensions and validated with experimental results. Then, different seismic isolation retrofitting cases are defined and isolation systems are designed for each case accordingly. Thereafter, the new metal damper, called the hexagonal honeycomb steel damper, is proposed and developed experimentally and numerically to determine its behavior and characteristics. Finally, the proposed damper is designed and modelled for the fully isolated cable-stayed bridge. The seismic response of each cable-stayed bridge retrofitting case is evaluated through a series of nonlinear time-history analysis. The comparative analysis indicates that the partial

seismic isolation of the cable-stayed bridge enhanced its seismic behavior in one direction only. In order to enhance the seismic performance of the cable-stayed bridge in both directions, the isolation system should be utilized at the end supports, as well as the deck-tower connection or base of the tower. The global and local seismic responses of the fully isolated cable-stayed bridge significantly improved, compared to the non-isolated bridge. However, the seismic displacement of the superstructure increased in the fully isolated bridge. The result of quasi-static cyclic test on the proposed damper showed that, the damper exhibited low yield displacement, excellent strength and ductility, and stable hysteretic behavior with high energy absorbing capability. Consequently, implementation of the metallic damper in the fully isolated bridge caused a significant reduction in superstructure displacement under earthquake loading, which also eliminated the earthquake-induced pounding effect at the bridge ends with adjacent abutments. The hybrid passive control system is beneficial in the protection of cable-stayed bridges in high-risk seismic zones. The system reduces the seismic demands on the structure and mitigates the seismic displacement of the superstructure as well as the likelihood of earthquake-induced pounding in the bridge.

Keywords: Cable-stayed bridges; Seismic performance; Passive control; Metallic dampers; Nonlinear dynamic analysis.

TINGKAH LAKU SEISMIK JAMBATAN KABEL TETAP DENGAN SISTEM HIBRID KAWALAN PASIF

ABSTRAK

Pembinaan jambatan-jambatan kabel tetap terus meningkat di seluruh dunia disebabkan oleh ciri-ciri mereka, seperti nilai estetika yang menarik, rentang yang lebih panjang dan ringan, di mana ia mempunyai nilai logistik dan ekonomi yang tinggi. Walau bagaimanapun, jambatan kabel yang tetap juga dikaitkan dengan redaman struktur yang rendah dan tempoh asasi yang lebih lama, yang menjadikan mereka sangat terdedah kepada ayunan amplitud yang besar semasa peristiwa seismik. Di samping itu, mod getaran yang mendominasi di kebanyakan jambatan kabel tetap adalah mod membujur, yang boleh meningkatkan kemungkinan godaman yang disebabkan oleh gempa bumi di jambatan. Oleh itu, kajian tentang tindak balas seismik dan perlindungan jambatan kabel tetap daripada beban seismik adalah penting. Penyelidikan ini mengkaji tentang tingkah laku seismik dan perlindungan jambatan kabel keluli sedia ada yang terletak di zon seismik berisiko tinggi di Kanada. Jambatan ini dipilih berdasarkan ketersediaan data terperinci dan hasil keputusan eksperimen. Contohnya, godaman yang disebabkan oleh gempa bumi telah menyebabkan kerosakan struktur dan kegagalan satu plat tambatan pada sokongan jambatan semasa gempa bumi Saguenay pada tahun 1988. Tujuan utama penyelidikan ini adalah untuk meningkatkan prestasi seismik jambatan kabel tetap dengan menggunakan sistem kawalan pasif hibrid, yang merupakan gabungan pengasingan seismik dan peredam logam yang baru untuk meminimumkan kerosakan pada masa akan datang yang mungkin disebabkan oleh gempa bumi. Pada mulanya, model jambatan kabel tetap telah dibangunkan dengan ketepatan tinggi dalam tiga dimensi dan disahkan dengan hasil eksperimen. Kemudian, senario pengasingan seismik yang berbeza ditentukan dan sistem pengasingan yang berbeza telah direka untuk setiap senario yang sewajarnya. Selepas itu, peredam logam yang baru, yang dikenali sebagai peredam keluli lebah

heksagon, telah direka dan dibangunkan secara eksperimen dan berangka untuk menentukan kelakuan dan ciri-cirinya. Akhir sekali, peredam yang dicadangkan direka dan dimodelkan untuk jambatan kabel tetap yang terasing sepenuhnya. Tindak balas seismik bagi setiap kes pengubahsuaian jambatan kabel tetap ditaksir melalui satu siri analisis sejarah-masa tidak linear. Analisis perbandingan menunjukkan bahawa pengasingan seismik separa bagi jambatan kabel tetap meningkatkan prestasi kelakuan seismik dalam satu arah sahaja. Untuk meningkatkan prestasi seismik jambatan kabel tetap di kedua-dua arah, sistem pengasingan harus digunakan pada sokongan akhir, serta pada sambungan menara dek atau pada tapak bagi menara. Tindak balas seismik global dan tempatan bagi jambatan kabel tetap yang terasing sepenuhnya meningkat dengan ketara berbanding jambatan yang tidak terasing. Walau bagaimanapun, anjakan seismik superstruktur meningkat bagi jambatan yang terasing sepenuhnya. Keputusan ujian kitaran kuasi-statik bagi peredam mempamerkan anjakan hasil yang rendah, kekuatan dan kemuluran yang sangat baik, dan tingkah laku histerisis yang stabil dengan keupayaan menyerap tenaga yang tinggi. Hasilnya, pelaksanaan peredam logam sepenuhnya di jambatan terpencil telah menyebabkan pengurangan ketara dalam anjakan superstruktur di bawah beban gempa bumi, yang juga menghapuskan kesan godaman akibat-gempa di hujung jambatan dengan tembok landas bersebelahan. Sistem kawalan pasif hibrid adalah berguna dalam melindungi jambatan kabel tetap yang berada di zon seismik berisiko tinggi. Sistem ini mengurangkan keperluan seismik ke atas struktur dan mengurangkan anjakan seismik bagi superstruktur serta kemungkinan godaman yang disebabkan oleh gempa bumi di jambatan.

Kata kunci: Jambatan kabel tetap; Prestasi seismik; Kawalan pasif; Peredam logam; Analisis dinamik tidak linear.

ACKNOWLEDGEMENTS

First and foremost, I am thankful to God for blessing me with an opportunity and able me to undertake this research work. I would express my sincere gratitude to my supervisor, Assoc. Prof. Zainah Ibrahim, for her kind and continuous support that has encouraged me to pursue my research curiosity. Her deep insight into the research area has greatly kept me on the right track of my research work. Through her profound and conscientious discussions offered to me, I have mastered a great deal of knowledge and greatly broadened my views on research. From her valuable and meticulous guidance, I have immensely developed my effective brainstorming, planning and scheduling skills. Her logic thinking, research enthusiasm, and deep insight has inspired me and will be of great benefits to my life-long study.

Special thanks to my dearest friend Mr. Khaled Ghaedi for his various contributions and support throughout my research.

Last but not least, I would like to extend my thanks to my beloved father, mother and my only brother, for their endless love, support, and encouragement. I am forever indebted to my family for giving me the opportunities and selflessly encouraging me to experience and explore new directions in my life. This journey would not have been possible without them and I proudly dedicate this milestone to them.

TABLE OF CONTENTS

Abstract	iii
Abstrak	v
Acknowledgements	vii
Table of Contents	viii
List of Figures	xiv
List of Tables	xxiii
List of Symbols and Abbreviations	xxv
 CHAPTER 1: INTRODUCTION	1
1.1 Introduction	1
1.2 Problem statement	2
1.3 Objectives of study	3
1.4 Scope of study	3
1.5 Research methodology	6
1.6 Significance of study	9
1.7 Outline of thesis	10
 CHAPTER 2: LITERATURE REVIEW	12
2.1 Introduction	12
2.2 Background	12
2.2.1 Classification of the cable-stayed bridges	12
2.2.2 Structural component of cable-stayed bridges	14
2.3 Seismic response of cable-stayed bridges	16
2.3.1 Modes of vibration	17
2.3.1.1 Pure vertical modes of deck	17

2.3.1.2	Pure torsional modes of deck	18
2.3.1.3	Transverse modes of deck	20
2.3.1.4	Tower modes	20
2.3.1.5	Stay cable interaction with bridge structure	21
2.3.2	Damping	23
2.3.2.1	Damping mechanisms of cable-stayed bridges	24
2.3.2.2	Practical simulation of damping sources	25
2.3.3	Dynamic analysis procedures	26
2.3.3.1	Inelastic seismic analysis procedures	26
2.3.3.2	Elastic seismic analysis procedures	28
2.3.3.3	Recommended analysis procedure for cable-stayed bridges	30
2.3.4	Seismic response of the towers	30
2.3.5	Deck-Tower and deck-piers connections	30
2.3.6	Soil-structure interaction	31
2.3.7	Seismic behavior of multiple-span cable-stayed bridges	32
2.4	Comparison of capacity design with mitigation design	33
2.5	Mitigation design	35
2.5.1	Seismic isolation	37
2.5.1.1	High damping rubber bearing	37
2.5.1.2	Lead-rubber bearing	38
2.5.1.3	Friction pendulum system	38
2.5.2	Passive energy dissipaters	39
2.5.3	Metallic dampers	41
2.5.3.1	Hysteresis behaviour of metallic dampers	42
2.5.3.2	Classification of metallic dampers:	43
2.5.3.3	Application	60

2.5.3.4	Fatigue life of metallic dampers	63
2.5.3.5	Specific advantages and disadvantages of yielding metallic dampers	64
2.6	Vibration control of cable-stayed bridges.....	65
2.6.1	Passive control devices.....	65
2.6.2	Active and semi active control devices	68
2.7	Summary.....	69
 CHAPTER 3: GLOBAL SEISMIC RESPONSE OF PARTIAL AND FULL ISOLATIONS OF THE CABLE-STAYED BRIDGE BY LEAD RUBBER BEARINGS.....		71
3.1	Introduction.....	71
3.2	Description of the cable-stayed bridge	71
3.3	Methodology.....	73
3.3.1	Structural modeling of the bridge.....	73
3.3.2	Experiment and validation of FEM	75
3.3.3	Pushover analysis of the cable-stayed bridge.....	77
3.3.4	Equations of motion	78
3.3.5	Nonlinear time-history analysis.....	78
3.3.5.1	Ground motions critria	79
3.3.5.2	Ground motion selection	79
3.3.6	Seismic isolation of cable-stayed bridge	81
3.3.6.1	Design and modelling of seismic isolators.....	81
3.3.6.2	Seismic isolation retrofitting cases of cable-stayed bridge	85
3.4	Results and discussion	87
3.4.1	Results of pushover analysis	87
3.4.2	Results of modal analysis	88

3.4.3	Results of time-history analysis:	90
3.4.3.1	Bridge displacement	90
3.4.3.2	Base shear	92
3.4.3.3	Base moment	94
3.4.3.4	Cable response	96
3.4.3.5	Hysteresis response of bridge	99
3.4.4	Overall seismic response	100
3.5	Conclusions	102

CHAPTER 4: SEISMIC RESPONSE CHARACTERISTICS OF THE FULLY ISOLATED CABLE-STAYED BRIDGE UNDER MODERATE TO MAJOR EARTHQUAKES.....104

4.1	Introduction.....	104
4.2	Ground motion selection.....	105
4.3	Results and discussion	106
4.3.1	Deck displacement and acceleration	106
4.3.2	Base shear	108
4.3.3	Base Moment.....	109
4.3.4	Tower response.....	110
4.3.4.1	Tower shear force	110
4.3.4.2	Tower bending moment	112
4.3.4.3	Tower axial force	113
4.3.5	Cable response.....	115
4.3.6	Hysteresis curves of isolators	116
4.3.7	Overall dynamic performance	117
4.4	Conclusions	120

CHAPTER 5: DEVELOPMENT OF A NEW YIELDING METALLIC DAMPER.....121

5.1	Introduction.....	121
5.2	Theoretical approach	124
5.3	Experimental study	126
5.3.1	Coupon test.....	126
5.3.2	Quasi-static cyclic test.....	127
5.3.2.1	Test setup.....	128
5.3.2.2	Parametric study.....	129
5.3.3	Experimental results and discussion.....	130
5.3.3.1	Tensile test results	130
5.3.3.2	Parametric study test results.....	132
5.4	Numerical analysis.....	148
5.4.1	Finite element modeling.....	148
5.4.2	FEA results	150
5.5	HHSD characteristic formula	156
5.6	Conclusions	157

CHAPTER 6: SEISMIC RESPONSE OF THE CABLE-STAYED BRIDGE EQUIPPED WITH HYBRID PASSIVE CONTROL SYSTEMS.....158

6.1	Introduction.....	158
6.2	Methodology.....	161
6.2.1	Thermal movement of the bridge	161
6.2.2	Abutment stiffness.....	161
6.2.3	HHSD design procedure.....	161
6.2.4	Constitutive model	164
6.2.5	Modeling in SAP2000	166

6.2.5.1	Gap element.....	166
6.2.5.2	Damper element	167
6.2.6	Ground motion selection	168
6.3	Results and discussion	170
6.3.1	Displacement and velocity	171
6.3.2	Base shear	174
6.3.3	Pounding force	176
6.3.4	Hysteresis curves of energy dissipaters	179
6.4	Conclusions	181
CHAPTER 7: CONCLUSIONS.....		183
7.1	Concluding remarks.....	183
7.2	Recommendations of future works.....	184
References		186
List of Publications and Papers Presented		201

LIST OF FIGURES

Figure 1.1: Shipshaw cable-stayed bridge	4
Figure 1.2: Seismic hazard map of Canada (Natural Resources of Canada, 2015)	5
Figure 1.3: Damage to the Shipshaw Bridge due to 1988 Saguenay earthquake (Filiatrault et al., 1993a, 1993b).....	5
Figure 1.4: Research methodology flowchart of the research.....	8
Figure 2.1: Main cable arrangement types in cable-stayed bridges.....	13
Figure 2.2: Different pylon geometries of cable-stayed bridges.....	13
Figure 2.3: Elastic response of structures with and without cable systems	16
Figure 2.4: Ideal models of deck and cables in terms of torsional and vertical frequencies (Gimsing, 1998)	19
Figure 2.5: Relative phase error as a function of the step-time ratio and vibration period ($\Delta t=T$) in several direct integration methods (Hilber et al., 1977).....	27
Figure 2.6: a) Diagonal and b) intersected cables stiffening in multiple-span cable-stayed bridges (Virlogeux, 2001)	33
Figure 2.7: Summary of control strategies in the seismic design of structures with few seismic devices (Huber & Medeot, 2005).....	34
Figure 2.8: Mitigation design objectives ([1] fundamental period elongation and [2] damping increment) recommended by Eurocode 8 (2004).....	35
Figure 2.9: Schematic view of high damping rubber bearing.....	38

Figure 2.10: Schematic view of lead-rubber bearing	38
Figure 2.11: Schematic view of friction pendulum system.....	39
Figure 2.12: Idealized Hysteresis behavior of a) metallic and b) SMA materials	43
Figure 2.13: a) U-Shaped steel, b) Torsional beam, c) Flexural beam, d) Single-axis e) Tapered cantilever and f) Taper Tube dampers	44
Figure 2.14: Schematic views of a) BRB, b) ARBRB (Zhao et al., 2011), c) different BRB core configurations and d) SUB (X.-Y. Hao et al., 2014).....	46
Figure 2.15: Steel plate-based dampers	48
Figure 2.16: Steel shear panel-based dampers. a) SPD, b) SSPD, c) YSPD, d) SAFYD and e) BRSPD (Deng et al., 2015)	50
Figure 2.17: Detailing of a) J-damper, b) Crawler damper and c) Cushion damper.....	51
Figure 2.18: Detailing of dampers proposed by Benavent-Climent (Benavent-Climent, 2010; Benavent-Climent et al., 2015)	52
Figure 2.19: Schematic view of pipe-based dampers, a) PD, b) DPD, c) IPD, d) TTD and e) VPD.....	53
Figure 2.20: Detailing of: a) EPSD (W. Hao et al., 2012), b) BRRPD (Yamazaki et al., 2016) c) AMD and d) FBD (Aghlara & Tahir, 2018).....	55
Figure 2.21: The aluminum shear-yielding damper	56
Figure 2.22: Lead dampers.....	57
Figure 2.23: Copper dampers. a) Plate and b) Round hourglass dampers	58

Figure 2.24: Schematic views of: a) SMA frame damper, b) SMA bar damper and c) RHD	59
Figure 2.25: Schematic view of self-centering SMA dampers (Dolce et al., 2000; Ma & Cho, 2008)	60
Figure 2.26: Schematic locations for the installation of metallic dampers in civil structures	62
Figure 2.27: Metallic damper fatigue life prediction	64
Figure 2.28: Plan view of proposed damper for the Vasco da Gama cable-stayed bridge (Branco et al., 2000)	66
Figure 2.29: FVD installation in a long-span cable-stayed bridge (Zhu et al., 2015)	67
Figure 3.1: Shipshaw cable-stayed bridge detailing	72
Figure 3.2: Three-dimensional finite element model of Shipshaw cable-stayed bridge	73
Figure 3.3: Stress-strain curves of steel and concrete materials used for modeling	74
Figure 3.4: Four flexural mode shapes of the cable-stayed bridge	76
Figure 3.5: Acceptance criteria of the plastic hinges defined by FEMA-273 (1997)	77
Figure 3.6 a) Spectral displacement and b) spectral acceleration of five earthquakes for the cable-stayed bridge with 5% of structural damping	80
Figure 3.7: Design flowchart of the seismically isolated bridge	83
Figure 3.8: Detailing and idealized hysteresis behavior of Lead Rubber Bearing (LRB)	84

Figure 3.9: Schematic hysteretic property of LRB in biaxial shear deformation (Computers and Structures Inc., 2015)	85
Figure 3.10: Results of pushover analysis of the bridge	88
Figure 3.11: Implementation effect of base isolators on the natural time periods of the bridge.....	89
Figure 3.12: Maximum bridge displacement under earthquake excitations	91
Figure 3.13: Maximum base shear response of towers subjected to earthquake excitations	94
Figure 3.14: Maximum base moment response of bridge subjected to earthquake excitations	95
Figure 3.15: Maximum cable tension forces of the bridge under earthquake excitations	97
Figure 3.16: Force-Displacement hysteresis curves of the bridge subjected to S. Dicky earthquake	88 99
Figure 4.1: Finite element model of the fully isolated cable-stayed bridge.....	105
Figure 4.2: a) Acceleration and b) displacement spectra of ground motions in longitudinal and transverse directions applied to the bridge considering 5% damping	106
Figure 4.3: Peak response of deck displacement during earthquake excitations in longitudinal and transverse directions.....	107
Figure 4.4: Acceleration time-history of the deck under Cape Mendocino earthquake excitation	108

Figure 4.5: Base shear peak response of the bridge during earthquake excitations in longitudinal and transverse directions.....	109
Figure 4.6: Maximum base moment response of the bridge under earthquake excitations in longitudinal and transverse directions.....	110
Figure 4.7: Maximum shear force response of the tower along its height under different ground motions	111
Figure 4.8: Bending moment distribution along the tower height in both directions under different ground motions.....	113
Figure 4.9: Maximum relative axial force of the tower along its height under different ground motions in both directions.....	114
Figure 4.10: Maximum tension forces of the cables during earthquake excitations in longitudinal and transverse directions.....	116
Figure 4.11: Force-Displacement hysteresis curve of the selected LRB at the left abutment	117
Figure 5.1: HSSD detailing and prototype.....	122
Figure 5.2: Schematics of HHSD implementation in various structures	123
Figure 5.3: Schematic of HHSD implementation in a bridge	123
Figure 5.4: a) Detailed schematics of a honeycomb structure and b) honeycomb deformation under shear load.....	124
Figure 5.5: Detailing of dog bone specimen based on ASTM-E8 2015 (all units are in mm)	126

Figure 5.6: The IPC UTM-1000 used for the tensile test.....	127
Figure 5.7: Loading protocol used for the quasi-static cyclic test on HHSD	128
Figure 5.8: HHSD experimental test setup	129
Figure 5.9: Stress-Strain curves for three samples obtained from the tensile test	131
Figure 5.10: Failure of dog bone samples after the coupon tensile test.....	131
Figure 5.11: Force-displacement hysteresis curve of steel material	132
Figure 5.12: Typical HHSD hysteresis curves.....	134
Figure 5.13: Sequence of plastic hinge formation in HHSD No. 1.....	134
Figure 5.14: Effect of depth on the force-displacement hysteretic behavior of HHSDs	136
Figure 5.15: a) Effect of depth on dissipated energy and viscous damping ratio, b) cumulative energy dissipated by HHSDs.....	137
Figure 5.16: HHSD failure mode related to the depth parameter	137
Figure 5.17: Effect of thickness on the force-displacement hysteretic behavior of HHSDs	138
Figure 5.18: a) Effect of thickness on dissipated energy and viscous damping, b) cumulative energy dissipated by HHSDs.....	139
Figure 5.19: HHSD failure mode related to the thickness parameter	139

Figure 5.20: Effect of height on the force-displacement hysteretic behavior of HHSDs	141
Figure 5.21: a) Effect of height on dissipated energy and viscous damping ratio, b) cumulative energy dissipated by HHSDs	142
Figure 5.22: HHSD failure mode related to the height parameter	142
Figure 5.23: Effect of cell size on the force-displacement hysteresis behavior of HHSDs	143
Figure 5.24: a) Effect of cell size on dissipated energy and viscous damping ratio, b) cumulative energy dissipated by HHSDs	144
Figure 5.25: HHSD failure mode related to the cell size parameter	145
Figure 5.26: Force-displacement hysteresis behavior of HHSD No.1, 11 and 12	146
Figure 5.27: a) Dissipated energy and viscous damping ratio, b) cumulative energy dissipated by HHSD No. 1, 11 and 12	147
Figure 5.28: Failed specimens at maximum load: a) HHSD No. 1, b) HHSD No. 11 and c) HHSD No. 12	147
Figure 5.29: a) FE model and b) HHSD mesh detailing in Abaqus software	148
Figure 5.30: Experimental and FEA result comparison	151
Figure 5.31: Equivalent damping ratio vs normalized stiffness for the HHSD models	154
Figure 5.32: Comparison of the failure mechanism in HHSD No. 1 according to FEA and the experiment	154

Figure 5.33: In-plane and out-of-plane hysteretic behavior of HHSDs	156
Figure 6.1: Schematic configuration of the passive hybrid control system in the cable-stayed bridge	160
Figure 6.2: HHSD design flow chart for isolated cable-stayed bridges.....	163
Figure 6.3: Bilinear force-displacement curves of the designed HHSDs	164
Figure 6.4: Mathematical model of hybrid passive control system in a single-degree-freedom system	165
Figure 6.5: Link element with the gap property in SAP2000	166
Figure 6.6: Nonlinear link element representing the HHSD in SAP2000	167
Figure 6.7: Finite element model of the bridge equipped with hybrid passive control systems.....	168
Figure 6.8: Scaled acceleration response spectra of ground motions adopted for analysis	170
Figure 6.9: Scaled time-history accelerogram of a) earthquake No. 1 and b) earthquake No. 5.....	170
Figure 6.10: Maximum seismic displacement of the bridge at the deck-tower connection	172
Figure 6.11: Displacement time-history response of the bridge at the deck-tower connection under earthquake No. 1.....	173

Figure 6.12: Velocity time-history response at the top of the tower under earthquake No. 1	174
Figure 6.13: Maximum base shear of the bridge with different control systems.....	175
Figure 6.14: Base shear time-history response of the bridge under earthquake No. 1 .	176
Figure 6.15: Maximum pounding force on the bridge at the left abutment	177
Figure 6.16: Maximum pounding force on the bridge at the right abutment.....	177
Figure 6.17: Pounding time-history response of the bridge at the left abutment subjected to earthquake No. 5	179
Figure 6.18: Pounding time-history response of the bridge at the right abutment subjected to earthquake No. 5	179
Figure 6.19: Hysteresis loops of control systems at the bridge ends in different cases	181
Figure 6.20: Hysteresis loops of control systems at the tower in different bridge cases	181

LIST OF TABLES

Table 3.1: Calculated cables' tension forces the cable-stayed bridge.....	75
Table 3.2: Natural time periods of the cable-stayed bridge (Filiatrault et al., 1993b)....	76
Table 3.3: Ground motions characteristics.....	80
Table 3.4: Different retrofitting cases with schematic locations of isolation systems....	86
Table 3.5: LRBs' characteristics used in numerical analysis.....	87
Table 3.6: Fundamental period of the bridge	89
Table 3.7: Summary of seismic responses of the bridge for different retrofitting cases	101
Table 4.1: Ground motion records characteristics	106
Table 4.2: Peak absolute acceleration response of the bridge deck under different ground accelerations.....	108
Table 4.3: Summary of maximum seismic responses of the non-isolated and isolated cable-stayed bridge.....	119
Table 5.1: Details of the loading protocol in the quasi-static cyclic test	128
Table 5.2: HHSD details for the experimental parametric study.....	130
Table 5.3: Coupon tensile test results	131
Table 5.4: Quasi-static cyclic test result summary	135
Table 5.5: Material properties used in FE modeling.....	149

Table 5.6: FEA result summary	151
Table 5.7: Comparison of theoretical values with FEA results (units: mm, kN).....	155
Table 6.1: Designed HHSD dimensions for the isolated cable-stayed bridge	164
Table 6.2: Characteristics of ground motions selected from PEER (2017)	169

University of Malaya

LIST OF SYMBOLS AND ABBREVIATIONS

A, β, γ	: Dimensionless quantities
$\delta_{y,t}$: Yield displacement of HHSD
ξ_d	: Damping ratio of HHSD
ξ_{isol}	: Damping ratio of isolator
$\bar{\sigma}$: Equivalent stress
σ_y	: Yield stress
μ	: Ductility
μ_{cum}	: Cumulative displacement ductility
α	: Coefficient of thermal expansion
Δ_{cum}	: Cumulative displacement
Δ_T	: Design thermal movement
Δ_u	: Ultimate displacement
Δ_y	: Yield displacement
ε	: Strain
ζ	: Equivalent viscous damping
$\zeta_{eq(hybrid)}$: Damping ratio of hybrid control system
ζ_{eq1}	: Effective damping of isolated bridge
σ_m	: Mean stress
ΔL	: Elongation ratio
δ	: Deflection
η	: Stress triaxiality
ϑ	: Poison ratio
$[\eta]$: Earthquake coefficient matrix
$[C]$: Damping matrix of structure

$[D]$: Location matrix of the restoring force of isolator or hybrid control system
$[F]$: Restoring force matrix of isolator or hybrid control system
$[K]$: Stiffness matrix of structure
$[M]$: Mass matrix of structure
$\{\dot{u}\}$: Relative velocity vector
$\{\ddot{u}\}$: Relative acceleration vector
$\{\ddot{x}_g\}$: Earthquake acceleration vector in principal direction
$\{f\}$: Restoring force of hybrid control system
$\{u\}$: Relative displacement vector
A_0	: Original area
A_f	: Austenitic temperature
B	: Lateral distance between cable planes
C_{cp}	: Vertical stiffness of each plane of cable
C_y	: Ratio of main to side span length
$d_{in.}$: Initial assumed displacement
D	: Depth of HHSD
d	: Total displacement of isolated bridge
d_{isol}	: Isolator displacement
d_{sub}	: Substructure displacement
d_y	: Isolator yield displacement
E	: Young's elasticity modulus
E_D	: Energy dissipated
E_s	: Strain energy
F^Y	: Yield force of isolator
f	: Frequency of loading

F	: Force
F_{isol}	: Isolator shear force
f_s	: Stiffness component of the force vector
f_v	: First vertical frequency of deck
f_y	: First transverse frequency of deck
G	: Shear modulus
h	: Seating height of abutment in Chapter 6
h, l	: Side dimensions of unit cell of HHSD in Chapter 5
I	: Moment of inertia
I_H	: Transverse moment of inertia of deck
$I_{m,x}$: Deck torsional mass amount of inertia
K	: Longitudinal stiffness of abutment
K_I	: Stiffness of isolated bridge
K_d	: Post-yield stiffness of isolator in Chapter 3
K_d	: Stiffness of HHSD in Chapter 5
K_{eff}	: Effective stiffness
k_G	: Stiffness of gap element
K_{hybrid}	: Stiffness of hybrid control system
K_{isol}	: Effective stiffness of isolator
K_u	: Elastic stiffness
L	: Span length
L_0	: Original length
L_p	: Main span length
m	: Mass of deck per unit length
M_d	: Deck mass
N_f	: Number of cycles to failure

$n_{x,y}$: Numbers of vertical cells in X and Y directions
P	: Applied force
P_u	: Ultimate strength
$P_{y,d}$: Yield force of unit cell of HHSD
$P_{y,t}$: Total yield force of HHSD
Q_d	: Characteristics strength of isolator
S_{Dl}	: Design spectral displacement
T	: Fundamental period of structure
t	: Thickness of HHSD
T_D	: EC8 corner vibration periods for design spectra
T_{eff}	: Effective period
T_{Max}	: Maximum designed temperature
T_{Min}	: Minimum designed temperature
$U_{2,3}$: Bearing displacement in 2 and 3 directions (local direction)
$U_{x,y,z}$: Support translation in X,Y, and X directions
W	: Superstructure weight
$W_{abut.}$: Width of abutment
ABRB	: Angle buckling-restrained brace
ADAS	: Added damping and stiffness
AMD	: Active mass damper
BRB	: Buckling-restrained brace
BRRPD	: Buckling-restrained rippled plate damper
BRSPD	: Buckling restrained shear panel damper
CQC	: Complete quadratic combination
CTF	: Comb-teeth damper

DPD	: Dual-pipe damper
EPSD	: Elastic-plastic steel damper
FD	: Friction damper
FEA	: Finite element analysis
FEM	: Finite element method
FPS	: Frictional pendulum system
HDR	: High-damping rubber bearing
HHSD	: Hexagonal honeycomb steel damper
IPD	: Infilled-pipe damper
LRB	: Lead rubber bearing
LVDT	: Linear variable differential transformer
MD	: Metallic damper
MDOF	: Multi-degree of freedom
MECS	: Multi element cable-system
MRD	: Magneto-rheological dampers
MRSA	: Modal response spectrum analysis
OECS	: One element cable-system
PB-FREI	: Partially bonded fiber-reinforced elastomeric isolator
PD	: Pipe damper
PGA	: Peak ground acceleration
PYSPD	: Perforated yielding shear panel damper
RB	: Rubber bearing
RHD	: Reusable hysteretic damper
RNC	: Roll-n-Cage isolator
SAFYD	: Shear-and-flexural yielding damper
SDOF	: Single-degree of freedom

SI	: International system of units
SMA	: Shaped memory alloy
SPD	: Shear panel damper
SSD	: Slit steel damper
SSPD	: Stiffened shear panel damper
SUB	: Steel unbuckling brace
TADAS	: Triangular-plate added damping and stiffness
TITD	: Tube-in-tube damper
TLD	: Tuned liquid damper
TMD	: Tuned mass damper
TTD	: Torsional pipe damper
ULM	: Unit load method
VE	: Viscoelastic
VPD	: Vertical pipe damper
YSPD	: Yielding shear panel damper

CHAPTER 1: INTRODUCTION

1.1 Introduction

The numbers of cable-stayed bridges construction have been increasing dramatically over the past few decades. Such bridge may consist of one or more pylons, which hold the stay cables from the bridge deck. The cables act as additional support to the bridge deck, hence minimizing the need for bridge piers. Their advantages such as longer span length, aesthetically appealing, fast construction rate, highly efficient load resistance, lightweight and small structural members make these among the most popular types of bridges nowadays. Nonetheless, they are associated with low structural damping and longer natural periods, which make them highly flexible and susceptible to large amplitude oscillation under dynamic loadings, such as wind, earthquake excitations, strong wind loads and traffic loads (Ali & Abdel-ghaffar, 1994, 1995). These characteristics make cable-stayed bridges extremely vulnerable to structural damage and catastrophic failure. For example, one of the anchorage plates in the support of the Shipshaw Cable-Stayed Bridge failed in 1988 due to overstress induced by seismic loadings. In addition, it was also reported that the pounding of the bridge with the end abutments caused severe damage in the Shipshaw Bridge (Filiatrault et al., 1993a, 1993b). Moreover, the Kobe earthquake in 1995 struck the Higashi-Kobe Bridge and caused several failures in different structural components of the bridge (Kitazawa et al., 2000). Another cable-stayed bridge that was damaged due to seismic activity is the Chi-Lu Bridge. This bridge was almost completed when the 1999 Chi-Chi earthquake ($M_w = 7.3$) occurred. It was reported that severe damage occurred in the deck, while the pylon below the deck suffered moderate cracks and significant concrete spalling at the pylon-cable connections (Chang et al., 2004). Thus, it can be concluded that understanding the seismic behavior and protecting cable-stayed bridges are essential to prevent such damage and failure in these types of structures.

The mitigation design is a promising solution for seismic retrofitting of existing structures. Structural control systems have been developed and implemented widely in various types of structures, to mitigate the vibrational response of structures due to different dynamic loadings. Seismic isolation such as lead rubber bearings are also implemented in structures like buildings and bridges. An isolation system elongates the fundamental period of the structure, hence reducing its seismic demand. Nonetheless, it also increases the seismic displacement of the superstructure. Hence, hysteresis devices are proposed to mitigate the seismic displacement of the superstructure. A hybrid passive control system comprises an isolation system and hysteresis devices, thus benefitting from both systems to reduce the structure's vibrational response (Skinner et al., 1974).

1.2 Problem statement

Bridges are key for transportation systems in this modern world. Some of the bridges, particularly cable-stayed bridges, are susceptible to large amplitude oscillation under seismic loads because of their low structural damping and longer fundamental periods. For instance, the Shipshaw Bridge, Higashi-Kobe Bridge, Ji Lu Bridge, Chi-Lu Bridge, Tsurumi Tsubasa Bridge and Yokohama-Bay Bridge have either failed or suffered severe damages from earthquake excitations. The protection of cable-stayed bridges from earthquakes has been challenging for engineers ever since. Moreover, cable-stayed bridge failure may be associated with human injury, losses and bridge serviceability disruptions in emergency after earthquake events. In order to minimize the potential damage and possible failure in cable-stayed bridges due to future earthquake excitations, the hybrid passive control system is proposed. This system consists of seismic isolator with a new yielding metallic damper called the Hexagonal Honeycomb Steel Damper (HHSD). In general, the seismic isolation system improves the seismic performance of the structure but also increases the superstructure's displacement during earthquakes. Therefore, in addition to seismic isolation, a new type of metallic damper with high ductility and energy

dissipation capability is applied in the cable-stayed bridge. The hybrid passive control system is made of seismic isolation system combined with a metallic damper that takes advantage of both systems. Here, the metallic damper acts as a fuse for the superstructure during earthquake excitations and mitigates the excessive seismic displacement of the superstructure. Besides, it prevents the likelihood of the earthquake-induced pounding phenomenon in the bridge.

1.3 Objectives of study

The main aim of this research is to enhance the seismic performance of the cable-stayed bridge in the longitudinal and transverse directions by implementing a hybrid passive seismic control system. To achieve the main aim, the following objectives shall be accomplished:

1. To identify the best seismic isolation case for retrofitting of the cable-stayed bridge subjected to ground motion accelerations.
2. To study the seismic characteristics of the fully isolated cable-stayed bridge under ground motion accelerations.
3. To develop a new metallic damper through experimentation and finite element analysis.
4. To evaluate the effectiveness of the hybrid passive control system on the seismic performance of the cable-stayed bridge.

1.4 Scope of study

Damage and failure have been reported in several cable-stayed bridges under seismic excitations. However, data availability for cable-stayed bridges is a challenge for modeling and verification proposes. In this research, the Shipshaw cable-stayed bridge is selected for the scope due to the availability of bridge details and the experimental result (Filiatrault et al., 1993a, 1993b). As Figures 1.1 and 1.2 show, the Shipshaw cable-

stayed bridge is located over the Saguenay River near Jonquiere city, Quebec Province, in a high-risk seismic zone of Canada. On 25 November 1988, this bridge experienced the Saguenay earthquake. The magnitude was $M_L=6.0$ with peak ground acceleration (PGA) of 0.15 g at Chicoutimi North Station, which is 15 km from the bridge site. As a result of seismic loading and stress concentration, one of the anchorage plates connecting the box girder to the East abutment failed as shown in Figure 1.3 (a). Besides, the earthquake-induced pounding due to the deck's longitudinal motion caused severe structural damage at the bridge ends (Figure 1.3 (b)), as reported by the Canadian National Committee on Earthquake Engineering inspection team (Filiatrault et al., 1993a, 1993b).



Figure 1.1: Shipshaw cable-stayed bridge

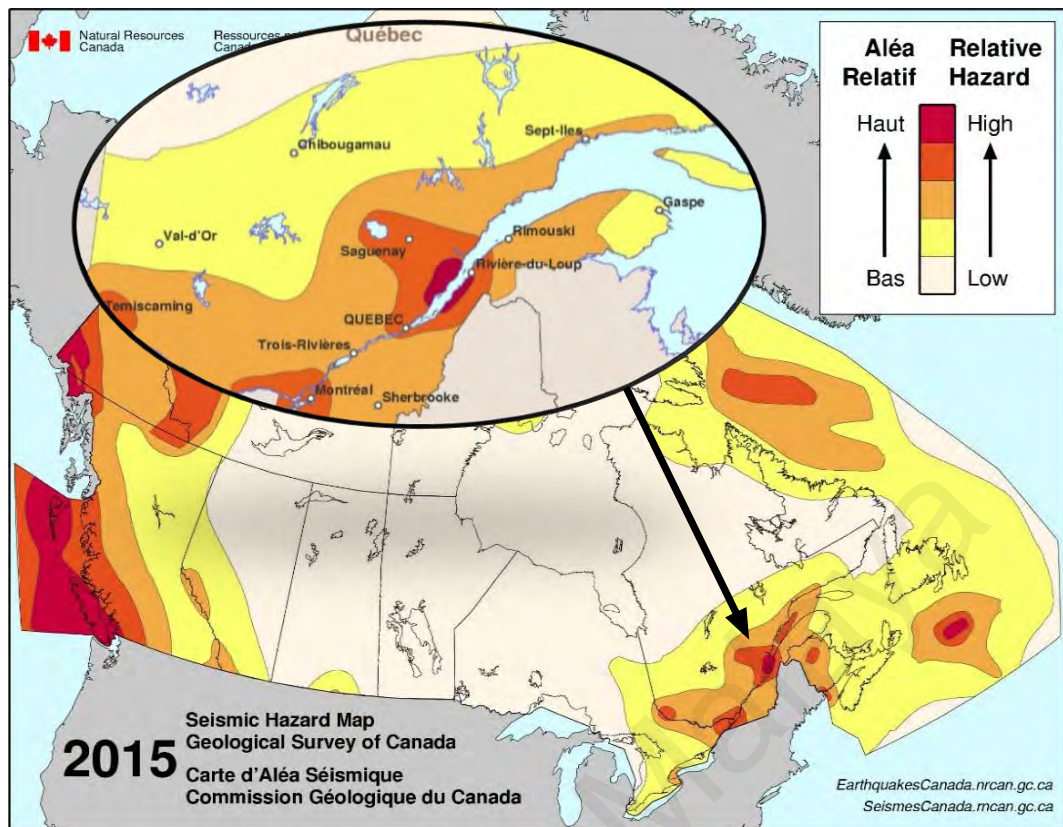


Figure 1.2: Seismic hazard map of Canada (Natural Resources of Canada, 2015)



a) Anchorage plate failure of the support at the East abutment



b) Damage to concrete cover at the West abutment

Figure 1.3: Damage to the Shipshaw Bridge due to 1988 Saguenay earthquake (Filiatrault et al., 1993a, 1993b)

1.5 Research methodology

To achieve the objectives of the research, several methodology stages are considered as follow:

- 1) The selected bridge is modeled in three dimensions using SAP2000 finite element software (Computers and Structures Inc., 2015) and validated with the previous experimental result. Different seismic isolator retrofitting cases are considered and seismic isolators are designed according to AASHTO (2010, 2012). A comparative study is performed to find the best seismic retrofitting case.
- 2) Based on the results of the first stage, the best retrofitting case is selected for further investigation. Once again, the seismic isolators are designed for moderate and strong earthquakes. The seismic performance of this bridge case and the original bridge is studied thoroughly using SAP2000 software.
- 3) The results of previous stages showed that the seismic displacement of isolated bridge significantly increased. Therefore, a new metallic damper is proposed (HHSD) to mitigate the unfavorable seismic displacement of the superstructure. The HHSD is developed and tested through the quasi-static cyclic test in the laboratory. In addition, a finite element model of the damper is created in Abaqus finite element software (Abaqus Inc., 2014) and validated with experimental results. A parametric study is performed on the damper to find its characteristics and behavior. Thereafter, the constitutive formulas of the damper are derived from results of experimental and numerical analyses.
- 4) At final stage, the hybrid passive control system (the combination of seismic isolator and the HHSD) is implemented in cable-stayed bridge to improve its seismic performance. In this stage, the design procedure of the HHSD for the fully isolated cable-stayed bridge is developed. Thereafter, the HHSD is designed and its properties are used to model the damper in the fully isolated bridge to compose

the hybrid passive control system. The effectiveness of bridge with hybrid control system is studied using SAP2000.

Figure 1.4 shows the flowchart of described methodology in this research. It should be noted that for each bridge retrofitting case, seismic performance of bridge is evaluated through a series of nonlinear time-history analyses. In each chapter, different ground motion records from minor to major earthquake class are used for the time-history analyses. This facilitates a wide range of analysis in evaluating the effectiveness of each seismic retrofitting strategy.

University of Malaysia

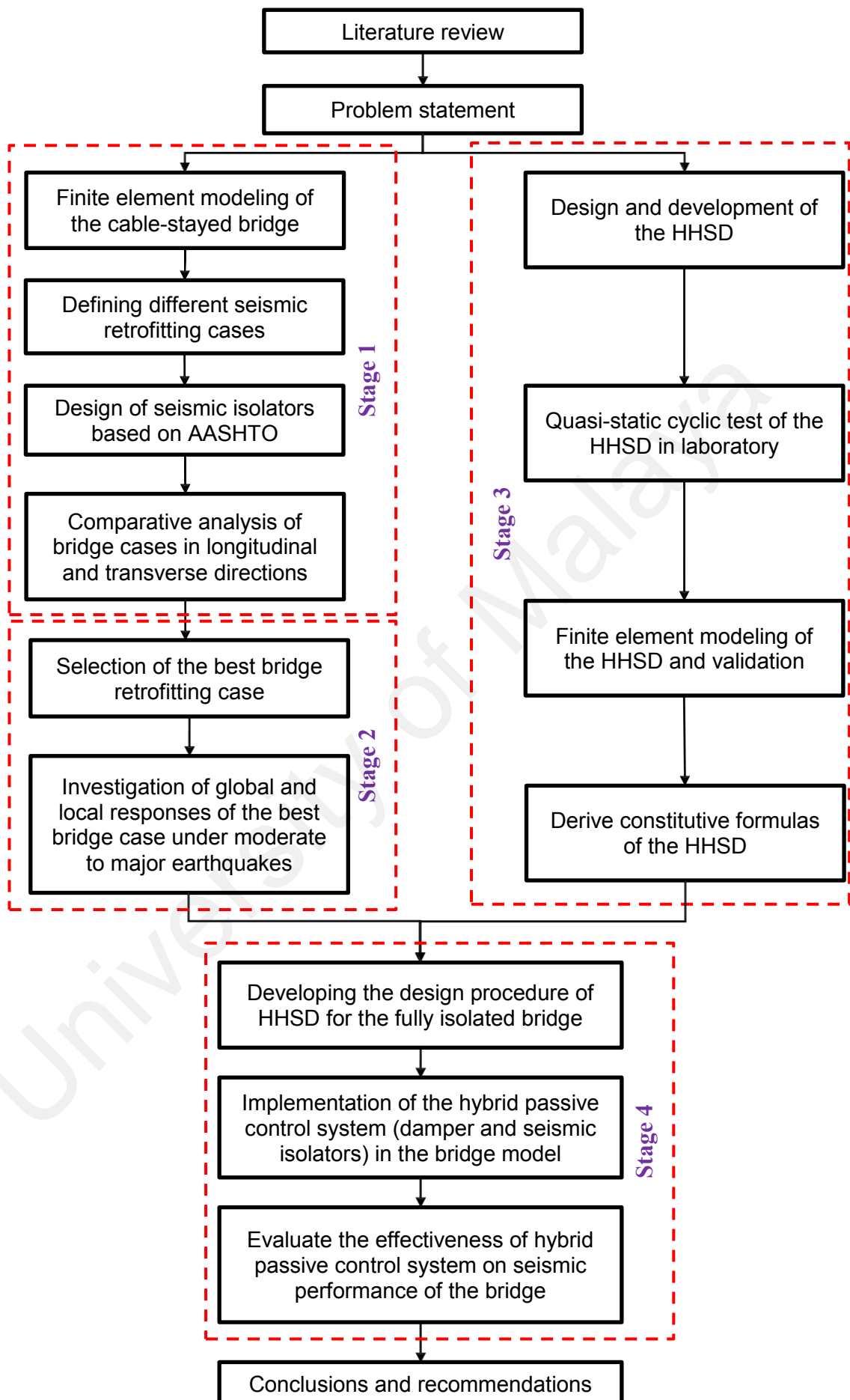


Figure 1.4: Research methodology flowchart of the research

1.6 Significance of study

The seismic protection of cable-stayed bridges is challenging for engineers due to the vulnerability of cable-stayed bridges to earthquake excitations. The passive control system appears to be one of the most affordable protection solutions for the seismic retrofitting of existing and new structures in earthquake prone zones. In contrast to active and semi-active control systems, the passive control system is inexpensive and protects the structure from seismic loads without any source of external energy and control algorithm during operation. In this research, a hybrid passive control system is proposed for the seismic retrofitting of bridges. The system is composed of the seismic isolation system and a new yielding metallic damper (HHSD). The HHSD takes the advantage of the honeycomb geometry and steel material in dissipating seismic energy. The seismic isolation helps enhance the seismic performance of the bridge and minimize seismic force transmission from the substructure to the superstructure. Furthermore, it reduces the seismic response demand on the piers and tower of the substructure. The metallic damper mitigates the seismic displacement of the superstructure and eliminates the earthquake-induced pounding phenomenon in the isolated structure. The locations of the dampers are chosen such that they can be inspected after earthquake events and replaced easily if required. In addition, the dampers can be utilized in different locations to distribute the supplemental damping accordingly to the cable-stayed bridge. The new metallic damper is inexpensive, rate independent, resistant to ambient temperature, reliable, highly ductile and with high energy dissipation capability. Thus, it acts as a fuse in the structure during earthquake events and can be easily replaced after failure.

1.7 Outline of thesis

This dissertation is presented in Article style format and divided into the following chapters:

Chapter 1 presents the background of the research and a description of the research problem, objectives, scope and significance.

Chapter 2 briefly reviews the dynamic behavior of cable-stayed bridges. Further, different dynamic analyses methods and recommendations for the seismic analysis procedure for cable-stayed bridges are explained. This chapter also includes a comprehensive review of different types of metallic dampers.

Chapter 3 describes the full detailing of the selected cable-stayed bridge and specification of the numerical modeling of the bridge, which is verified with experimental results. The modal and pushover analyses of the bridge are also described in this chapter. Furthermore, different seismic retrofitting cases are defined and seismic isolation systems are designed for each case. Subsequently, a comparative study of the seismic behavior of the bridge in the longitudinal and transverse directions is conducted through nonlinear time-history analysis.

Chapter 4 studies the seismic performance of the non-isolated and fully isolated cable-stayed bridges (global and local responses of the bridge) subjected to moderate and major ground motions.

Chapter 5 presents the development of the new yielding metallic damper proposed through experimental and numerical analyses. The constitutive formulas of the metallic damper are also derived.

Chapter 6 discusses the seismic performance of the cable-stayed bridge with the hybrid control system. The metallic damper is designed and modeled in the fully isolated bridge and its effectiveness is studied through a series of time-history analyses.

Chapter 7 presents a summary and major conclusions of the research with respect to each objective. Recommendations for future work are also given in this chapter.

University of Malaya

CHAPTER 2: LITERATURE REVIEW

2.1 Introduction

This chapter covers the background and various literatures involved in this study. The dynamic aspect and seismic response of the cable-stayed bridges is briefly discussed. In addition, the overall review of different control systems with emphasis on metallic damper is presented. Finally, different seismic control systems in the cable-stayed bridges is reviewed. The static behavior of cable-stayed bridges is well studied by several researchers, hence it is not covered in this research (Nazmy & Abdel-Ghaffar, 1990; Okamoto & Nakamura, 2011; Oliveira Pedro & Reis, 2010; Shattarat et al., 2008).

2.2 Background

The very first cable-stayed bridge was built from timber in 1784. However, the first significant cable bridge structure was a suspension bridge and the cable-stayed system was made of cast iron. At the end of the 19th century, the hybrid design and construction of cable-stayed bridges were induced. Nowadays, cable-stayed bridges are constructed widely with longer span lengths and enhanced materials.

2.2.1 Classification of the cable-stayed bridges

In general, cable-stayed bridges are classified based on stay cable arrangement, number of planes and pylon geometry. Figure 2.1 shows four major types of cable arrangements as follows:

- I. Mono: Only a single cable is attached to the tower and deck girder of the bridge. This is a rare case of a cable-stayed bridge.
- II. Harp: Cables from deck girders are connected to the tower in parallel with equal spacing. The harp arrangement offers a delicate appearance and less complexity, which makes it the most common type of cable-stayed bridge.

- III. Fan: Several cables from different points on the bridge girders are attached to a single point at the top of the tower.
- IV. Semi-Fan: Cables are connected at the top of the tower with close spacing. The semi fan arrangement generates minimum moment in the tower.

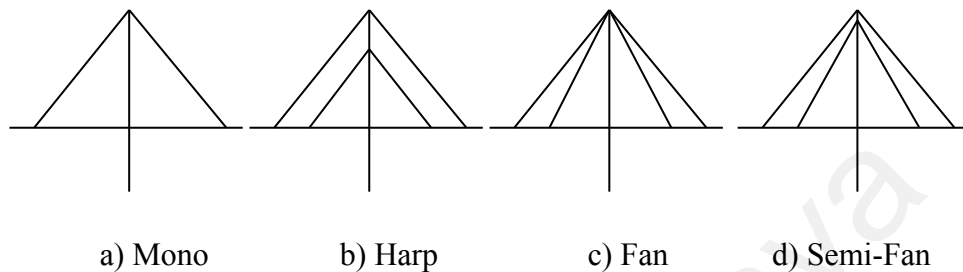


Figure 2.1: Main cable arrangement types in cable-stayed bridges

Based on the plane of the cables, they are classified as single plane or double plane. If the cables are arranged in a single plane on the tower, it is called a single plane cable-stayed bridge (Figure 2.2 (e)) and if the cables are arranged in two planes, it is called a double plane cable-stayed bridge (Figures 2.2 (a),(b),(c) and (d)). However, there may be more than two planes based on the architectural design and shape of the pylon (Figure 2.2 (f)). Figure 2.2 shows a few common pylon geometries constructed around the world.

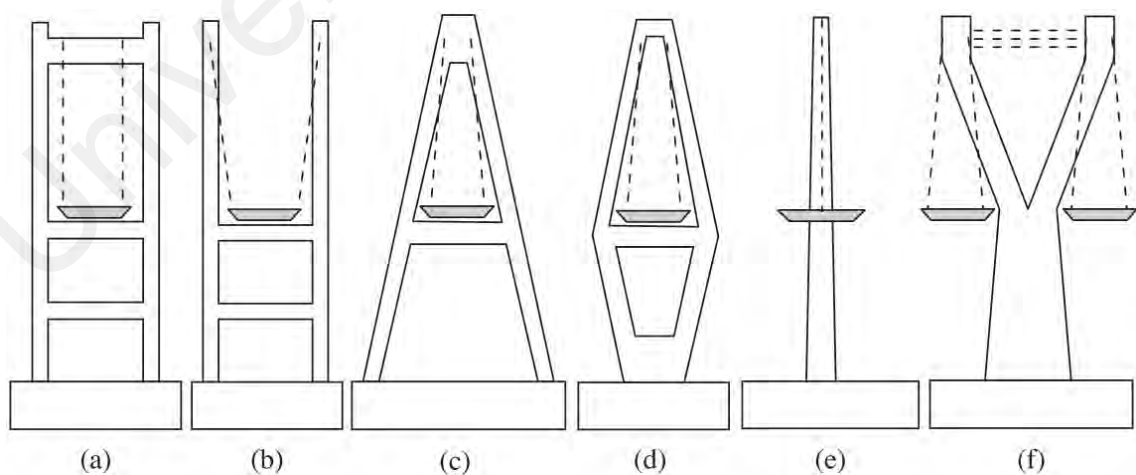


Figure 2.2: Different pylon geometries of cable-stayed bridges

2.2.2 Structural component of cable-stayed bridges

The main structural components of cable-stayed bridges are elaborated as follows:

1. Pylon (or tower):

In principle, pylons in cable-stayed bridges are tower structures. The aesthetic consideration of pylons is considerable for engineers. The pylon should be able to withstand heavy loads, which are axial forces generated by the cables. As mentioned earlier, pylons may have different shapes. The pylon base can be fixed or hinged. Fixed base pylons offer large bending moment at the base that increases pylon stiffness. On the other hand, a hinged base minimizes the tower's bending moment at the base and simplifies the analysis procedure.

Pylons are usually made of box sections that are strong against buckling, hence facilitating a significant reduction in material amount. Pylons may be made of steel, reinforced concrete or pre-stressed concrete. Steel pylons are fabricated and erected faster, whereas concrete pylons are more economical.

2. Deck (or girder):

The primary structural purpose of the deck is to carry vehicle and train loads. These loads are transferred through the deck to the stayed cables. Deck girders are constructed or assembled through the free cantilever method, which significantly reduces construction time and costs. Decks of cable-stayed bridges with a single central cable plain should have higher torsional stiffness, whereas for bridges with more than one cable plain the torsional stiffness is not crucial.

Nowadays, decks or girders are precast, thus increasing the rate of construction substantially. Decks are classified based on material as follows:

I. Concrete deck

Concrete decks may be precast or cast in situ. Precast concrete decks and girders reduce the construction time. They can be pre-stressed or posttensioned and the cost is relatively low. However, concrete increases the dead load of the bridge, which may lead to enlarged dimensions of piers, pylons, and cables.

II. Steel deck

Steel decks and girders are used widely in long span bridges. The advantages of steel decks are the lightweight and various possibilities for cross-section design.

III. Composite deck

Composite decks are made of concrete slabs with steel beams and stringers. This kind of deck is relatively lighter than concrete decks.

3. Cables:

Cables are the main elements in cable-stayed bridges. The stay cable technology has been developing considerably recently. A cable is composed of high-strength strand wires. Based on the cable-stayed bridge design, the diameter and number of strands may change. Strands have high tensile strength with high corrosion resistant. Cables are strong in tension but weak in compression and bending. They can be in tension up to 80% of their characteristic tensile strength. In addition, they are light, economical and can stand heavy loads.

Geometric nonlinearity plays an important role in the static and dynamic behavior of cable-stayed bridges. Material nonlinearity is also clearly distinguished in civil structures

as a significant analysis aspect. The geometric sources of nonlinearity are identified as: (i) the beam-column effect due to the combination of the axial load of towers and bending moment of girders, (ii) large displacement effect known as $P-\Delta$ effect and (iii) cable sag effect (Ali & Abdel-Ghaffar, 1995; Ren & Obata, 1999; Ren & Peng, 2005; Wang & Yang, 1996). The geometric nonlinearities introduced by stay-cables lead to the increase of the structural stiffness when demanding forces are enlarged, presenting cable-stayed bridges a slight geometric hardening in the elastic range which distinguishes this typology from the rest (Fleming & Egeseli, 1980; Karoumi, 1998). Although material nonlinearity dominates in the advanced demand stages, leading to stiffness degradation in conventional structures, geometric nonlinearity in cable-stayed bridges governs the structure's response in the early loading stages. Figure 2.3 shows the difference in the elastic response of cable-stayed structures and other types of structures. In this figure, area O-B is dominated by geometric nonlinearity and above area B is dominated by material nonlinearity (Alfredo Cámara Casado, 2011).

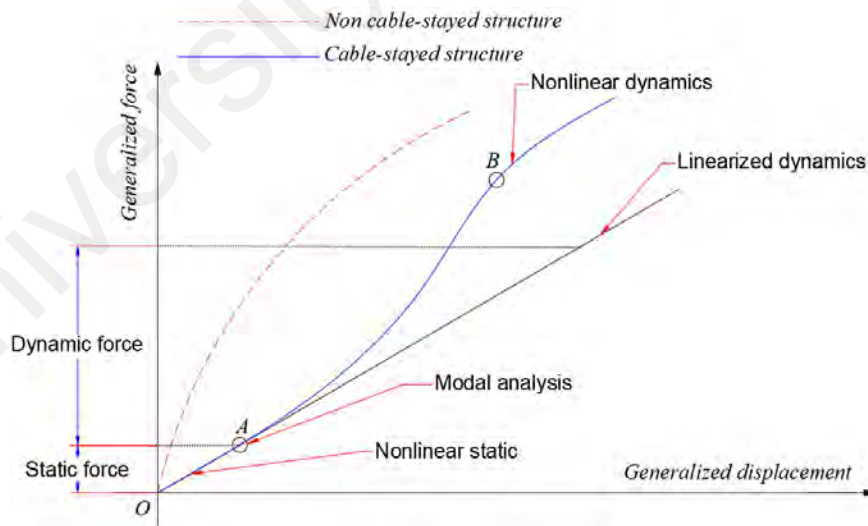


Figure 2.3: Elastic response of structures with and without cable systems

2.3 Seismic response of cable-stayed bridges

This section contains comprehensive details of the type and procedure of analysis of the dynamic and seismic behavior of cable-stayed bridges. Generally, cable-stayed

bridges are characterized by longer natural time periods with low spectral acceleration. The stayed cables act as elastic supports for the deck that dissipate forces generated from the vertical component of the earthquakes. On the other hand, cable-stayed bridges are associated with high flexibility and low structural damping, which make them vulnerable to large amplitude oscillations due to the horizontal components of the earthquakes.

2.3.1 Modes of vibration

The dynamic response characteristics rely on the vibration characteristics. Modal parameters, such as frequencies, participation factors, modal deformation and damping ratio are crucial parameters prior to the seismic response of any structure.

Cable-stayed bridges are complex structures whose vibration modes differ from other types of structures. Furthermore, these are associated with coupling modes, such as coupling between the transverse flexure and torsional response of the bridge. Modal coupling mostly governs when the main span of the bridge is longer than other. Moreover, modal analysis of cable-stayed bridges considers a large number of modes due to the structural complexity. Generally, the first vibration mode has a longer natural time period, where the deck contributes the most to the mode shape (1st flexural mode)(Bruno & Leonardi, 1997). The mode shapes involved in the modal analysis of cable-stayed bridges are briefly described in the following sections.

2.3.1.1 Pure vertical modes of deck

The vertical mode shape of decks in cable-stayed bridges is governed by the cable system. In addition, the main span length, the ratio of the side to the main span length and the tower height are parameters contributing to the vertical deck mode. Kawashima et al. (1993) proposed the following equation to find the first vertical bending frequency of cable-stayed bridges:

$$f_v = 33.8L_p^{-0.763} \quad (2-1)$$

Where L_p is the main span length in meters. Higher vertical deck modes have more zero-displacement nodes along the length of the deck. In higher modes of vertical deck bending, the contribution of axial force to stay cables decreases and deck stiffness has the main role.

2.3.1.2 Pure torsional modes of deck

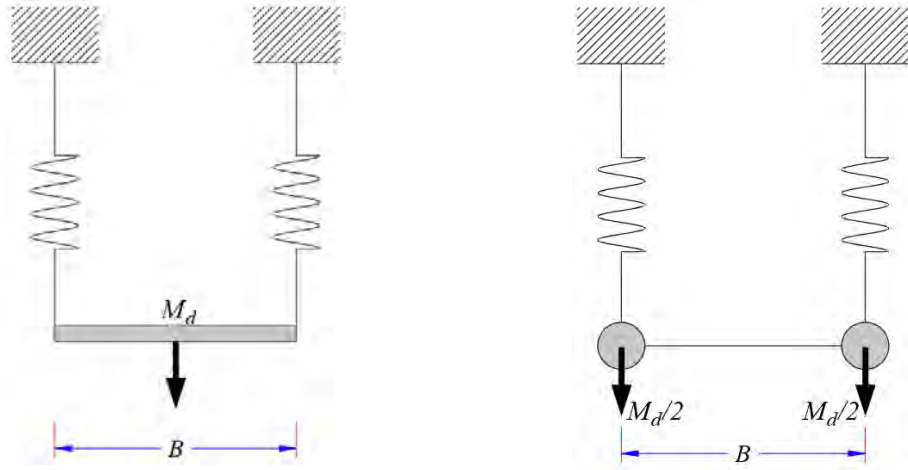
The torsional stiffness of the deck is influenced by the cable system arrangement and/or the cross-section of the deck rather than the cable system's axial stiffness. Kawashima et al. (1993) also recommend Equation 2-2 for the first torsional frequency of the deck:

$$f_\theta = 17.5L_p^{-0.453} \quad (2-2)$$

If the deck consists of a box girder, the fundamental torsional frequency of the deck is governed by the torsional rigidity of the box girder. As a result, a bridge with central cable plane arrangement has torsional rigidity of higher magnitude at which the cable governs about 10 to 20% extra rigidity beyond the deck rigidity (Virlogeux, 1999). Wyatt (1991) proposed an equation for the fundamental torsional frequency of the deck and neglected the cable-system contribution to this mode. However, Gimsing (1998) developed this equation by accounting for the contribution of stay cables in the first torsional mode of the deck and neglecting the deck stiffness. The model consists of two vertical cables, as shown in Figure 2.4. The expression proposed by Gimsing is:

$$f_v = \frac{1}{2\pi} \sqrt{\frac{2C_{cp}}{M_d}}; f_\theta = \frac{1}{2\pi} \sqrt{\frac{C_{cp} \cdot B^2}{2I_{m,x}}} \quad (2-3)$$

Where C_{cp} is the stiffness of each cable plane, M_d is the deck mass, B is the lateral distance between cable planes and $I_{m,x}$ is the deck torsional mass moment of inertia.



a) Distributed mass with central cable arrangement

b) Concentrated masses with lateral cable arrangement

Figure 2.4: Ideal models of deck and cables in terms of torsional and vertical frequencies (Gimsing, 1998)

Figure 2.4 shows two ideal models with different mass concentrations, where (a) the mass is distributed uniformly throughout the deck cross section, hence $I_{m,x} = M_d B^2 / 12$ and (b) the mass is modeled as two concentrated masses in each cable plane with $I_{m,x} = M_d B^2 / 4$. However, in reality, the mass distribution of the deck is somewhere between these two conditions, and therefore, for both expressions of the moment of inertia, ratio f_θ / f_v is between 1 and $\sqrt{3}$. In practice, the observed ratio f_θ / f_v ranges from 1.5 to 1.6, which is in close agreement with Gimsing's proposal. Thus, cable-stayed bridges may involve vertical and torsional modes at closer fundamental frequencies, especially if (a) the deck torsional and vertical stiffness are relatively smaller than the cable system and (b) the mass concentration is on the deck sides. Furthermore, the pure torsional mode governs the tower with two planes of cables that may require an anti-phase motion element in the tower, e.g. H-shaped towers involve the lateral movement of each plane. Meanwhile, A-shaped and inverted Y-shaped towers, where two cable planes meet at the same location on the tower, exhibit significantly smaller torsional modes.

2.3.1.3 Transverse modes of deck

The transverse modes of decks in cable-stayed bridges are dominated by the deck's transverse flexural stiffness. The stay cables induce minor transverse restraints to the deck, hence the contributions of the cable system and tower flexibility are negligible. The transverse frequency of the deck may be calculated as a continuous beam of the same span arrangement. Wyatt (1991) calculated the first transverse frequency for the deck as a beam model with the following expression:

$$f_y = \frac{1}{2} \sqrt{\frac{\pi^2 C_y E I_H}{m L_p^4}} \quad (2-4)$$

Where C_y is the ratio between the main span to the side span of the deck, E is the modulus of elasticity, m is the mass of the deck per unit length and I_H is the transverse moment of inertia of the deck. The transverse frequency of the deck is governed by the deck width and may not be easily controlled by the designer. Kawashima et al. (1993) experimentally determined the following expression for the first transverse frequency of a cable-stayed bridge as a function of the main span:

$$f_y = 482 L_p^{-1.262} \quad (2-5)$$

If the values of f_θ and f_y are in the same range, the coupling of the torsional and transverse modes of the deck is observed in cable-stayed bridges during modal analysis; otherwise, the coupling of these modes is weak (Wyatt, 1991).

2.3.1.4 Tower modes

The cable system significantly affects the longitudinal mode of the tower, whereas on the transverse axis, the effect is just as considerable. If the cable plane has a deep slope, the cable system also significantly affects the tower response in the transverse direction. Hence, the pure transverse mode of the tower is expected before the longitudinal mode.

The pure transverse mode of the tower can be approximated by cantilever models of the tower.

2.3.1.5 Stay cable interaction with bridge structure

Cable-stayed bridges are also characterized by the local mode of the cable system. The interaction between the local modes of the cable and the global modes is called the cable-structure interaction, which Leonhardt and Zellner (1980) studied. They found that the cable-structure interaction improves the seismic response of cable-stayed bridges to some extent. However, this effect may also increase the risk of damage to the structure if the bridge is subjected to specific dominant frequencies of an earthquake. The discretization of stay cables has an important role in the seismic analysis of cable-stayed bridges. Two discretization systems are available for cable systems: (i) One Element Cable-System (OECS) and (ii) Multi Element Cable-System (MECS). If one finite element is considered per stay-cable, it is known as a one element cable-system (OECS). In OECS, the local modes of the cables and the dynamic interaction between the deck and cables are neglected, but this neglect is less favorable during the seismic analysis of bridges (Abdel-Ghaffar, 1991). The vibration of cables produces more energy in higher modes, at which the contribution is significant during seismic excitation in terms of force but is less significant in terms of displacement (Abdel-Ghaffar, 1991; Abdel-Ghaffar & Khalifa, 1992).

MECS is associated with a large number vibration modes at lower frequencies. These local modes comprise out-of-plane and in-plane lateral flexural modes, but these modes do not affect the seismic response of bridges subjected to ground motions (Abdel-Ghaffar & Khalifa, 1992; Tuladhar et al., 1995). Caetano et al. (2000a, 2000b) compared the numerical modal analysis results for these two discretization systems with experimental modal analysis results. They concluded that OECS simplified the model and neglected

the local cable vibrations, hence significantly reducing model complexity. Meanwhile, MECS induced several closely spaced local modes for the cables, which increased model complexity. In addition, the first frequency of the cables was much larger than the global fundamental frequency of cable-stayed bridges. As a conclusion, the two cable discretization systems showed no substantial difference in results and had a close correlation with the experimental results. Later, Caetano (2007) performed a sensitivity analysis on the minimum required number of cable elements for the Vasco da Gama Bridge. It concluded that 9 elements per cable is the optimum number for discretization in order to find the first three local vibration modes of the cables with maximum of 5% error even for the longest cable of 226 m.

A number of research works have been conducted to find the required number of discretization elements of the cables to create an accurate model for the seismic response of cable-stayed bridges (Abdel-Ghaffar & Khalifa, 1992; Au et al., 2001; Ko et al., 2001; Tuladhar et al., 1995). According to the outcome of these research works, it is recommended to discretize cables for multiple elements for the seismic analysis of bridges. Ni et al. (2000) elaborated that multiple cable discretization is applicable for longer cables (about 465 m). For shorter stay cables, one element per cable was sufficient to obtain the modal parameters of the Ting Kau Bridge.

If broadband excitation oscillates the bridge, then the cable-structure interaction is beneficial in reducing the seismic forces to the cable-stayed bridge. However, if the bridge is excited by a narrow-band earthquake, the cable-structure interaction may increase the seismic responses. The local cable vibration effects on the global response of cable-stayed bridges have been investigated widely. Several control devices have been used to control the vibration induced by rain and wind as well as to help enhance the seismic response of

bridges. These control devices improve system damping by about 0.05% to 4% and also improve the energy dissipation of the bridge (Abdel-Ghaffar & Khalifa, 1992).

2.3.2 Damping

In general, cable-stayed bridges demonstrate low structural damping, whereas the standard assumed value of critical damping (ζ) of 5% falls on the unsafe side (Kawashima & Unjoh, 1991). Damping estimation is important for structures but is complicated, as structural damping depends on the relative damping of all constitutive elements (cables, deck and towers) as well as on their interaction with each other and their configuration.

Generally, three procedures can be used to account for structural damping:

- i. By considering the realistic representation of the sources of nonlinearity in the structure, which may develop under seismic loads; this is one of the most precise methods that considers energy dissipation during earthquake loadings, which develop nonlinearities. The Rayleigh or Caughey damping theory is used in this method to decompose the structural damping.
- ii. By performing dynamic modal analysis; each vibration mode is associated with different damping, and prior modal analysis is essential to find the frequency range with the most significant contribution to the dynamic response. Damping values of 2 to 5% are usually adopted, while higher damping values are associated with higher modes whose participation is negligible and may cause instability during numerical analysis. Yamaguchi and Furukawa (2004) concluded that Rayleigh (or Caughey) damping is inappropriate in the seismic analysis of the Yokohama Bay cable-stayed bridge (Japan) due to the special connection between the deck and towers.

- iii. By considering a constant fraction of the critical damping for all modes of vibration ($\xi = 2$ to 5%); this procedure has been deployed by many researchers and also in design codes (Ali & Abdel-Ghaffar, 1995; Morgenthal, 1999).

Kawashima and Unjoh (1991) concluded that the vibration mode highly affects damping, as each element is excited based on the mode shape. Moreover, damping depends on the velocity of wave propagation, modal coupling and foundation size, among other parameters. In addition, damping is strongly governed by the amplitude of ground excitation as well as cable-system arrangement. The harp cable arrangement demonstrates higher damping values than the fan cable arrangement in the longitudinal direction (Siringoringo & Fujino, 2006).

2.3.2.1 Damping mechanisms of cable-stayed bridges

Walker (2009) did a practical revision of the sources of damping in cable-stayed bridges, and the concluding outcomes are as follows:

(a) Structural damping

In general, the materials in structures are able to dissipate energy owing to their hysteresis loops that may reach elastic limits. Nonetheless, structural damping increases significantly beyond the plastic limit and dominates the energy dissipation of the bridge. Structural damping depends on the vibration amplitude and is unaffected by frequency (Chopra, 2014).

(b) Friction at bearings

Damping is produced by the bearings when the deck and abutments experience relative movements. The bearings, such as sliding and rubber bearings, dissipate energy through their hysteretic characteristics. This damping depends on the vibration mode and amplitude.

(c) Cable slippage in the cable-system

The internal slippage of wires in stays also dissipates energy if the threshold amplitude exceeds the internal friction of the wires. Such damping depends on the vibration amplitude and cable type.

(d) Foundation radiation damping

The subsoil condition and soil interaction with the foundation also cause energy dissipation. This type of damping may be greater than the damping associated with superstructures and it depends on the vibration mode.

(e) Aerodynamic damping

Superstructure vibrations are caused by the surrounding air, which provides resistance proportional to the square of the relative velocity. Air damping is considered viscous damping since it is rate-dependent. Air damping is naturally unsure in conventional cable-stayed bridges due to the low air density, smaller superstructure contact area and the large associated inertia forces involved in seismic movement.

(f) System damping

System damping is caused by the interaction between the towers, deck and cable system. This source of damping dissipates a large amount of energy in classic cable-stayed bridges when the vibration modes are associated with the deck and coupling effects (Caetano et al., 2000b).

2.3.2.2 Practical simulation of damping sources

In practice, a constant viscous damping factor is considered in the design codes for bridges and buildings. This is to avoid modeling uncertainties and also to be on the safe side when obtaining a solution where the explained dissipation mechanisms are ignored.

2.3.3 Dynamic analysis procedures

Several methods are available for the seismic analysis of structures subjected to earthquake loadings. Depending on the structure type and source of nonlinearities, an appropriate method should be deployed for seismic analysis. Very early seismic analysis procedures for cable-stayed bridges were presented by Wethyavivorn and Fleming (1987) and Abdel-Ghaffar (1991).

In this section, the different seismic analysis methods available are presented. The classical procedure of solving dynamic problems was developed by Chopra (2014), where the equation of motion for an N-degree of freedom structure under earthquake excitation is:

$$[M]\{\ddot{u}\} + [C]\{\dot{u}\} + [K]\{u\} = -[M][\eta]\{\ddot{x}_g\} \quad (2-6)$$

$$\{u\} = \{x_1, x_2, \dots, x_N\}^T \quad (2-7)$$

Where $[M]$, $[C]$ and $[K]$ are the mass, damping and stiffness matrices of the bridge, respectively; $\{\ddot{u}\}$, $\{\dot{u}\}$ and $\{u\}$ are the bridge acceleration, velocity and displacement vectors, respectively; parameter $[\eta]$ is the earthquake coefficient matrix; and $\{\ddot{x}_g\}$ is the earthquake acceleration vector.

2.3.3.1 Inelastic seismic analysis procedures

Several procedures are available to solve nonlinear dynamic problems, which are explained from the more to less time-demanding procedures.

(a) *Non-Linear Response History Analysis*

Nonlinear Response History Analysis (NL-RHA) is a direct, step-by-step integrated solving method that considers the tangential stiffness at each iteration to linearize the

problem. Several algorithms are available to directly solve the coupled system, among which the HHT scheme (Hilber et al., 1977) is the most commonly used.

NL-RHA is one of the most accurate methods of predicting the inelastic seismic demand in a structure. The NL-RHA procedure fully takes into account the material and geometric nonlinearities and has the capability of analyzing the effect of the seismic control system in a structure. The mathematical model is able to adequately represent the cyclic load-deformation of all constitutive elements in a structure (Bommer & Ruggeri, 2002; Chopra, 2014; Krawinkler & Seneviratna, 1998). Uncertainties arise when the nonlinear cyclic behavior of materials and the interaction between them must be described. Priestley et al. (1996) recommended direct nonlinear dynamics if only specific aspects of the bridge design need to be evaluated. Moreover, the direct integration method may be associated with larger phase errors, as the step-time ratio (Δt) increases with the vibration period (T) as shown in Figure 2.5 (Hilber et al., 1977). This figure presents phase errors in different integration methods; Houbolt; Wilson; Hilber - Hughes - Taylor (HHT) with different numerical damping values α_a ; and Newmark.

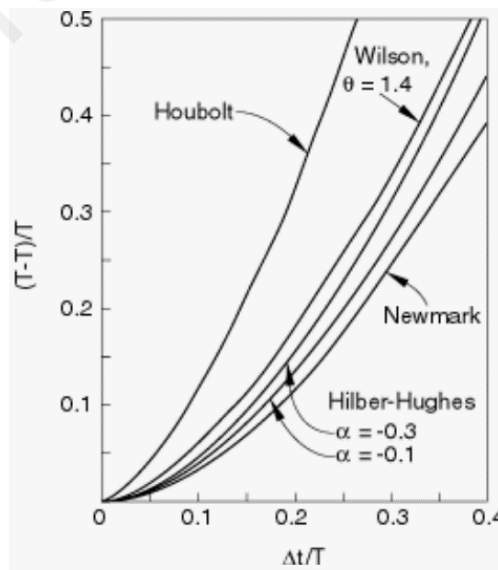


Figure 2.5: Relative phase error as a function of the step-time ratio and vibration period ($\Delta t=T$) in several direct integration methods (Hilber et al., 1977)

(b) Non-linear Static Procedures

Nonlinear Static Procedures (NSP) are known as pushover methods that recently have gained great popularity (ATC-40, 1996; FEMA-273, 1997). The ultimate goal is to estimate the nonlinear seismic response of the structures through static calculations. In this procedure, the structure is pushed to the target displacement using load patterns that represent the distribution of inertia forces.

These methodologies discover design weaknesses that may remain hidden in an elastic analysis and significantly reduce computational cost (Krawinkler & Seneviratna, 1998). For these reasons, several codes and guidelines recommend pushover analysis to investigate the inelastic seismic response of structures (ATC-40, 1996; FEMA-356, 2000; FEMA-440, 2005). The nonlinear response of a Multi-Degree of Freedom (MDOF) structure is assumed to be the same as the response of an equivalent Single-Degree of Freedom (SDOF) system that is controlled by a single mode and its shape remains constant throughout the analysis (Krawinkler & Seneviratna, 1998).

2.3.3.2 Elastic seismic analysis procedures

Seismic analysis is extremely simplified if the forces on the stiffness component of the structure are related to the deformation matrices through a linear elastic stiffness matrix ($f_s = k u$). Based on this assumption, the following producers are explained.

I. Modal Response History Analysis (MRHA):

Modal Response History Analysis (or modal dynamics) is based on the modal superposition of the uncoupled equations of motion, when the behavior is elastic ($f_s = k u$) and if the damping matrix c is the classical damping; therefore, is able to be decomposed. This damping property is achievable through the Rayleigh or Caughey damping matrices. These assumptions remain in the analysis of the

structure in the elastic range and exclude the use of control devices except the viscoelastic or viscous liquid dampers (Villaverde, 2009).

According to seismic code (e.g. Eurocode 8 (2004)), the number of modes required for analysis is obtained when 90% of the total mass is participated. On the contrary, cable-stayed bridges have a large number of flexible elements and the mass of the tower close to the foundation level can be excited in higher-order modes that exhibit a considerable percentage of the total mass. In cable-stayed bridges, exceeding 70 to 80% of the modal participation without including a great number of vibration modes is complicated (Morgenthal, 1999). The Ritz vector or subspace iteration procedures are used to compute the modes.

II. Modal Response Spectrum Analysis (MRSA):

Response spectrum analysis directly finds the peak response of each considered SDOF through the design spectrum of a given earthquake. MRSA provides the results with no approximation. However, it does not offer the instant structural response during an earthquake and it only gives the structure's global response.

Walker (2009) reviewed the different existing combination rules and evaluated them in the seismic analysis of cable-stayed bridges. Walker concluded that the Complete Quadratic Combination (CQC) (Kiureghian, 1980) approach is the most adequate modal combination method for cable-stayed bridges due to the strong modal coupling capability of this method.

Ren and Obata (1999) investigated the inelastic seismic behavior of a cable-stayed bridge and concluded that nonlinearities can be neglected even for strong earthquakes. They found that the linear analysis was correct, but the superposition principle was inappropriate because of the complexity of the dynamic coupling of cable-stayed bridges.

2.3.3.3 Recommended analysis procedure for cable-stayed bridges

It is recommended to use the step-by-step approach to study the seismic behavior of cable-stayed bridges (Ren & Obata, 1999; Ren & Peng, 2005).

Step 1: Obtain the deformation of the bridge under its own weight through nonlinear static analysis.

Step 2: Perform modal analysis starting from nonlinear static analysis and extract the modal parameters.

Step 3: Carry out nonlinear seismic analysis following Step 2.

2.3.4 Seismic response of the towers

Casado (2011) studied the effects of different factors on the elastic and inelastic seismic responses of towers, such as: (a) damping associated with the tower, (b) longitudinal and transverse shapes of the tower (geometry consideration), (c) earthquake characteristics, (d) imperfections in the steel tower construction, (e) cable arrangement, (f) soil-structure interaction, (g) types of deck-tower connection, and (h) tower materials, particularly concrete.

2.3.5 Deck-Tower and deck-piers connections

The dynamic response of cable-stayed bridges depends remarkably on how the deck is connected with the tower and piers (abutments). The three possible connections between the deck and tower are: i) rigid connection, ii) movable connection and iii) intermediate connection, which can limit the movement (e.g. dampers) (Calvi et al., 2010; Hui Li et al., 2009; Sharabash & Andrawes, 2009). Investigations have shown that a rigid connection between the deck and towers results in damage concentration at the towers when the bridge is subjected to horizontal component of earthquake (Hui Li et al., 2009). Meanwhile, the floating or movable system increases the deck displacement under

seismic excitations (Sharabash & Andrawes, 2009). On the other hand, the intermediate solution exhibits enhanced seismic response to earthquake accelerations (Calvi et al., 2010).

2.3.6 Soil-structure interaction

The soil-structure interaction plays an important role during earthquakes. Earthquake signals differ in terms of amplitude, frequency and duration. The effect of the soil-structure interaction becomes more significant if the foundation soil is classified as soft and its characteristic frequencies are close to the dominating bridge modes (Zheng & Takeda, 1995). When the soil is classified as rock, the foundation is considered rigid.

In modeling the soil-structure interaction, a large area of the soil surrounding the foundation is discretized in the numerical model or by using contour finite elements that prevents the rebound of the waves in the borders of the model. The most common practice in soil-structure interaction modeling is to model the soil by using a series of springs and dashpots with the corresponding degrees of freedom and characteristics of each soil layer. Zheng and Takeda (1995) showed that springs are able to simulate the effect of the surrounding soil accurately when its movement governing frequency is low displacement. However, when the movement frequency is higher, the model is less accurate. It can be concluded that mass-spring modeling is an appropriate approach of modeling the subsoil stiffness for flexible structures like cable-stayed bridges (Morgenthal, 1999).

Abdel-Raheem and Hayashikawa (2003) proved that the nonlinear seismic behavior of soil and its interaction with the cable-stayed bridge cause a reduction in the tower's seismic demands. On the other hand, Fan et al. (1994) indicated that the soil-structure interaction might increase the seismic force and displacement of the tower more than a stiff foundation model and specifically for cable-stayed bridges with floating systems. Furthermore, cable-stayed bridges are considered lightweight flexible structures that

eventually cause the reduction in seismic force transmitted from the bridge to the foundation during an earthquake. Therefore, as it is justified in this section, the soil-structure interaction is neglected in the current study (Clough & Penzien, 1993; Walker, 2009).

2.3.7 Seismic behavior of multiple-span cable-stayed bridges

Tuladhar et al. (1995) investigated the boundary conditions as well as the number of spans required to represent an entire multi-span cable-stayed bridge for analysis. Morgenthal (1999) analyzed the seismic response of the Rion-Antirion Bridge that has four towers. The conceptual design of continuous cable-stayed bridges with three pylons was studied by Virlogeux (2001), who considered two configurations to reduce the longitudinal displacement of the tower (Figure 2.6). Furthermore, several researchers have studied the seismic response of Ting Kau bridge with three towers and diagonal stabilization cables (Ko et al., 2001; Ni et al., 2000).

Okamoto and Nakamura (2011) studied the static and seismic behavior of hybrid towers in multi-span cable-stayed bridges considering different types of deck-tower connections. The focus of this specific study was on the connection and performance of the hybrid tower. Zong et al. (2014) performed a shaking table test on the Wuhan Erqi Yangtze river multi-span bridge. The scaled cable-stayed bridge was subjected to multi-support excitation and then numerical analysis was conducted for result consistency. The progressive failure of the bridge according to the shaking table test was updated in the numerical model. The numerical model may be used as a benchmark for further seismic control and investigations.

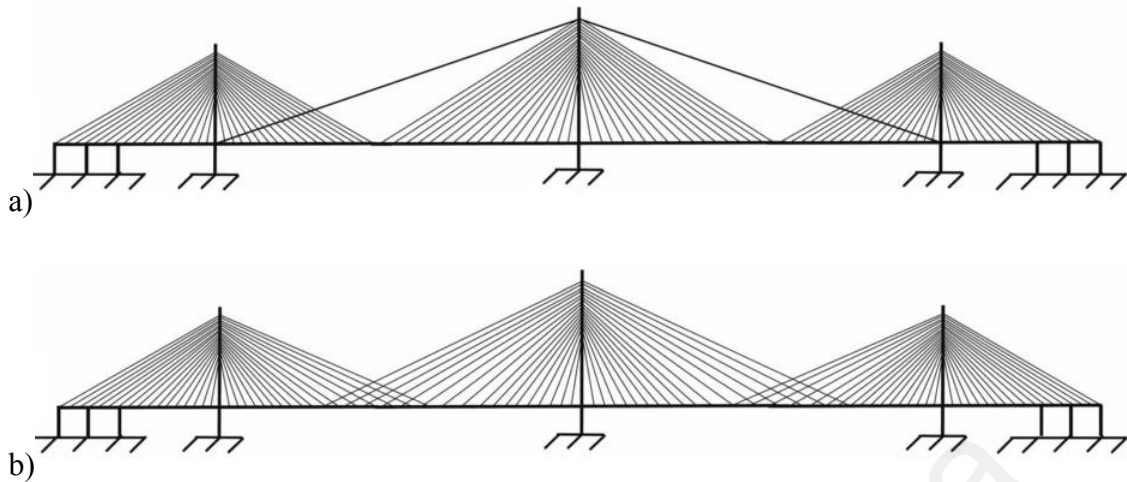


Figure 2.6: a) Diagonal and b) intersected cables stiffening in multiple-span cable-stayed bridges (Virlogeux, 2001)

2.4 Comparison of capacity design with mitigation design

In general, there are three methods of designing structures against seismic actions as follows:

1. The structure is designed to remain in the elastic range during seismic events. With this method the sections are considerably large, leading to higher construction costs. It is thus discouraged in current codes of practice. This method is not discussed further because the scope of this research regards existing cable-stayed bridges.
2. Certain structure members (members with high likelihood of plastic hinge formation) are designed for sufficient ductility. In these members, controlled damage occurs and the seismic energy is dissipated through hysteresis cycles. This method is called a capacity design, whereby the designer avoids the seismic demands from the most crucial members like the deck.
3. The third method is mitigation design. With this method, seismic devices are designed and used to reduce the seismic demands on structures.

A summary of structure capacity and mitigation designs is presented in Figure 2.7. In capacity design, the ductility of sections where the formation of plastic hinges is expected should be high enough to withstand seismic demands. In concrete structures, the required ductility is achieved by providing longitudinal and transverse reinforcements in such areas that require higher confinement.

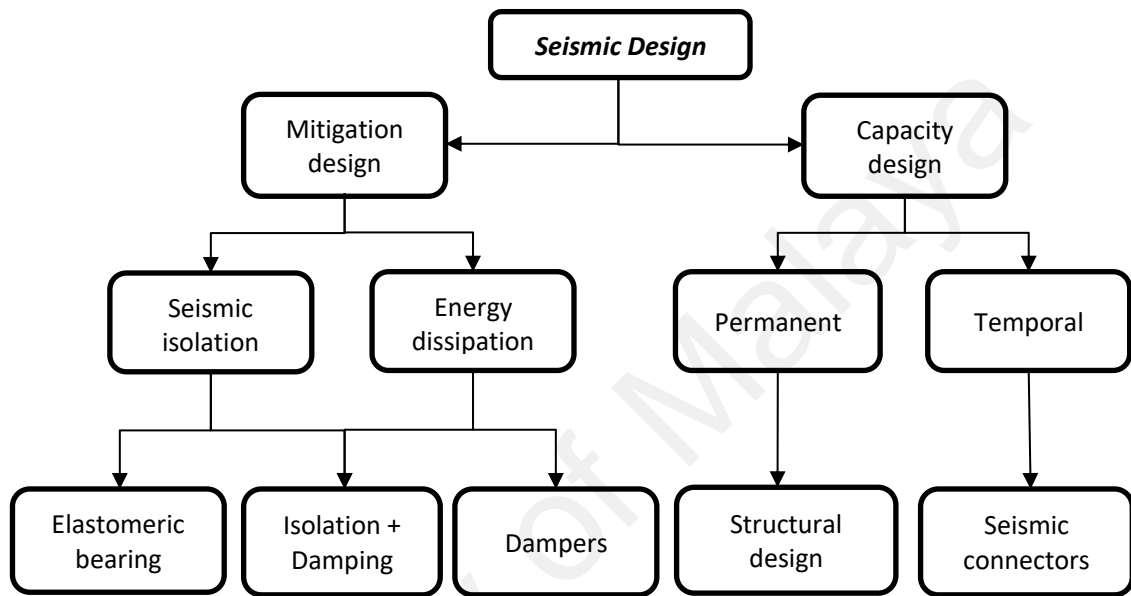


Figure 2.7: Summary of control strategies in the seismic design of structures with few seismic devices (Huber & Medeot, 2005)

Nowadays, seismic mitigation is a common design practice for cable-stayed bridges in seismic zones. The reason is that towers mostly remain in the elastic range during earthquakes and it is favorable since towers have an important role in the global response of bridges. Seismic devices reduce the seismic demands on structures and can be easily repaired or replaced, unlike the tower sections. Mitigation design causes a reduction in the size of members that remain in the elastic range and are subjected to strong earthquakes. As discussed earlier, cable-stayed bridges are associated with low structural damping; therefore, adding seismic energy dissipaters is beneficial in increasing the structural damping. The following sections briefly explain the key aspects of mitigation design.

2.5 Mitigation design

Two objectives are achievable with the mitigation design. The first objective is to lengthen the fundamental time periods of a structure that reduces the associated spectral accelerations. The second objective is to increase the dissipation capability by means of added damping. Figure 2.8 shows a design acceleration spectrum in the acceleration-displacement response spectrum (ADRS) in order to visualize these two effects. As the period is lengthened from $T_{f,0}$ to $T_{f,1}$, the spectral acceleration decreases while the spectral displacement remains constant. If the vibration period is greater than $T_D = 2$ Sec. When the vibration period is slightly below T_D , its increment assumes moderate acceleration reductions and large displacements. Regardless of the type of result and the governing vibration period, damping increments always cause reductions in seismic response, but the effectiveness drops beyond certain damping increment levels, as shown in Figure 2.8 (when the damping changes from $\zeta = 4\%$ to 15% and 30%).

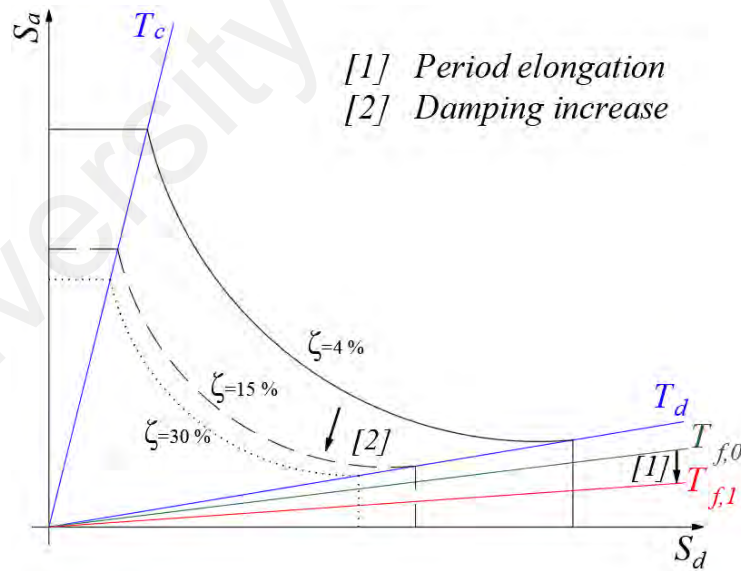


Figure 2.8: Mitigation design objectives ([1] fundamental period elongation and [2] damping increment) recommended by Eurocode 8 (2004)

Based on these objectives, seismic devices are developed in attempts to achieve one or both effects at the same time. Thus, seismic devices are classified as:

- Seismic isolation devices: elongate the fundamental period of structures. For instance, the laminated Rubber Bearings (RB) is one of the most practical seismic isolators on the market.
- Dampers: add damping to the structure and dissipate seismic energy through various methods, such as metallic dampers.
- Seismic isolation plus damping devices: elongate the fundamental period of structures as well as add damping to structures. Lead-Rubber Bearings (LRB), High-Damping Rubber Bearings (HDR) and Frictional Pendulum Systems (FPS) are the most common seismic isolation plus damping devices used in structures.

Furthermore, these seismic devices are divided into three major groups:

- **Passive control systems** dissipate seismic energy without any external energy source. These are the most practical seismic devices because they are robust, reliable and economical.
- **Active control systems** require external energy sources to dissipate seismic energy. When an earthquake is happening, the sensors detect ground motions and the actuators induce additional energy through the designed algorithms in the opposite direction, which may compromise structure stability.
- **Semi-active control systems** required small external sources of energy unlike active control systems, and do not compromise structure stability, as they do not add any external energy to the structure.

Ghaedi et al. (2017) and Saaed et al. (2013) reviewed developments in vibration control systems for civil structures based on the passive, active and semi-active classification.

2.5.1 Seismic isolation

Seismic isolation is an approach to reduce the seismic force to, or near the elastic capacity of the structure members, thereby eliminating inelastic deformation. The main aim of utilizing an isolation system is to decrease the fundamental frequency of structural vibration to a value lower than the predominant energy-containing frequency of an earthquake. Broadly speaking, the performance criteria of isolated bridges in earthquake design may be specified by the bridge owner: (i) the displacement ductility demand reduction in columns to keep the bridge open for emergency vehicles after the earthquake, (ii) to keep the bridge response fully elastic, (iii) for an existing bridge there should not be any impacts at the abutments and there should be minimum or zero ductility demand in the columns, and (iv) the reduction of substructure forces in case the bridge is located on weak soil to lower the foundation cost.

A number of seismic isolator devices have been introduced by different authors, such as the partially bonded fiber-reinforced elastomeric isolator (PB-FREI), carbon FRP-elastomeric isolator and the roll-n-cage (RNC) isolator (Dezfuli & Alam, 2013; Engelen et al., 2011; Ismail et al., 2010). Nonetheless, in practice only few isolation systems have been used in structures, which are discussed in the following section.

2.5.1.1 High damping rubber bearing

The high damping rubber bearing (HDRB) was proposed by Simo and Kelly in 1984. It is made of steel and rubber plates placed in alternate layers as shown in Figure 2.9. In general, the HDRB has high damping capacity, high vertical stiffness and horizontal flexibility. The damping constant of the system varies considerably with the strain level of the bearing (generally in the order of 10%). The HDRB decouples the structure from the horizontal components of ground motion by interposing a layer of low horizontal

stiffness between the superstructure and substructure. These devices are resistant to environmental effects and can be easily manufactured.

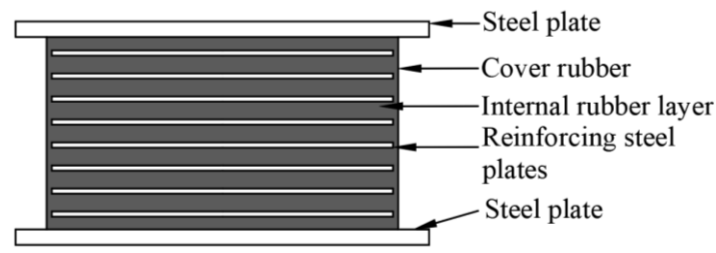


Figure 2.9: Schematic view of high damping rubber bearing

2.5.1.2 Lead-rubber bearing

The lead-rubber bearing (LRB) was invented by Robinson and Tucker (1977) in New Zealand. The LRB benefits from the combined features of vertical load support, horizontal flexibility and restoration, and damping capabilities (Skinner et al., 1974). As shown in Figure 2.10, such seismic isolator is developed based on the rubber bearings but has a central lead core that provides an additional means of energy dissipation. The LRB also has energy-absorbing capacity through the additional hysteretic damping in lead core yielding that reduces the isolator's lateral displacements, especially under ambient vibrations.

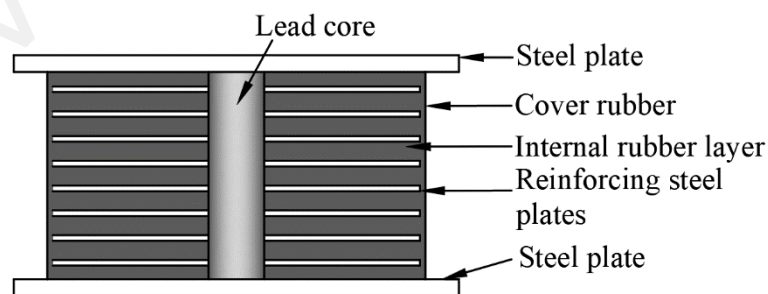


Figure 2.10: Schematic view of lead-rubber bearing

2.5.1.3 Friction pendulum system

Sliding isolation devices are among the most popular and effective seismic isolators. Sliding systems exhibit excellent performance under a variety of severe earthquake

loadings and are very effective in reducing large superstructure acceleration. Friction Pendulum System (FPS) is characterized by insensitivity to the frequency content of earthquake excitation owing to the sliding system's tendency to reduce and spread the earthquake energy over a wide range of frequencies. Another advantage of sliding isolation systems over the conventional rubber bearing is that because of frictional force development at the base, it is proportional to the structure mass, and the center of the mass and center of resistance of the sliding support coincide. Consequently, the torsional effects produced by a typical asymmetric structure are diminished. The concept of sliding bearings has been combined with the concept of a pendulum type response, resulting in a conceptually interesting seismic isolation system known as the friction pendulum system (FPS) as shown in Figure 2.11. In FPS, isolation is achieved by means of an articulated slider on a spherical, concave chrome surface (Zayas et al., 1990). The slider is faced with a bearing material, which, once in contact with the polished chrome surface, results in friction force development. The concave surface produces a restoring force proportional to its radius. The FPS develops a lateral force equal to the combination of the mobilized frictional force and the restoring force developed due to the rising of the structure along the spherical concave surface.

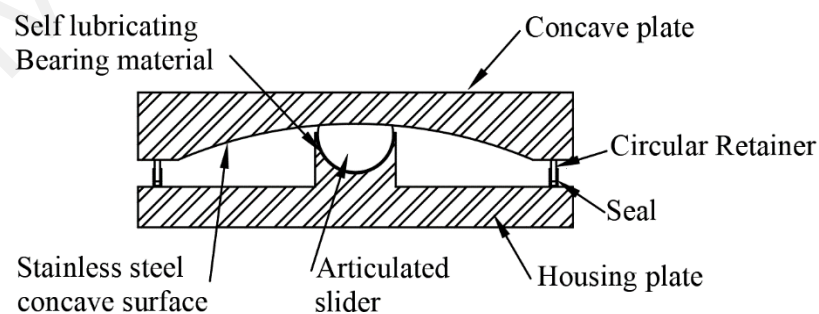


Figure 2.11: Schematic view of friction pendulum system

2.5.2 Passive energy dissipaters

This section describe the passive energy dissipation technology applied in structures. Over the past few decades, many dampers have been proposed and implemented in

various types of structures. Passive dampers are generally divided into four categories (Villaverde, 2009): (i) yielding metallic dampers, (ii) viscoelastic dampers, (iii) friction dampers and (iv) tuned dampers. It should be noted that the emphasis of this thesis is on yielding metallic dampers, to which this section is devoted. Nonetheless, a short description of other dampers are also provided.

Friction dampers (FD) dissipate kinetic energy through the sliding of surfaces with high friction coefficients. More than 30 years of experience and the large number of buildings equipped with these devices guarantee their incorporation. However, the difficulty to maintain their properties over long time intervals is also well-known due to the corrosion of metallic surfaces and normal load relaxation (Soong & Dargush, 1997; Villaverde, 2009).

Viscoelastic (VE) dampers use the phase-lag between the shear strain and corresponding stress in viscoelastic materials to dissipate energy. VE dampers have been successfully deployed to reduce the dynamic vibrations of buildings due to wind loads and have good re-centering capability. For seismic applications, the viscoelastic material stiffness should be significantly higher. Furthermore, the energy of earthquakes is usually spread over a wider range of frequencies and the remarkable dependency of VE dampers on frequency could be clearly a problem, besides the influence of ambient temperature on their performance (Soong & Dargush, 1997).

The biggest drawback of friction and viscoelastic dampers is the age-problems. The operation of these dampers is affected by adverse environmental conditions, especially in the case of bridges. Hence, these dampers must be inspected regularly.

Tuned mass dampers (TMD) are very appealing in controlling the dynamic response of a structure. The number of bridges equipped with these devices is expected to rise

considerably in the near future. With this control strategy, some structural vibrational energy is transferred to the tuned dampers, which simply oscillate elastically (linearly or nonlinearly). The tuned liquid damper (TLD) operates with the same principle as the TMD. There are two types of TLD: dampers based on sloshing liquids and column TLDs.

Nonetheless, the broad frequency content of earthquake excitation (far different than harmonic loads), besides detuning due to inelastic demand and consequent vibration period elongation, may be detrimental to tuned damper performance. These are key drawbacks that question their use as passive systems for the seismic control of a structure under large earthquakes. However, several research works have suggested that strong ground shaking and significant modifications of natural periods do not lead to inadmissible reductions in the effectiveness of TMD (Pinkaew et al., 2003). In principle, structures governed by one vibration mode are good candidates for control by tuned dampers that are properly adjusted to this frequency. However, cable-stayed bridges involve complex modal couplings and several modes contribute significantly to their response.

2.5.3 Metallic dampers

The Metallic dampers (MD) dissipate energy through inelastic deformation of the metal material. The advantages of metallic dampers over active and semi-active dampers are stable hysteretic behavior, rate independence, resistance against ambient temperature, reliable with good fatigue life and finally, material behavior that is familiar to practicing engineers. As one of the objectives of this thesis is to develop a new metallic damper for mitigating the seismic demands on civil structures, this section is devoted to the classification, behavior and application of metallic dampers.

2.5.3.1 Hysteresis behaviour of metallic dampers

Since metal materials have nonlinear behavior, the hysteretic behavior of metallic materials is advantageous in dissipating dynamic energy, especially in linear systems. This section briefly describes how metal materials behave under cyclic loadings. The metallic material under static loading is plasticized when the stress level exceeds the elastic limit (σ_y) and thereafter enters the stress hardening phase if subjected to larger stresses. Under cyclic loadings, the elastic modulus (E) of the material recovers as the material unloads. If a load is applied in the opposite direction, the material begins to yield and soften at a lower stress level than the yield stress, which is known as the Bauschinger effect (Bannantine et al., 1990). The hysteretic behavior of the material continues as long as the strain does not exceed the yield plateau and the maximum positive and negative stresses remain within the yield stress ($\pm\sigma_y$). The material follows the initial elastic stiffness even after unloading from the stresses higher than the yield plateau. The Bauschinger effect becomes more dramatic as the material tends toward maximum strain. The metal material promotes a certain post-yield stiffness and the yield plateau disappears during this range of cyclic loading. General schematic hysteresis loops of metallic materials are shown in Figure 2.12(a) (Azevedo & Calado, 1994). However, the hysteretic behavior may slightly differ depending on the geometry of the metallic damper. The hysteresis trends of metals, such as steel, aluminum, lead and copper are similar. The stress-strain relationship of steel material is often simplified as a bilinear or trilinear elastoplastic model. The shape memory alloy (SMA) hysteretic behavior is slightly different from other metal materials. The hysteresis loops of SMA are shown in Figure 2.12(b). SMA exhibits two different behaviors based on the material temperature relative to its austenitic finish temperature, A_f (Miller & Doh, 2014). As the temperature rises above A_f , the strains obtained during loading recover after unloading. During this process, a significant amount of energy dissipates without any sign of residual strains, which is

called superelasticity. The residual strains remain after unloading if the material temperature is below A_f and thereafter the residual strains recover if the material reheats again. This effect is known as the shape memory effect.

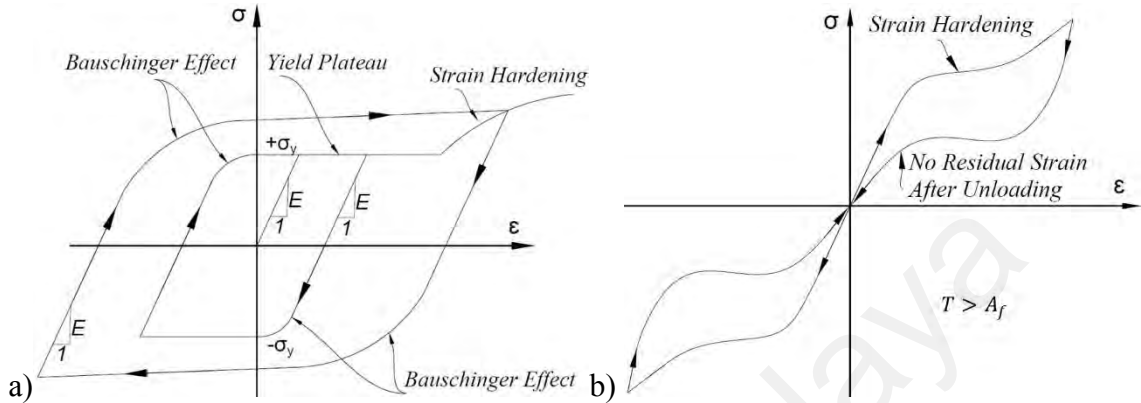


Figure 2.12: Idealized Hysteresis behavior of a) metallic and b) SMA materials

2.5.3.2 Classification of metallic dampers:

The damping mechanism and performance of metallic dampers are greatly dependent on the constitutive material, such as steel, aluminum, copper, etc. Therefore, metallic dampers are classified according to their constitutive material into the following categories.

(a) Steel dampers

The very first steel dampers were proposed by Kelly et al. in the early 1970s (Kelly et al., 1972). Thereafter, the U-strip damper, torsional beam damper, flexural beam damper and single-axis damper were developed and tested for implementation in structures as shown in Figure 2.13(a-d) (Skinner et al., 1974). The U-strip damper consists of a U-shape steel strip placed between the moving plates (Figure 2.13(a)). The U-strip damper is deformed in one direction, thus exhibiting large deformation in the elastic range. The torsional beam damper is made of a square or rectangular plate with fixed ends, whereby the middle segment is subjected to the predominating torsional and flexural movements (Figure 2.13(b)). The torsional beam damper has high load-bearing capacity and may be

implemented at the base of structures to prevent structural uplifting caused by severe earthquakes. In contrast, the flexural beam damper is slightly more complex. The main part of the damper is a square or circular section anchored at the bottom and top, allowing rotation and movement (Figure 2.13(c)). This damper is robust and dissipates seismic loads bidirectionally. The single-axis beam damper is made of a wide beam with high loading capacity (Figure 2.13(d)). Two or more beams may be used together to form a compact damper, which is suitable for the diagonal element of flexible frame structures.

The tapered-steel energy dissipation device was suggested by Tyler (1978b). This device is comprised of a taper-shaped round steel bar or steel plate welded to the anchorage plate at the base to form a cantilever (Figure 2.13(e)). The device dissipates energy, taking advantage of the steel material's plastic deformation. Pinelli et al. (1993) proposed a different type of steel damper based on a steel tube. The proposed device is made of a rectangular steel tube cut into a taper shape at two sides, such that the stresses distribute uniformly along the tapered section of the tube (Figure 2.13(f)).

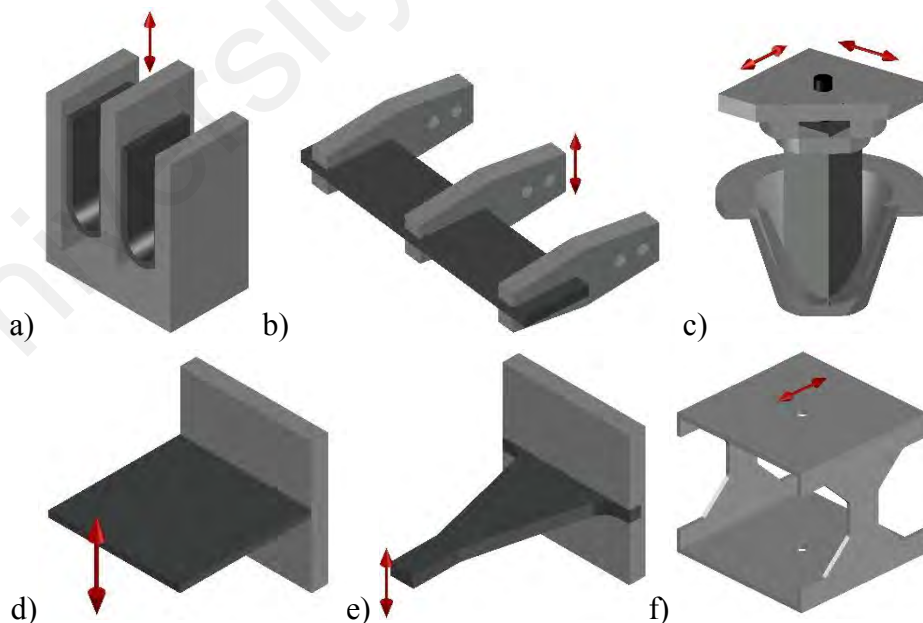


Figure 2.13: a) U-Shaped steel, b) Torsional beam, c) Flexural beam, d) Single-axis e) Tapered cantilever and f) Taper Tube dampers

The buckling-restrained brace (BRB) is another type of steel damper that was initially introduced by Takeda et al. in 1976. As shown in Figure 2.14(a), the BRB entails conventional bracing (as the core) encased with a square, hollow steel section filled with mortar material. The steel core sustains axial loads while the infilled material eliminates the shear transfer under compression loading to the outer tube. The BRB was further developed with different core configurations, like circular core (CBRB), cross and crosswise core and linear core (Figure 2.14(c)) (Black et al., 2004; Wada et al., 1989). These have been implemented extensively worldwide, especially in Japan and the United States since 1987 (Black et al., 2002). For instance, Black et al. (2004) conducted comprehensive testing on BRB and concluded that the BRB is a more reliable and practical alternative than conventional bracing systems. Due to the key concerns with BRBs such as inconsistent material behavior, low-cycle fatigue life and steel core geometric imperfections, Zhao et al. (2011) introduced another BRB device called the angle buckling-restrained brace (ABRB), as depicted in Figure 2.14(b). The ABRB consists of four angled steel plates welded together at the ends with stiffeners and connectors. Two other angle plates are welded together around the four angle plates to form a square tube. ABRB failure has been observed at the welded ends of the angle plates. Furthermore, it was designed such that the steel core would remain in the elastic range during rapid loadings. Hao et al. (2014) developed the H-type steel unbuckling brace (SUB) consisting of a steel plate core confined in steel element. The end of the steel core plate is connected to Phillips shaped steel plates as shown in Figure 2.14(d). The confining element prevents steel core buckling under compression and tension loadings. The SUB damper controls structural displacement by adding stiffness to the frame system. Recently, Dongbin et al. (2016) proposed a new type of BRB damper with a circular core configuration (CBRB). The damper is composed of three circular steel tubes, where the core tube with slotted holes is restrained by the inner and outer tubes against any out-of-

plane buckling deformation. The restrained tubes are spot welded in the middle to the core tube. CBRB is relatively lighter than existing conventional BRBs.

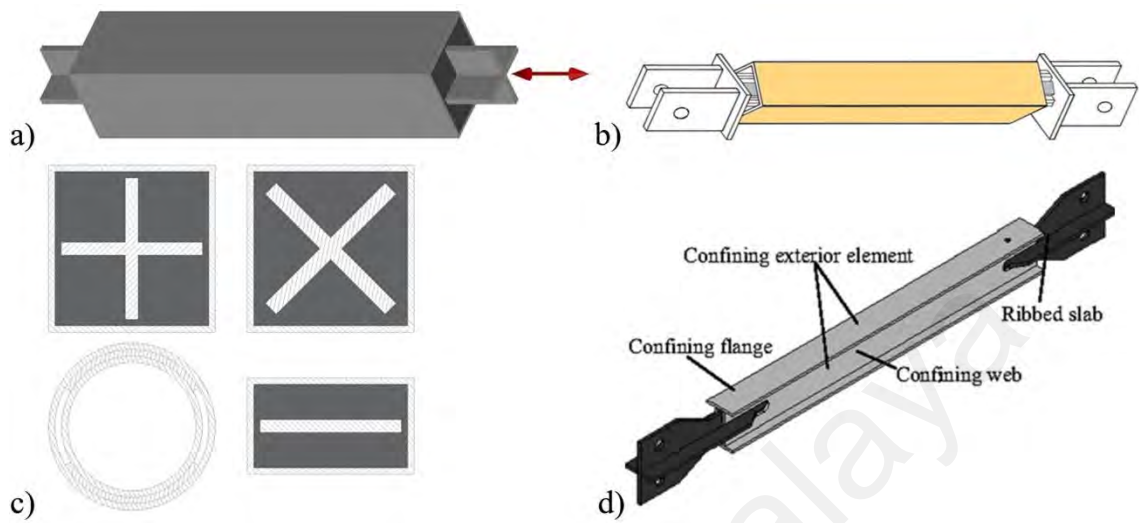


Figure 2.14: Schematic views of a) BRB, b) ARBRB (Zhao et al., 2011), c) different BRB core configurations and d) SUB (X.-Y. Hao et al., 2014)

A very famous metallic damper, the added damping and stiffness (ADAS) device, was proposed by Bergman (1987). ADAS consists of X-shaped steel plates connected in parallel to base plate using bolts that add extra damping and stiffness to the structure (Figure 2.15(a)). Afterwards, Tsai et al. (1993) developed the triangular-plate added damping and stiffness (TADAS) device based on the ADAS concept. The TADAS mechanism is similar to ADAS, whereby several triangular steel shaped plates are welded in parallel to the base plate and the narrow end is locked to another plate with bolts (Figure 2.15(b)). Both ADAS and TADAS dampers are suggested for moment resistant frames to increase the damping and stiffness of the structures. Shih et al. (Shih et al., 2004; Shih & Sung, 2005) developed a rhombic ADAS damper using low yield strength steel with hinge supports at both ends (Figure 2.15(c)). The hinge supports eliminate unfavorable axial forces on the plate. The strain hardening quality of low yield strength steel helps control the problem of local fractures in the damper. In addition, the mechanical properties of low yield strength steel reduce the yield displacement and enhance the

energy dissipation capability and ductility of the damper (Han et al., 2014). Damper symmetry also reduces the effects of welding on the performance of the damper.

Li and Li (2007) introduced the dual function damper with three different geometries: single round-hole, X-shaped and double X-shaped metallic dampers as illustrated in Figure 2.15 (d-f). Dual function dampers are a type of ADAS. The single round-hole metallic damper is made of a hollow circular cross-section in the middle of an X-shaped steel plate, whereas the X-plate damper has a narrower section in the middle of the X-plate. The dual X-shaped damper consists of two Xs placed in series. The load is applied parallel to a round-hole damper and perpendicular to X-shaped and double X-shaped dampers. The slit steel damper (SSD) was invented by Chan and Albermani (2008) and was subsequently developed by several others researchers (Ghabraie et al., 2010; Hedayat, 2015; Jie et al., 2015; Karavasilis et al., 2012). The SSD is made of a standard structural wide-flange section with several slits cut in the web section as shown in Figure 2.15 (g). The slits are rounded at the ends to prevent stress concentration during seismic events. The device can be connected to the primary structure using bolts, therefore preventing uncertainties associated with welding. The first suggested installation of the SSD was in an inverted V-brace system. Oh et al. (2009) tested the SSD performance at the beam-column connection of steel structures and found significant enhancement in the seismic performance of the connection.

Garivani et al. (2016) introduced the comb-teeth damper (CTD) for use in chevron bracing systems. As Figure 2.15(h) illustrates, the CTD is made of a steel plate cut in the shape of comb teeth. The top and bottom parts of the CTD damper are connected to a frame with bolts. A CTD subjected to in-plane flexural deformation dissipates energy through the yielding of the comb teeth. The CTD has shown out-of-plane behavior during experimental tests, which was eliminated by enlarging the CTD plate thickness. Fan et al.

(2016) took advantage of low yield strength steel and developed a new two-stage energy dissipation device, as depicted in Figure 2.15(i). The device is composed of several parabola openings in the steel plate. The plate is welded to the top and bottom anchorage plates. The device dissipates energy through shear deformation of the plate inflection points. Wang and Chien (2009) presented a device based on bent steel strips, as shown in Figure 2.15(j). The device consists of two pre-bent steel strips bolted to connectors. The device is loaded axially and the strips are subjected to buckling deformation. The force-displacement hysteresis loops of a pre-bent steel strip damper found to be asymmetric. Nonetheless, symmetric hysteresis behavior is achieved when pre-bent steel strip dampers are coupled. Hsu and Halim (2017) proposed a steel curved damper for moment-resisting frames. The damper has a curve shape and is made from steel plates (Figure 2.15(k)). The damper's performance was tested in a beam-to-column connection. The lateral movement generated eccentricity to the curved damper, thereby increasing the lateral stiffness of the beam-column connection.

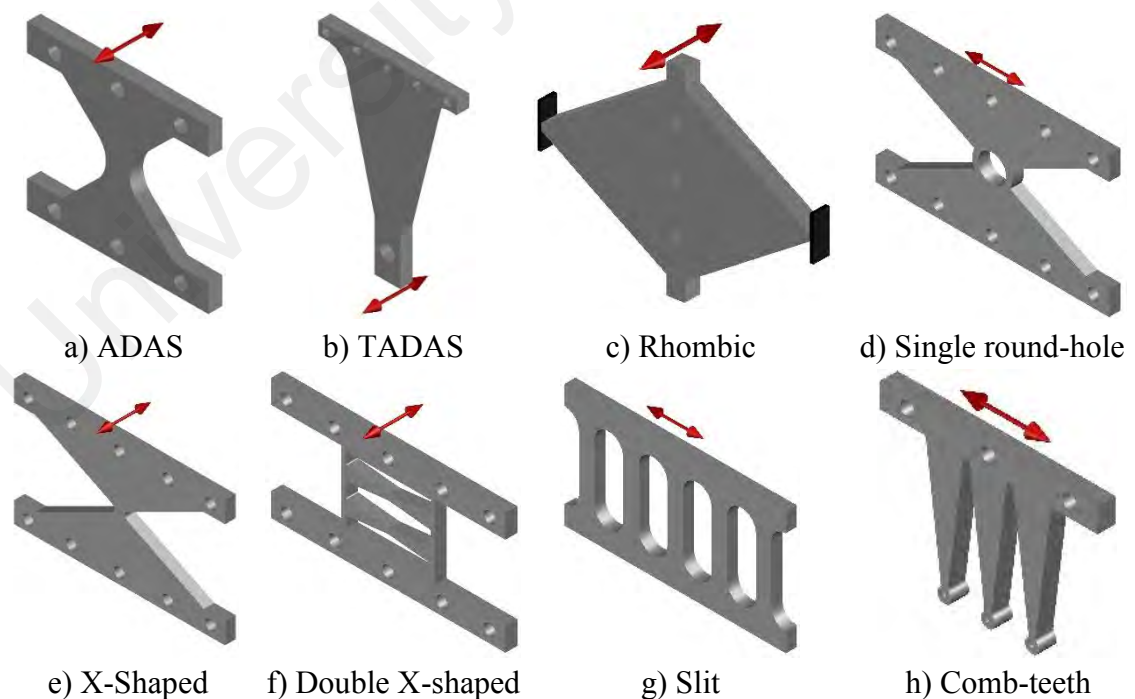
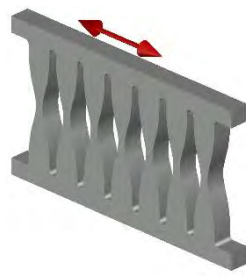


Figure 2.15: Steel plate-based dampers



i) Parabolic



j) Pre-bent strips



k) Curved steel dampers

Figure 2.15, Continued

Nakashima et al. (1994) proposed the shear panel damper (SPD), which contains a steel plate welded to top and bottom plates (Figure 2.16(a)). The SPD has large energy dissipation capacity. Abebe et al. (2015) pointed out the failure modes of the SPD, i.e. failure at the shear panel center, failure at the shear panel corners and flange weld failure. Chen et al. (2005, 2006) enhanced the SPD performance by adding a stiffener. The stiffened shear panel damper (SSPD) illustrated in Figure 2.16(b) is made of a shear panel with horizontal and vertical stiffeners. The stiffness of SSPD is relatively higher than conventional SPDs, as it promotes large deformation with no signs of pinching and strength degradation. Subsequently, Zhang et al. (2012) improved the SPD performance using low yield strength steel. In addition, the shape optimization method was used to optimize the damper's dissipation performance (Deng et al., 2014). Chan et al. (2008) proposed the yielding shear panel device (YSPD). This device is made of a thin steel plate welded inside a short segment of square hollow steel (Figure 2.16(c)). YSPD is subjected to in-plane loading and the steel plate undergoes shear deformation to harvest the induced energy. Moreover, Chan et al. (2013) proposed another damper called the perforated yielding shear panel device (PYSPD). This is a modified version of YSPD as the thin steel plate has a number of circular holes. The undesirable local deformation in the YSPD corners can be eliminated by perforating the steel plate in PYSPD.

Sahoo et al. (2015) used a combination of the X-plate and SPD to innovate a new energy dissipating device known as the shear-and-flexural yielding damper (SAFYD). This damper consists of a shear steel plate at the center and two X-shaped steel plates on both ends, as illustrated in Figure 2.16(d). The damper energy dissipation mechanism is a combination of the flexural deformation of the X-plates and the shear deformation of the web plate. Consequently, great lateral strength and stiffness are exhibited in SAFYD. Deng et al. (2015) proposed another type of SPD, namely the buckling restrained shear panel damper (BRSPD), which is made of a steel shear panel restrained by two plates (Figure 2.16(e)). The restrained plates sandwich the shear panels by means of bolts to reduce out-of-plane buckling deformation of the shear panels.

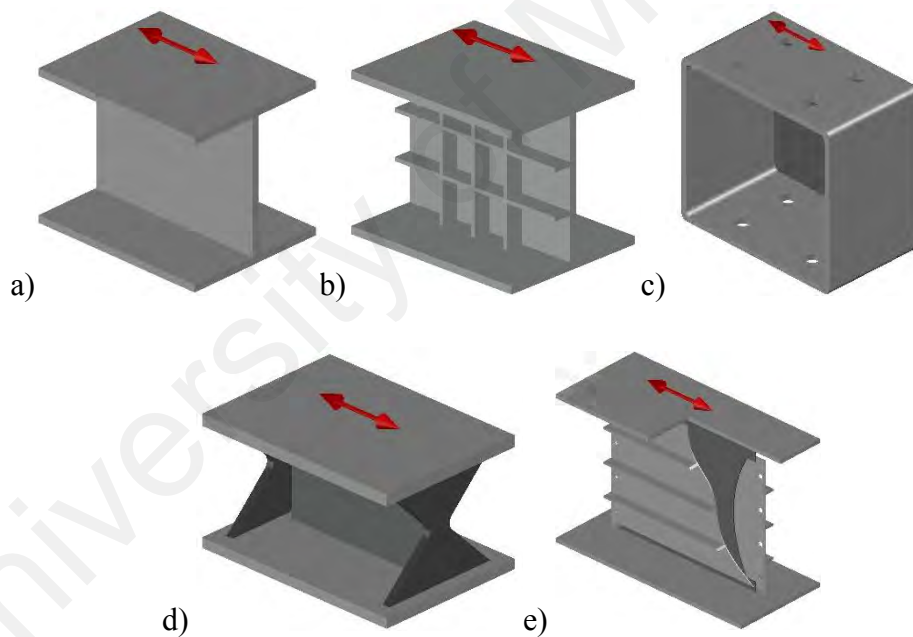


Figure 2.16: Steel shear panel-based dampers. a) SPD, b) SSPD, c) YSPD, d) SAFYD and e) BRSPD (Deng et al., 2015)

The J-damper, made of four J-shaped plates and arranged as shown in Figure 2.17(a), was invented by Kato et al. (2005). All J-shaped plates are bolted to a plate in the middle with roller supports at the plate's end. The damper dissipation mechanism is based on the roll-bending movement of the steel plates that work effectively under large deformation

due to the plates' shape. Deng et al. (2013) developed the crawler steel damper that benefits from U-shaped steel plates. The damper contains two U-shaped steel plates facing each other and clamped between two connection plates. The plate arrangement, as illustrated in Figure 2.17(b), prevents stress concentration in one plate, hence substantially improving the damper performance during low cycle fatigue loadings. Subsequently, the damper's dissipation capacity is mostly dominated by the U-shaped plates' height and thickness. The steel cushion was introduced as an energy harvesting device in chevron bracing systems (Özkaynak, 2017). As Figure 2.17(c) demonstrates, the cushion is a cushion-shaped steel plate bolted to the primary structure. The device undergoes in-plane shear deformation to dissipate energy and has a high displacement capacity under low to moderate earthquake loads.

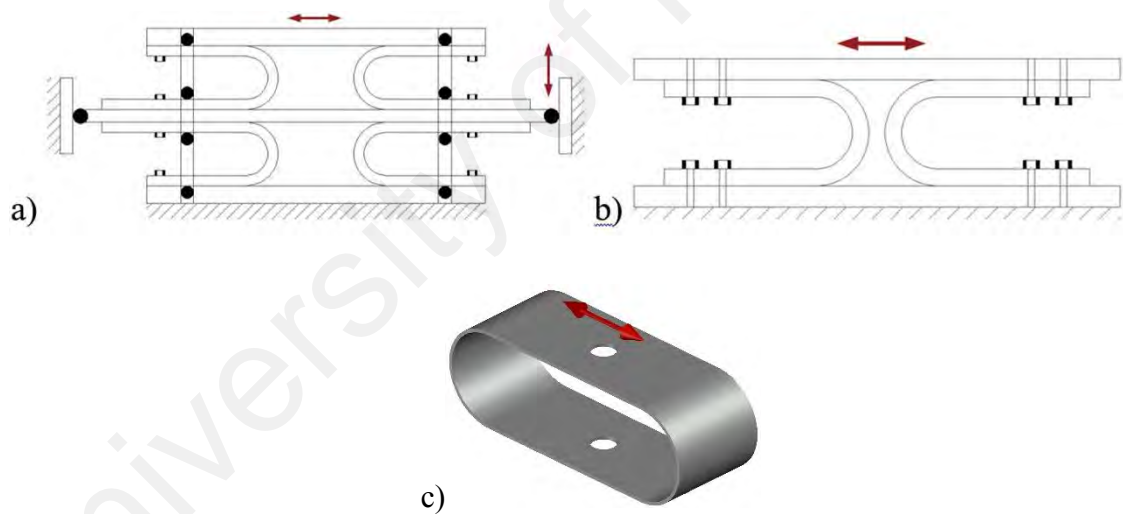


Figure 2.17: Detailing of a) J-damper, b) Crawler damper and c) Cushion damper

The tube-in-tube damper (TITD) was invented by Benavent-Climent (2010). The concept of TITD is inspired from BRB and SSD and was proposed for bracing systems. The TITD consists of two concentric rectangular hollow sections inserted into each other. The outer tube had several slit cuts. As Figure 2.18(a) demonstrates, the two tubes are welded to a plug and fillet. The damper is loaded axially at the ends of the two tubes, while the slit strips dissipate the load through plastic deformation. Furthermore,

Benavent-Climent et al. (2015) took advantage of the structural I-beam or wide flange to reduce the welding uncertainties in metallic dampers to develop another energy dissipation device. The device comprises several short segments of I-beams placed in parallel and bolted to two auxiliary elements (Figure 2.18(b)). The auxiliary elements are subjected to axial loads in the brace system, while the web of I-beams is subjected to out-of-plane bending.

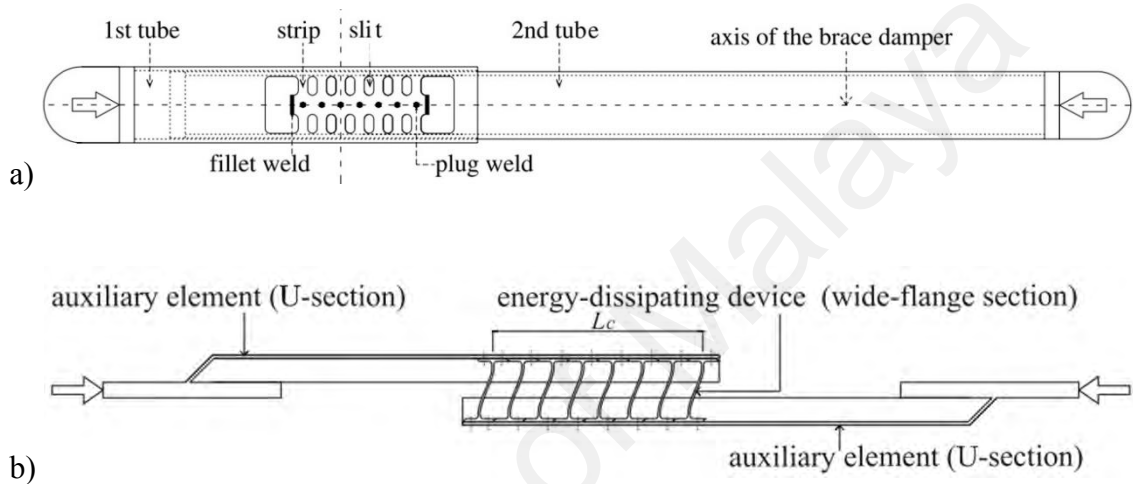


Figure 2.18: Detailing of dampers proposed by Benavent-Climent (Benavent-Climent, 2010; Benavent-Climent et al., 2015)

The pipe damper (PD) is made of a short structural steel pipe segment placed horizontally and welded to bottom and top plates. The PD was presented by Maleki and Bagheri (2010a) and is shown in Figure 2.19(a). In addition, Maleki and Mahjoubi (2013) also investigated the behavior of a dual-pipe damper (DPD). The DPD mechanism is similar to PD, with two pipes welded to each other (Figure 2.19(b)). The DPD demonstrates higher energy dissipation capacity than the PD. Thereafter, Maleki and Mahjoubi (2014) used different infills to enhance the energy dissipation capability of the PDP. Similarly, the infilled-pipe damper (IPD) has two pipe sections welded to two smaller diameter concentric pipes. The gap between the two concentric pipes is filled with lead or zinc materials, as presented in Figure 2.19(c). Two cover plates are bolted at the

sides of the pipes to prevent the squeezing out of the infill materials during operation. The plastic deformation of the inner and outer steel pipes as well as the infill materials is the main IPD feature to mitigate the shear stresses caused by lateral forces. Consequently, the IPD performance is significantly better than the PD and DPD. Franco et al. (2010) proposed a torsional tube damper (TTD), which consists of a central tube of low-carbon steel fixed at both ends and connected in the middle to a lever arm. The lever arm is attached to the anchorage supports and rotates in a torsional manner (Figure 2.19(d)). Thereby, the shear and bending loads are eliminated, ultimately leading to high cumulative displacement and energy dissipation. Furthermore, Javanmardi et al. (2017) presented a vertical pipe damper (VPD) made of a short vertical pipe segment welded to two anchor plates (Figure 2.19(e)). The VPD is able to dissipate energy bidirectionally and has greater ductility and energy dissipation capability than the PD and DPD.

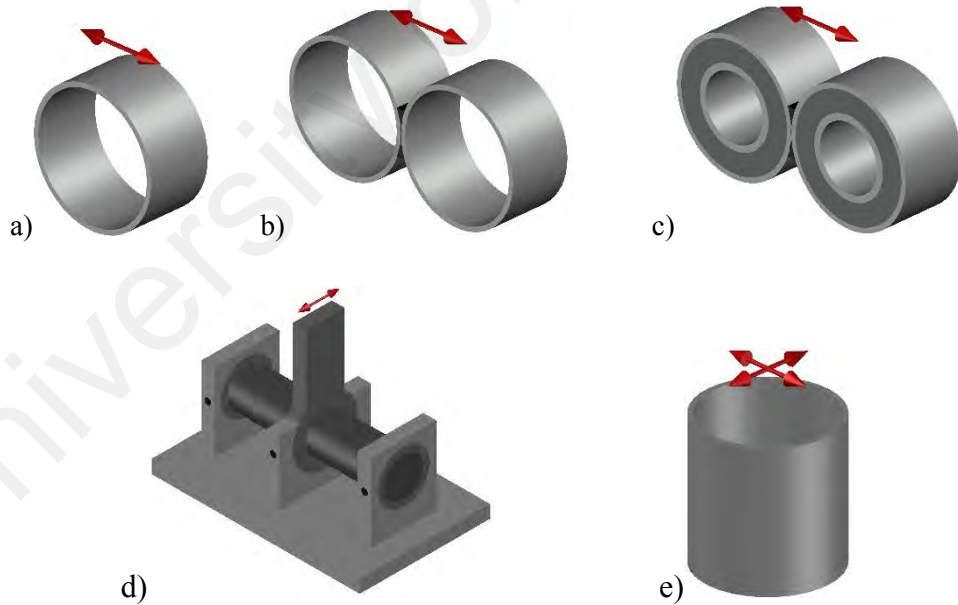


Figure 2.19: Schematic view of pipe-based dampers, a) PD, b) DPD, c) IPD, d) TTD and e) VPD

The elastic-plastic steel damper (EPSD) is made of several E-shaped steel plates with hinged ends and attached with pins to the connecting plate. The EPSD was developed by Wang et al. (2012) and is depicted in Figure 2.20(a). The E-shaped plates can be arranged

symmetrically either on both sides or only on one side of the connecting plate. The EPSD dissipates shear force from the connecting plate through the pins to the E-shaped plates. Yamazaki et al. (2016) proposed a novel buckling-restrained rippled plate damper (BRRPD) for use in the event of large earthquakes. The BRRPD contains a rippled core plate with two restraining plates on both sides (Figure 2.20(b)). The restraining steel plates are bolted to the rippled core plate and the base plate. The governing factor in BRRPD design is identified as the gap size between the core plate and restraining plates. The device demonstrates two deformation modes: (i) expansion deformation and (ii) out-of-plane global buckling deformation. The BRRPD has exhibited stable hysteretic behavior and high-energy dissipation capacity in different experimental tests.

The accordion metallic damper (AMD) was developed based on the mechanism of shock absorbers in the machinery industry (Motamedi & Nateghi-A., 2018). The AMD is fabricated from a thin-wall accordion steel tube, both ends of which are welded to end plates (Figure 2.20(c)). The axial load dissipates by plastic formation in the corrugated tube. The AMD exhibits asymmetric hysteretic behavior, but symmetric behavior is achieved when AMDs are coupled. Aghlara and Tahir (Aghlara & Tahir, 2018) invented the bar-fuse damper (FBD), which is made of inner, outer and fuse parts (Figure 2.20(d)). The outer part consists of a square steel tube, while the inner part comprises two C-channels welded to each other with a middle plate. The middle plate and outer part have several holes to accommodate the fuse bars. The steel bars are bolted to the inner and outer parts. The FBD is loaded axially and dissipates energy through the plastic deformation of the steel bars. The key feature of FBD is the easy replacement of the steel bars after failure. Thereafter, Aghlara et al. (Aghlara et al., 2018) developed the pipe-fuse damper (PFD) based on the FBD concept. PFD also consists of inner, outer and fuse parts similar to FBD. However, in the fuse part, the steel bars are replaced with steel pipes.

PFD also has the same energy dissipation mechanism as FBD, except PFD has higher energy dissipation capability.

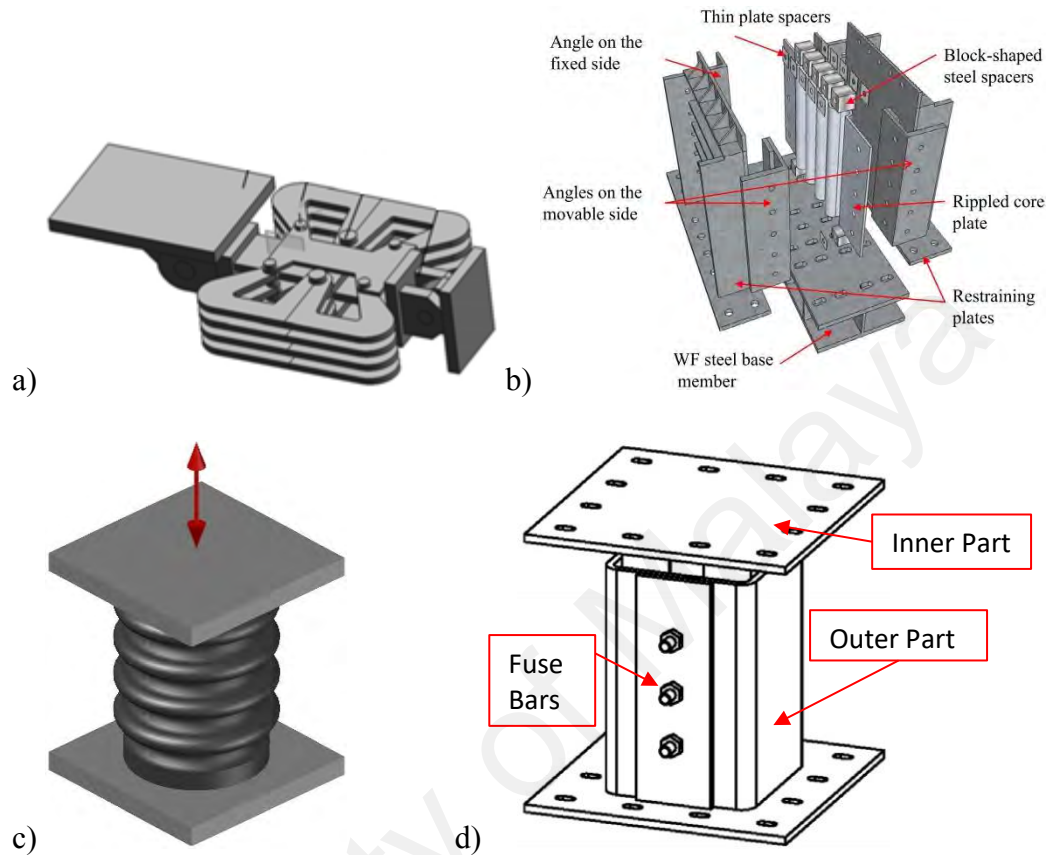


Figure 2.20: Detailing of: a) EPSD (W. Hao et al., 2012), b) BRRPD (Yamazaki et al., 2016) c) AMD and d) FBD (Aghlara & Tahir, 2018)

(b) Aluminum damper:

Aluminum offers greater ductility and lower yielding displacement compared to mild steel and low yield strength steel. Matteis et al. (2007, 2011) presented an energy dissipating device based on pure aluminum with the same geometry as the YSPD. The shear panel is used in the steel moment-resisting frame for lateral stability of the structure. The device is made of thin aluminum plates to form a short H-section segment with stiffeners as shown in Figure 2.21. The damper's performance was tested in a frame system through the shaking table test and it was proven that the device is perfectly capable

of reducing the base shear, overturning moment and floor acceleration of the frame structure (Rai et al., 2013).

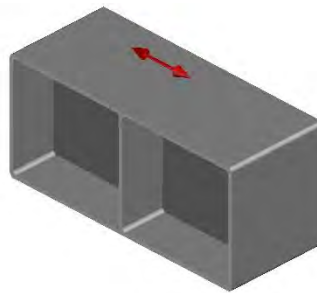


Figure 2.21: The aluminum shear-yielding damper

(c) Lead dampers:

Engineers find lead a favorable dissipation material due to its unique characteristics, including rapid recrystallization at room temperature and high cycle fatigue life. The first lead dampers were introduced by Robinson and Greenbank (1976) with two different configurations. As Figure 2.22(a) illustrates, the first damper is the constricted-tube extrusion energy absorber, which contains two concentric cylinders. Lead is enclosed by the inner cylinder, while the outer cylinder has an orifice around its mid-length. The inner cylinder is separated by a thin lubricant layer for the movement of the piston within the outer tube. The outer cylinder is fixed while the inner shaft is loaded axially. As the shaft moves back and forth, the lead extrudes back and forth through the outer cylinder's orifice. Figure 2.22(b) shows the second lead damper configuration, named the bulged-shaft extrusion energy absorber, which works with the same principle. The damper has a central shaft with a bulge in the middle. The central shaft is surrounded by lead with bearings at both sides to grip the lead in place. The bulge section extrudes the lead material as the central piston is loaded. As the shaft moves in the tube, the lead extrudes back and forth through the orifice formed by the bulge. Thereby, the energy dissipates through the extrusion of the lead material, causing plastic deformation in the lead. Lead dampers are dependent on operation temperature. Lead recrystallization occurs below

20°C; hence, lead dampers are able to recover and recrystallize rapidly. Soydan et al. (2014) tested the application of the extrusion damper in steel connections. The results indicated that the restoring force of the connection significantly improved after damper implementation. In addition, the connection displacement reduced substantially compared to the bare connection. Curadelli and Riera (2007) developed the ringed-type lead damper, as demonstrated in Figure 2.22(c). The damper consists of two concentric cylinders. The inner cylinder has several lead ring sections attached to a shaft. As the shaft end moves back and forth, the lead in the rings is subjected to shear and compressive stresses. Plastic deformation occurs as the rings deform. Cheng et al. (2017) presented the clapboard-type lead damper. The lead material is clamped between several steel slots, and the slots are hinged to the top and bottom plates (Figure 2.22(d)). Two steel plates are provided on the damper sides to prevent the squeezing out of the lead material during seismic loading. Experimental and numerical studies have proven that the proposed damper exhibits low yield displacement and excellent energy dissipation capability under different types of dynamic loading.

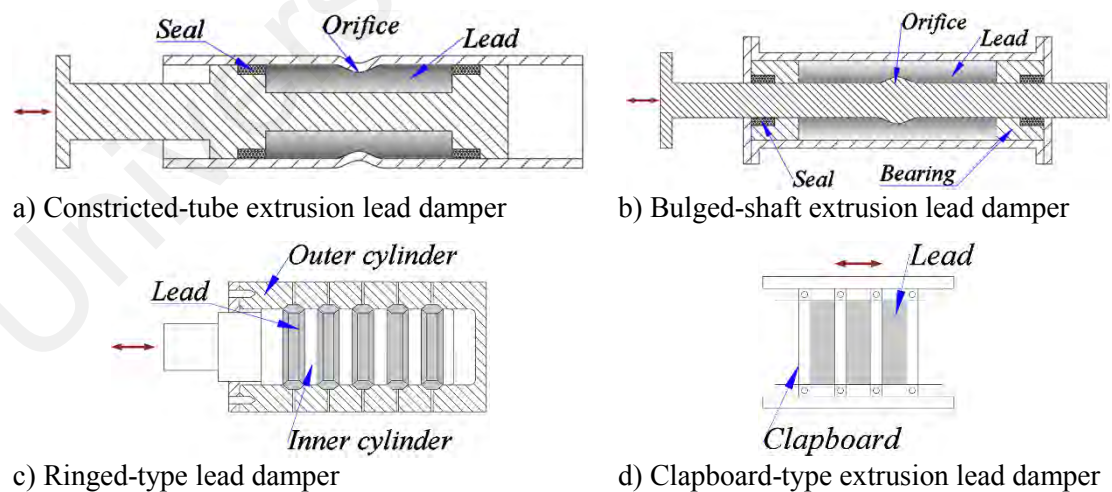


Figure 2.22: Lead dampers

(d) Copper dampers

The characteristics of copper are high ductility, low yield capacity and corrosion resistance. Copper in the shape of an hourglass was suggested as an energy dissipation device by Llera et al. (2004) and Briones and Llera (2014). It can be seen in Figure 2.23 that the copper damper is highly dependent on the aspect ratio of its height to the middle hourglass thickness. The copper damper is more efficient during non-impulsive ground motions and less efficient when the structure enters the inelastic range. Copper dampers have been analyzed experimentally and numerically to construct a constitutive model and produced large numbers of fat hysteresis loops with low yield displacement.

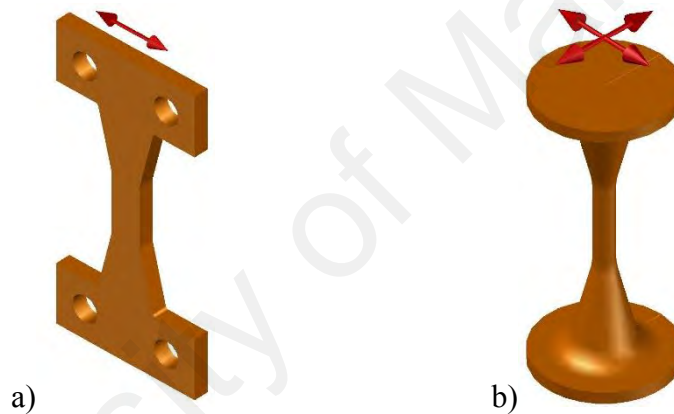


Figure 2.23: Copper dampers. a) Plate and b) Round hourglass dampers

(e) Shaped memory alloy dampers

Shape memory alloy (SMA) is effective in energy dissipation systems due to a number of advantages, including superelasticity, shape memory effect, low and high fatigue life, high damping, corrosion resistance, and young's modulus-temperature relations. SMA is able to tolerate large strains with no signs of residual deformation when it is unloaded. Casciati et al. (1998) proposed an SMA frame damper made of three vertical steel columns connected to each other by an SMA beam as illustrated in Figure 2.24 (a). The two outer legs are anchored to the bridge deck while the middle leg is attached to the vibration source. The damper shows good ductility and service life for bridge

applications. DesRoches and Delemont (2002) presented a round SMA energy dissipation device for bridge applications (Figure 2.24(b)). The proposed damper is installed between the bridge deck and the pier to enhance the seismic performance of the bridge. Sepúlveda et al. (2008) proposed a bar-shaped damper using a combination of copper and SMA to take advantage of both materials for energy dissipation. The copper-based SMA damper performance was evaluated through the shaking table test while it was installed in a beam-to-column connection. Zhang and Zhu (2007) proposed a reusable hysteretic damper (RHD) composed of two sliding steel blocks with Teflon sheets laid between them. Each block has two anchor fixtures to hold the pre-stressed SMA wires (Figure 2.24(c)). The damper may be adjusted for several sets of SMA wires according to the required configuration. Moreover, the proposed RHD can be reused even after earthquake events owing to its long-term reliability.

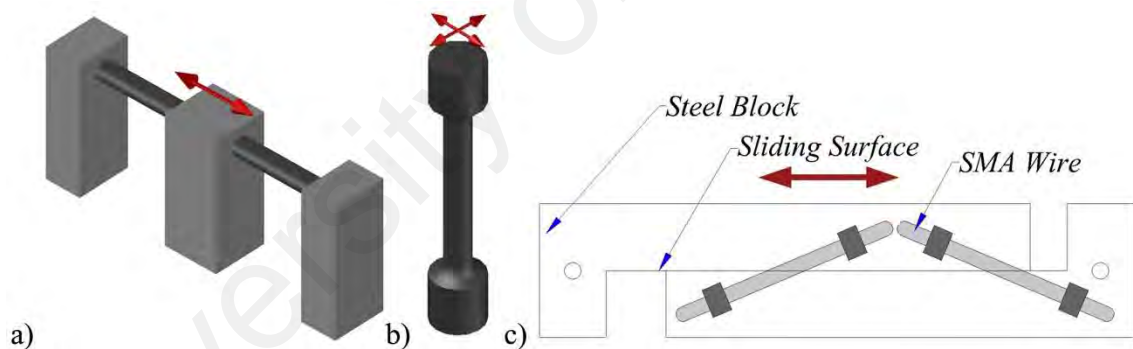


Figure 2.24: Schematic views of: a) SMA frame damper, b) SMA bar damper and c) RHD

Dolce et al. (2000) proposed a self-centering SMA-based energy dissipating device made of two concentric steel pipes and several studs inserted between them. Four sets of SMA wires are connected to the studs: two sets are re-centering wire loops and the two other sets are dissipating wire loops as shown in Figure 2.25 (a). The re-centering SMA wires are pre-tensioned according to the required force in order to bring the device back to the initial position. The device performance was tested in the bracing system of a

concrete frame, where the tension and compression forces were dissipated by SMA wires (Dolce et al., 2005). The device enhanced the frame performance and helped the frame to have minimal residual displacement after an earthquake event. Figure 2.25(b) shows another type of self-centering SMA-based damper proposed by Ma et al. (Ma & Cho, 2008; Ma & Yam, 2011) that consists of five groups: i.e., internal shaft group, external tube group, SMA wire group, springs, and roller system connection group. The internal shaft group is composed of a shaft with two moveable shim plates at the ends and one anchor fixed in the middle. The external tube group consists of a steel tube with two anchors at both ends. The two pre-compressed springs are connected to the middle fixed anchor and the shim plates, while the springs surround the pre-tensioned SMA wires. The damper benefits from the energy dissipation capability of the spring and SMA groups. It exhibits full re-centering capability, a high number of working cycles and excellent damping ratio.

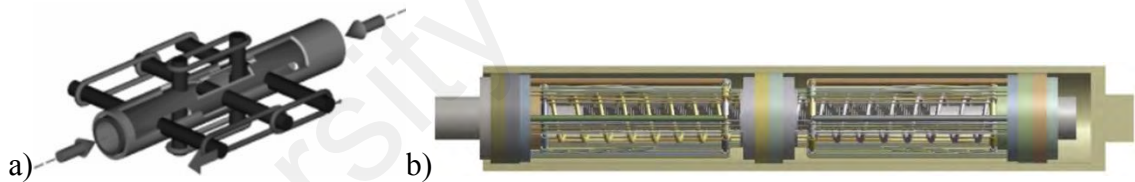


Figure 2.25: Schematic view of self-centering SMA dampers (Dolce et al., 2000; Ma & Cho, 2008)

2.5.3.3 Application

Metallic damper configurations may be altered to achieve the design requirements of engineers for mitigating dynamic loads in various types of structures (Vargas & Bruneau, 2007). Metallic dampers may be implemented in flexible frames, as a connecting element between the frame and rigid tower, in structures with a stepping tower and in base-isolated structure as illustrated in Figure 2.26 (a-d) (Kelly et al., 1972; Mazzolani, 2008; Skinner et al., 1974; Vargas & Bruneau, 2009). ADAS dampers are recommended for use in

moment resisting frames such as the chevron bracing system, and thereafter, a large number of other metallic dampers are also suggested for use in the same location of concrete or steel frame systems (Bergman, 1987; Mazzolani, 2008; Mazzolani et al., 2009; Nuzzo et al., 2014). The conventional bracing system may not be adequate for dynamic loadings; hence, metallic dampers have been proposed instead (e.g. diagonal and X-type) as depicted in Figure 2.26(e-g) (Chan & Albermani, 2008; Takeda et al., 1976). Dampers may also be used as shear walls to enhance the seismic performance of frames. In addition, it has been recommended to install a metallic damper in the middle of a secondary column (inner column) to increase the lateral stability of the frame system (Figure 2.26(h)) (Z. Chen et al., 2005, 2006). Tagawa et al. (2016) suggested placing metallic dampers in various configurations of the seesaw bracing system (Figure 2.26(i-k)). Utilizing metallic dampers in the beam-to-column connections of moment resisting structures is advantageous, as they provide large openings in the frame bays (Figure 2.26(l)) (Hsu & Halim, 2017; Maleki & Mahjoubi, 2013; Oh et al., 2009). Nonetheless, metallic dampers can also be installed between decks and piers or abutment of the bridges in the principal and transverse directions (Figure 2.26(m)) (Deng et al., 2013; Ge et al., 2011; Maleki & Bagheri, 2010b; Yamazaki et al., 2016). The installation of dampers in different structures is shown schematically in Figure 2.26.

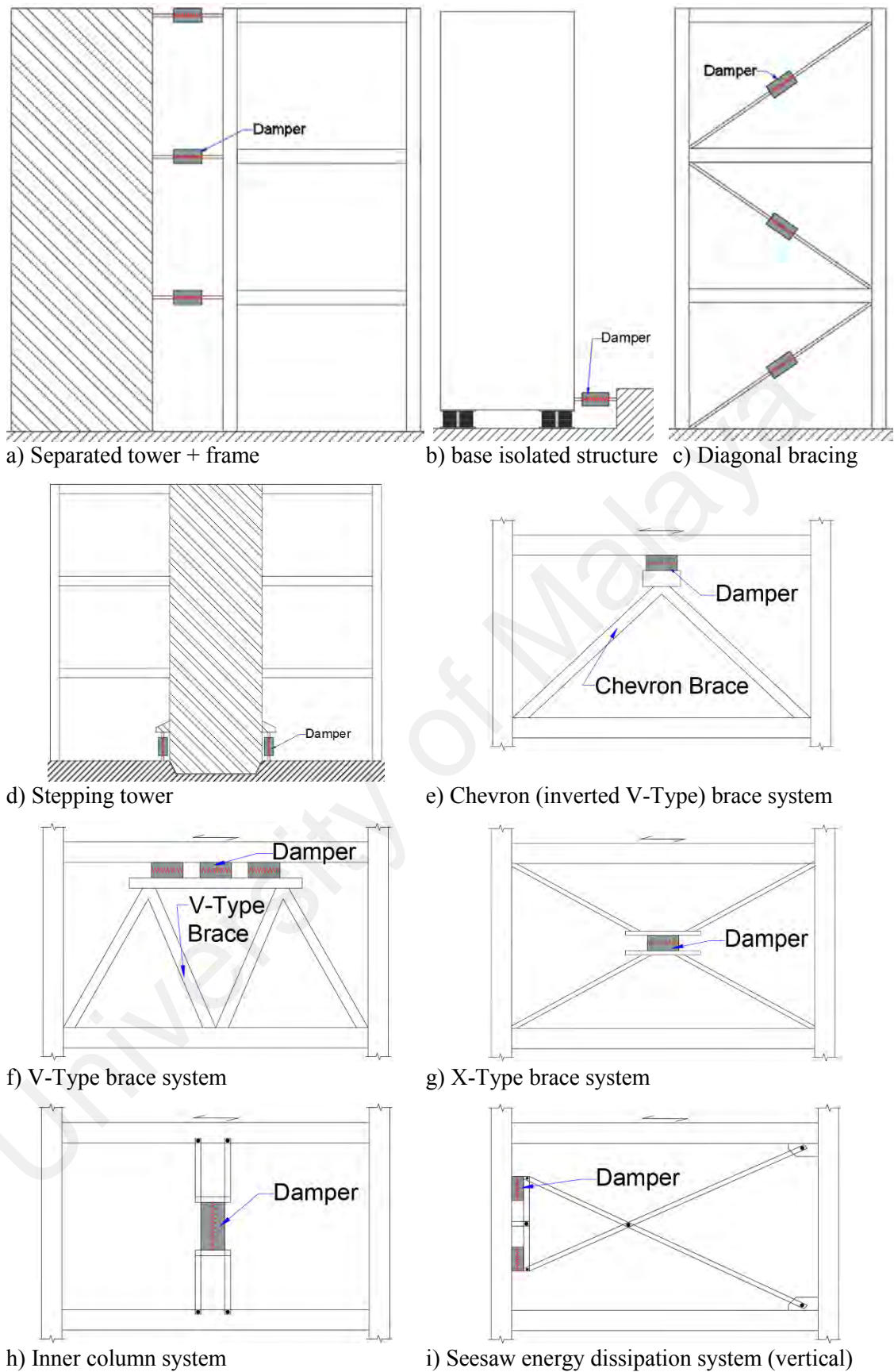


Figure 2.26: Schematic locations for the installation of metallic dampers in civil structures

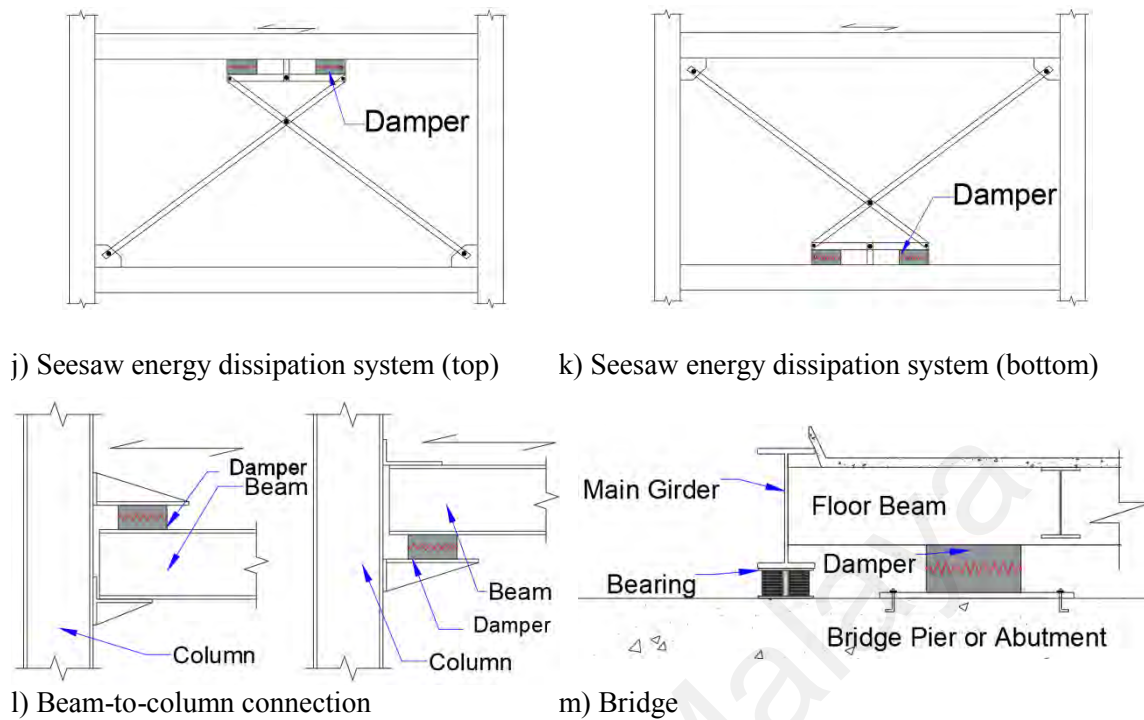


Figure 2.26, Continued

2.5.3.4 Fatigue life of metallic dampers

It is widely recognized that metals subjected to a limited number of excursions (e.g. <1000) well into the inelastic range may experience severe problems, or a phenomenon called low-cycle fatigue. This mechanism involves the growth and interconnection of micro-cracks, eventually leading to failure (Soong & Dargush, 1997).

Priestley et al. (1996) recommended limiting the maximum strain range during earthquakes based on the low-cycle fatigue experimental results of typical yielding dampers obtained by Tyler (1978a). In general, the device should be design such how to resist several design earthquakes and one extreme earthquake. Thus, typical maximum strain amplitude values for mild steel dampers fall in the range of 3% for design earthquakes and 5% for the extreme earthquake. With these limits, there is a sufficiently large number of cycles to failure, N_f , as shown in Figure 2.27.

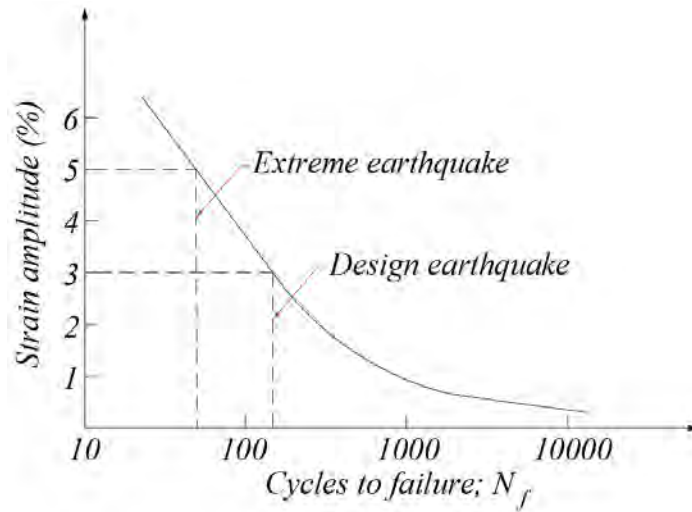


Figure 2.27: Metallic damper fatigue life prediction

2.5.3.5 Specific advantages and disadvantages of yielding metallic dampers

Metallic dampers are perhaps the most economic and robust seismic devices. Another clear advantage over other solutions is that they are virtually insensitive to environmental actions and age effects. A significant portion of energy dissipated by hysteresis loops in these dampers will be converted into heat; however, for reasonable devices, no significant change in the mechanical properties due to the increase in temperature is expected (Housner et al., 1997).

On the other hand, metallic dampers have the following disadvantages: (i) the possibility of premature fatigue failure; (ii) if not properly controlled, steels commonly employed to fabricate MDs may have a wide range of yield strengths, thus introducing uncertainties; (iii) MDs may leave the structure with significant permanent offset after an earthquake (no re-centering capability); (iv) these devices can generate high-frequency vibrations due to the sudden change in global structure stiffness after damper yielding; and (v) the structure's response might be worse with yielding metallic dampers than without for specific configurations and earthquakes. Hence, a complete nonlinear dynamic study of several design possibilities is necessary.

2.6 Vibration control of cable-stayed bridges

Several researchers have studied the seismic control of cable-stayed bridges in order to reduce the destructive effects of seismic activities on the structural members. The seismic control of cable-stayed bridges is divided into two main categories: (i) passive control and (ii) active and semi-active control.

2.6.1 Passive control devices

The first research on the seismic control of cable-stayed bridge was conducted in the early 90s by Ali and Abdel-Ghaffar (1995). Seismic isolators were installed between the deck and supports. As a result, the vibration periods increased and the effective reduction in seismic demand due to the energy dissipated by hysteresis loops was verified; however, the seismic displacement increased. Ali and Abdel-Ghaffar (1995) also found that the efficiency of passive devices reduced as the main span length increased.

Branco et al. (2000) investigated hysteresis damper behavior in the Vasco da Gama cable-stayed bridge. The proposed damper was installed between the deck and tower (Figure 2.28) in order to reduce the longitudinal and transverse displacements under seismic loadings.

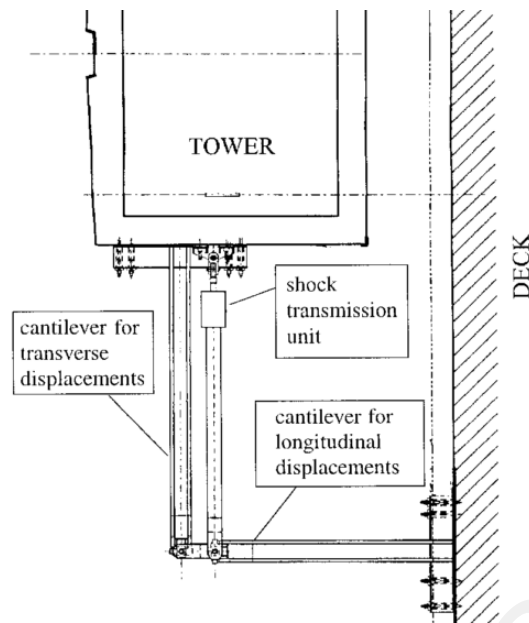


Figure 2.28: Plan view of proposed damper for the Vasco da Gama cable-stayed bridge
(Branco et al., 2000)

Abdel-Raheem and Hayashikawa (2003) proposed an effective and economic seismic protection by means of viscoelastic isolating devices and hysteresis loops in transverse struts linking both sides of the H-shaped towers, thus verifying the elastic behavior of the main structural tower parts. Wesolowsky and Wilson (2003) evaluated the base shear reduction of isolated cable-stayed bridges for near-field ground motions. They stated that the characteristics of near-field ground motions must be considered when designing the base isolators.

Dyke et al. (2003) developed a benchmark control problem for the seismic response of cable-stayed bridges. Several researchers have used this benchmark control problem to evaluate the effectiveness of different vibrational control systems on cable-stayed bridges (Chang & Loh, 2006; He et al., 2015; He et al., 2001; He & Agrawal, 2007; Iemura & Pradono, 2003; Ismail & Casas, 2014; Ok et al., 2007; Park et al., 2003; Saha & Jangid, 2009; Sharabash & Andrawes, 2009).

Soneji and Jangid (2007b) compared the performance of HDRB, LRB and FPS in cable-stayed bridges. Later, they attempted to enhance the performance of base isolated cable-stayed bridges with a hybrid control system. The hybrid control system is a combination of an isolation system with a semi-active damper (Saha & Jangid, 2009; Soneji & Jangid, 2007a). Ismail and Casas (2014) proposed a novel isolation device (RNC isolation system) for the seismic control of cable-stayed bridges subjected to near-fault earthquakes. They proved that the RNC isolation system is able to protect cable-stayed bridges against near-fault earthquakes.

Valdebenito (2009) utilized FVDs in different cable-stayed bridges and investigated their seismic behavior under strong ground motions. Over 55% of the input energy in the bridge models was dissipated by the FVDs. The FVDs showed good energy dissipation capability under near-fault and far-fault ground motions and they were insensitive to the stay cable layout. Moreover, Zhu et al. (2015) studied the effectiveness of FVDs on long-span cable-stayed bridges under seismic loadings. As shown in Figure 2.29, the FVD was implemented at the deck-tower connection to mitigate the longitudinal seismic demand of the bridge. It was found that nonlinear FVDs are more effective in enhancing the longitudinal seismic response of the bridge than linear FVDs.

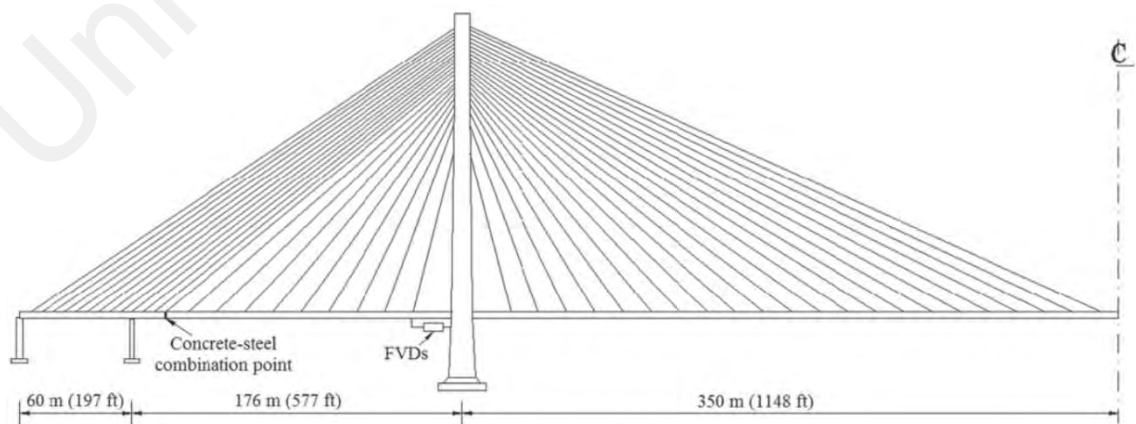


Figure 2.29: FVD installation in a long-span cable-stayed bridge (Zhu et al., 2015)

Guan et al. (2017) used metallic dampers in the lateral seismic control of a cable-stayed bridge with a heavyweight concrete girder in a high-risk seismic zone. They concluded that the metallic damper is cost effective, durable and capable of reducing the lateral seismic demand. Javanmardi et al. (2018) incorporated metallic dampers in a steel cable-stayed bridge and concluded that the metallic dampers can effectively reduce bridge and abutment pounding. However, the seismic global response of the bridge showed insignificant improvement.

2.6.2 Active and semi active control devices

Early analytic and experimental studies of cable-stayed bridges with active and semi-active control devices were done by Schemmann (1998b, 1998a). Substantial reduction in extreme seismic forces was observed and it was recommended that the actuators should optimally be close to the main span center. Furthermore, it was concluded that to reduce displacements it is only necessary to control the first vibration modes. However, higher modes also need to be controlled by the seismic device if the aim is to effectively reduce the seismic forces. This again highlights the significance of such high frequencies in the seismic response of cable-stayed bridges.

Park et al. (Park, Jung, et al., 2003; Park et al., 2003) proposed a hybrid control system for the Memorial Bill Emerson Bridge (USA). The proposed system is a combination of LRBs and active or semi-active devices to control the subsequent increase in displacements. Li et al. (2001) studied the seismic response of cable-stayed bridges equipped with active mass dampers (AMD). They observed drastic reductions in the seismic demand and lateral displacement of the bridge. AMDs modify the properties of conventional tuned mass dampers (TMD) taking into account the properties of seismic excitation in real time.

Iemura and Pradono (2003) stated that viscous dampers plus elastic bearings and variable orifice viscous dampers are highly effective in controlling the seismic response of cable-stayed bridges. Variable orifice dampers, employed in semi-active control, present the advantage of requiring actuators only in the device itself, which shows a pseudo-negative stiffness suited to dissipate large amounts of seismic energy. Ok et al. (2007) adopted the fuzzy logic algorithm with the magneto-rheological damper (MRD) to enhance the seismic performance of cable-stayed bridges. This is considered a semi-active control system that does not require a primary controller. It was concluded that the semi-active fuzzy control system has robust performance and improves the seismic performance of cable-stayed bridges. The MRD implemented in Dongting Lake Cable-Stayed Bridge to minimized the adverse effect of rain-wind-induced cable vibration (Chen et al., 2003).

2.7 Summary

This chapter discussed the dynamic and seismic behavior of cable-stayed bridges. Different seismic analysis methods for cable-stayed bridges were explained briefly. Further, the seismic analysis procedure for cable-stayed bridges was also recommended. Moreover, different structural control systems were explained with emphasis on metallic dampers. The literature indicates that for the existing structures, the structural control system is one of the best alternatives for minimizing the damages to the structures in earthquake zones. Metallic dampers appear to be advantageous in terms of design, reliability, performance, robustness and cost-effectiveness. Moreover, seismic isolators i.e. LRB take into account the energy characters of the earthquakes that result in minimizing the seismic demands on the superstructures. It is reported that short-to-medium span cable-stayed bridges may experience more severe seismic damages as compared to long-span cable-stayed bridges (Valdebenito., 2009). A brief discussion on the implementation of various control systems in cable-stayed bridges indicated that the

dampers are the most used control systems. The dampers are mainly used to control the vibration of cables due to the wind and rain effects. In addition, hybrid control systems that are combinations of passive and active devices are used in cable-stayed bridges, which are accompanied by high initial and operational costs. Further, the seismic behavior of the cable-stayed bridge having the seismic isolators at the deck level had been investigated. Nonetheless, the studies of the seismic behavior of the cable-stayed bridge were limited to the global responses. Meanwhile, the local seismic behavior of isolated cable-stayed bridge in specific the tower responses (in substructure and superstructure) are more crucial for the investigation. The seismic analysis and protection of existing short-to-medium span cable-stayed bridges that were designed according to traditional standards are indispensable. Nevertheless, there is a lack of knowledge of partial isolation effects on the seismic behavior of the cable-stayed bridge, where the full isolation of the bridge is inconvenient and yet the bridge is vulnerable to seismic loadings. Lastly, it is clear that passive hybrid control systems such as the combination of seismic isolators with metallic dampers have not been considered or studied as potential alternatives in mitigating the seismic demands on cable-stayed bridges.

CHAPTER 3: GLOBAL SEISMIC RESPONSE OF PARTIAL AND FULL ISOLATIONS OF THE CABLE-STAYED BRIDGE BY LEAD RUBBER BEARINGS

3.1 Introduction

This chapter discloses the seismic response of the cable-stayed bridge having different seismic isolation cases. The configuration of the bridge details and the previous experimental modal analysis of the bridge are briefly described. A rigorous three-dimensional finite element model of the bridge with all sources of geometric nonlinearities is created. The bridge model is validated with results of the previous experiment. Pushover analysis of the bridge in the longitudinal and transverse directions is performed in order to get an insight on the failure mechanism of the bridge during earthquake excitations. Thereafter, different retrofitting case are defined and seismic isolators are designed for each case according to AASHTO (2010, 2012). The seismic behavior of the cable-stayed bridge is analyzed based on the recommended procedure for seismic analysis of cable-stayed bridges in Chapter 2. A comparative study between each case is conducted through a series of time-history analysis.

3.2 Description of the cable-stayed bridge

The Shipshaw bridge constructed in 1972 (Figures 1.1) and is an asymmetric cable-stayed bridge with two planes of cables arranged in a fan shape spanning the Saguenay river, which is located in Canada. The bridge is made of a double leg steel tower and a composite deck supported by two box girders. The overall length of the bridge is 183.2m with two spans and a 4% downward slope from the East (right) to the West (left) abutment in the longitudinal direction. The bridge site is classified as rock (Filiatrault et al., 1993a). The tower base is hinged, which allows rotation in the longitudinal direction. The bridge end bearings are roller supported to allow for longitudinal displacement as well as to

withhold the uplifting of the bridge deck exhibited by the cable forces. The connection between the tower and the deck is a rigid connection.

The deck has an 11 m wide concrete slab that is 165 mm thick with two non-structural precast parapets on the sides. In addition, five longitudinal stringers support the deck at equal intervals of 2.4 m. Floor beams transfer the stringer loads to the box girders and are spaced equally at 7 m intervals in the transverse direction. The dimensions of the box girder are 1.5 x 3 m with a web and flange thickness of 50 mm. The tower is 43 m tall and consists of two 2.4 x 1.5 m rectangular box girders with a flange and web thickness of 50 mm. The box girders and tower sections are stiffened with several stiffeners at certain distances to prevent both the global and local buckling due to axial forces. Each tower is connected by four cables to the top flange of the box girders at equal intervals. Each cable comprises nine strands of 65.1 mm² cross-sectional area. Figure 3.1 shows the geometric detailing of the bridge. The details of the bridge are taken from these references (Christopoulos & Filiatrault, 2006; Martínez-Rodrigo & Filiatrault, 2015).

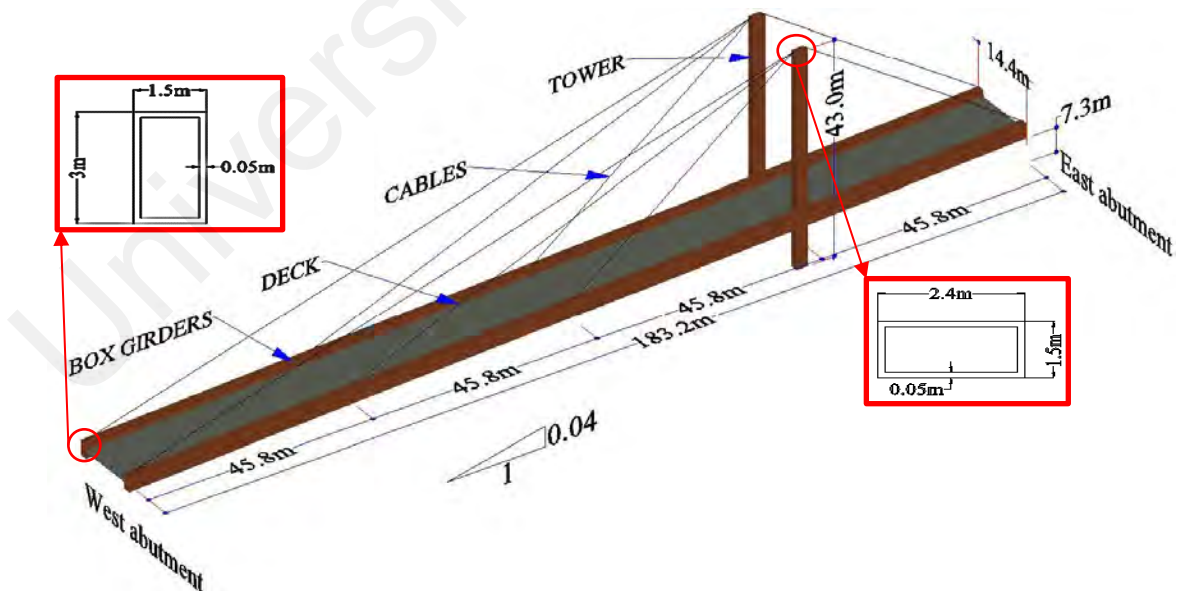


Figure 3.1: Shipshaw cable-stayed bridge detailing

3.3 Methodology

3.3.1 Structural modeling of the bridge

Since cable-stayed bridges are complex structures with high degree of redundancy and have a large number of degrees of freedom (Hassan et al., 2012; Mozos & Aparicio, 2010a, 2010b), the simplification of the model leads significant reduction in number of degrees of freedom and hence reduces the size of stiffness matrix and decreases the analysis time consumption. The nonlinear dynamic time-history analysis of Shipshaw cable-stayed bridge is performed using SAP2000 software (Computers and Structures Inc., 2015). The numerical analysis is conducted on a three-dimensional full-scale model of the bridge; as shown in Figure 3.2.

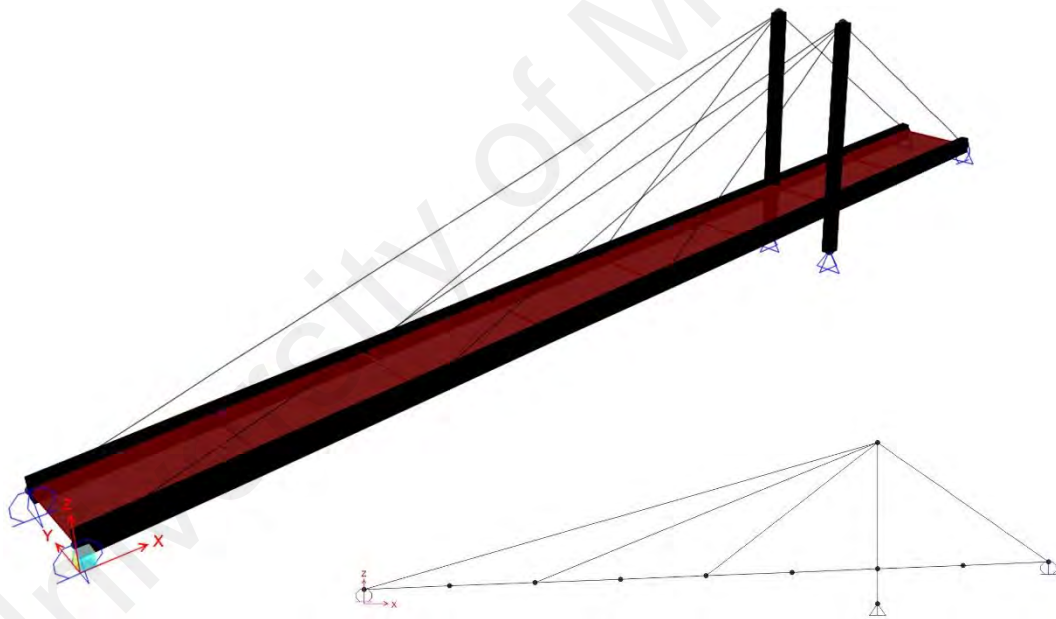


Figure 3.2: Three-dimensional finite element model of Shipshaw cable-stayed bridge

The 0.165 m thick concrete slab is modeled as a shell element. The tower and box girders are modeled as 3D beam elements. The ultimate tensile strength and young modulus of the steel members are 448 MPa and 200 GPa, respectively. The compressive strength of the concrete deck is 27.5 MPa and it has an elastic modulus of 24.8 GPa. The nonlinear behavior of the steel and concrete materials is shown in Figure 3.3. The cables

are modeled as a cable element with an area of 585.9 mm². A young's modulus of 175 GPA with a yield and ultimate strength of 1500 MPa and 1725 MPa, respectively, are assigned to the cables. The data on cables' tension forces are unavailable; therefore, from the literature, the cable forces are calculated. The Unit Load Method (ULM) proposed by Janjic et al. (2003) is used to calculate the tension force of cables. ULM takes into account the effect of geometric nonlinearities in the cable-stayed bridges. This method determines the required factors that have to be multiplied by the applied unit load to find the optimum values of cable forces. The criteria to find the optimum values of cable force is to minimize the vertical deflection of the deck at the middle of the longer span, which is achieved through an iterative process in a spreadsheet. The calculated tensioning forces of the cables are shown in Table 3.1 and assigned to each cable in the bridge model. The cable element is able to model the catenary behavior of the cable under its self-weight. The tower base is hinged, which permits the tower to rotate along its longitudinal and transverse axes ($U_X=U_Y=U_Z=0$). At the abutments, the bridge can move freely along its longitudinal axis and it is restrained in both the transverse and vertical directions ($U_Y=U_Z=0$).

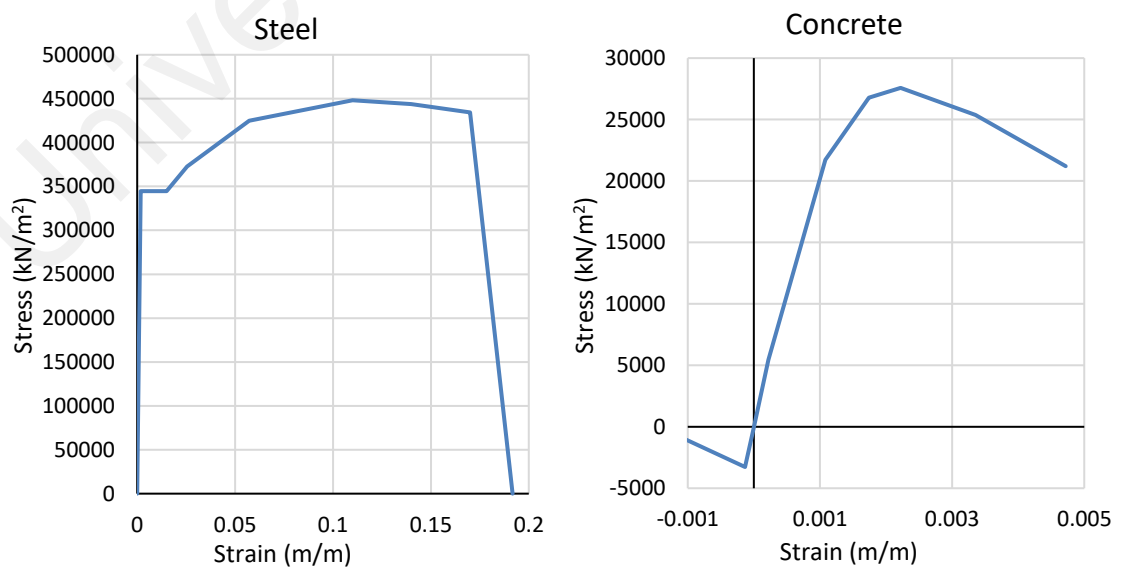


Figure 3.3: Stress-strain curves of steel and concrete materials used for modeling

Table 3.1: Calculated cables' tension forces the cable-stayed bridge

	Cable 1	Cable 2	Cable 3	Cable 4
Tension force (kN)	5520.95	8931.65	4882.00	21150.00

The failure criteria for the box girder and tower are defined as a series of plastic hinges with different properties for the frame elements. A 3D P-M2-M3 interaction surface is considered for the tower section. The P-M2-M3 hinge property represents the combined axial load and biaxial-bending moment behavior of the tower. A 2D M2-M3 interaction surface is considered for the box girder. The M2-M3 hinge property represents the biaxial bending moment behavior of the box girder. The moment-rotation interaction curves for each member are calculated using section designer in SAP2000. For all the hinges, the relevant hinge length is set to be 90% of the section depth. Since the cables are always modeled as tension members only, the failure criterion of this element is the elongation of the member up to rupture point, which is set to be 3.5% of the total length. Once the hinge reaches its maximum load carrying capacity it drops to zero. The static nonlinear analysis under the self-weight of the bridge is performed considering the material and geometrical nonlinearity to simulate the nonlinearity behavior of the cable-stayed bridge, which is followed up by modal analysis.

3.3.2 Experiment and validation of FEM

A full-scale field vibration test was conducted on the bridge using seven accelerometers. The accelerometers were placed on the top flanges of the box girders. A 44-ton truck with a constant speed of 80 km/h was used as the source of excitation. The rolling and break tests were performed to vibrate the bridge at different frequencies. The ULTRA (Felber & Stierner, 1992) signal processing software was used for spectral analysis. The peak picking method was used to find the modal parameters from the

Fourier spectrum. More details of the experiment test may be found in the research of Filiatrault et al. (1993a, 1993b).

In the present study, a numerical analysis is carried out and verified by experiment. Figure 3.4 shows the four flexural mode shapes of the cable-stayed bridge from the numerical analysis. The sum of the modal mass of the first four flexural modes is 95.3% of the total mass of the bridge. The dominating flexural mode is the second mode with a mass participation percentage of 64.27%. The four time periods of the bridge from the experiment and numerical modal analysis are illustrated in Table 3.2. As the table illustrates, the natural time periods of the cable-stayed bridge from the experiment and numerical analysis have a reasonable correlation.

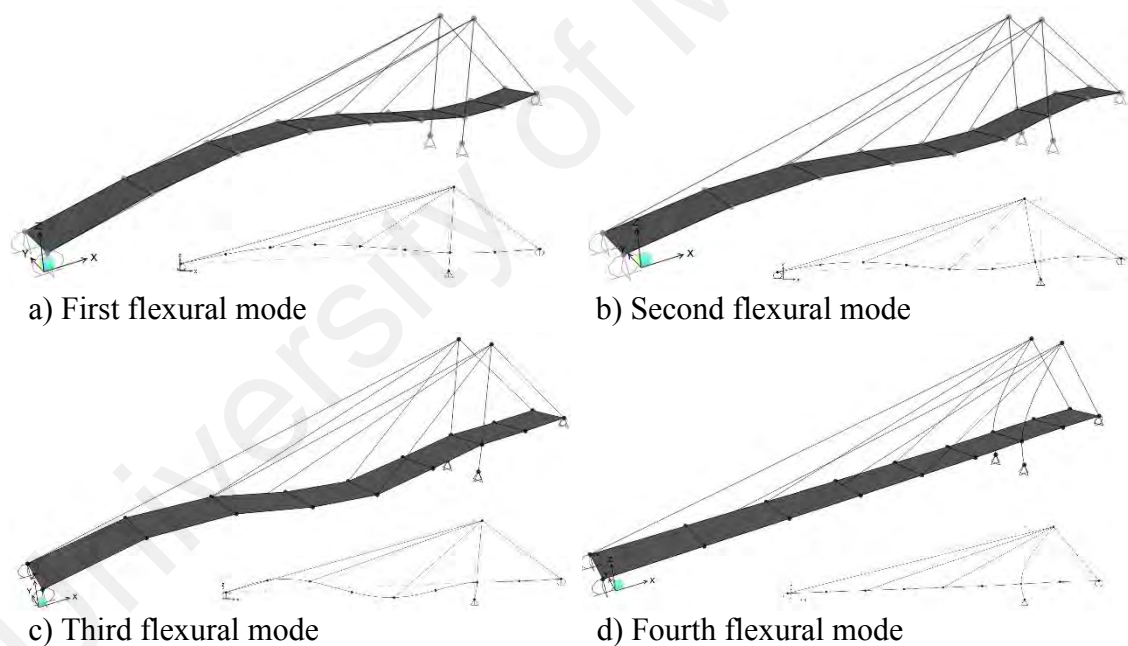


Figure 3.4: Four flexural mode shapes of the cable-stayed bridge

Table 3.2: Natural time periods of the cable-stayed bridge (Filiatrault et al., 1993b)

Mode shape	Time periods (s)		Numerical effective modal mass (%)	Error (%)
	Experimental	Numerical		
1 st Flexural	1.85	2.09	2.16	12.9
2 nd Flexural	0.85	0.86	64.27	1.2
3 rd Flexural	0.57	0.57	18.28	0.0
4 th Flexural	0.38	0.42	10.59	10.5

3.3.3 Pushover analysis of the cable-stayed bridge

In this section, pushover analysis of the bridge in longitudinal and transverse directions is investigated. The static-nonlinear pushover analysis provides the details of elastic and inelastic responses of the bridge and gets an insight information about the expected global and local failure mechanisms of the bridge during earthquake excitations. The bridge is subjected to progressively increasing displacement-control load that is proportional to the mass distribution of the tower and the deck till global failure of the bridge occurs. The pushover analysis is continued from static nonlinear analysis to account for the cable-sag effect, the material nonlinearity, P-delta and large displacement. Figure 3.5 shows the typical force (moment) – displacement (rotation) curvature and the three performance levels defined by FEMA-273 (1997). The points A, B, C, D, and E define the force-displacement relation of the hinge while the points IO (Immediate-Occupancy), LS (Life-Safety) and CP (Collapse-Prevention) define the performance acceptance criteria of the hinges.

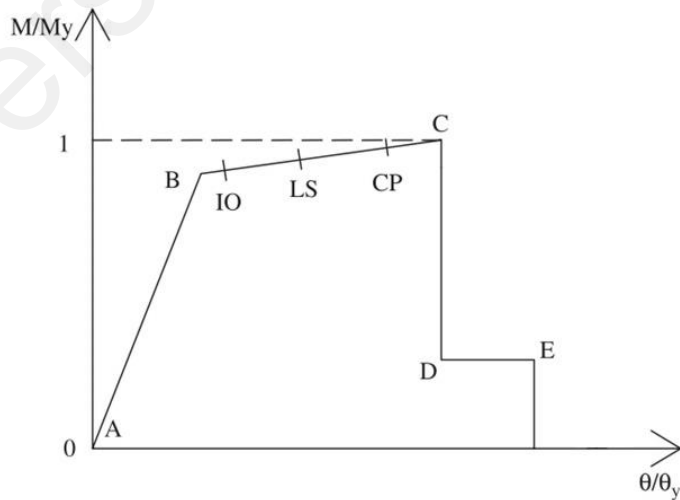


Figure 3.5: Acceptance criteria of the plastic hinges defined by FEMA-273 (1997)

3.3.4 Equations of motion

The equations of motion for the cable-stayed bridge under earthquake excitations is (Chopra, 2014):

$$[M]\{\ddot{u}\} + [C]\{\dot{u}\} + [K]\{u\} = -[M][\eta]\{\ddot{x}_g\} \quad (3-1)$$

$$\{u\} = \{x_1, x_2, \dots, x_N\}^T \quad (3-2)$$

Where $[M]$, $[C]$ and $[K]$ are the mass, damping and stiffness matrixes of the bridge, respectively. $\{\ddot{u}\}$, $\{\dot{u}\}$ and $\{u\}$ are the bridge acceleration, velocity and displacement vectors, respectively. The parameter $[\eta]$ is the earthquake coefficient matrix. $\{\ddot{x}_g\}$ is the earthquake acceleration vector in the longitudinal and transverse directions.

After the implementation of the seismic isolator in the cable-stayed bridge, the equations of motion under earthquake excitations is modified as follow:

$$[M]\{\ddot{u}\} + [C]\{\dot{u}\} + [K]\{u\} + [D]\{F\} = -[M][\eta]\{\ddot{x}_g\} \quad (3-3)$$

Where $[D]$ is the location matrix for the restoring forces of seismic isolators and $\{F\}$ is the restoring force vectors of the isolators.

3.3.5 Nonlinear time-history analysis

Nonlinear structures are associated with either material or geometric nonlinearities or both. The nonlinear analysis method should be used in structural modeling if the structure is associated with high degrees of nonlinearities. The nonlinear analysis can be either static or dynamic analysis. The cable-stayed bridges are highly nonlinear; therefore, the geometric and material nonlinearities are essential in modeling and analyzing such structures.

Nonlinear time-history analysis is a dynamic-nonlinear analysis which can be solved by the fast nonlinear analysis or direct integration method. In either solving method, the source of nonlinearities such as material nonlinearity and P-delta effect should be considered for cable-stayed bridges. After the validation of the bridge model by the experimental results, the direct integration method is used for the nonlinear time-history analyses of the bridge cases under different ground motions.

3.3.5.1 Ground motions criteria

One of the challenges for structural engineers is the selection of the appropriate ground motions. Each ground motion record has unique characteristics. Long-span bridges such as cable-stayed bridges have longer fundamental periods and their seismic responses are affected by the velocity and displacement of the ground motions (Chopra, 2014). Eurocode 8 (2005) classified the elastic response into three zones; (i) zone 1 ($T < 0.4$ Sec) which is affected by acceleration, (ii) zone 2 ($0.4 < T < 3$ Sec) which is affected by velocity, and (iii) zone 3 ($T > 3$ Sec) is affected by displacement (T represents the fundamental period of the structure). Moreover, the characteristics of selected ground motion should be consistent with site seismic hazard. The vertical component of the ground motions is ignored in this research as the stayed cables of the cable-stayed bridges are behaving as elastic supports and isolating the deck from seismic actions in the vertical direction (Walther et al., 1988).

3.3.5.2 Ground motion selection

Five pairs of ground motion records are selected to take into consideration the average of the response parameter in the assessment of the structural response. It is worth mentioning that, according to Eurocode 8 Part 1 (Eurocode8, 2005), a minimum of 3 accelerograms is required for time-history analyses. Each ground motion has two components in which the component with the higher PGA is applied in the longitudinal direction, and the

component with the lower PGA is applied in a transverse direction. One of the selected ground motion records corresponds to the actual ground motion that damaged the bridge, while the other four ground motion records are selected from the same seismic zone; as shown in Table 3.3. The computed response acceleration and displacement spectra for 5% structural damping are shown in Figure 3.6. This figure helps to understand the energy-containing frequency of each ground motion employed in the analysis. The earthquakes are applied uniformly along all the supports, and because the structure is founded on bedrock, the selected time-histories had been recorded on the rock or hard soil.

Table 3.3: Ground motions characteristics

ID	Earthquake	Station	Country	Magnitude	Distance (Km)	PGA Directions (g)	
						Long.	Trans.
M. HL 03-82	Miramichi-1982/03	Hickey Lakes-Site 3	Canada	5	6.5	0.397	0.186
M. HL 05-82	Miramichi-1982/05	Hickey Lakes-Site 3	Canada	3.9	6.5	0.111	0.110
M. IB II 82	Miramichi-1982/03	Indian Brook II	Canada	5	5.1	0.342	0.290
NH. FFD 82	New Hampshire-1982	Franklin Falls Dam	USA	4.5	10.4	0.313	0.126
S. Dicky 88	Saguenay-1988	Dicky	Canada	5.9	194.7	0.092	0.063

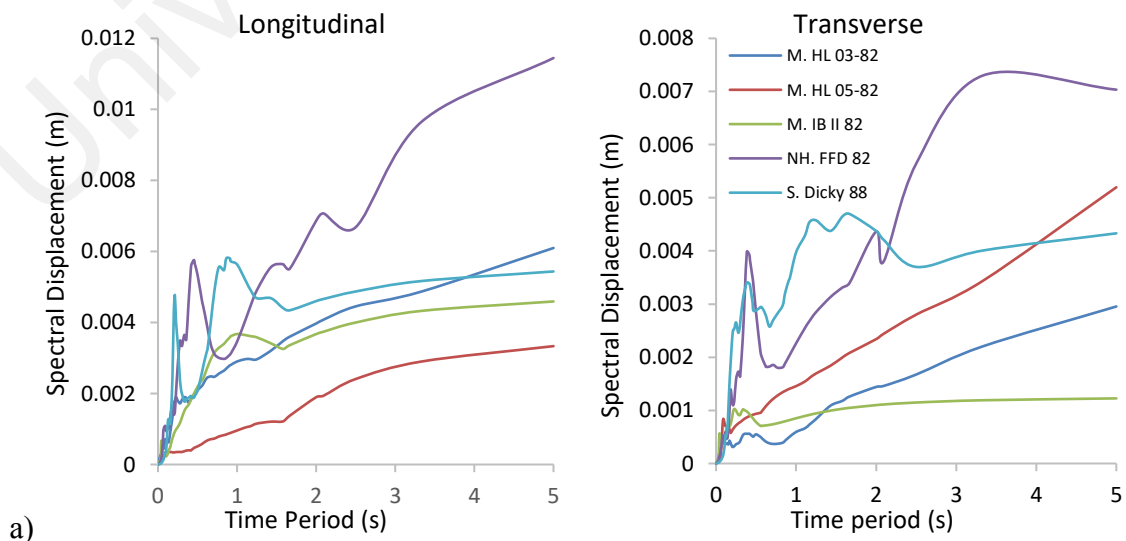


Figure 3.6: a) Spectral displacement and b) spectral acceleration of five earthquakes for the cable-stayed bridge with 5% of structural damping

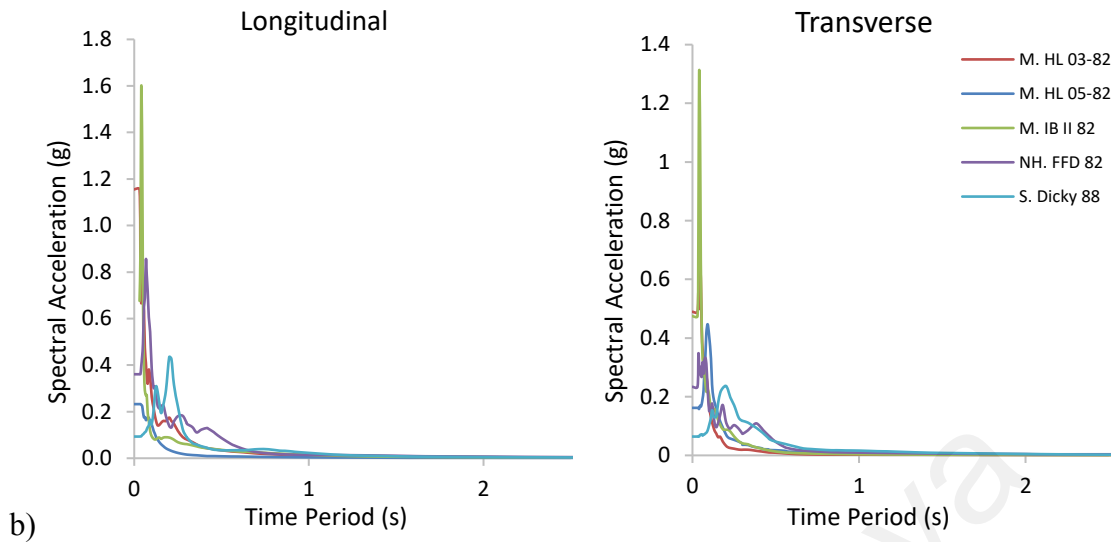


Figure 3.6, Continued

3.3.6 Seismic isolation of cable-stayed bridge

3.3.6.1 Design and modelling of seismic isolators

As discussed in chapter 2, there are several passive seismic isolators available in the market at which their characteristics are well studied. In this research, Lead-Rubber Bearing is selected for isolation of cable-stayed bridge. The Lead-Rubber Bearing (LRB) is invented by Robinson and Tucker (1977) in New Zealand. It has been widely implemented in civil engineering structures such as buildings and bridges. The design procedure of LRB devices are based on the Guide Specifications Seismic Isolation Design (GSID) (AASHTO, 2010) and LRFD Bridge Design Specifications (LRFD) (AASHTO, 2012). It is assumed that the superstructure is relatively rigid in comparison with isolators and deformation mainly occurs in isolators. The methodology flowchart has five steps as shown in Figure 3.7. Initially, the cable-stayed bridge is analyzed statically under its self-weight. Seismic hazard of the site to be determined using (i) acceleration coefficients (ii) site class and site factors (iii) seismic zone of the site. Later on, these data are used to plot design response spectrum for the bridge. Thereafter, the obtained data will be used in analyzing a single-degree-freedom-model of the bridge by the simplified method in both

directions, as specified in GSID (AASHTO, 2010). The simplified method is also known as direct displacement method which consists of several iterative processes to converge. As shown in Figure 3.8, the designed values are used to show the bilinear hysteretic response of LRB. For each case study conducted the bridge is analyzed for the strongest earthquake based on International System of Units (SI base units) at which, the initial structural displacement, d_{in} , can be assumed as (AASHTO, 2010):

$$d_{in} = 0.254 \times S_{DI} \quad (3-4)$$

Where S_{DI} is the designed spectral displacement. The characteristics strength, Q_d should be selected so that the isolator is stiff for non-seismic forces but yield under earthquake forces; hence, Equation 3-5 is found to be suitable for this purpose (Buckle et al., 2011):

$$Q_d = 0.05 \times W \quad (3-5)$$

Where W is the superstructure weight on each isolator. Also, post-yield stiffness, K_d , is the minimal lateral restoring force at the design displacement which is calculated as (AASHTO, 2010):

$$K_d = 0.05 \frac{W}{d} \quad (3-6)$$

And the effective period, T_{eff} of the bridge and viscous damping ratio, ξ is computed according to Equations 3-7 and 3-8, respectively (AASHTO, 2010):

$$T_{eff} = 2\Pi \sqrt{\frac{W}{gK_d}} \quad (3-7)$$

$$\zeta = \frac{2Q_d(d_{isol} - d_y)}{\Pi(K_{isol}(d_{isol} + d_{sub}))^2} \quad (3-8)$$

Where d_{isol} is the isolator displacement, d_y is the isolator yield displacement, d_{sub} is the substructure displacement and K_{isol} is the effective stiffness of isolator. Therefore, the total bridge displacement is (AASHTO, 2010):

$$d = \frac{0.249S_{D1}T_{eff}}{B_L} \quad (3-9)$$

Where B_L is damping coefficient. The total displacement obtained from Equation 3-9 and the initial assumed displacement calculated from Equation 3-4 should have a close agreement. The iterative process in the spreadsheet is used to achieve this.

The last parameter is the lateral force of isolation system which is obtained by (Buckle et al., 2011):

$$F_{isol} = K_{isol} \times d_{isol} \quad (3-10)$$

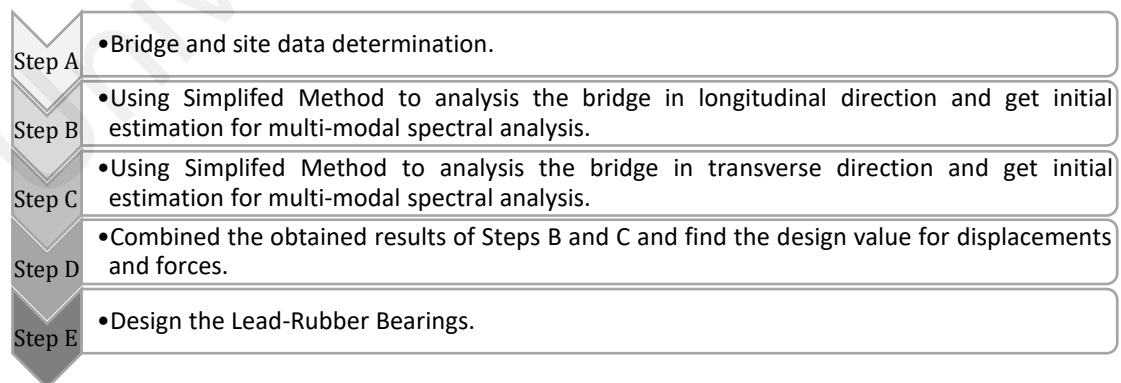


Figure 3.7: Design flowchart of the seismically isolated bridge

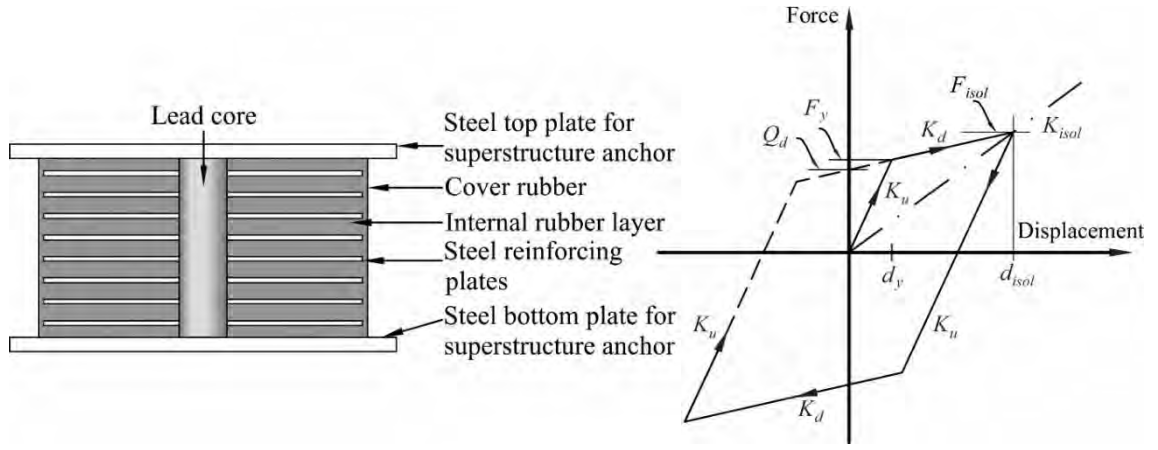


Figure 3.8: Detailing and idealized hysteresis behavior of Lead Rubber Bearing (LRB)

The forces mobilized and biaxial interaction behavior of LRB can be obtained by (Built, 1982):

$$F_2 = \alpha \frac{F^Y}{Y} U_2 + (1 - \alpha) F^Y Z_2 \quad (3-11)$$

$$F_3 = \alpha \frac{F^Y}{Y} U_3 + (1 - \alpha) F^Y Z_3 \quad (3-12)$$

Where α is the ratio of post-yield stiffness to pre-yield stiffness, Y is yield displacement, F^Y is the yield force, U_2 and U_3 are bearing displacements with respect to local axes as shown in Figure 3.9 (2 and 3 directions); while Z_2 and Z_3 are unit-less hysteretic quantities which represent the direction and biaxial interaction of hysteretic forces. Z_2 and Z_3 can be calculated by the coupled differential equations (Park et al., 1986):

$$Y \begin{pmatrix} \dot{Z}_2 \\ \dot{Z}_3 \end{pmatrix} = A \begin{pmatrix} \dot{U}_2 \\ \dot{U}_3 \end{pmatrix} \begin{bmatrix} Z_2^2 [\gamma \sin(\dot{U}_2 Z_2) + \beta] & Z_2 Z_3 [\gamma \sin(\dot{U}_3 Z_3) + \beta] \\ Z_2 Z_3 [\gamma \sin(\dot{U}_2 Z_2) + \beta] & Z_3^2 [\gamma \sin(\dot{U}_3 Z_3) + \beta] \end{bmatrix} \quad (3-13)$$

Where A , β , and γ are dimensionless quantities. The LRB in SAP2000 software is modeled using the nonlinear link element to produce its orthotropic behavior when α and the yield force vary in 2 and 3 directions (the local directions).

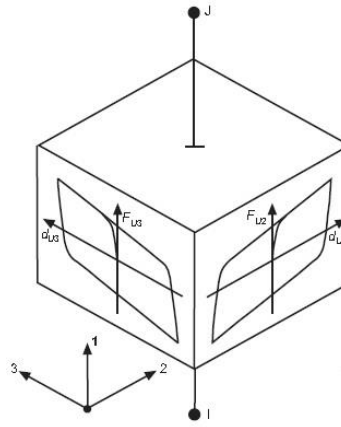


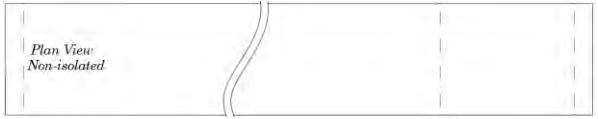
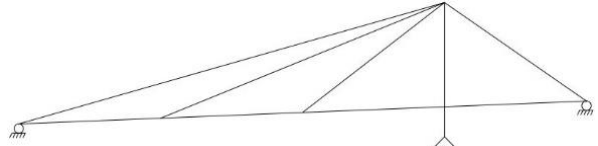

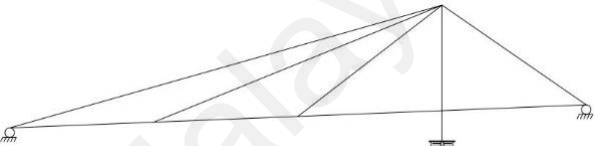

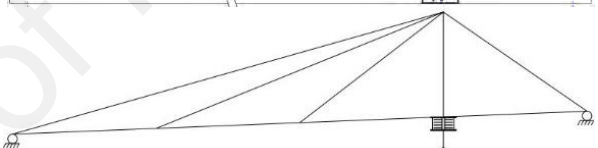
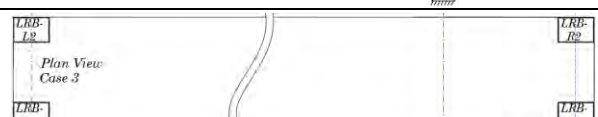
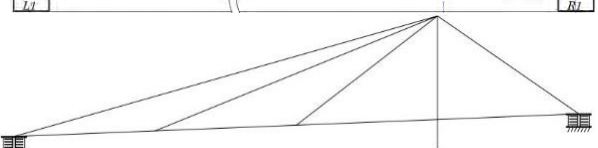

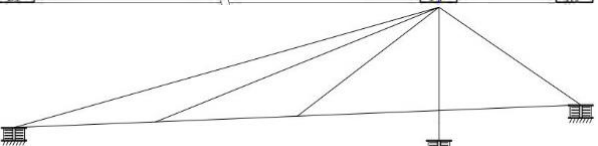
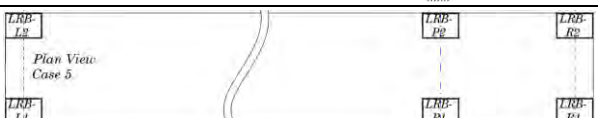
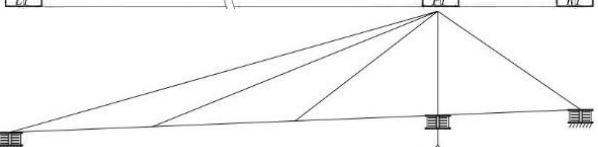
Figure 3.9: Schematic hysteretic property of LRB in biaxial shear deformation

(Computers and Structures Inc., 2015)

3.3.6.2 Seismic isolation retrofitting cases of cable-stayed bridge

Generally, the isolation system separates the superstructure from the substructure at the deck level. As mentioned earlier the deck-tower connection greatly affects the dynamic behavior of the cable-stayed bridge. At the deck-tower connection, it is possible to implement isolators by permitting the deck to sit on the base isolators. Nonetheless, the base isolator can be used below the tower base by separating the tower legs from the foundation. However, the possibility of implementing base isolators at the tower base has not been taken into consideration in practice. Accordingly, a total of five combinations of the base isolators are found to be possible to identify the appropriate retrofitting solution for the cable-stayed bridge. Table 3.4 illustrates the non-isolated and isolated cases of the bridge with schematic locations of the isolation systems. As the table shows, the bridge is partially isolated in case 1, 2 and 3, while it is fully isolated for case 4 and 5.

Table 3.4: Different retrofitting cases with schematic locations of isolation systems

Bridge cases	Partial / Full isolation	Location of base isolators	Schematic locations of LRB isolators
Non-Isolated	Partial isolation	Original configuration	 
Case 1	Partial isolation	At tower base	 
Case 2	Partial isolation	At deck-tower connection	 
Case 3	Partial isolation	At abutments	 
Case 4	Full isolation	At tower base and abutments	 
Case 5	Full isolation	At deck-tower connection and abutments	 

The LRBs characteristics are calculated in spreadsheets for the selected earthquakes based on the design procedure explained. These designed values are further used in numerical model. At each location of the bridge two LRBs are placed (Table 3.4) that have the same properties in longitudinal and transverse directions. Table 3.5 illustrates the LRBs characteristic strength for each locations of the bridge. It should be noted that LRBs have same properties in each case of seismic retrofitting.

Table 3.5: LRBs' characteristics used in numerical analysis

LRB	Stiffness (kN/m)	Yield strength (kN)	Post yield stiffness ratio
LRB-L	212	70	0.1
LRB-P	12000	350	0.1
LRB-R	637	212	0.1

3.4 Results and discussion

3.4.1 Results of pushover analysis

The displacement at top of the tower versus the bridge base shear is used to plot the results of the pushover analysis. Figure 3.10 shows the results of pushover analysis along the longitudinal and transverse directions of the bridge. In the longitudinal direction, the plastic hinge formation is observed at the tower section just below the deck when the base shear is reached to 23858 kN and the displacement of the tower at the top is reached to 0.443 m. Thereafter, the bridge is reached to its ultimate strength, while the same plastic hinge is failed and eventually the stiffness of the bridge is degraded. In the transverse direction, the bridge is shown higher stiffness compared to the longitudinal direction (due to boundary conditions). The first plastic formation is also formed at the tower section below the deck-tower connection when the base shear is reached to 106116 kN at 4.57 m displacement at top of the tower. As a conclusion, the damage concentration in both

directions is at the tower section below the deck-tower connection and the global failure of the bridge happened due to sudden failure of the tower hinges.

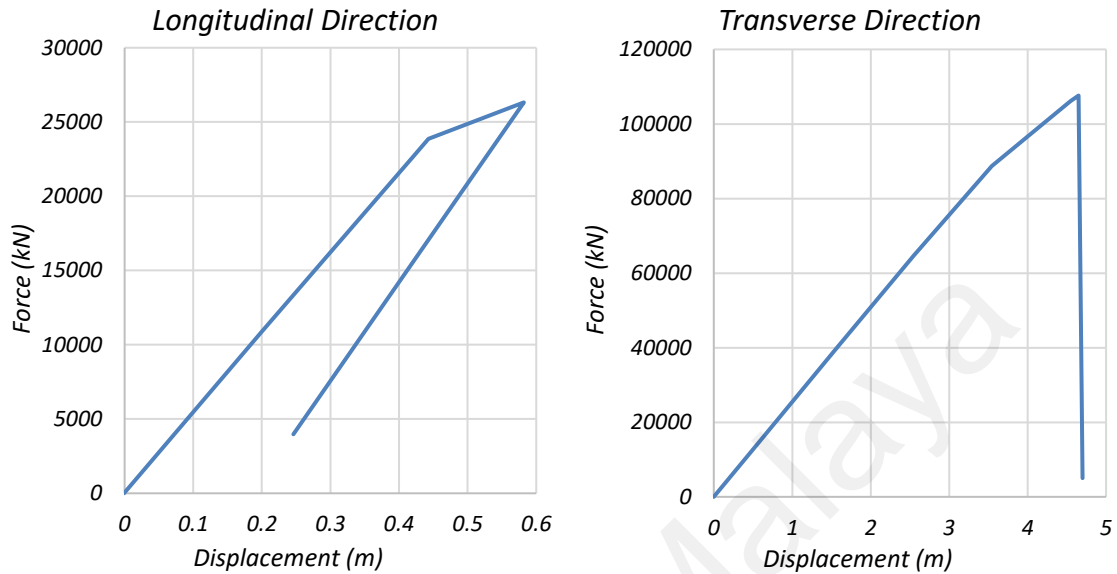


Figure 3.10: Results of pushover analysis of the bridge

3.4.2 Results of modal analysis

The natural time period and the relevant mass participation ratio of the bridge for non-isolated and different isolated cases from modal analysis are illustrated in Table 3.6. The natural time period of the retrofitted bridge should not exceed 1.7 times the original natural time period as it increases the seismic displacement response of the bridge (Iemura & Pradono, 2002). The isolation system has no significant effect on the natural time period of the bridge in cases 1 and 2. However, in cases 3, 4, and 5 the isolation system lengthens the natural time period by 16.75%, 18.66%, and 43.54%, respectively. Therefore, the flexibility of the cable-stayed bridge is increased in cases 3, 4, and 5. The mass participation ratio of the bridge in all isolated cases is incremented in the range of 82.68% to 92.99%. As a consequence, the first mode becomes the main contributing mode of the bridge after the implementation of isolators in all retrofitting cases; as shown in Table 3.6.

Table 3.6: Fundamental period of the bridge

	Non-isolated	Isolated-case 1	Isolated-case 2	Isolated-case 3	Isolated-case 4	Isolated-case 5
First time period (s)	2.09	2.11	2.09	2.44	2.48	3.00
Mass participation ratio (%)	2.16	92.99	89.60	82.68	89.93	92.62

The 12 modes versus the natural time periods of the bridge are illustrated in Figure 3.11. The implementation of base isolators led the bridge to have higher flexibility behavior than the original configuration. The dynamic behavior trend of the bridge is notably changed in the retrofitting cases, as the natural time periods are increased compared to the original bridge time period. For cases 1 and 2, the trend of the natural time periods is almost similar with consistent flexibility until the 7th mode of the bridge. Consequently, it can be seen that these two have similar seismic responses, in which the isolators are utilized along the tower base and deck-tower connection. Furthermore, the highest impact is seen in case 5 where the fundamental period is increased by 43.54%. These dynamic changes in the bridge are favorable, which leads to a reduction in the seismic forces transmitted from the substructure to the superstructure.

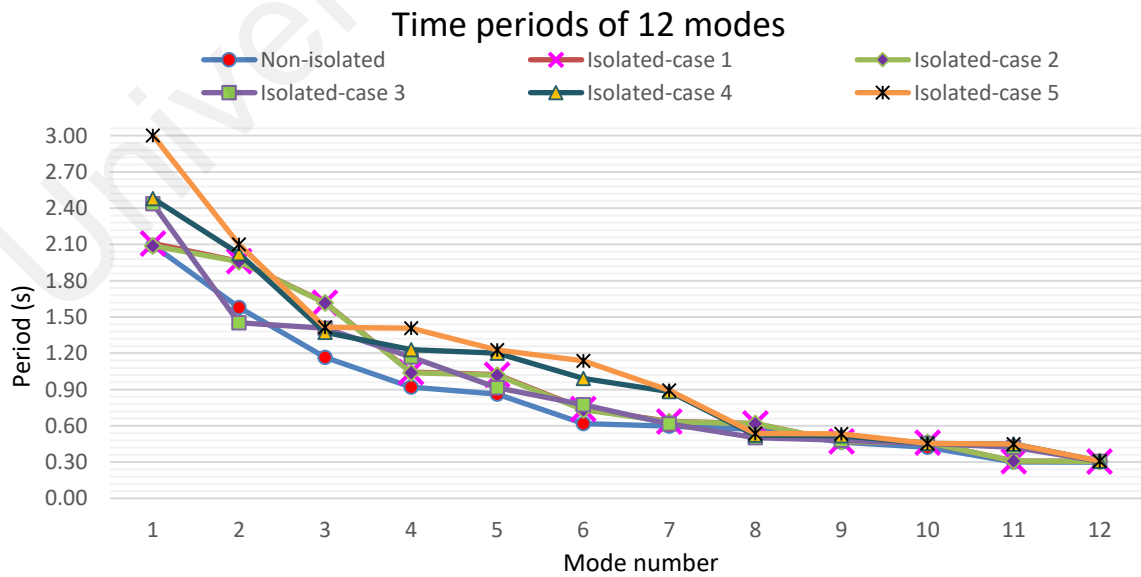


Figure 3.11: Implementation effect of base isolators on the natural time periods of the bridge

3.4.3 Results of time-history analysis:

3.4.3.1 Bridge displacement

Figure 3.12 shows the bridge displacements at the tower base, deck-tower connection, left and right ends for all the cases. When the isolation system is implemented at the base of the tower in cases 1 and 4, the displacements in the longitudinal and transverse directions are observed. The maximum tower displacements in these cases are 7 mm and 3 mm under the NH. FFD 82 earthquake in the longitudinal and transverse directions, respectively. The bridge displacement at the deck-tower connection is increased in the longitudinal direction in all seismic isolation cases except case 3. Under the NH. FFD 82 earthquake, the longitudinal displacement of this point is increased by 250%. For this point, the transverse displacement is recorded for cases 1, 2, 3, 4, and 5. The maximum transverse displacement of the deck-tower connection is 5 mm due to the NH. FFD 82 earthquake. In the longitudinal direction, the bridge ends in the initial configuration were free to move. After the implementation of the isolation systems, the bridge end displacements increases in all cases except for case 3. In case 3, the isolation system is installed at the bridge ends, while the deck-tower connection and tower base have the same configuration as the non-isolated. The displacement of the left and right ends of the bridge is increased up to 250% under NH. FFD 82 in cases 1, 2, 4, and 5. In the transverse direction for non-isolated case 1 and case 2, zero displacement is observed as the bridge is restrained in this direction. After the implementation of the isolators at the bridge ends, transverse displacements are detected in cases 3, 4, and 5. The maximum displacement increment for both the left and right ends of the bridge is 50% recorded under the NH. FFD 82 and S. Dicky 88 earthquakes, respectively. The utilization of the seismic isolation system at the tower base or deck-tower connection has increased the longitudinal displacement of the bridge. Hence, the rigid connection of the deck and tower and the tower support condition are the dominating factors in controlling the longitudinal seismic

displacement of the bridge. From Figure 3.12 it can be seen that the bridge displacements are relatively very small in both directions; up to a few millimeters even after the implementation of the isolation system. The bridge displacements are limited to the designed displacements obtained by the simplified analysis of the bridge in the design of the seismic isolation.

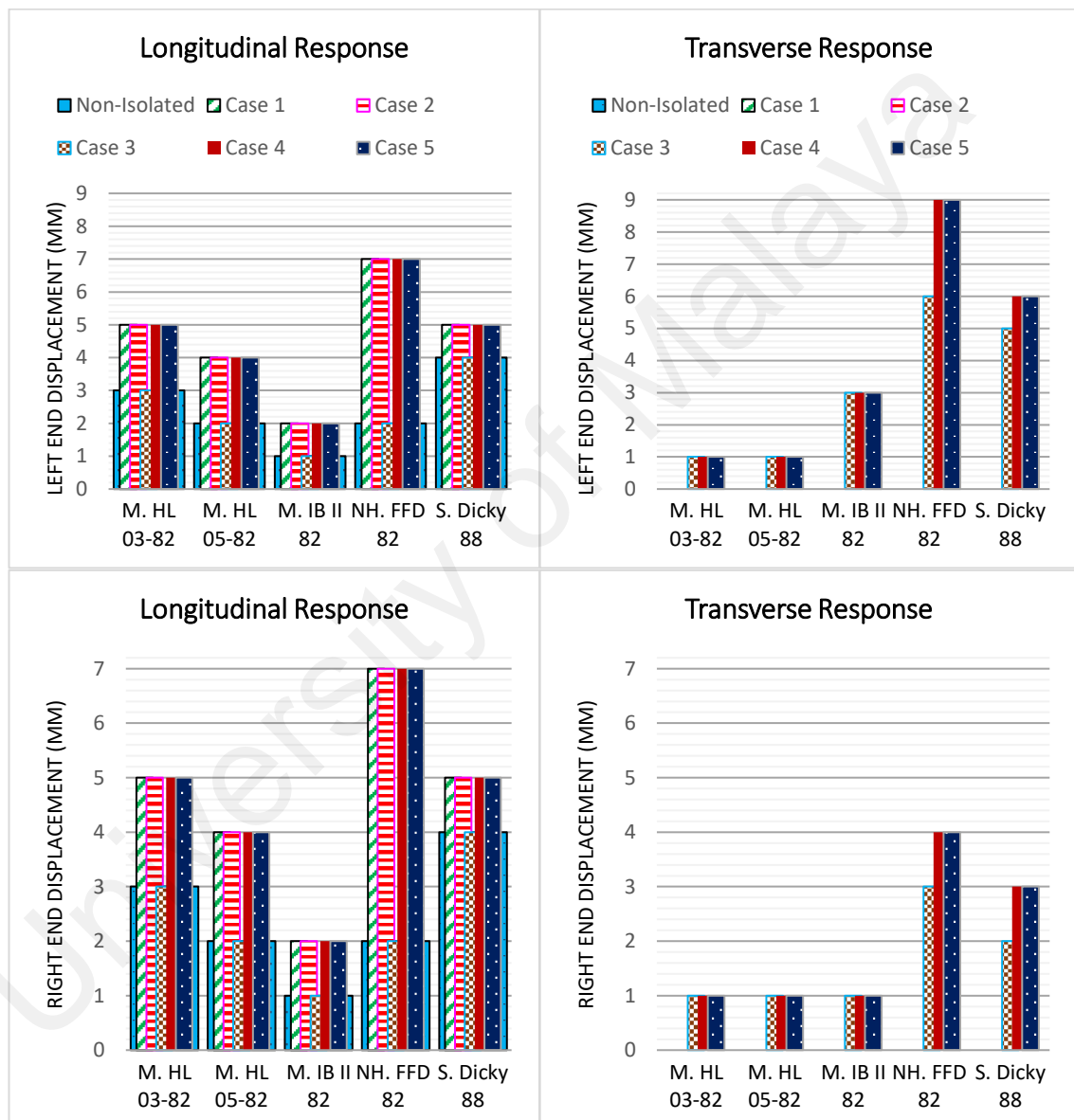


Figure 3.12: Maximum bridge displacement under earthquake excitations

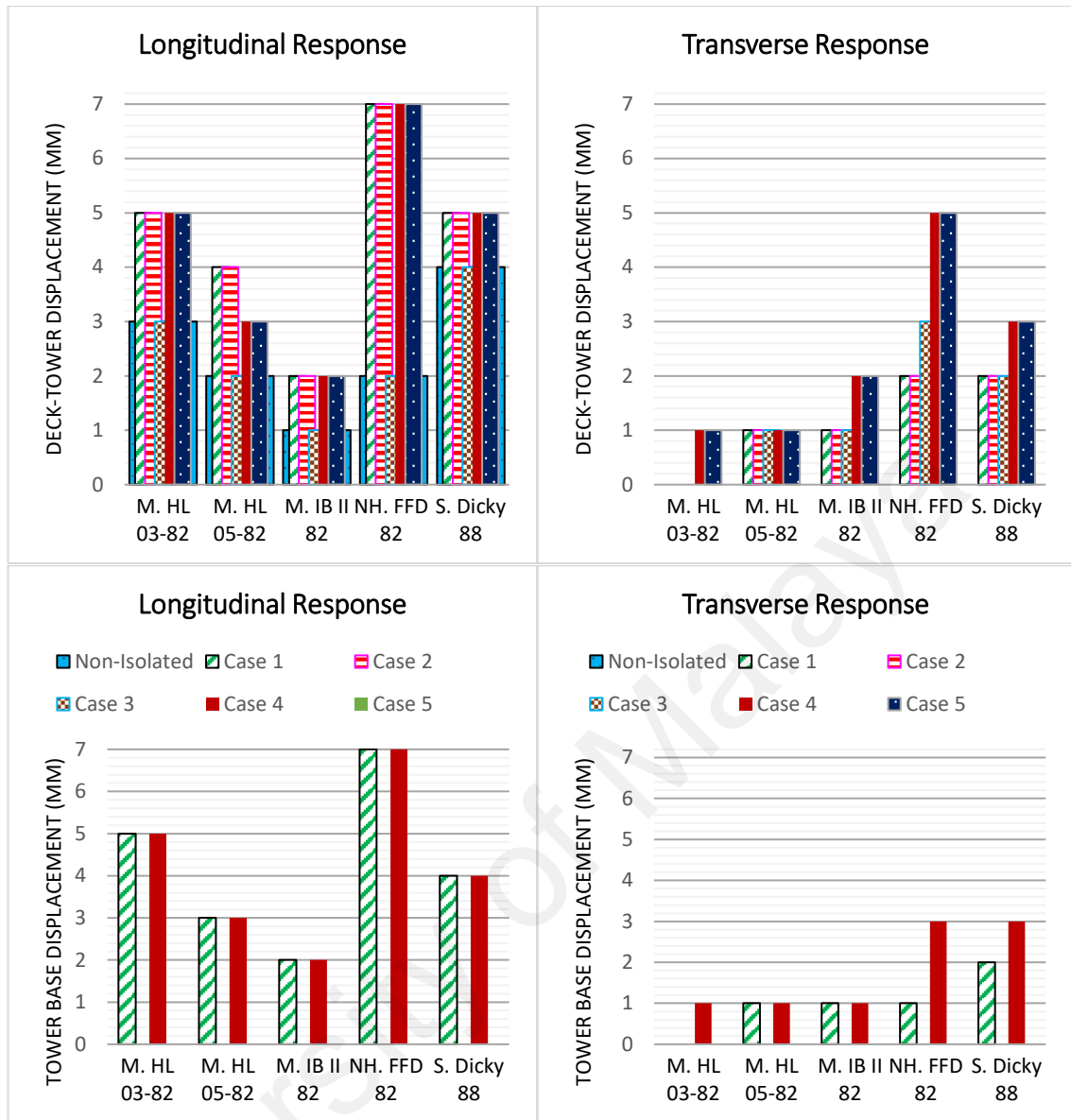


Figure 3.12, Continued

3.4.3.2 Base shear

One of the main aims of seismic isolation is to minimize the base shear of the bridge under seismic excitations. The implementation of isolation systems may not always reduce the base shear in both directions; as demonstrated in Figure 3.13. As the results of the numerical study show, the base shear in cases 1 and 2 is reduced in the range of 65.53% to 85.04% in the longitudinal direction. However, in the transverse direction, the base shear for cases 1 and 2 shows a significant increase. The maximum base shear increments observed in cases 1 and 2 are 15.10% and 14.42%, respectively, which occurred under the S. Dicky 88 earthquake. This is because, in the original configuration

of the bridge, the tower is allowed to freely rotate in a transverse direction while the implementation of the isolators at the tower base and tower-deck connection restrains the transverse rotation of the tower through the stiffness of the isolators. In case 3, in the longitudinal direction, the base shear for all the earthquakes increases significantly. The base shear increases up to 14.9%. However, for this case, the base shear reduces up to 90% in the transverse direction. The non-isolated bridge supports at the abutments are free to move in the longitudinal direction but are restrained in the transverse direction; while, in case 3, the isolators restrain the longitudinal movement of the bridge but allow limited transverse movement. This led to an increment of the base shear in the longitudinal direction and a reduction of the base shear in the transverse direction. The base shear in both directions is reduced significantly for cases 4 and 5. In case 4, the maximum base shear reductions in the longitudinal and transverse directions are 81.47% and 97.44%, respectively, which occurred under the S. Dicky 88 and M. HL 05-82 earthquakes. In case 5, the base shear reduction is 85.15% in the longitudinal direction under the S. Dicky 88 earthquake, while the base shear is reduced by 91.7% in the transverse direction under the M. HL 03-82 earthquake. The results prove that the implementation of base isolators at one or two supports is insufficient to reduce the base shear in both directions. A remarkable base shear reduction is observed in the cases in which the isolation systems are implemented at three locations of the bridge, simultaneously.

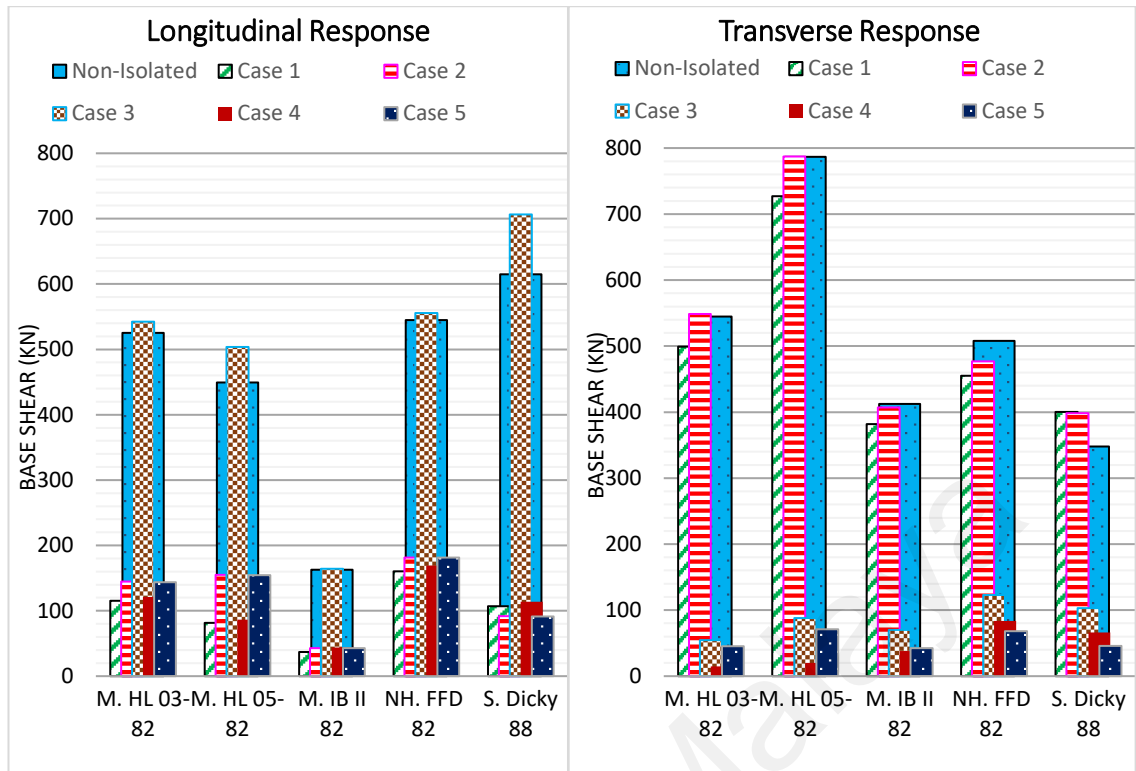


Figure 3.13: Maximum base shear response of towers subjected to earthquake excitations

3.4.3.3 Base moment

The maximum bending moments of the bridge in both directions are presented in Figure 3.14. In the longitudinal direction, the base moment for all the cases significantly decreases except in case 3. The maximum base moment reduction is 99.54% in case 4 under the M. HL 05-82 earthquake. In contrast, the base moment in case 3 increases by 3% and 3.61% under M. HL 05-82 and M. IB II 82 ground motions, respectively. This is due to the change in the configuration of the bridge abutments with the base isolators. The roller supports of the original configuration have zero longitudinal stiffness, while, the isolated cases have stiffness.

In the transverse direction, the isolation system in cases 1 and 2 cause a notable increment in the base moment of the bridge. The base moment increments are in the range of 2% to 42.6% since the original tower base is allowed to rotate freely in both directions but the implementation of the base isolators restricts the rotation due to their stiffness.

The maximum base moment increment occurs in case 2 where it reaches 3011.7 kN-m under the S. Dicky 88 earthquake. Nonetheless, in cases 3, 4, and 5 the base moment reduces remarkably. In case 3, the base moment reduces by up to 99.6%, as the original configuration of the bridge is restricted from moving in a transverse direction at the abutments and because the base isolators omit this restriction with movement up to the design displacement. In case 4 the base moment is reduced to 9.7, 13.5, 12.2, 50.4 and 42 kN-m under M. HL 03-82, M. HL 05-82, M. IB II 82, NH. FFD 82 and S. Dicky 88 ground motions, respectively. Similarly, the percentage reduction in case 5 is 99.55%, 99.71%, 98.06%, 94.5% and 96.35% when the bridge is subjected to M. HL 03-82, M. HL 05-82, M. IB II 82, NH. FFD 82 and S. Dicky 88 earthquakes, respectively.

For cases 4 and 5, the base moment enhancement is more significant due to the combination of the isolation system along the bridge supports and the deck-tower connection. However, the case 4 performance is still more remarkable than case 5.

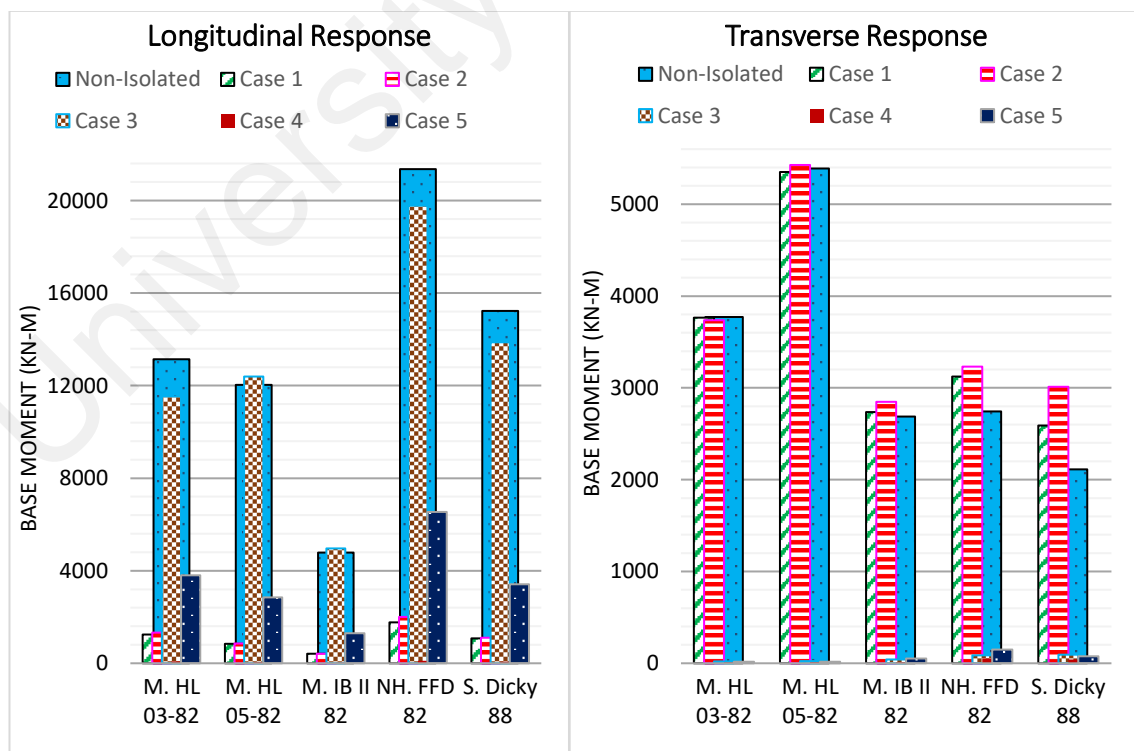


Figure 3.14: Maximum base moment response of bridge subjected to earthquake excitations

3.4.3.4 Cable response

Since in the transverse direction the bridge is symmetric, the cables on one side of the bridge are chosen for the investigation. The numbering of the cables from the left to the right abutments is 1, 2, 3, and 4, respectively. The cable force should remain within the nominal range and never approach zero. The cables' forces for each case of the bridge under the selected earthquake are illustrated in Figure 3.15. It can be seen from the figure that the cable forces vary during vibration of the bridge; these variations are within the range of $0.2T$ to $0.7T$ specified by Dyke et al. (2003). The implementation of seismic isolators causes a notable reduction in the variations in the force in all the cables for all cases except case 3. The cable force changes are varied up to 96.74% and 95.71% in the longitudinal and transverse directions, respectively. In the longitudinal direction for case 3, the cable forces increase up to 8.5%, 5.6%, 33.1% and 8.9% for cables 1, 2, 3, and 4, respectively. However, in the transverse direction, the cable forces in case 3 are considerably reduced. Furthermore, the tension forces in cables 3 and 4 are larger compared to cables 1 and 2 under earthquake excitations, because they are connected to the box girder at closer distances to the tower.

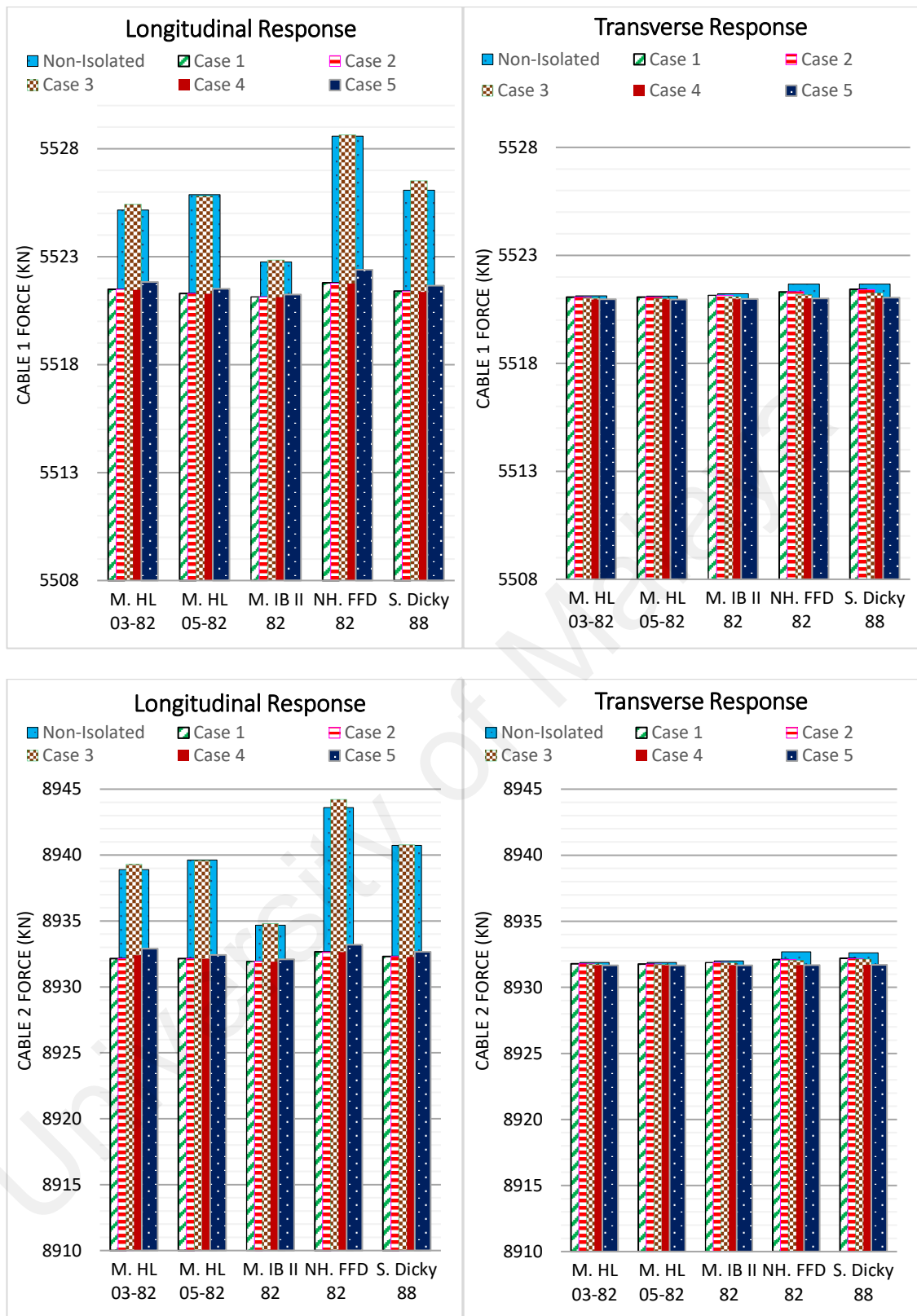


Figure 3.15: Maximum cable tension forces of the bridge under earthquake excitations

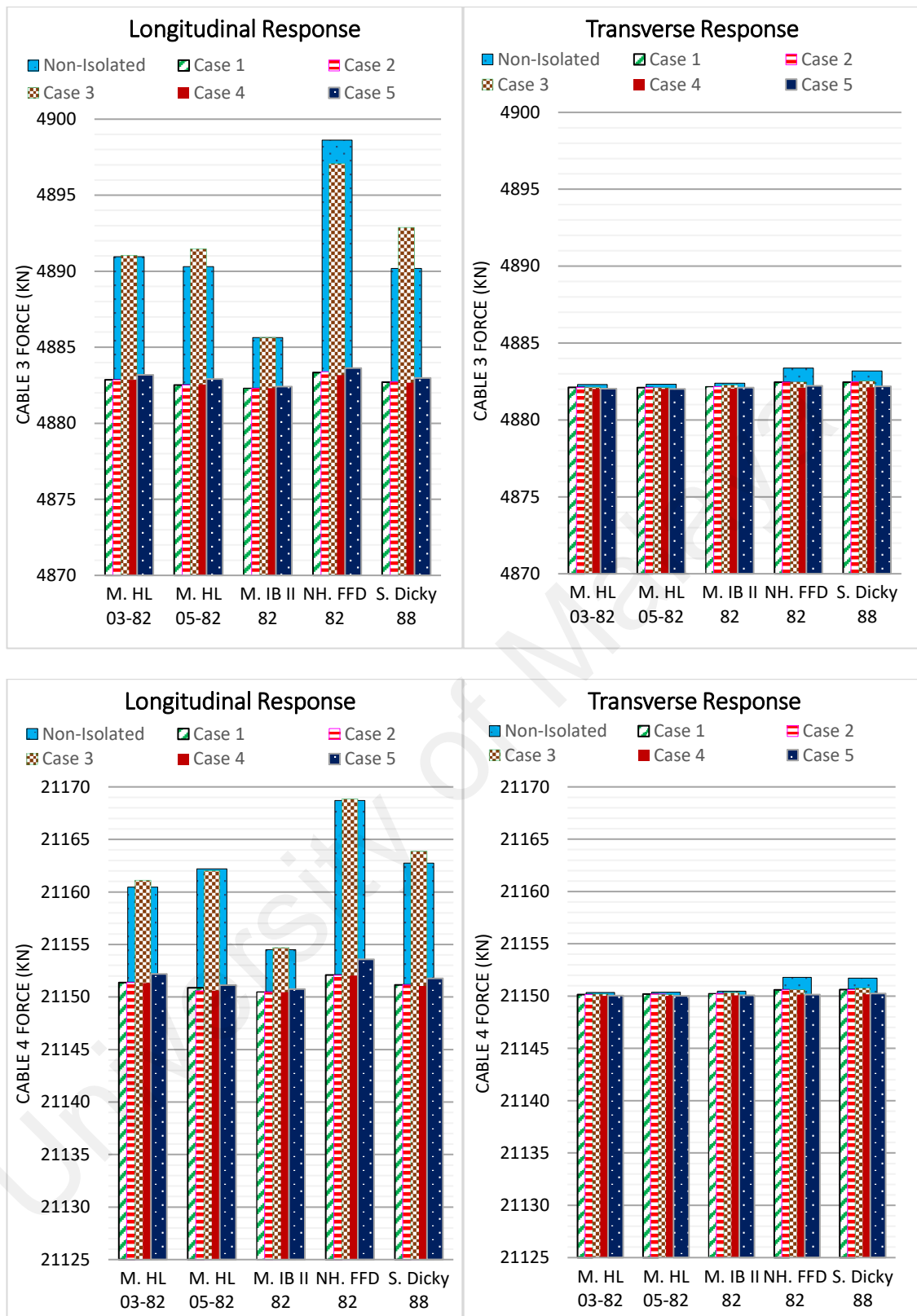


Figure 3.15, Continued

3.4.3.5 Hysteresis response of bridge

In this section, the hysteresis behavior of the bridge for different cases is investigated. The S. Dicky 88 earthquake is the actual event that caused the failures in the bridge; therefore, to avoid too many hysteresis graphs, only the hysteric curves of the bridge under the S. Dicky 88 earthquake are presented in both directions. Figure 3.16 represents the hysteresis curves of the base shear of the tower versus the displacement of the bridge at the deck-tower connection. As the figure shows, the implementation of the isolation system causes a significant enhancement in the bridge response in the longitudinal direction. However, the improvement in the response of the bridge is not the same in all cases. In the transverse direction, the bridge response increases for cases 1 and 2, which have almost the same hysteric curves, while in other cases the bridge response improves through implementation of the isolation system. The original configuration of the bridge experiences a large number of yielding cycles, while the isolated bridge in cases 4 and 5 shows no inelastic cycles in either direction.

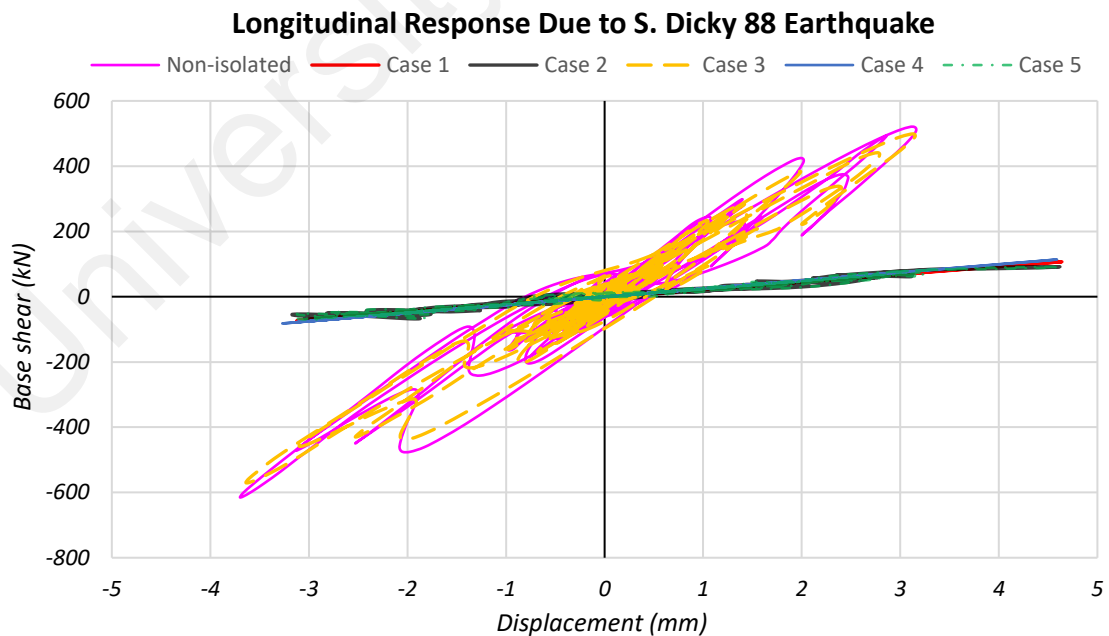
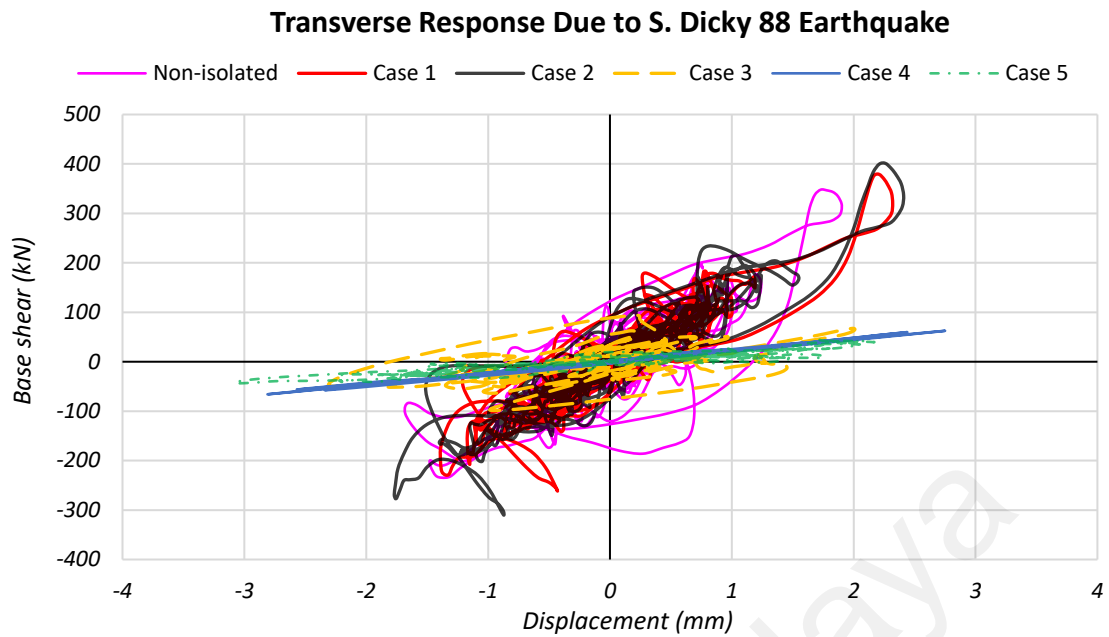


Figure 3.16: Force-Displacement hysteresis curves of the bridge subjected to S. Dicky 88 earthquake



3.4.4 Overall seismic response

The overall seismic responses of the cable-stayed bridge are summarized and presented in Table 3.7. However, the displacements of the bridge ends are not included since the displacement values are very small and readable in Figure 3.12. As the table indicates, cases 4 and 5 have similar seismic responses. These two cases are the most favorable retrofitting cases, in which the overall seismic performance of the bridge is enhanced substantially in both directions under all the earthquake excitations. Subsequently, in cases 1 and 2, the longitudinal performance of the bridge is improved while in the transverse direction no significant improvement is observed. Finally, the seismic performance of the bridge is only improved in the transverse direction for case 3.

Table 3.7: Summary of seismic responses of the bridge for different retrofitting cases

Earthquake	Bridge Case	Base shear (kN)		Base moment (kN- m)		Cable 1 force (kN)		Cable 2 force (kN)		Cable 3 force (kN)		Cable 4 force (kN)	
		X	Y	X	Y	X	Y	X	Y	X	Y	X	Y
M. HL 03-82	Non-isolated	525.1	544.7	13147.1	3772.5	5525.17	5521.13	8938.90	8931.89	4890.96	4882.30	21160.46	21150.34
	Case 1	115.3	499.4	1239.7	3766.1	5521.49	5521.06	8932.16	8932.78	4882.86	4882.11	21151.36	21150.14
	Case 2	144.6	548.6	1325.3	3736.8	5521.49	5521.06	9832.15	8931.78	4882.86	4882.11	21151.37	21150.14
	Case 3	542.3	54.5	11534.3	19.1	5525.43	5521.03	8939.30	8931.77	4891.04	4882.14	21161.11	21150.19
	Case 4	121.2	14.8	77.5	9.7	5521.47	5520.96	8932.41	8931.66	4882.86	4882.02	21151.32	21150.03
	Case 5	143.9	45.2	3797.1	16.9	5521.83	5520.97	8932.90	8931.66	4883.19	4882.03	21152.20	21150.04
M. HL 05-82	Non-isolated	449.2	786.55	12033.1	5388.8	5525.88	5521.12	8939.63	8931.89	4890.30	4882.40	21162.19	21150.38
	Case 1	81.3	727.0	840.2	5351.2	5521.29	5521.06	8932.15	8931.77	4882.52	4882.16	21150.87	21150.21
	Case 2	154.8	787.3	861.7	5427.9	5521.29	5521.06	8932.15	8931.77	4882.52	4882.17	21150.57	21150.21
	Case 3	503.5	88.2	12391.2	23.1	5521.81	5521.01	8939.59	8931.75	4891.48	4882.27	21162.04	21150.15
	Case 4	86.4	20.1	54.9	13.5	5521.28	5520.96	8932.13	8931.66	4882.56	4882.03	21150.61	21150.02
	Case 5	154.3	71.1	2843.5	15.5	5521.51	5520.96	8932.43	8931.66	4882.91	4882.09	21151.11	21150.02
M. IB II 82	Non-isolated	162.9	412.5	4786.6	2688.1	5522.76	5521.23	8934.68	8931.99	4885.63	4882.40	21154.51	21150.48
	Case 1	37.0	382.0	418.5	2735.1	5521.14	5521.15	8931.93	8931.87	4882.30	4882.16	21150.48	21150.24
	Case 2	43.0	407.0	412.2	2848.7	5521.14	5521.15	8931.93	8931.87	4882.30	4882.17	21150.48	21150.24
	Case 3	164.3	69.9	4959.5	40.5	5522.84	5521.09	8934.81	8931.86	4885.65	4882.27	21154.69	21150.34
	Case 4	44.0	37.8	27.9	12.2	5521.13	5520.97	8934.92	8931.67	4882.30	4882.03	21150.46	21150.07
	Case 5	42.7	42.3	1299.3	52.2	5521.25	5520.98	8932.09	8931.67	4882.42	4882.09	21150.76	21150.08
NH. FFD 82	Non-isolated	544.7	508.1	21361.1	2744.1	5528.58	5521.68	8943.61	8932.69	4898.62	4883.37	21168.72	21151.78
	Case 1	160.3	454.9	1761.9	3124.5	5521.79	5521.31	8932.67	8932.09	4883.34	4883.45	21152.10	21151.59
	Case 2	181.5	476.9	1996.9	3231.5	5521.77	5521.32	8932.65	8932.10	4883.40	4882.46	21152.07	21150.60
	Case 3	555.8	123.0	19786.9	87.0	5528.64	5521.19	8944.21	8932.03	4897.08	4882.48	21168.85	21150.62
	Case 4	169.4	83.8	107.9	50.4	5521.76	5521.00	8932.65	8931.68	4883.17	4882.08	21185.03	21150.15
	Case 5	181.4	68.3	6543.3	151.0	5522.40	5521.01	8933.21	8931.68	4883.63	4882.22	21153.59	21150.14
S. Dicky 88	Non-isolated	615.0	347.9	15231.9	2112.4	5526.08	5521.67	8940.74	8932.62	4890.18	4883.19	21162.74	21150.73
	Case 1	107.0	400.5	1075.1	2591.3	5521.40	5521.43	8932.31	8932.19	4882.71	4882.47	21151.14	21150.62
	Case 2	92.0	398.1	1108.2	3011.7	5521.41	5521.42	8932.31	8932.18	4882.72	4882.47	21151.14	21150.61
	Case 3	706.6	103.1	13867.9	92.9	5526.52	5521.26	8940.78	8932.13	4892.88	4882.55	21163.88	21150.78
	Case 4	113.9	66.0	72.6	42.0	5521.37	5521.01	8932.26	8931.70	4882.68	4882.12	21151.06	21150.16
	Case 5	91.3	46.0	3418.1	77.1	5521.66	5521.05	8932.67	8931.69	4882.98	4882.19	21151.77	21150.24

3.5 Conclusions

From the comparative analyses of each seismic retrofitting case the following conclusions are drawn:

- The base isolation retrofitting prevented the damage and failure in the tower and prevented the occurrence of damage concentration in the cable-stayed bridge. It also reduced the transmission of seismic forces from the substructure to the superstructure.
- The base isolation system at the tower base or the deck-tower connection increased the flexibility of the bridge in the longitudinal direction while the utilization of the base isolators at the end supports increased the flexibility of the bridge in the transverse direction, and, hence, minimized the longitudinal and transverse induced seismic forces, respectively.
- In both directions, the cable forces variation substantially reduced in almost all the cases except case 3. The variation of the cable forces had a significant influence on the deck stability and the reduction of the variations in the forces in the cables, which is helpful in reducing oscillation of the deck.
- The longitudinal seismic performance of the cable-stayed bridge improved in cases 1, 2, 4, and 5. In case 3, the seismic performance of the bridge only improved in the transverse direction. The base isolators at the abutments limited the longitudinal movement of the bridge, which led to an incrementation in the base shear and the base moment. Further, only cases 4 and 5 showed significant seismic improvement in the transverse direction.
- Partial seismic isolation of the bridge only led to an improvement in the seismic response of the cable-stayed bridge in one direction. In addition, the changes to the supports of the cable-stayed bridge significantly influenced its seismic behavior.

- To maximize the benefits of the isolation system for the overall enhancement of the seismic performance of the bridge in the longitudinal and transverse directions, it is necessary to utilize the isolation system along the supports and deck-tower connection of the cable-stayed bridge.

University of Malaya

CHAPTER 4: SEISMIC RESPONSE CHARACTERISTICS OF THE FULLY ISOLATED CABLE-STAYED BRIDGE UNDER MODERATE TO MAJOR EARTHQUAKES

4.1 Introduction

From the analysis of each seismic retrofitting cases of the bridge in the previous chapter, it is observed that the seismic performance of the bridge was significantly enhanced in both directions when the isolators were implemented at abutments and tower base or deck-tower connection (cases 4 and 5). However, the utilization of the base isolator at the tower's base is impractical for this bridge since the bridge had been constructed few decays ago. In addition, the result pushover analysis of the bridge indicated that the bridge failure occurred at the tower near to deck, which means the seismic demand on the bridge tower should be minimized at the deck-tower connection. Consequently, in this chapter, the LRBs are implemented at bridge ends and deck-tower connection. The seismic response characteristics of the non-isolated and isolated bridge under moderate to major ground motions are thoroughly studied. The numerical model of the fully isolated bridge is shown in Figure 4.1. The seismic isolators are designed based on the methodology explained in the previous chapter (Section 3.3.6.1). However, the isolators are redesigned for the selected earthquakes in this chapter and the new properties values are assigned in the fully isolated bridge model. A comparative study on the non-isolated and isolated bridge is performed by using the nonlinear time-history analysis.

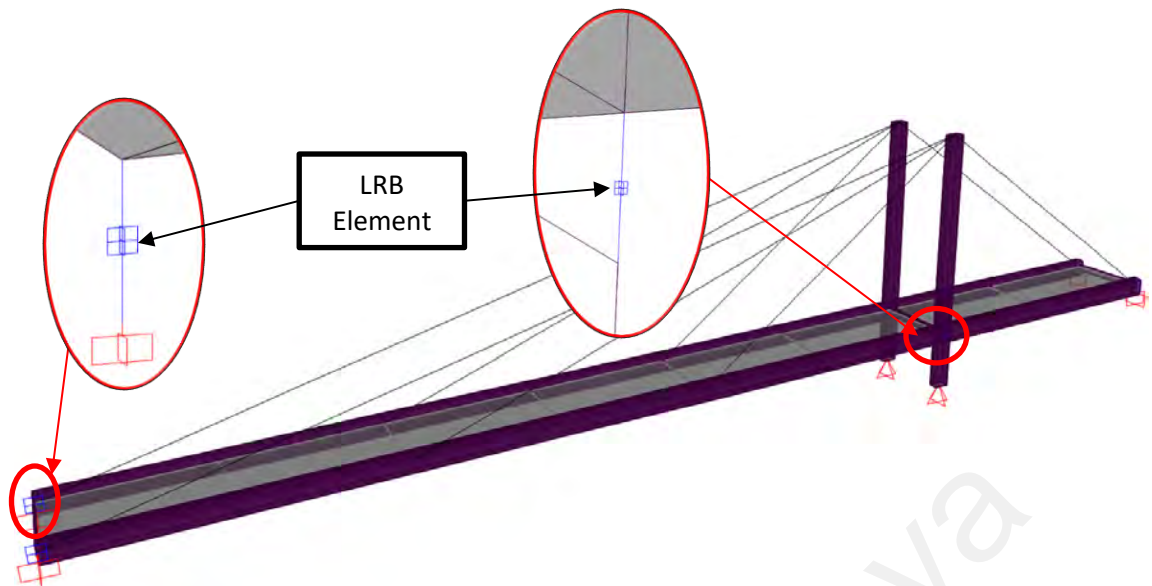


Figure 4.1: Finite element model of the fully isolated cable-stayed bridge

4.2 Ground motion selection

The characteristics of earthquake ground motion are highly affected on the seismic responses of the bridge. Therefore, in this chapter, the moderate to major earthquakes are selected for analysis, in order to evaluate the excessive seismic performance of the fully isolated bridge. Table 4.1 shows the ground motions characteristics used in the analysis. The acceleration and displacement response spectra for 5% structural damping of the four ground motions are represented in Figure 4.2. The maximum ordinates of the spectral accelerations for Sierra Madre, South Napa, Cook Strait and Cape Mendocino are 1.513, 0.618, 2.257 and 1.759g occurring at 0.18, 0.08, 0.13 and 0.07 sec, respectively along the longitudinal direction. While, in the transverse direction, the maximum ordinates of the spectral accelerations for Sierra Madre, South Napa, Cook Strait and Cape Mendocino are 0.444, 0.426, 1.812 and 1.367g occurring at 0.23, 0.08, 0.09 and 0.17 sec, respectively. The ground motions are imposed uniformly at all bridge supports.

Table 4.1: Ground motion records characteristics

Earthquake	Station	Magnitude	Distance (Km)	longitudinal direction		Transverse direction	
				PGA (g)	PGV (cm/s)	PGA (g)	PGV (cm/s)
Sierra Madre-1991	Altadena, Easton Canyon Park	6.7	12.5	0.447	27.2	0.179	7.8
South Napa-2014	Huichica Creek	6.0	12	0.403	57.66	0.293	22.5
Cook Strait-2013	Ward Fire Station	5.9	15	1.035	33.75	0.807	21.09
Cape Mendocino-1992	Petrolia	7.0	15.5	1.497	126.1	1.039	40.5

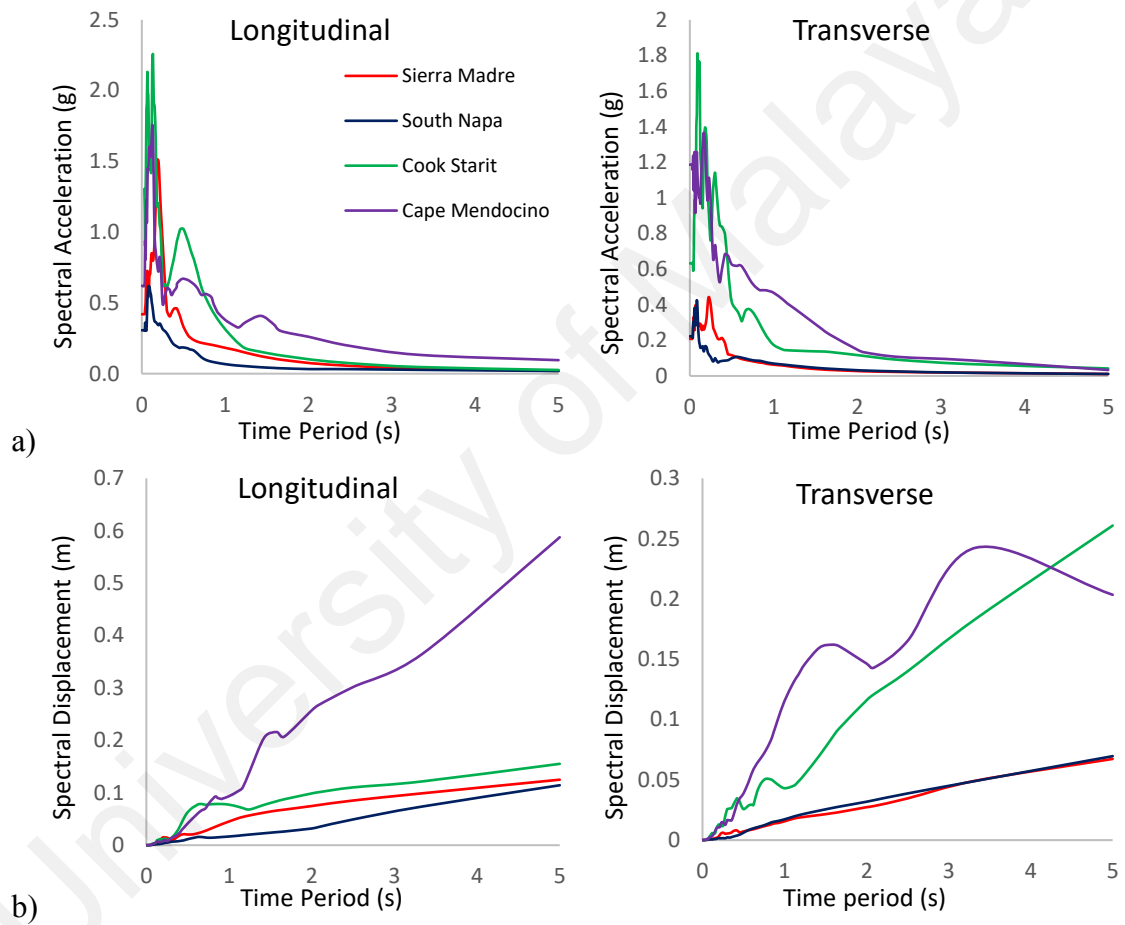


Figure 4.2: a) Acceleration and b) displacement spectra of ground motions in longitudinal and transverse directions applied to the bridge considering 5% damping

4.3 Results and discussion

4.3.1 Deck displacement and acceleration

The deck displacement is measured at deck-tower intersection. As Figure 4.3 presents, the maximum deck displacement of the isolated bridge is larger than the non-isolated

bridge under all the ground motions. The maximum longitudinal displacement of the deck is increased from 5.8 cm to 12.4 cm after implementation of the base isolation system, hence an increment of 113.8% is observed under Cape Mendocino earthquake. Similarly, in the transverse direction, the maximum deck displacement is enlarged from 5.9 cm to 10.2 cm under Cape Mendocino earthquake, which indicates 178.3% increase of deck displacement in this direction. The deck displacements are increased because the isolators changed the boundary conditions of the bridge, at which it removed the transverse restraints of the bridge at the abutments and changed the deck-tower configuration from a rigid connection to a moveable connection. Therefore, despite the deck displacement incremented in the isolated bridge, these displacements were limited to the design displacements obtained by the simplified analysis of the bridge.

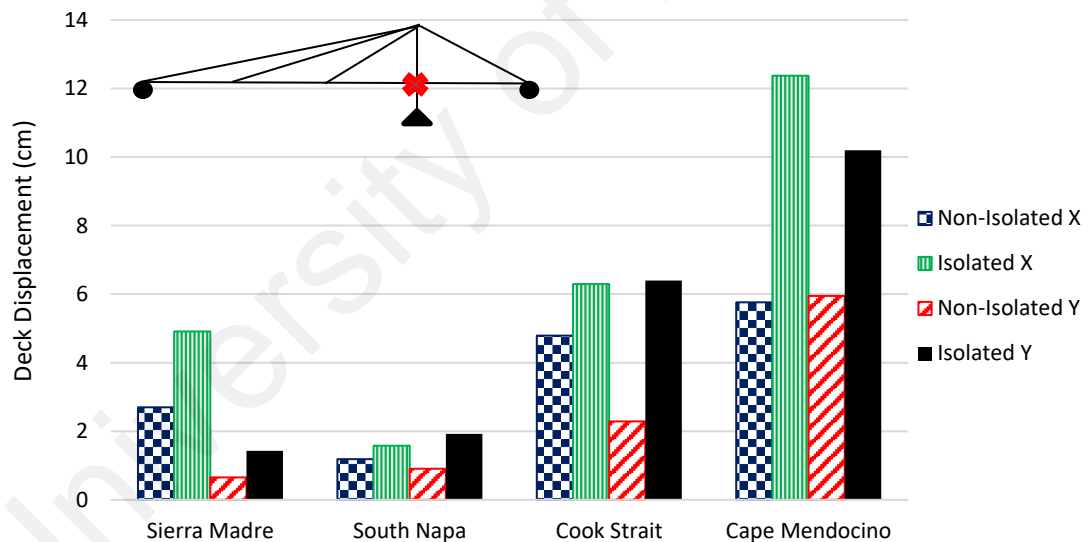


Figure 4.3: Peak response of deck displacement during earthquake excitations in longitudinal and transverse directions

The acceleration of the deck is also recorded at deck-tower intersection. As Table 4.2 indicates, the non-isolated bridge is experienced larger deck accelerations all ground motions as compared to the bridge with LRBs in both directions. The maximum deck acceleration reductions are 62.26% and 35.38% in longitudinal and transverse directions,

respectively, which, was subjected to Cook Strait ground motion. Figure 4.4 shows the deck acceleration time-history responses of the non-isolated and isolated bridge under Cape Mendocino ground motion. Further, the peak of deck acceleration is dropped from 17.13 m/sec^2 to -7.75 m/sec^2 in the longitudinal direction, while in the transverse direction the peak acceleration is reduced from -18.23 m/sec^2 to 14.55 m/sec^2 . This figure clearly shows how the isolation system has reduced the peak of deck acceleration and also reduced oscillation of the deck acceleration in both directions, substantially.

Table 4.2: Peak absolute acceleration response of the bridge deck under different ground accelerations

	Sierra Madre		South Napa		Cook Strait		Cape Mendocino	
	Non-Isolated	Isolated	Non-Isolated	Isolated	Non-Isolated	Isolated	Non-Isolated	Isolated
Acceleration in X direction (m/sec^2)	7.90	3.38	4.03	2.72	21.15	7.98	17.13	7.75
Acceleration in Y direction (m/sec^2)	2.55	2.01	3.12	2.58	8.28	5.35	18.23	14.55

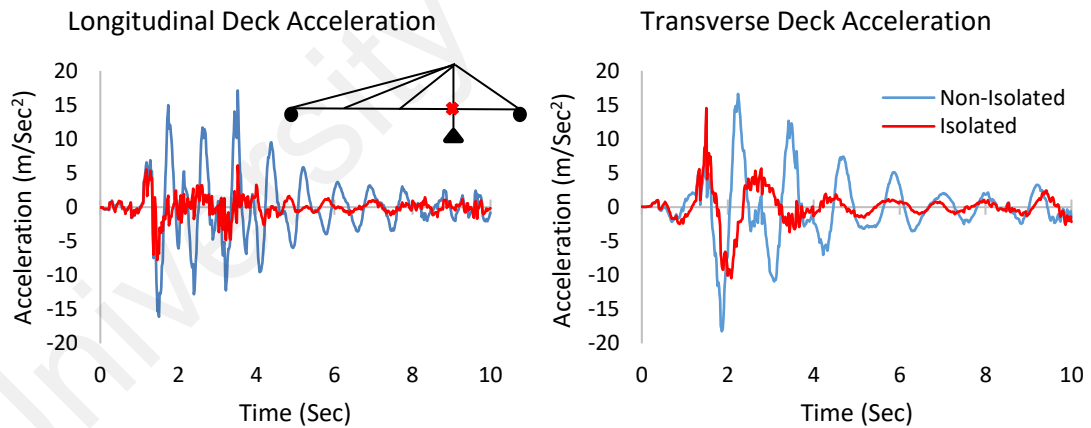


Figure 4.4: Acceleration time-history of the deck under Cape Mendocino earthquake excitation

4.3.2 Base shear

As Figure 4.5 depicts, the base isolators reduce the base shear produced by different ground motions excitations. The maximum value of the base shear in the longitudinal direction is 9823.2 kN due to Cape Mendocino earthquake and it is dropped to 8612.7 kN when the isolation system was utilized in the bridge. Following this, it can be seen that

the maximum base shear reduction in the longitudinal direction is 49.33% under Cook Strait earthquake, while the minimum reduction of base shear in this direction is 14.05%, which occurred under Cape Mendocino earthquake. Subsequently, the maximum peak response of the base shear of the non-isolated bridge in the transverse direction is 9208.2 kN which is reduced to 3894 kN in the isolated bridge. Thereupon, in the transverse direction, the maximum base shear reduction is 57.71% under Cape Mendocino earthquake and the minimum observed reduction is 27.39% under South Napa earthquake. It is observed that the base shear mitigation in the transverse direction is more significant as compared to the longitudinal direction. This is due to the fact that, the movement of the non-isolated bridge is restrained in the transverse direction, whilst, in the isolated bridge the transverse movement is permitted up to the design displacement. Thus, a satisfactory base shear mitigation can be expected for the cable-stayed bridges equipped with base isolation system in seismic regions.

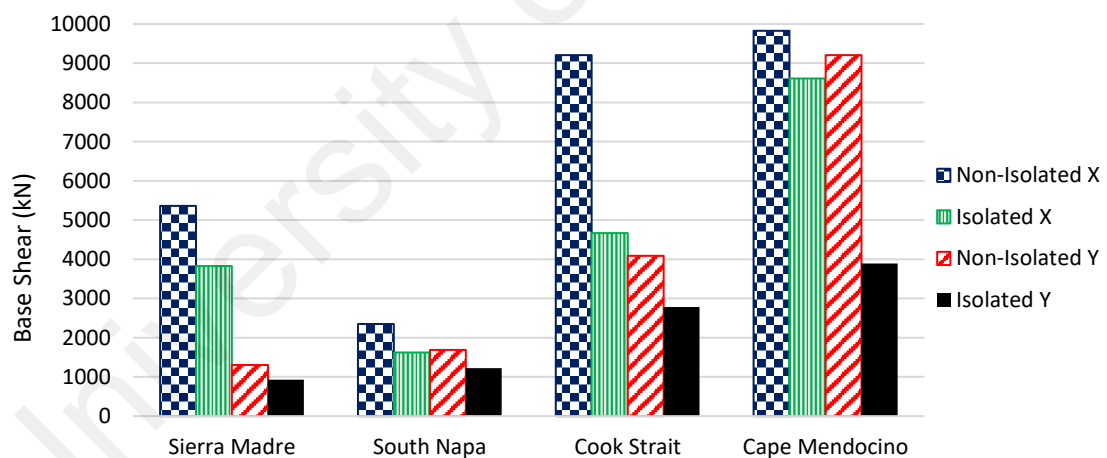


Figure 4.5: Base shear peak response of the bridge during earthquake excitations in longitudinal and transverse directions

4.3.3 Base Moment

The value of the base moment in the non-isolated bridge is quite large, especially in the longitudinal direction as shown in Figure 4.6. The maximum and minimum base moment reductions are 80.53% and 52.48% under Cook Strait and Cape Mendocino in the longitudinal direction, respectively. Further, the maximum moment decrement in the

transverse direction is 84% under Cape Mendocino earthquake, whereas, the minimum reduction percentage is 42.06% under Sierra Madre earthquake.

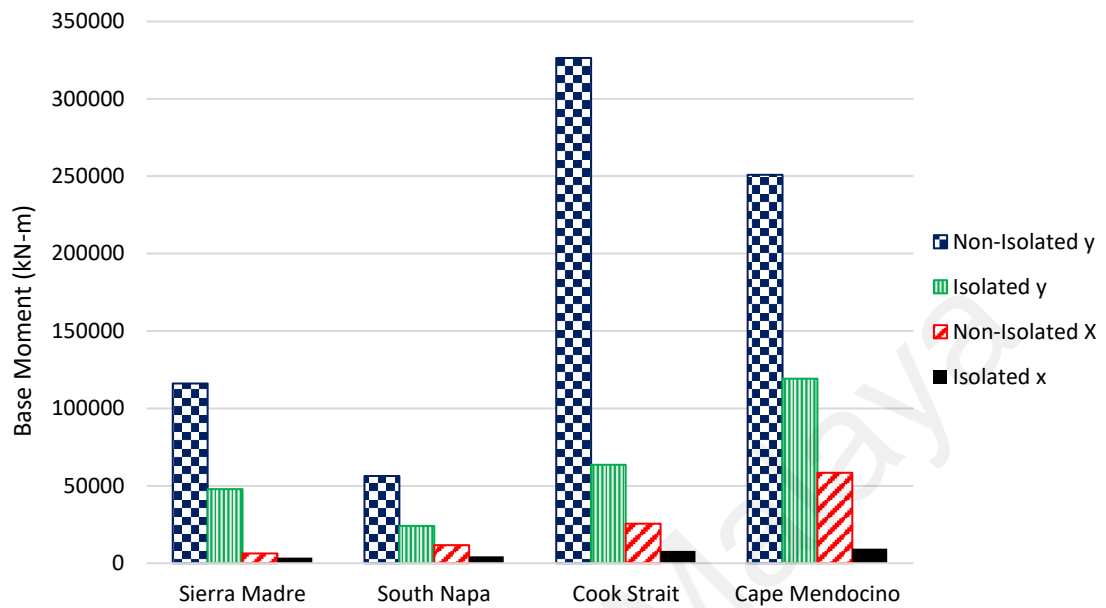


Figure 4.6: Maximum base moment response of the bridge under earthquake excitations in longitudinal and transverse directions

4.3.4 Tower response

In cable-stayed bridges, the entire cable system relies on the tower, therefore, the failure or instability of the tower may lead to failure of the entire bridge. Thus, it is necessary to study the seismic behavior of the tower under seismic loading (Li et al., 2009; Nazmy & Abdel-Ghaffar, 1992; Okamoto & Nakamura, 2011; Soyluk & Dumanoglu, 2000). In this study, owing to the symmetry of bridge in the transverse direction, only one side of the tower is selected for comparison of the results.

4.3.4.1 Tower shear force

Figure 4.7 illustrates the shear force of the tower as a function of its height. According to this figure, the utilization effect of the LRBs on the reduction of tower shear force is prominent. The shear force reduction of the tower in the superstructure are up to 85.5% and 54.9% in longitudinal and transverse directions, respectively. Subsequently, in

longitudinal and transverse directions, up to 62.9% and 37.8% decrement of shear force of the tower in substructure are observed. The shear force in the tower above the deck level is reduced significantly; as the isolators dissipated seismic force transmits from the substructure to the superstructure. This reduction ultimately increases the stability of the superstructure in both directions, even under the strongest earthquakes. Consequently, the shear force for the tower below the deck level also decreases as some of the forces are dissipated through the characteristics of LRB and hence, the possibility of damage to substructure is reduced.

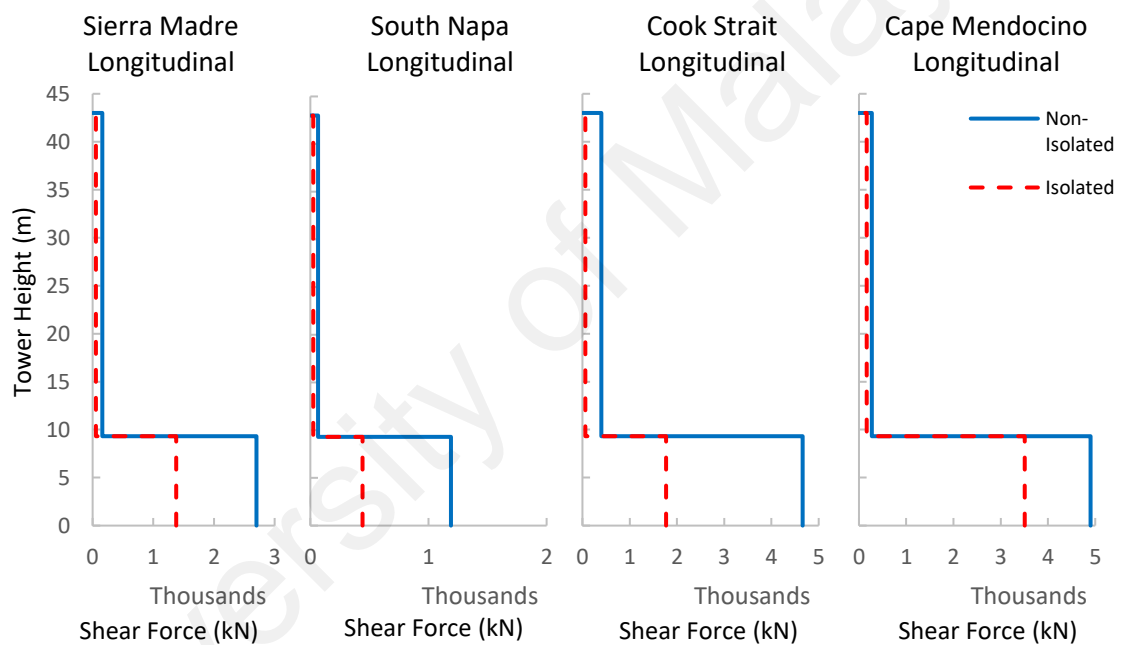


Figure 4.7: Maximum shear force response of the tower along its height under different ground motions

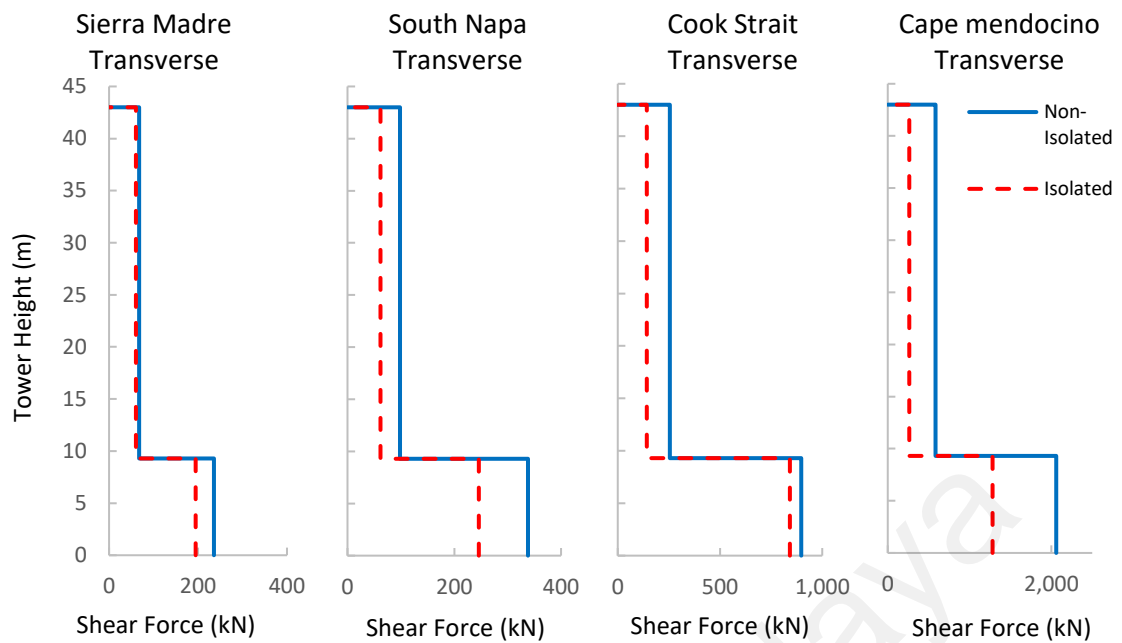


Figure 4.7, Continued

4.3.4.2 Tower bending moment

Figure 4.8 shows the bending moment distribution along the tower height. The bending moment of the tower in substructure section is reached to its maximum value at deck level in both directions. The tower bending moment of isolated bridges followed the same trend of the non-isolated bridge. As shown in the figure, after the implementation of the base isolators, this trend is significantly changed and caused a significant decrement in bending moment of the tower in both superstructure and substructure. The maximum reduction of bending moment in the tower is 85.4% observed in longitudinal direction whilst, the minimum bending moment decrement is 9.3% which lied in the substructure. Thereupon, utilization of base isolation system in the bridge results in a remarkable minimization of tower bending moment of and base moment responses of the bridge in both directions.

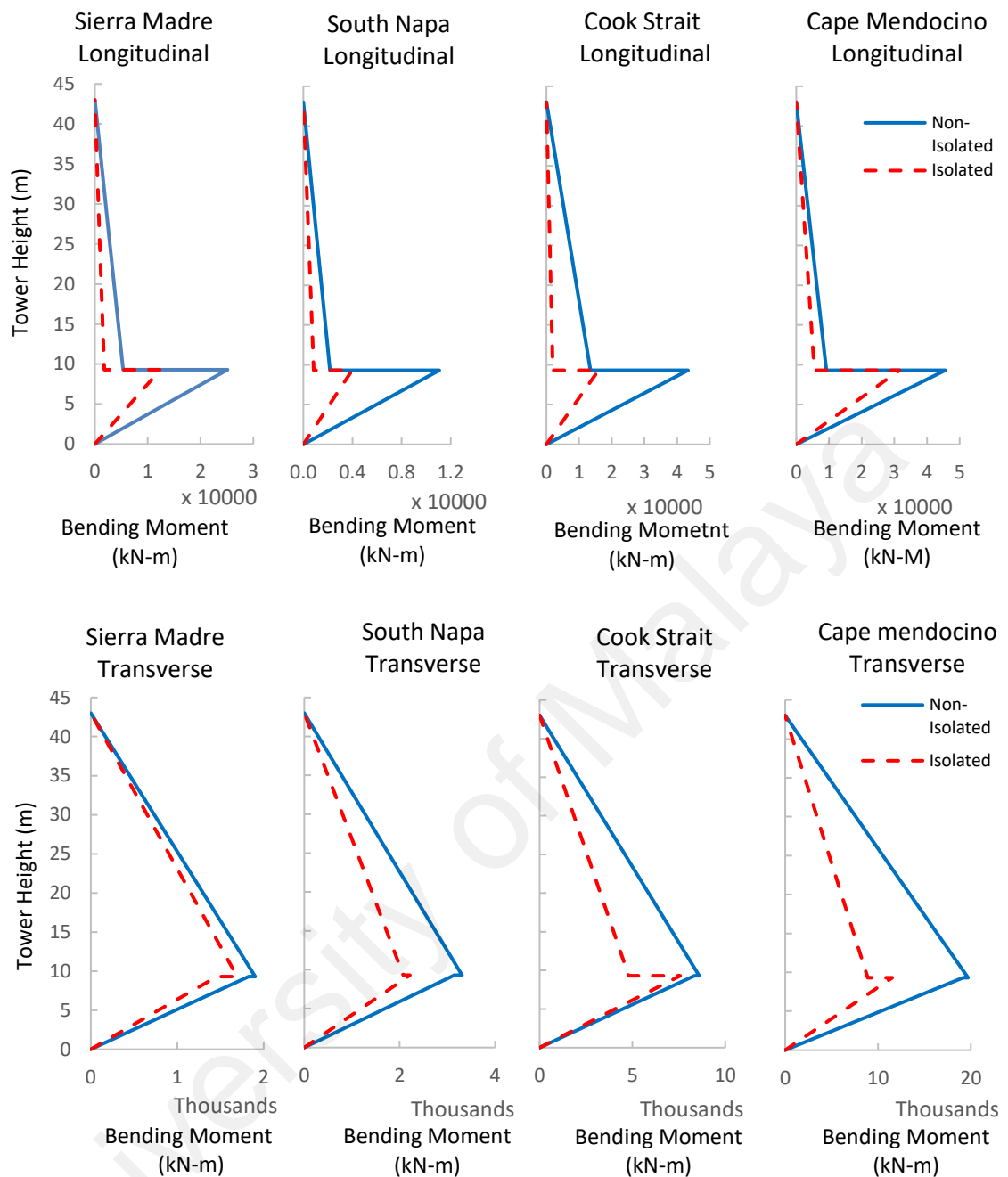


Figure 4.8: Bending moment distribution along the tower height in both directions under different ground motions

4.3.4.3 Tower axial force

The relative tower axial force under different ground motions is shown in Figure 4.9. As the figure indicates, the axial force of the tower in substructure is noteworthy larger than the tower axial force in superstructure section. In the longitudinal direction, the isolation systems reduced the axial forces of tower up to 82.2% in both substructure and

superstructure sections. Meanwhile, in the transverse direction, the isolation systems slightly reduced the axial force of the tower above the deck level, whereas, the axial force in tower below the deck is increased from 48.73% to 72.22%. The reason is that the base isolators are separated the superstructure from substructure at the deck-tower connection (from rigid configuration to movable configuration) and removed the transverse restraints of the bridge at abutments. Therefore, a flexible plane is produced at the deck level, which led to an unfavorable torsional moment when earthquakes are applied in the transverse direction. These torsional moments are transmitted from box girders to the substructure and caused a notable increment in tower axial force in the tower section that lied in the substructure.

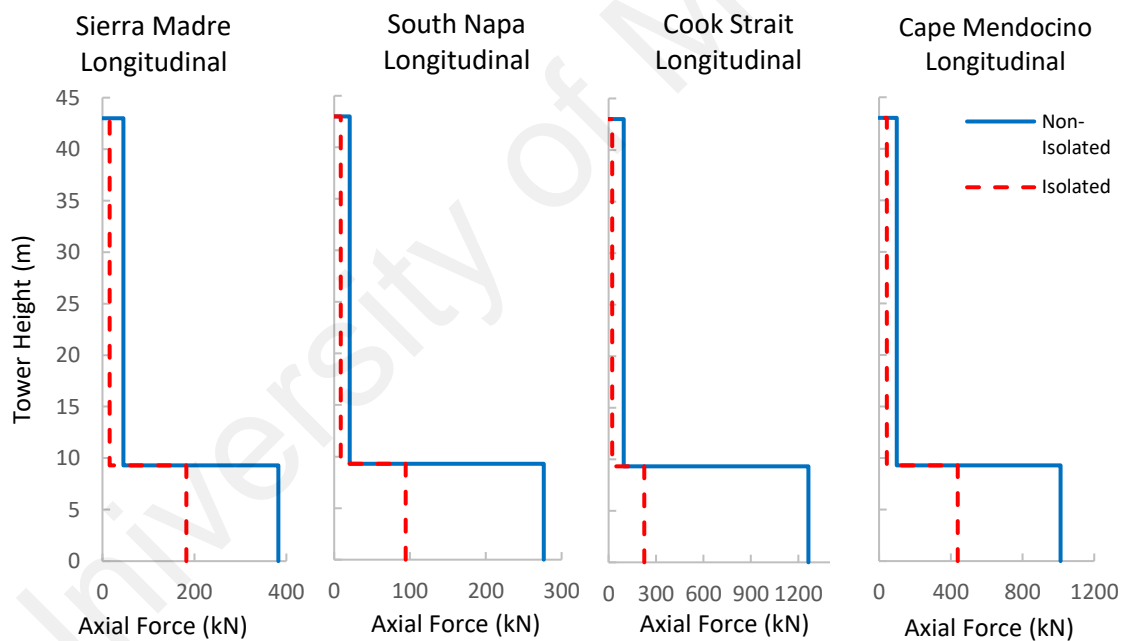


Figure 4.9: Maximum relative axial force of the tower along its height under different ground motions in both directions

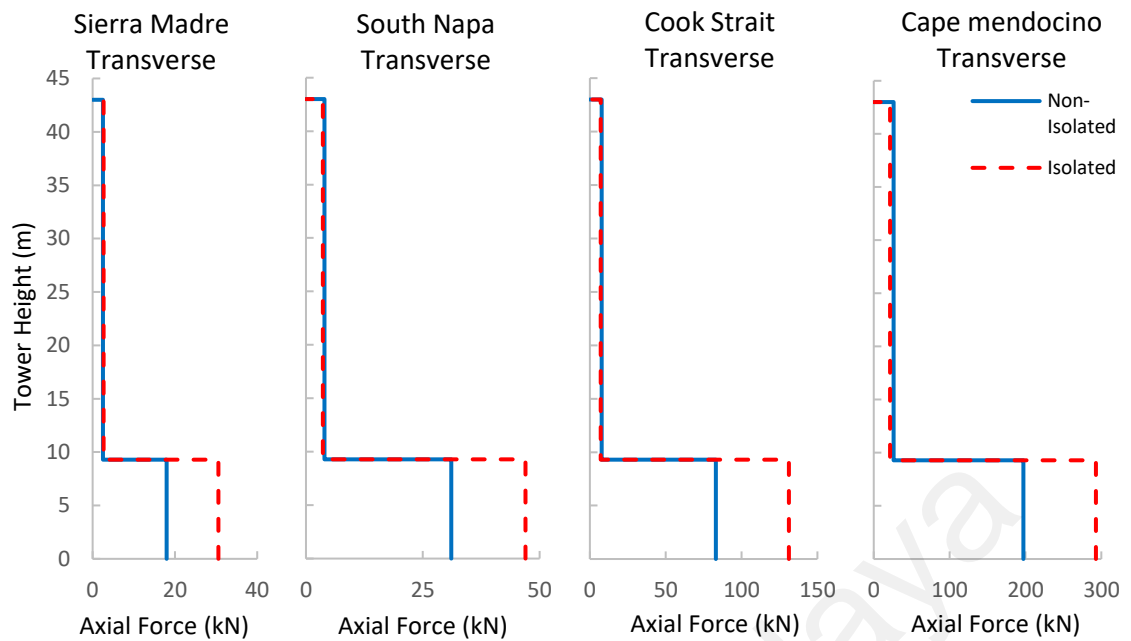


Figure 4.9, Continued

4.3.5 Cable response

Herein, since the bridge is symmetric in the transverse direction, only half side of the bridge cables are selected for the presentation of the results. The cables are numbered as 1, 2, 3 and 4 from the left to the right, respectively. Figure 4.10 shows the cable forces for non-isolated and isolated bridges under earthquake excitations. The tension force in cables 3 and 4 are higher as compared to cables 1 and 2, for the reason that, their connected end to box girders have closer distances to the tower. From the figure, it can also be seen that the base isolators caused a significant reduction in all cables' force variation in both directions subjected to different intensity earthquakes. The cables force variation is reduced up to 81.8% and 89.6% in longitudinal and transverse directions, respectively.

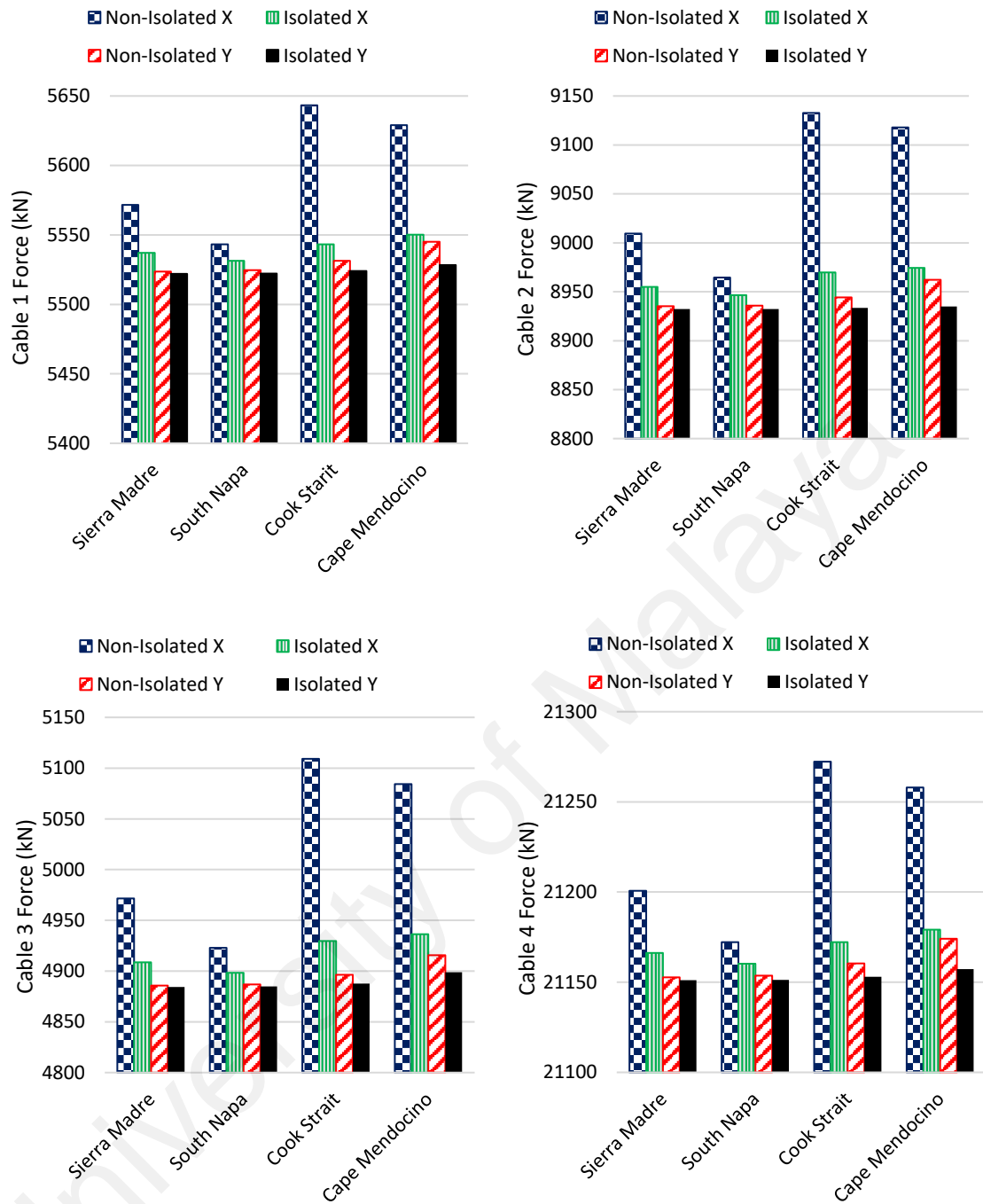


Figure 4.10: Maximum tension forces of the cables during earthquake excitations in longitudinal and transverse directions

4.3.6 Hysteresis curves of isolators

The force-displacement hysteresis curves of LRB under two components of each earthquake are investigated. Figure 4.11 demonstrates the hysteresis behavior of a selected LRB at the left abutment under four earthquakes. As the figure indicates, the isolator hysteresis curves reached the maximum yield force under Cook Strait and Cape

Mendocino earthquakes. This performance confirmed that the isolators are perfectly able to dissipate the induced seismic forces to the superstructure. In addition to this, the isolator dissipated the induced energy by moderate earthquakes in the linear state of its characteristic.

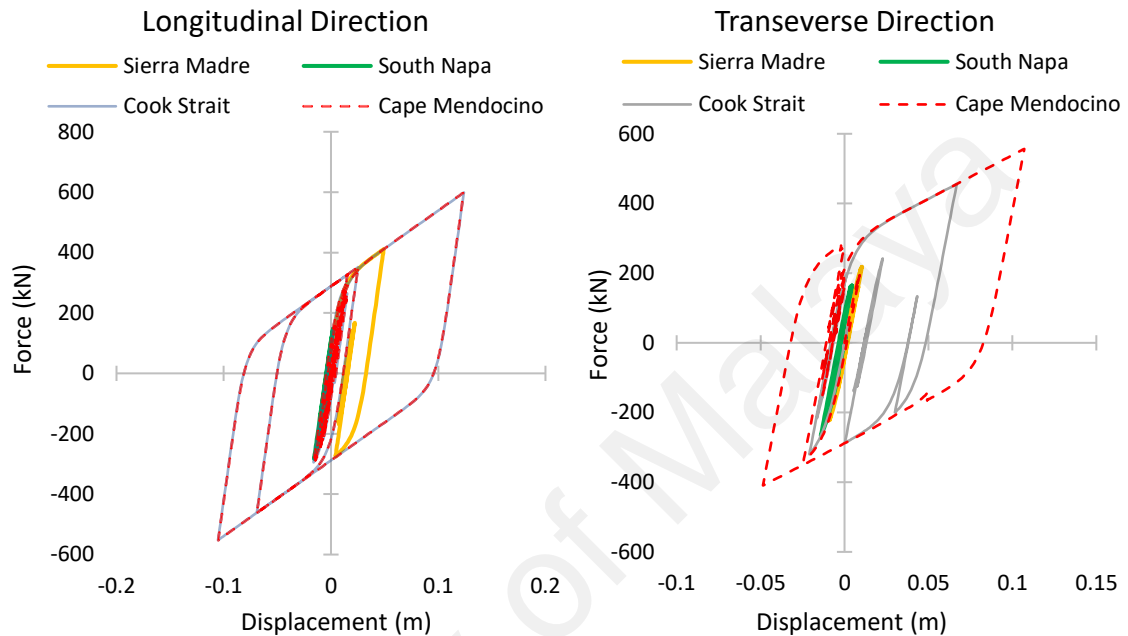


Figure 4.11: Force-Displacement hysteresis curve of the selected LRB at the left abutment

4.3.7 Overall dynamic performance

A summarized comparison of maximum seismic responses of the cable-stayed bridge is made in Table 4.3. The performance comparison of the original configuration (non-isolated) and isolated cable-stayed bridge showed that the isolation system is positively able to mitigate the unwanted response of the structure under destructive seismic loads. In other words, the overall seismic performance of the cable-stayed bridge is remarkably improved by utilizing the seismic isolators at the deck-tower connections and the end supports. Additionally, the isolators are able to minimize the transmission of seismic forces from substructure to superstructure, and hence, mitigate the damage to the superstructure. Following this, as the bridge is an existing structure, which is located at

high seismic zone and suffered damages due to earlier seismic excitations, the seismic isolation system can be considered as possible alternatives solution for seismic retrofitting strategy.

University of Malaya

Table 4.3: Summary of maximum seismic responses of the non-isolated and isolated cable-stayed bridge

Ground motions		Sierra Madre		South Napa		Cook Strait		Cape Mendocino	
Response	Direction	Non-Isolated	Isolated	Non-Isolated	Isolated	Non-Isolated	Isolated	Non-Isolated	Isolated
Displacement of deck (cm)	X	2.7	4.9	1.2	1.6	4.8	6.3	5.8	12.4
	Y	0.7	1.4	0.9	1.9	2.3	6.4	5.9	10.2
Acceleration of deck (m/s ²)	X	7.9	3.4	4.0	2.7	21.2	8.0	17.13	7.8
	Y	2.5	2.0	3.1	2.6	8.3	5.3	18.22	14.6
Base shear (kN)	X	5359.4	3828.3	2348.2	1626.5	9206.4	4664.5	9823.2	8612.7
	Y	1308.6	932.4	1691	1227.6	4088.9	2779.9	9208.8	3894
Base moment (kN-m)	X	116078	47804	56390	24063	326496	63537	250991	119268
	Y	6398.9	3707	11597.3	4476.9	25483.3	7912.6	58487.3	9361
Cable force 1 (kN)	X	5571.65	5537.19	5543.20	5531.30	5643.25	5543.18	5628.95	5550.16
	Y	5523.70	5522.06	5524.63	5522.25	5531.44	5532.96	5545.16	5528.24
Cable force 2 (kN)	X	9009.34	8954.97	8964.45	8946.70	9132.74	8969.74	9117.90	8974.30
	Y	8935.33	8932.50	8935.95	8932.44	8944.30	8933.65	8962.31	8934.90
Cable force 3 (kN)	X	4971.60	4908.72	4922.81	4898.40	5109.20	4929.54	5084.34	4936.26
	Y	4885.74	4884.23	4886.85	4884.80	4896.45	4887.81	4915.73	4898.94
Cable force 4 (kN)	X	21200.65	21166.19	21172.20	21160.30	21272.25	21175.18	21257.95	21179.16
	Y	21152.70	21151.06	21153.63	21151.25	21160.44	21152.96	21174.16	21157.24

4.4 Conclusions

From the detailed analyses, the implementation consequences of the seismic isolation systems in cable-stayed bridge led to the following conclusions:

- The isolation system was significantly capable of reducing the base shear and base moment of the bridge under selected ground motions.
- The reduction of bending moment and shear force in the tower proved that the isolation system is able to dissipate the seismic forces transmitted from substructure to superstructure, hence, reduced the likelihood of damage to the superstructure.
- The implementation of the isolation system between superstructure and substructure increased the deck flexibility, especially in the transverse direction and caused torsional deformation under transverse earthquake component. This torsional moment transferred to substructure through base isolators and enlarged the axial force of the tower in the substructure.
- The cable force variation reduced substantially and enhanced the stability of the deck under serviceability condition.
- Even though the deck displacement of isolated bridge increased in longitudinal and transverse directions, but it remained in the range of the design displacement of the bridge. Meanwhile, the isolation system caused a remarkable reduction of the deck acceleration in both directions.
- The mitigation of maximum seismic responses might occur under strongest earthquake, as the isolations were stiff for the moderate earthquakes. Therefore, the seismic zones are an important parameter in the design of base isolators for cable-stayed bridges.

CHAPTER 5: DEVELOPMENT OF A NEW YIELDING METALLIC DAMPER

5.1 Introduction

From the results of Chapters 3 and 4, it can be seen that the seismic isolators remarkably enhanced global and local seismic responses of the cable-stayed bridge. On the other hand, the seismic displacement of the superstructure increased after the utilization of seismic isolators in the cable-stayed bridge. Therefore, the use of a new metallic damper is proposed in the isolated cable-stayed bridge to control the superstructure seismic displacement. Accordingly, a new metallic damper called the Hexagonal Honeycomb Steel Damper (HHSD) is developed in this chapter. As the name indicates, HHSD benefits from the advantages of hexagonal honeycomb geometry and steel material in terms of dissipating the induced energy to civil structures in specific cable-stayed bridges.

In general, honeycombs comprise identical groups of prismatic cells that are placed together to form a plane. Various honeycomb materials are used broadly in different engineering structures in the aerospace and automobile industries for instance. Honeycombs are light in weight and can sustain excessive loads, such as buckling, bending, and in-plane and/or out-of-plane shear loads (Gibson & Ashby, 1997). For example, honeycombs are also used in sandwich cores and impact absorbers. The hexagonal shape is the most common for honeycombs, but circular, square and other geometries are deployed as well for honeycomb structures. Honeycombs under high strains behave nonlinearly due to their geometry and cell walls' material nonlinearity (Gibson et al., 1982).

As discussed in Chapter 2, metal materials such as steel exhibit nonlinear behavior, which is beneficial in energy dissipation systems. Metallic dampers dissipate energy through their materials' yield or inelastic deformation. Advantages of metallic dampers

over active and semi-active dampers include stable hysteretic behavior, rate independence, resistance to ambient temperature, reliable and the fact that their material behavior is familiar to practice engineers.

An HHSD is made of thin steel sheets with several small hexagonal honeycomb openings that are placed uniformly. The hexagons have regular unit cells with the same side lengths and 120° angles. As shown in Figure 5.1, the HHSD is welded to anchor plates at the top and bottom in order to install in the primary structures by bolts. This feature enables replacing the failed damper after seismic events. The HHSD characteristics are studied through quasi-static cyclic test. Furthermore, a 3-dimensional Finite Element (FE) model of HHSD is rigorously created and validated with experimental results. Finally, the HHSD constitutive formula is derived.

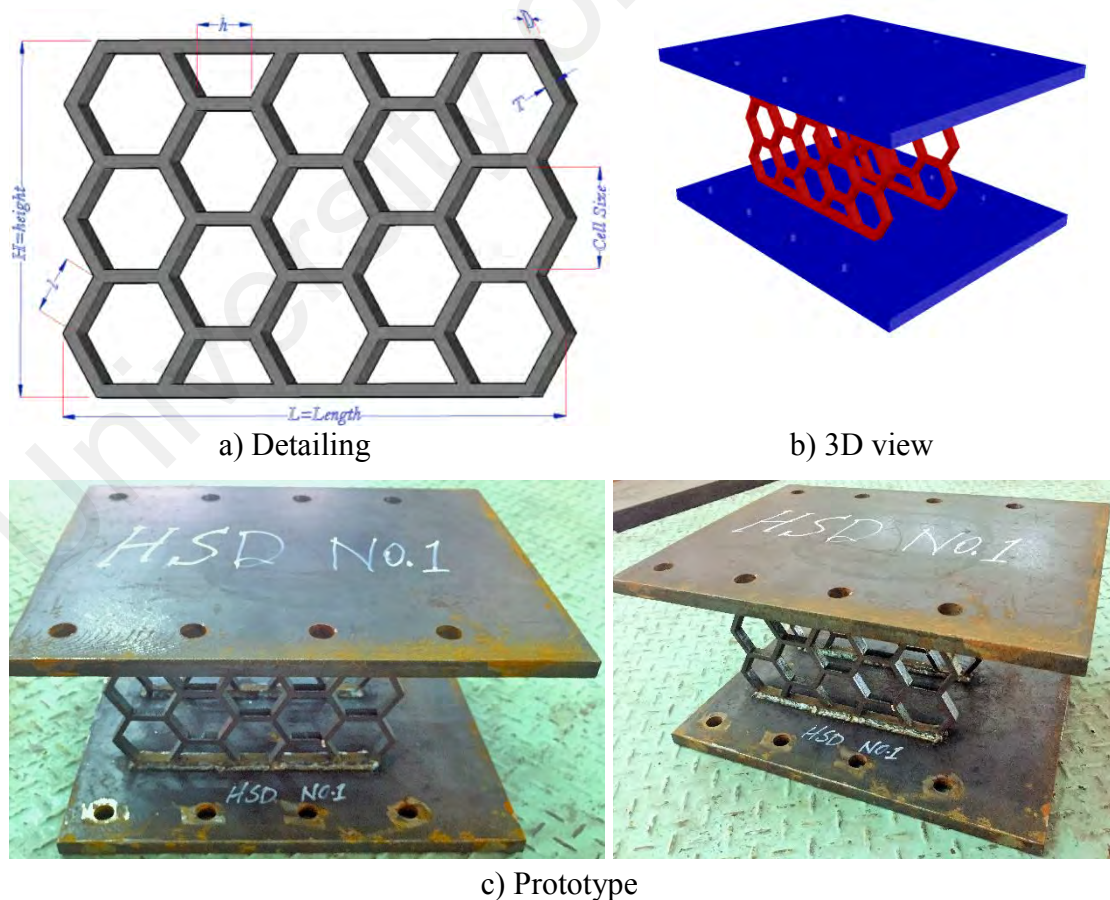


Figure 5.1: HSSD detailing and prototype

A few potential HHSD locations in various structures are shown in Figure 5.2: a) chevron bracing system, b) V-type bracing system, c) diagonal bracing system and d) beam-column connection. In bridge structures, the HHSD can be implemented between the bridge deck and pier/strut/column in order to enhance the seismic performance of bridges. An example of a bridge equipped with HHSD is shown schematically in Figure 5.3. Chapter 2 suggested more details on HHSD implementation locations.

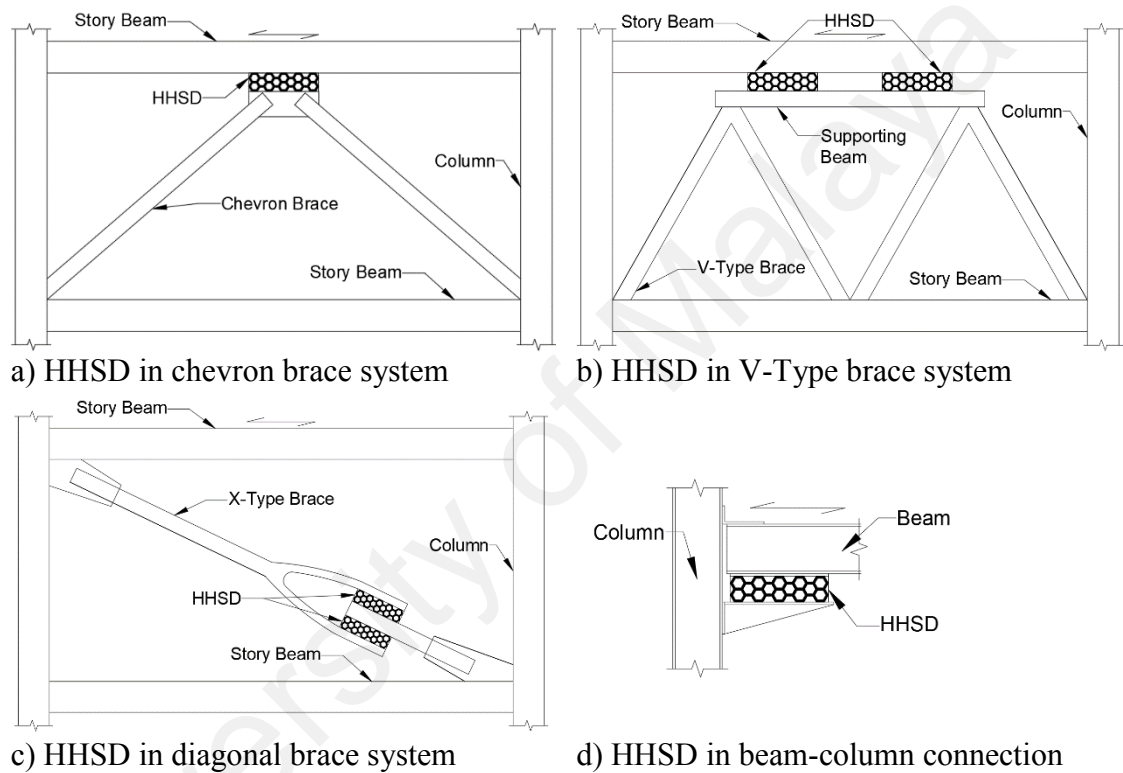


Figure 5.2: Schematics of HHSD implementation in various structures

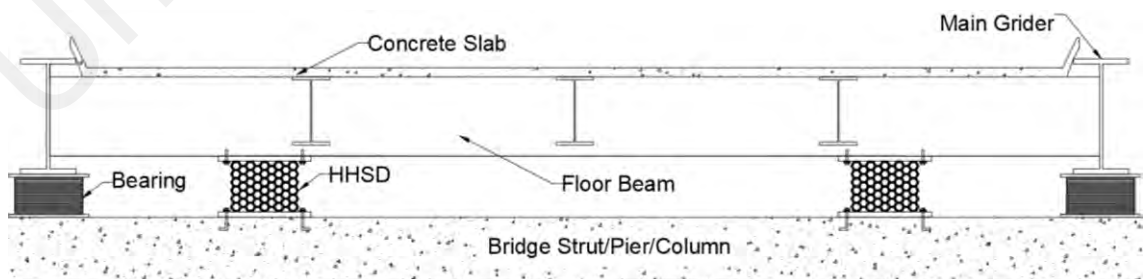


Figure 5.3: Schematic of HHSD implementation in a bridge

5.2 Theoretical approach

In this section, the behavior of the HSSD under in-plane shear force is studied through the theoretical approach. Consider a unit cell of an HSSD as shown in Figure 5.4. A unit cell has sides with equal lengths l ($h=l$), equal internal angles of 120 degrees (α), uniform thickness (t) and uniform out-of-plane depth (D). The regular honeycombs have in-plane isotropic behavior and two independent elastic moduli, i.e. young's modulus E and shear modulus G . Young's modulus of the steel plate is obtained through tensile testing and the shear modulus can be calculated with the following formula:

$$G = \frac{E}{2(1+\vartheta)} \quad (5-1)$$

Where ϑ is the steel plate's Poisson's ratio. When shear force P is applied parallel to a honeycomb unit cell, it deforms in a linear-elastic manner (Figure 5.4).

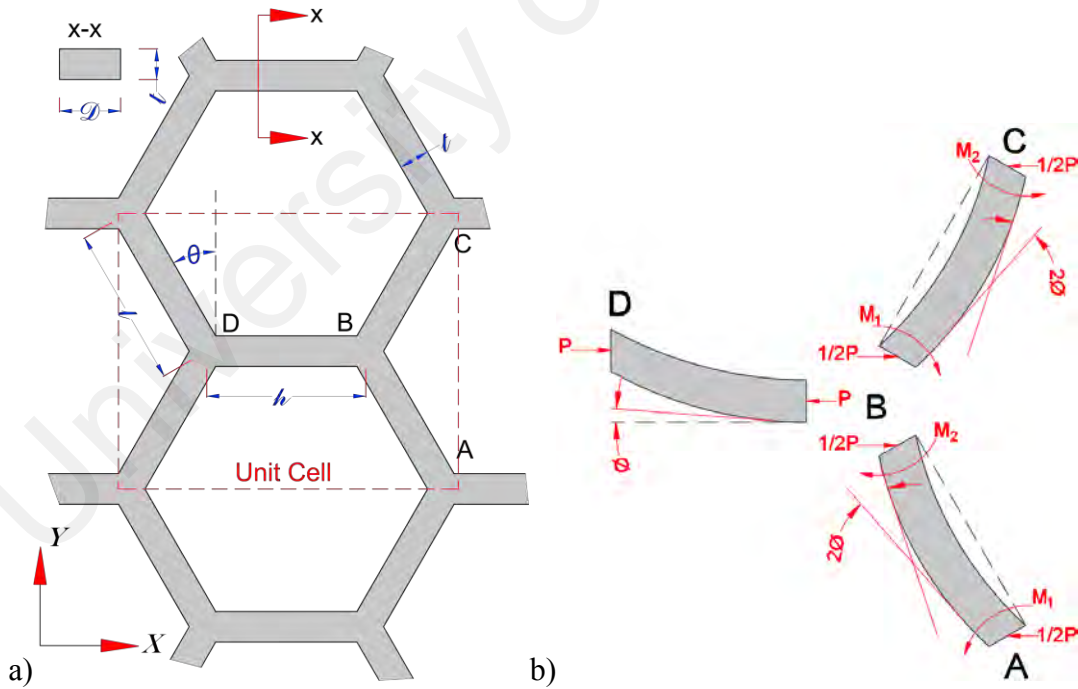


Figure 5.4: a) Detailed schematics of a honeycomb structure and b) honeycomb deformation under shear load

The force-displacement relationship of regular hexagonal cells is used to determine the stiffness of each cell. The moment at the end of DB due to shear load on the vertical cell wall is:

$$M = Pl \sin\theta \quad (5-2)$$

The stress formula for a beam subjected to moment is:

$$\sigma = \frac{My}{I} = Pl \sin\theta \times \frac{t}{2} \times \frac{12}{Dt^3}$$

$$\sigma = \frac{6Pl \sin\theta}{Dt^2} \quad (5-3)$$

Therefore, when σ_y is the material's yield stress, the yield force is obtained by:

$$P_{y,d} = \frac{\sigma_y Dt^2}{6l \sin\theta} \quad (5-4)$$

For an HHSD with a number of vertical cell walls in the X direction equal to n_x and when the total length is L , the yield force is:

$$P_{y,t} = n_x \times \frac{\sigma_y Dt^2}{6L \sin\theta} \quad (5-5)$$

$$\text{Where, } L = [(n_x + 1) \times t + (n_x + (n_x + 1)\sin\theta) \times l] \quad (5-6)$$

The standard formula for beam deflection is:

$$\delta = \frac{Ml^2}{6EI} \quad (5-7)$$

Where I is the second moment of the area ($I=Dt^3/12$) and substituting Equation 5-2 in Equation 5-6 gives:

$$\delta = \frac{2P \sin\theta}{ED} \times \left(\frac{l}{t}\right)^3 \quad (5-8)$$

By substituting Equation 5-4 in the above equation, the yield deflection of an HHSD with a number of vertical cell walls in the Y direction equal to n_y is:

$$\delta_{y,t} = n_y \times \frac{\sigma_y l^2}{3Et} \quad (5-9)$$

5.3 Experimental study

5.3.1 Coupon test

The tensile coupon test is essential to determine the mechanical properties of a steel plate. Three standard samples were prepared for the uniaxial tensile test according to the Standard Test Methods for Tension Testing of Metallic Materials (ASTM-E8, 2015). All three samples had the same thickness and dimensions as shown Figure 5.5. The test setup is illustrated in Figure 5.6 and consists of a 1000 kN Universal Testing Machine (IPC UTM-1000). The samples were mounted with the help of grips and loaded in tension at a constant strain rate until sample failure or fracture. A computer data logger connected to the UTM recorded the stress and strain, or in other words, the applied tension load with the relevant displacement. The specimens' characteristics, including the Poisson's ratio, yield strength, modulus of elasticity and ultimate strength were obtained from the stress-strain graph.

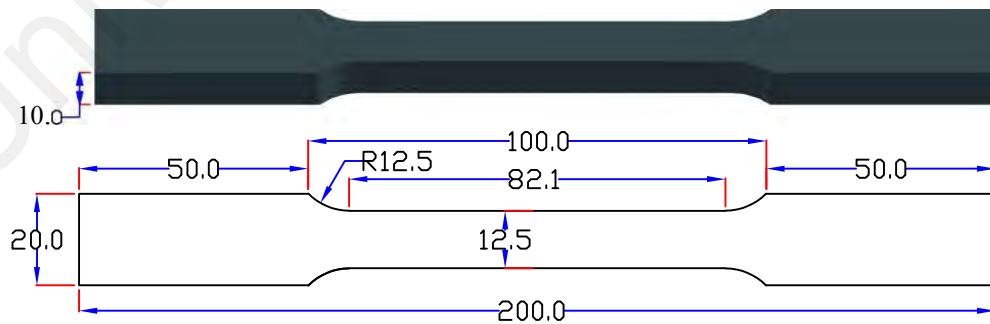


Figure 5.5: Detailing of dog bone specimen based on ASTM-E8 2015 (all units are in mm)



Figure 5.6: The IPC UTM-1000 used for the tensile test

5.3.2 Quasi-static cyclic test

The HHSD was tested experimentally in order to determine its performance and characteristics. A quasi-static cyclic test based on FEMA-461 (Federal Emergency Management Agency, 2007) was performed on the HHSD. FEMA-461 proposed the incremental displacement loading protocol to find the capacity and seismic performance of the structures. The loading protocol is based on the drift ratio, which is converted into displacement based on the specimen's height. Table 5.1 lists the loading protocol details for each step. Thirteen incremental steps starting from 0.02% drift ratio and ending at 5% drift ratio (maximum target displacement of 50 mm) were used as the loading protocol. Each step had 3 constitutive cycles; therefore, the loading protocol had a total 39 cycles. The loading protocol implemented in this research is presented in Figure 5.7. The loading frequency for each step is calculated with:

$$f = 1 / \left[\left(\frac{4d}{v} \right) \times 60 \right] \quad (5-10)$$

Where d is displacement (mm) and v is UTM loading speed (mm/min).

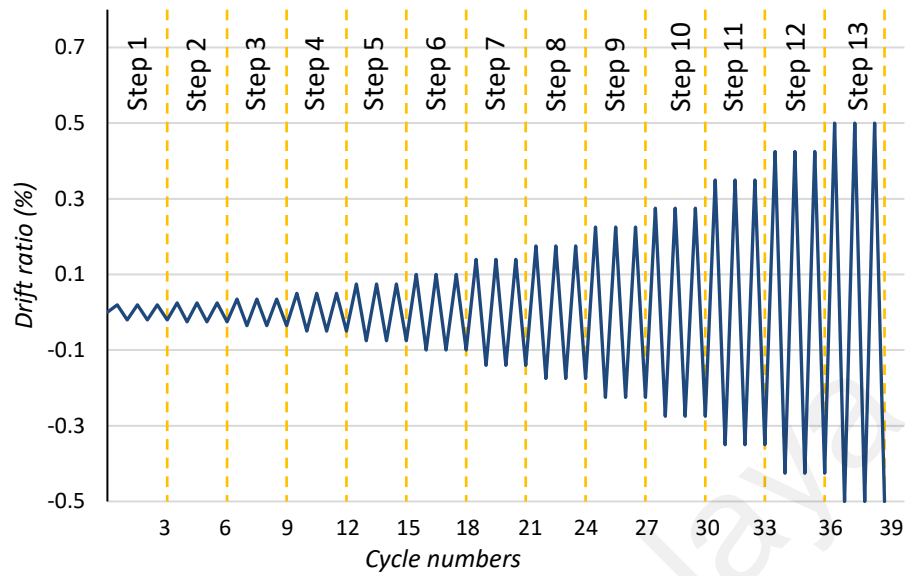


Figure 5.7: Loading protocol used for the quasi-static cyclic test on HHSD

Table 5.1: Details of the loading protocol in the quasi-static cyclic test

Steps	No. of cycle	Displacement (mm)		Speed rate (mm/s)	Frequency (Hz)
1	3	2	-2	0.25	0.031
2	3	2.5	-2.5	0.25	0.025
3	3	3.5	-3.5	0.25	0.018
4	3	5	-5	0.25	0.013
5	3	7.5	-7.5	0.45	0.015
6	3	10	-10	0.45	0.011
7	3	14	-14	0.45	0.008
8	3	17.5	-17.5	0.45	0.006
9	3	22.5	-22.5	0.8	0.009
10	3	27.5	-27.5	0.8	0.007
11	3	35	-35	0.8	0.006
12	3	42.5	-42.5	0.8	0.005
13	3	50	-50	0.8	0.004

5.3.2.1 Test setup

An Instron Universal Testing Machine with a 1000kN load hydraulic actuator and 25mm actuator displacement capacity was used for the quasi-static cyclic test. An

assembly was attached to the actuator head to mount the HHSD vertically. The mounting assembly was used for full cyclic loading (push and pull). The HHSD was designed for lateral loadings, while the actuator in the laboratory was vertical; therefore, the HHSD was rotated by 90 degrees. The HHSD was installed on the mounting assembly with 8 bolts. The other side of the HHSD was fastened with 8 bolts to a fixed support system. A 2D schematic view and the test setup of the quasi-static cyclic experiment are shown in Figure 5.8. The Instron WaveMatrix software was used for data acquisition from the UTM. The thirteen steps were input as displacement control with respective speed rate illustrated in Table 5.1.

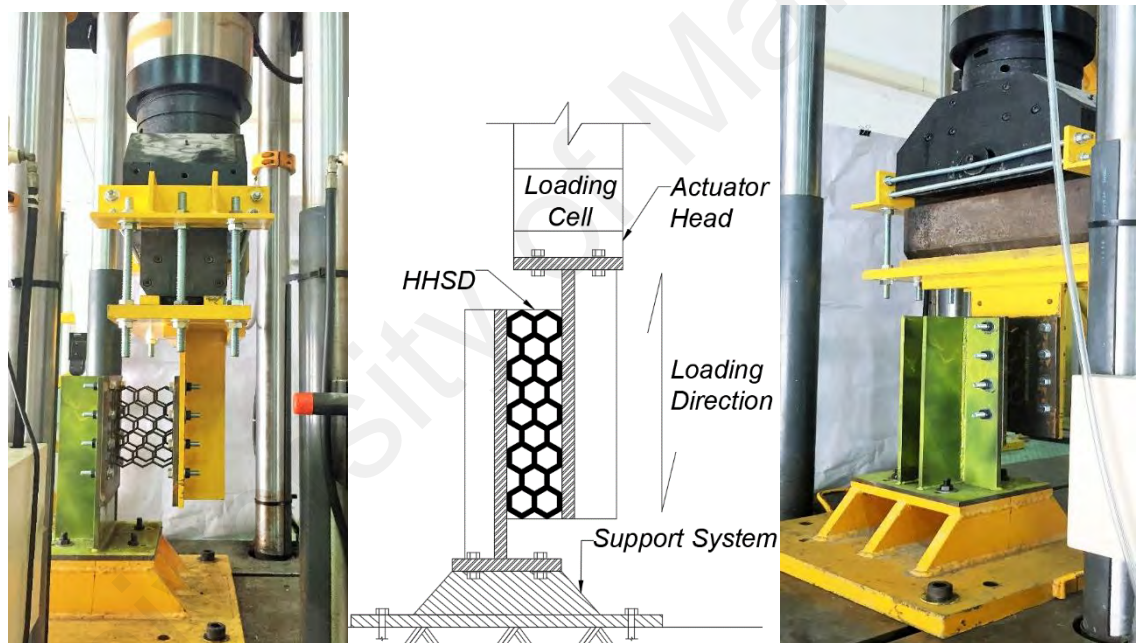


Figure 5.8: HHSD experimental test setup

5.3.2.2 Parametric study

According to the HHSD geometry and the theoretical approach, it can be understood that several different parameters affect HHSD behavior. A parametric study performed to find the effect each parameter on HHSD performance. Different parameters including the height, length, depth, thickness and cell size were determined possible for the parametric study. A total of 12 HHSD samples were fabricated for the experimental test. The details

of each specimen are presented in Table 5.2. HHSD No. 1 was selected as the benchmark and the effects of parameter variations were compared against HHSD No. 1.

Table 5.2: HHSD details for the experimental parametric study

HHSD No.	Height	Length	Depth	Thickness	Cell dimensions		Remarks
	H (mm)	L (mm)	D (mm)	T (mm)	l (mm)	h (mm)	
1	140.00	213.62	10.00	5.00	23.09	23.09	Benchmark
2	140.00	213.62	8.00	5.00	23.09	23.09	D changed
3	140.00	213.62	12.00	5.00	23.09	23.09	D changed
4	150.00	228.05	10.00	7.50	23.09	23.09	T changed
5	145.00	219.39	10.00	10.00	20.09	20.09	T changed
6	95.00	213.62	10.00	5.00	23.09	23.09	H changed
7	185.00	213.62	10.00	5.00	23.09	23.09	H changed
8	130.00	207.85	10.00	5.00	11.55	11.55	l and h decreased
9	185.00	213.62	10.00	5.00	29.83	23.09	l increased
10	140.00	223.72	10.00	5.00	29.83	58.09	h increased
11	135.68	230.00	10.00	5.00	23.09	23.09	HHSD rotated by 90°
12	140.00	213.62	10.00	5.00	23.09	23.09	Combine shape of hexagon & rhombic

Where total height is:

$$H = [2 \times n_y \times h \times \cos\theta + (n_y + 1) \times t] \quad (5-11)$$

5.3.3 Experimental results and discussion

The results are discussed for two different tests. The results from the tensile test on the dog bone samples are presented first, followed by the HHSD results from the quasi-static cyclic test.

5.3.3.1 Tensile test results

The stress-strain curves for three dog bone samples that underwent the tensile coupon test are plotted in Figure 5.9. From this figure, the yield stress, ultimate stress, Young's modulus and elongation of each sample are obtained. Figure 5.10 depicts the three samples after failure. Strain is defined as the ratio of elongation (ΔL) to the original length (L_0), while stress is defined as the force (F) divided by the original area (A_0). The strain and stress of each sample can be obtained with Equations. 5-9 and 5-10. Furthermore, the mechanical properties of each sample and their average are summarized in Table 5.3.

$$\varepsilon = \frac{\Delta L}{L_0} \quad (5-12)$$

$$\sigma = \frac{F}{A_0} \quad (5-13)$$

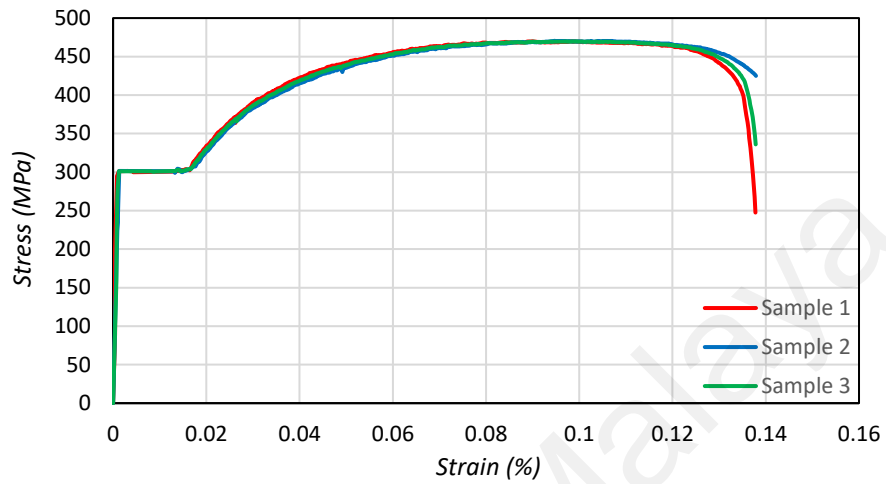


Figure 5.9: Stress-Strain curves for three samples obtained from the tensile test



Figure 5.10: Failure of dog bone samples after the coupon tensile test

Table 5.3: Coupon tensile test results

Sample	Young's modulus (GPa)	Yield stress (MPa)	Ultimate stress (MPa)
1	201	301.50	487.35
2	200	302.02	488.19
3	199	299.67	479.35
Mean	200	301.06	484.97

5.3.3.2 Parametric study test results

The behavior of metallic dampers is commonly evaluated through quasi-static cyclic testing. A force-displacement hysteresis curve represents the damper's capacity. The curve is used to obtain different results, such as the yield displacement (Δ_y), yield strength (P_y), elastic stiffness (k_d), ultimate displacement (Δ_u) and ultimate strength (P_u) as illustrated Figure 5.11. Other results that can be calculated from the curve are for cumulative displacement (Δ_{cum}), effective stiffness (K_{eff}), ductility (μ), cumulative displacement ductility (μ_{cum}), energy dissipated (E_D) and equivalent viscous damping (ξ).

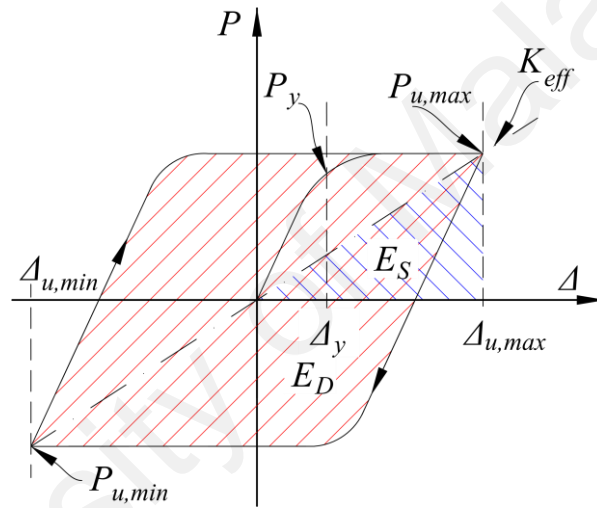


Figure 5.11: Force-displacement hysteresis curve of steel material

Cumulative displacement is defined as the absolute summation of all positive and negative cyclic displacements till maximum load, as follows:

$$\Delta_{cum} = \sum_{i=0}^N (|\Delta_i^{u,max}| + |\Delta_i^{u,min}|) \quad (5-14)$$

The effective stiffness can be determined with the following equation:

$$K_{eff} = \frac{|P_{u,max}| - |P_{u,min}|}{|\Delta_{u,max}| - |\Delta_{u,min}|} \quad (5-15)$$

Ductility is defined as the ratio of ultimate displacement to yield displacement:

$$\mu = \frac{\Delta_u}{\Delta_y} \quad (5-16)$$

The equivalent viscous damping of a metallic damper can be obtained with the following equation (Chopra, 2014):

$$\xi = \frac{1}{4\pi} \times \frac{E_D}{E_S} \quad (5-17)$$

Where E_D is the area of the force-displacement loop at ultimate load and E_S is the strain energy.

The UTM recorded the force and displacement from its embedded load cell and Linear Variable Differential Transformer (LVDT). Figure 5.12 depicts a typical force-displacement hysteresis curve for the HHSD (benchmark specimen) that dissipates energy based on the steel material's plasticity. Inelastic buckling was observed in the first 3 loading cycles for most specimens tested due to the actuator characteristics and other uncertainties of the test setup. Therefore, the yield displacement and force could not be obtained from the HHSD hysteresis graph. The inelastic buckling of dampers in the initial loading cycles was also reported by Sahoo et al. (2015). All 12 specimens exhibited stable hysteretic behavior and a gradual transition from elastic to inelastic state under cyclic loading. A slight pinching effect was observed in the hysteresis curve for the first few positive cycles of displacement near zero displacement. The pinching effect has also been reported in other metallic dampers (Chan et al., 2013; Z. Chen et al., 2013; Vasdravellis et al., 2012). After about 19 load cycles, HHSD No. 1 reached its ultimate load of 32.56 kN at 10 mm displacement, after which it started losing about 20% of its capacity in each consecutive step. This HHSD feature helped dissipate the induced energy even after reaching ultimate capacity. In addition, a considerable amount of energy dissipated in the last damper cycle before strength deterioration. Strength degradation started when plastic hinges formed at the node bonds (vertical cell walls) in the middle of the HHSD and subsequently, the other vertical cell walls failed. The formation of plastic hinges in vertical cell bonds caused crack initiation, followed by brittle failure of the bond cells.

The inclined cells were still able to dissipate energy but gradually failed and caused total HHSD failure. Figure 5.13 shows the plastic hinge locations in HHSD No. 1 after reaching ultimate load. The experimental test results for all twelve specimens are summarized in Table 5.4. It was difficult to identify the yield strength due to the inelastic buckling in the hysteresis curve for the first few positive cycles. The plastic strength increased gradually in each displacement cycle. This behavior is known as cyclic hardening, which may occur in ductile metals as it relies on the molecular structure of the steel material. It should be noted that no sign of welding failure was observed in any of the specimens.

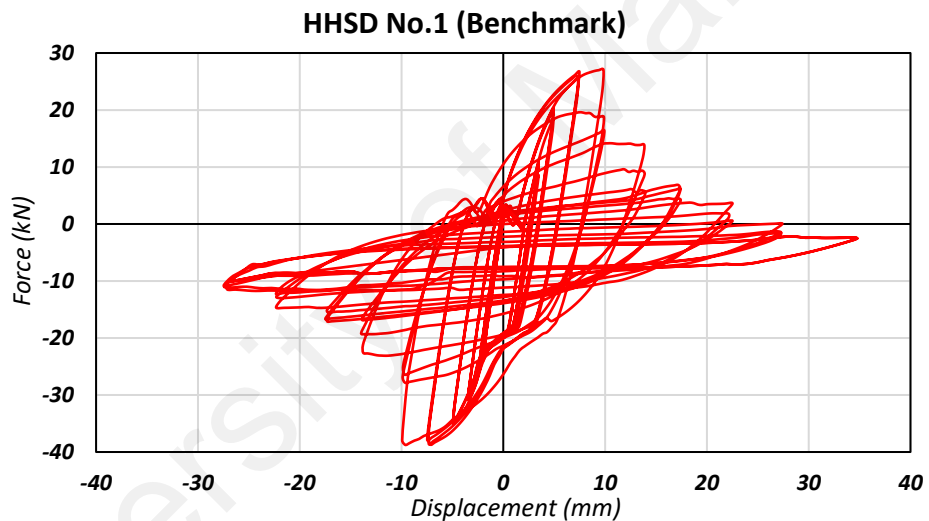


Figure 5.12: Typical HHSD hysteresis curves

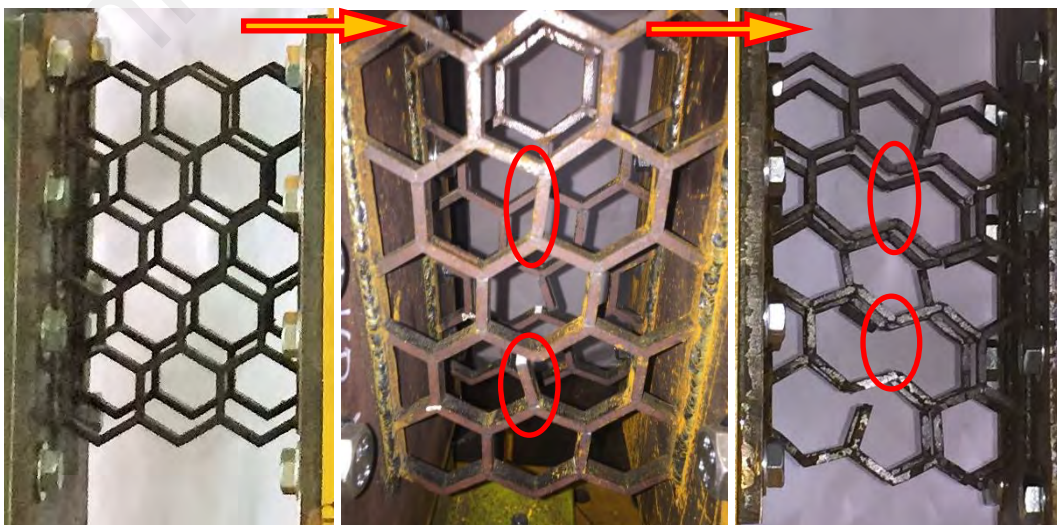


Figure 5.13: Sequence of plastic hinge formation in HHSD No. 1

Table 5.4: Quasi-static cyclic test result summary

Reference No.	Δu_{max} (mm)	$P_{u,max}$ (kN)	Δu_{min} (mm)	$P_{u,min}$ (kN)	K_{eff} (kN/mm)	E_D (kJ)	E_S (kJ)	ξ %
No.1	9.8	27.10	-9.6	-38.7	55.2	602.1	133.33	35.95
No.2	9.9	18.31	-9.7	-31.5	66.0	331.9	90.36	29.24
No.3	13.9	34.02	-13.8	-44.9	121.1	1103.6	235.93	37.24
No.4	9.8	64.2	-9.7	-71.9	59.4	1007.8	314.90	25.48
No.5	13.9	124.53	-13.8	-109.6	214.0	2660.9	862.99	24.55
No.6	7.5	40.8	-7.3	-25.5	76.4	450.0	153.00	23.42
No.7	13.9	20.49	-13.8	-35.5	136.8	848.6	142.00	47.58
No.8	9.9	114.3	-9.8	-118.2	32.8	1279.0	566.93	17.96
No.9	13.9	18.9	-13.8	-25.6	67.2	665.3	130.98	40.44
No.10	9.9	28.01	-9.7	-18.2	49.1	235.1	138.09	13.56
No.11	9.9	31.3	-9.6	-39.3	38.1	669.6	154.15	34.58
No.12	7.4	38.4	-7.2	-38.9	3.3	431.7	141.12	24.36

(a) Effect of out-of-plane depth

The effect of HHSD depth on HHSD performance was studied by increasing the depth from 8 to 12 mm. The HHSD out-of-plane depth (D) had a direct effect on force-displacement hysteresis behavior. Figure 5.14 illustrates the hysteresis curves of HHSD No. 1, 2 and 3. For these three specimens, the Bauschinger effect and kinematic hardening were observed and the plastic strength increased gradually in each cycle with low stiffness degradation under displacement control loading. These three samples, especially HHSD No. 3, absorbed a notable amount of energy during the quasi-static cyclic test. As the depth was increased, the pinching of the HHSD hysteresis curves reduced. The three specimens thus exhibited stable hysteretic behavior. As the figure indicates, with depth increment the HHSD's energy absorbing capability increased. The curve trends were quite similar, except as the depth increased, the damper strength also increased. When the depth increased from 8 to 10 mm, the maximum load enlarged by 22.8%. As the depth was increased two-fold in HHSD No. 3, the maximum load and displacement increased by 42.5% and 43.75%, respectively. For the HHSDs with depths of 8 and 10 mm the maximum drift ratio was 1%, but for 12 mm depth the drift ratio reached 1.4%.

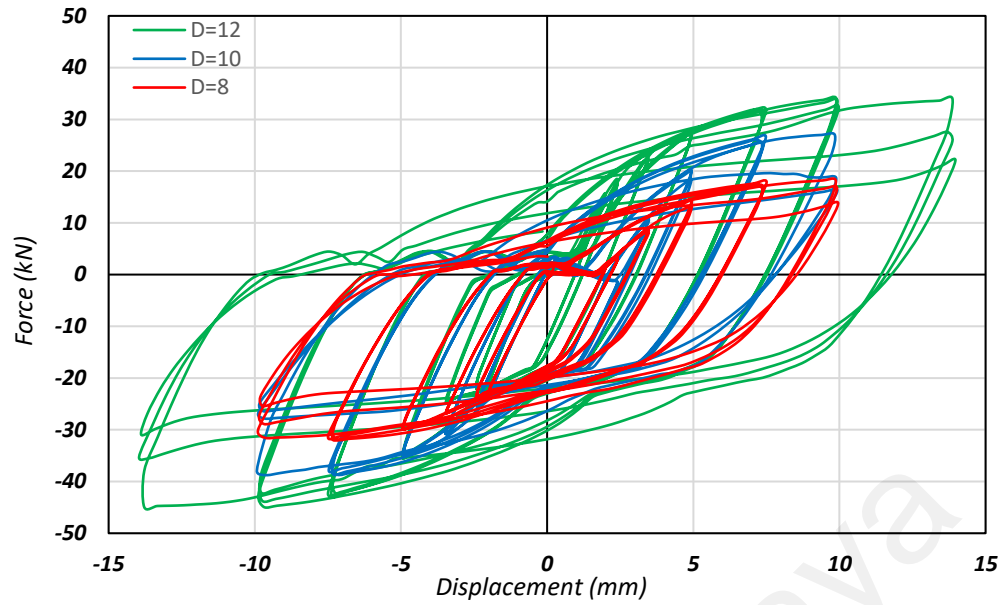


Figure 5.14: Effect of depth on the force-displacement hysteretic behavior of HHSDs

Figure 5.15 (a) shows the dissipated energy and equivalent viscous damping of HHSDs with various depths. According to this figure, both HHSD energy dissipation capability and viscous damping increased with depth increment. The cumulative energy dissipated versus cumulative displacement in each cycle is shown in Figure 5.15 (b). At lower cumulative displacement, all three specimens dissipated almost the same amount of energy. However, when the cumulative displacement reached 1000 mm, the cumulative energy dissipated increased with depth increment. The HHSD with 12 mm depth dissipated the largest amount of energy of up to 7000 kNmm and tolerated around 7200 mm of cumulative displacement up to failure. This result indicates that HHSD No. 3 with 12 mm depth outperformed the specimens with 8 and 10 mm depths, which failed at lower drift ratios. The plastic hinge locations and bond cell failure in specimens with different depths are shown in Figure 5.16. The figure indicates that failure occurred in the same locations for all three specimens. It can be concluded that the HHSD with 12 mm depth tolerated greater deformation and had the highest damping ratio, which is useful for dissipating large amounts of energy.

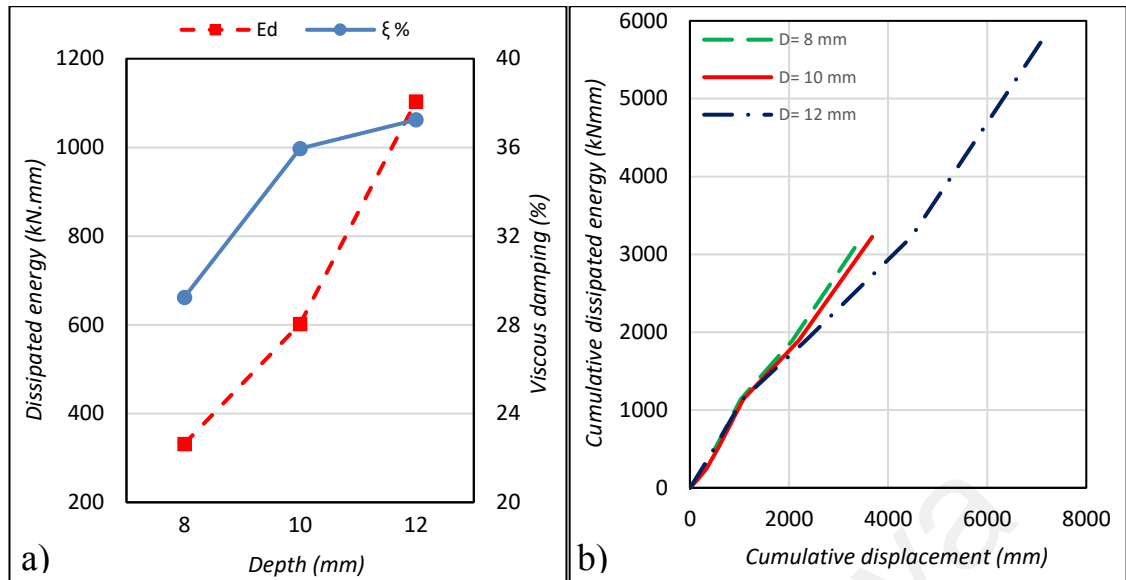


Figure 5.15: a) Effect of depth on dissipated energy and viscous damping ratio, b) cumulative energy dissipated by HHSDs

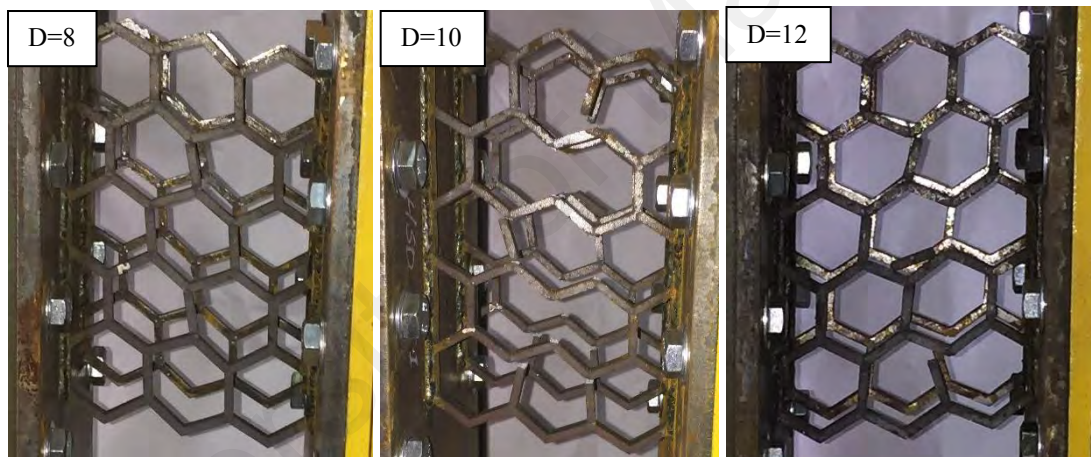


Figure 5.16: HHSD failure mode related to the depth parameter

(b) Effect of thickness

In this section, HHSD cell thicknesses from 5 to 10 mm are investigated. Figure 5.17 shows the force versus displacement in specimens with three different thicknesses. The Bauschinger effect and kinematic hardening are evident in the hysteresis curves of all three specimens. The pinching effect was observed again around zero displacement and the elastic regime transitioned gradually to inelastic regime. The three specimens deformed in a stable manner under the cyclic loading test. The HHSD hysteresis loops enlarged considerably as the thickness increased. Table 5.4 indicates that the HHSD yield force increased from 9.1 to 14.8 and 21.4 kN as the depth augmented by 25% and 50%.

Similarly, the ultimate HHSD strength increased by 16% and 85.8% when the thickness changed from 5 to 7.5 and 10 mm. Apart from this, the maximum HHSD drift ratio was 0.1% when the thickness was 5 and 10 mm; once the thickness was 10 mm, the maximum drift ratio reached 0.14%. It can be concluded that HHSD thickness had a direct effect on the dampers' hysteretic behavior and thicker HHSDs had larger hysteresis loops.

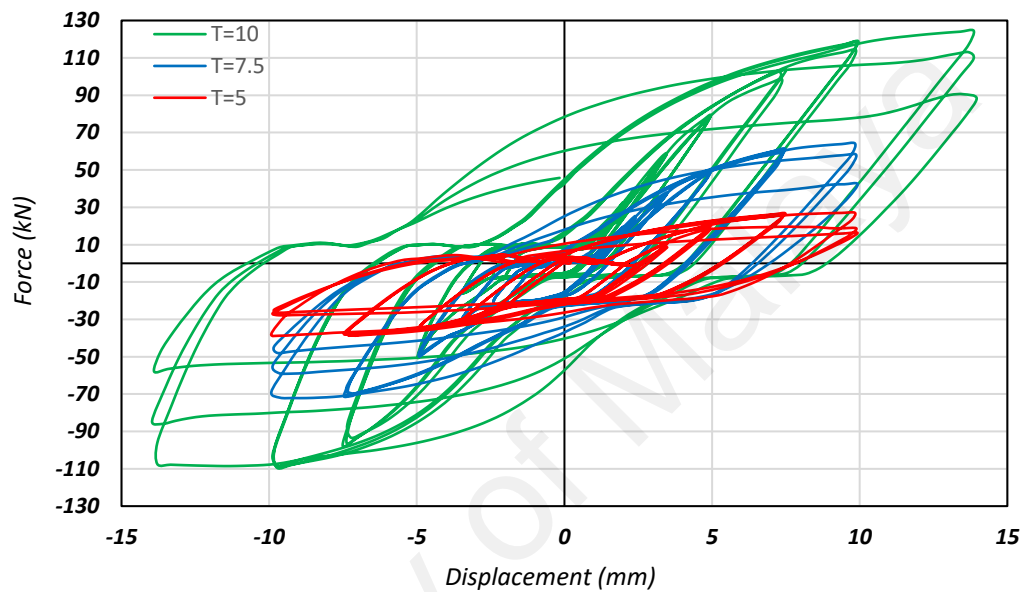


Figure 5.17: Effect of thickness on the force-displacement hysteretic behavior of HHSDs

Figure 5.18 (a) presents the effect of HHSD thickness variation on the dissipated energy and equivalent viscous damping behavior of HHSDs. The energy dissipation of the HHSDs grew dramatically as depth increased. On the other hand, the equivalent viscous damping of the dampers decreased with an increment in HHSD thickness. The equivalent damping of 7.5 and 10 mm thick HHSD was similar. Figure 5.18 (b) shows the total energy dissipated over the total displacement for different HHSD thicknesses. In the elastic zone, the HHSDs dissipated energy linearly with the distance traveled. The cumulative dissipated energy was similar in the elastic zone of all three specimens. However, in the plastic zone, with increasing thickness the energy dissipation grew considerably. As this figure indicates, the 10 mm thick HHSD absorbed up to 6000 kNmm

of energy over a total displacement of 13200 mm. Figure 5.19 shows the HHSDs with three different thicknesses after reaching the ultimate load. All three samples underwent the same failure mechanism. The damage concentration started at both ends of the cell bonds and cracks initiated from there. As the drift ratio increased, the cracks propagated, which led to cell bond brittle failure as depicted in Figure 5.19. It can be stated that HHSD thickness had a direct effect on damper performance and the thickest HHSD was able to absorb more energy.

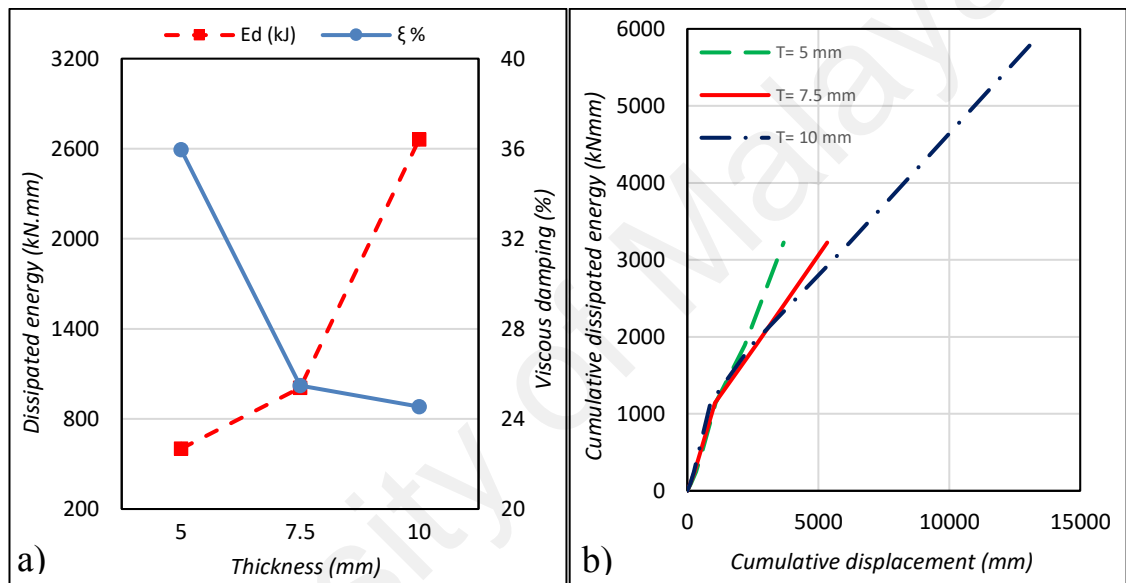


Figure 5.18: a) Effect of thickness on dissipated energy and viscous damping, b) cumulative energy dissipated by HHSDs

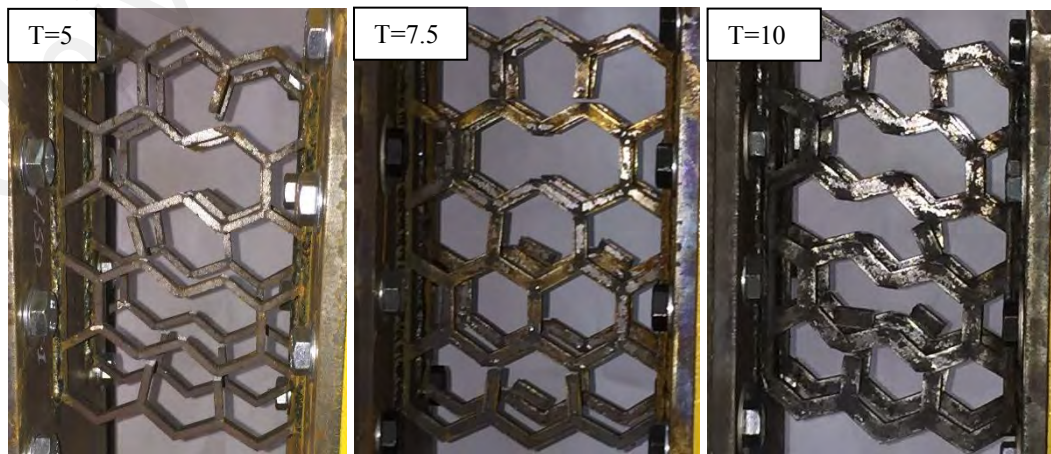


Figure 5.19: HHSD failure mode related to the thickness parameter

(c) Effect of height

This section elaborates on the effect of HHSD height on performance. The height variation was based on the numbers of rows in the hexagonal honeycomb. Accordingly, 95, 145 and 185 mm heights were designed for two, three and four hexagonal honeycomb rows in the HHSD. Figure 5.20 displays the force-displacement curves for three specimens with different heights. Similar to the results in the previous sections, pinching of the hysteresis curves was observed near zero displacement. However, the pinching effect reduced as the height increased. The three specimens showed stable behavior with smooth stiffness degradation under cyclic displacement. As expected, the highest specimen had lower yield displacement and strength, while it sustained greater deformation due to its flexibility. Table 5.4 demonstrates that when the height was increased from 95 to 145 and 185 mm, the yield force decreased from 17.82 to 12.33 and 8.3 kN. As the HHSD height increased, the ultimate strength decreased, while the maximum HHSD drift ratio at failure increased. Decrements of 33.6% and 50% in the maximum force of HHSDs were observed with respect to 52.6% and 94.7% increments in height. On the contrary, the maximum HHSD displacement under ultimate load increased from 7.5 to 10 and 14 mm as the HHSD height increased from 95 to 145 and 185 mm, respectively.

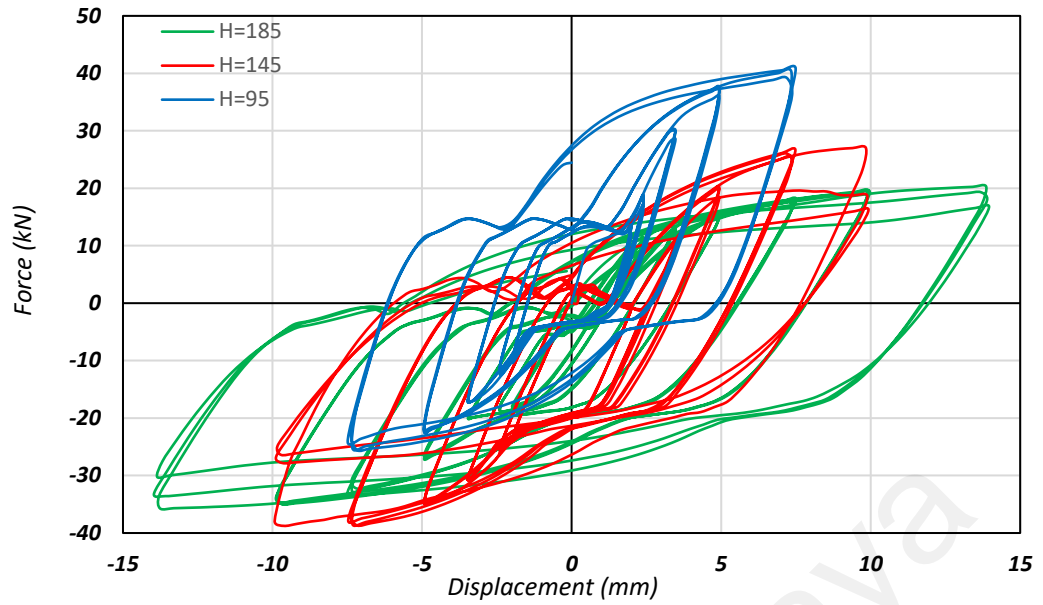


Figure 5.20: Effect of height on the force-displacement hysteretic behavior of HHSDs

Figure 5.21 (a) indicates that when the HHSD height was enlarged, the dissipated energy also increased. The dissipated energy values were 450, 602 and 848.63 kNmm for HHSDs with heights of 95, 145 and 185 mm, respectively. Moreover, it can be seen that the equivalent HHSD viscous damping ratio increased proportionally with incrementing height. The equivalent HHSD viscous damping exhibited linear increments of 53.56% and 32.35% with HHSD height increments of 52.63% and 27.6%. The cumulative displacement versus cumulative dissipated energy in each loading cycle is shown in Figure 5.21 (b). In the elastic zone, the shortest HHSD dissipated a higher amount of energy and tolerated greater displacement. In terms of the plastic zone, the tallest HHSD absorbed more energy and traveled a longer distance till failure. As a result, the HHSD with 185 mm height traveled a distance of 5264 mm and absorbed around 5837 kNmm of energy. Like the other parameters, the HHSD failure mechanism was similar when the HHSD height increased as shown in Figure 5.22. The HHSD cell bonds started to yield and failed as the HHSD reached the ultimate force. As a conclusion, increasing the HHSD height boosted the flexibility and energy absorption capability of the HHSD.

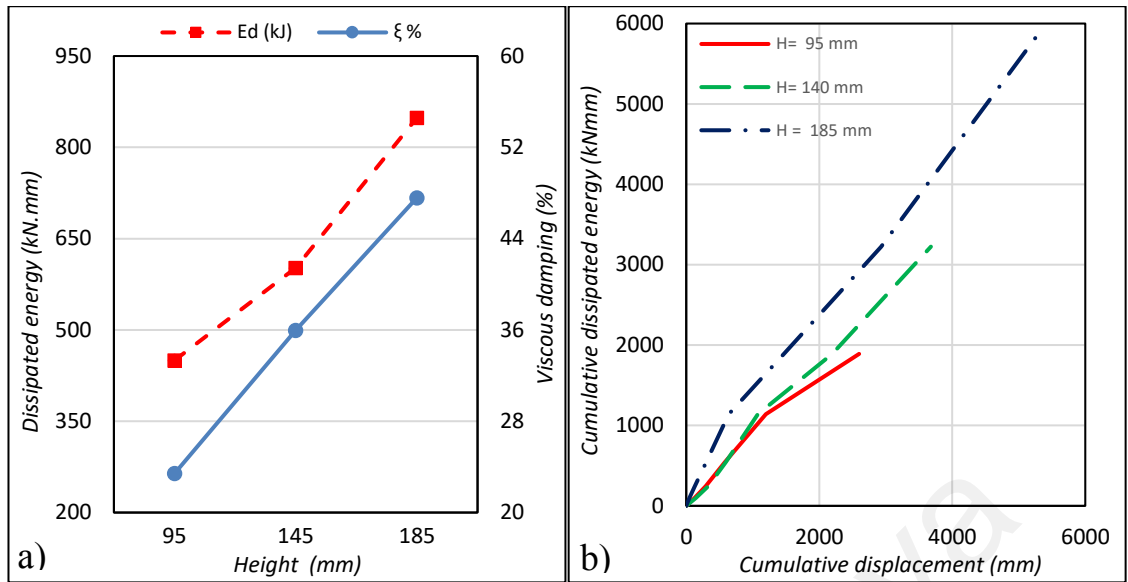


Figure 5.21: a) Effect of height on dissipated energy and viscous damping ratio, b) cumulative energy dissipated by HHSDs

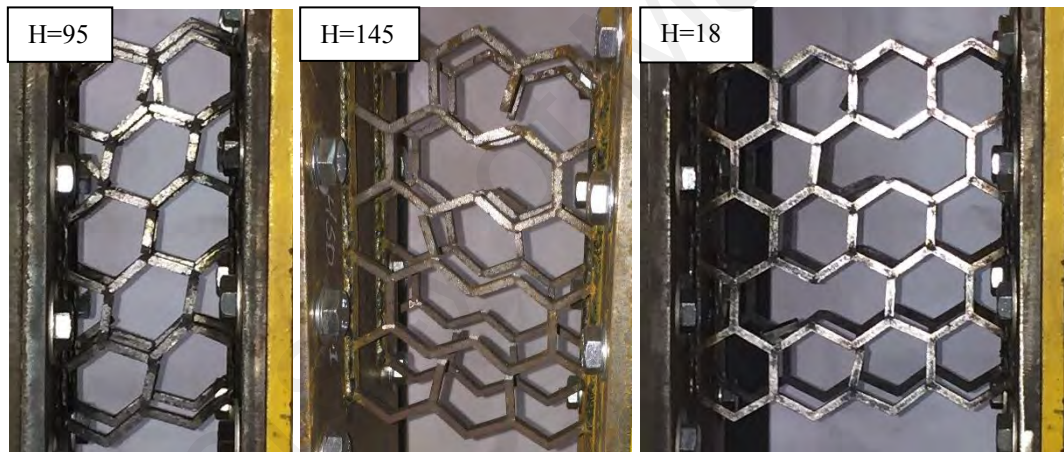


Figure 5.22: HHSD failure mode related to the height parameter

(d) Effect of cell dimensions

This section investigates the effect of changes in the vertical and inclined HHSD cell walls on the performance of HHSDs. The inclined cell wall “ l ” and vertical cell wall “ h ” sizes in the HHSD were decreased and increased. The load-displacement graph for cell wall variation is depicted in Figure 5.23. As the figure indicates, the HHSD with smaller cell walls was significantly stiffer than the benchmark specimen, which failed at the same drift ratio. HHSD No. 8 showed stable hysteretic behavior with negligible Bauschinger and pinching effects. HHSD No. 8 with $l=h=11.5$ mm cell wall dimensions could

withstand up to 115 kN at 10 mm displacement. When the inclined cell wall size was increased to 29.83 mm and the vertical cell wall size was kept constant, the pinching effect reduced notably. However, the Bauschinger effect was still observed in the hysteresis curves. For HHSD No. 9, the maximum load reached 19 kN and it sustained up to 14 mm deformation. It should be noted that because the height of this specimen was increased to 185 mm, greater deformation occurred. On the other hand, the hysteresis loops and ultimate force of this specimen were smaller than HHSD No. 7 with the same height. As the length of the vertical cell walls was increased to 58.09 mm the HHSD load-bearing capacity decreased slightly, but it failed at the same drift ratio of 0.1%. The pinching effect in the hysteresis curves reduced significantly for HHSD No. 10.

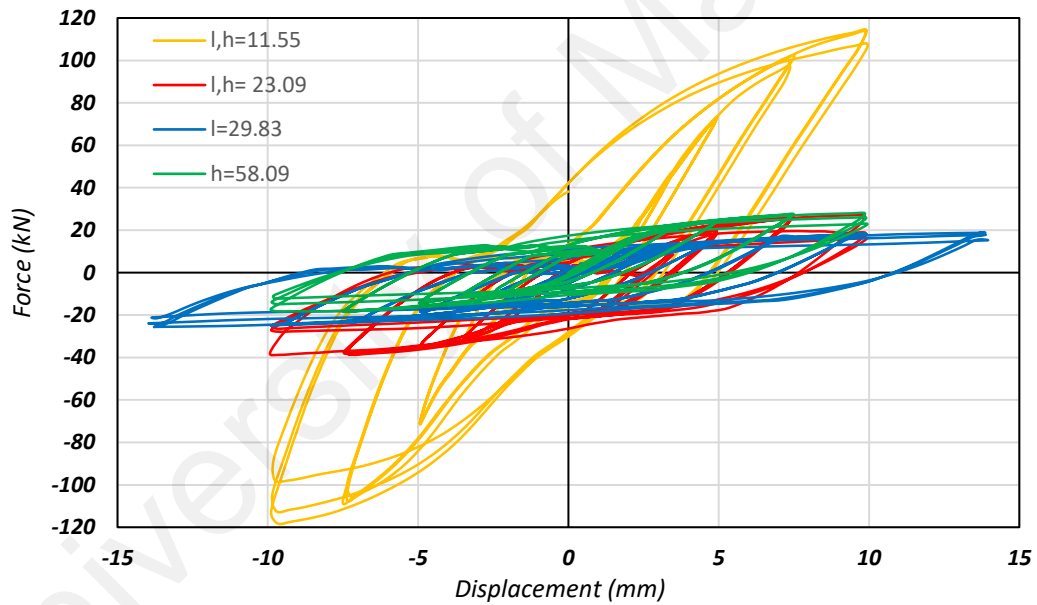


Figure 5.23: Effect of cell size on the force-displacement hysteresis behavior of HHSDs

Figure 5.24 (a) illustrates that when both cell wall dimensions were increased 2 times the dissipated energy decreased almost 2 times as well. Furthermore, as the length of the inclined walls was increased from 23.09 to 29.89 mm, the dissipated energy increased slightly from 602.1 to 665.32 kNmm. Finally, for the specimen with longer vertical cell walls, the dissipated energy dropped to 235.12 kNmm. The equivalent viscous damping

increased 100% when the cell walls were enlarged from 11.5 to 23.09 mm. For HHSD No. 9, a 12.5% increment in equivalent viscous damping was observed compared to the benchmark specimen. A 62.3% drop in equivalent viscous damping was observed as the vertical wall dimensions increased from 23.09 to 58.09 mm. Figure 5.24 (b) demonstrates the cumulative displacement of the HHSDs with respect to cumulative displacement. The specimen with smaller cell walls exhibited greater displacement but dissipated the same amount of energy compared to the benchmark specimen. The specimen with longer inclined walls dissipated quite a larger amount of energy and also exhibited larger displacement. Although this specimen (HHSD No. 8) had the same height as HHSD No. 7, its cumulative dissipated energy and displacement were lesser. Finally, the specimen with longer vertical cell walls was traveled less than the benchmark specimen and yet dissipated the same amount of energy. Figure 5.25 shows the four specimens after reaching ultimate loading. Similar to the previous specimens with different parameters, plastic hinge formation was observed at both ends of the vertical cell walls, which eventually led to crack initiation and failure of the vertical cell walls and the HHSDs.

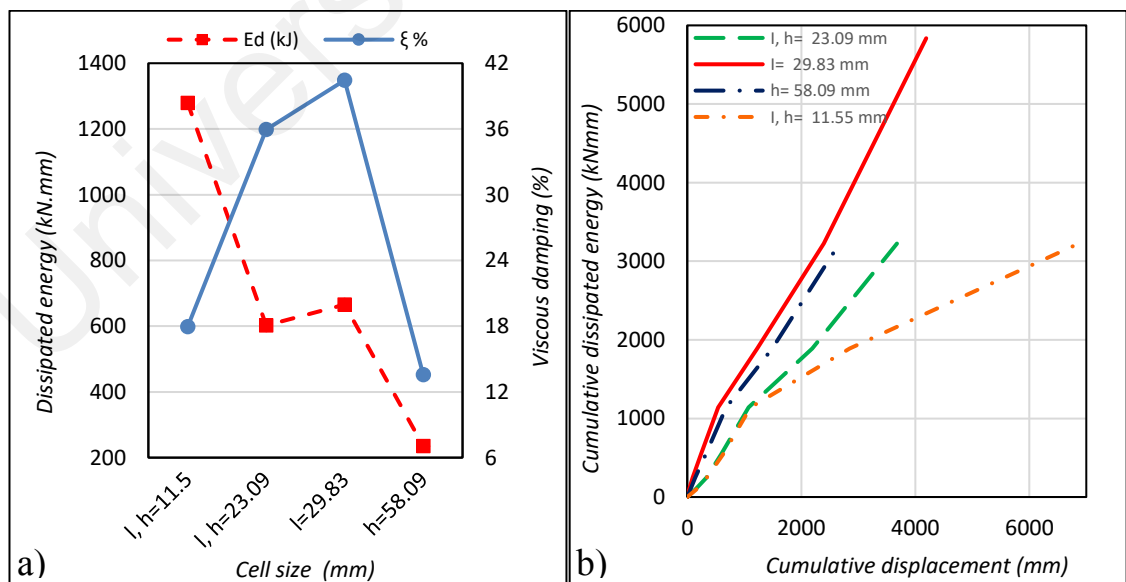


Figure 5.24: a) Effect of cell size on dissipated energy and viscous damping ratio, b)

cumulative energy dissipated by HHSDs

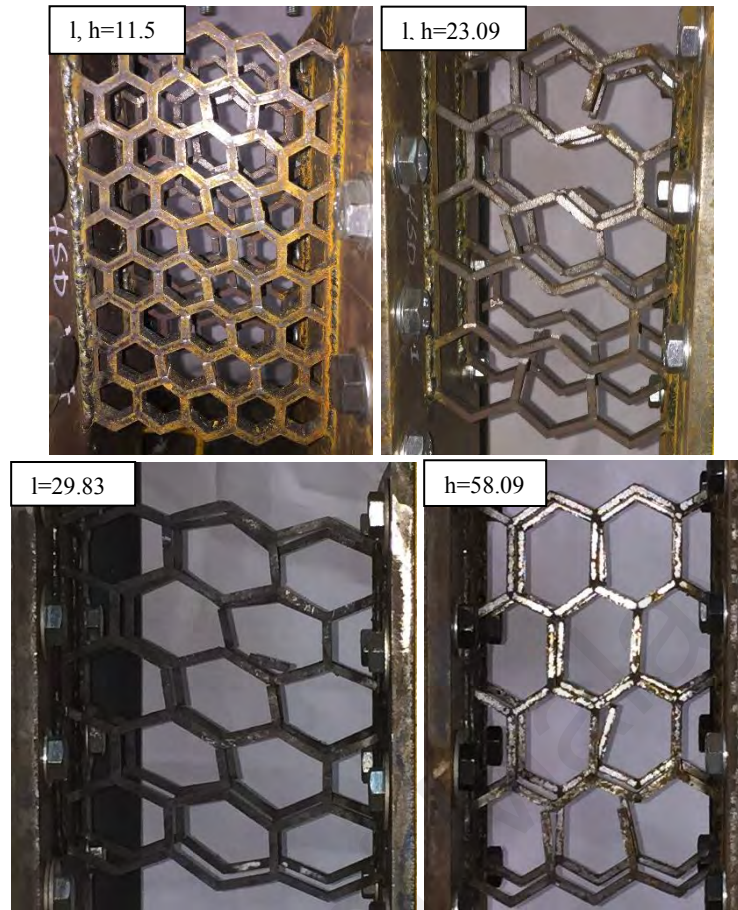


Figure 5.25: HHSD failure mode related to the cell size parameter

(e) Effect of other parameters

This section explains two other possible HHSD alterations. A comparison force-displacement diagram for HHSD No. 11 and 12 and the benchmark specimen is demonstrated in Figure 5.26. HHSD No. 11 had the same thickness, depth and cell size as the benchmark specimen, but its cells were rotated 90 degrees about the X-axis. This alteration helped find a configuration with better energy dissipation capability. According to this figure, HHSD No. 11 had a hysteresis curve similar to the benchmark specimen that showed the pinching effect in the first few cycles. However, the Bauschinger effect was slightly less severe for this specimen. HHSD No. 11 failed at 0.1% drift ratio and 31.27 kN maximum load. As explained before, HHSD No. 1 to 10 had a similar failure mechanism. All these specimens failed due to vertical cell wall failure. Therefore, based on the failure mechanism of other specimens, a combination of hexagonal and rhombic

geometries was used for HHSD No. 12. This geometric combination made this specimen stiffer than the benchmark specimen. However, the maximum displacement at failure was only 7.5 mm. The hysteresis curve for this specimen was stable with less pinching and Bauschinger effects.

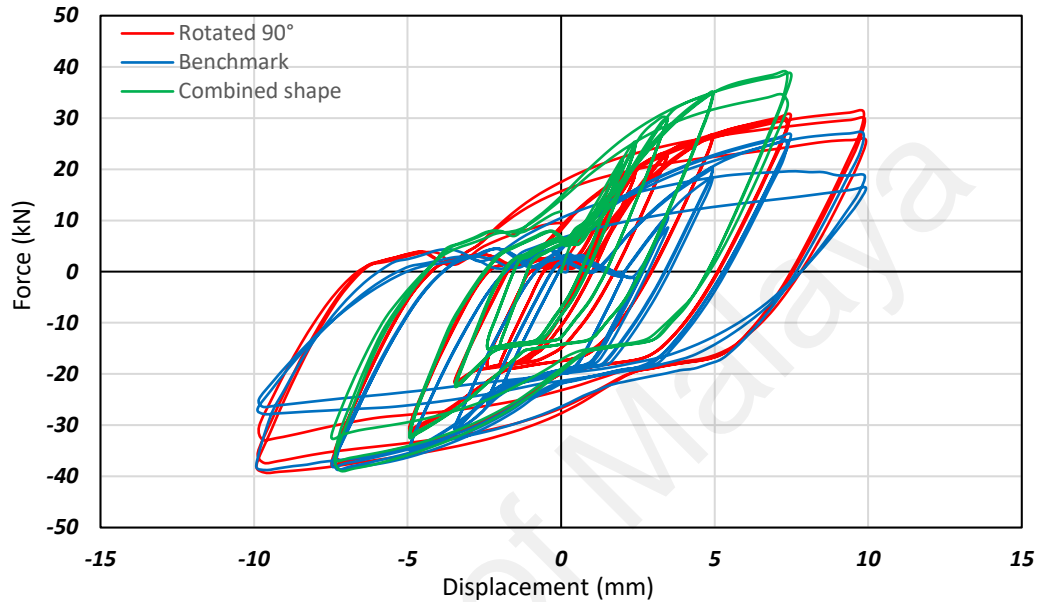


Figure 5.26: Force-displacement hysteresis behavior of HHSD No.1, 11 and 12

When the cells were rotated 90 degrees, the dissipated energy slightly increased from 602.1 kNmm to 669.6 kNmm while the equivalent viscous damping ratio of the HHSD was reduced by 4% (Figure 5.27 (a)). The specimen with combined geometry dissipated 28.3% less energy compared to the benchmark specimen. Moreover, its equivalent damping ratio was 1.5 times smaller than the benchmark specimen. As seen in Figure 5.27 (b), the benchmark specimen traveled a longer distance and dissipated a higher amount of energy than HHSD No. 11 in the elastic zone. Overall, the cumulative displacement of HHSD No. 11 was slightly higher than the benchmark specimen. The specimen with combined geometry traveled a shorter distance and dissipated less cumulative energy compared to HHSD No. 1. The failure mechanisms of these three specimens are compared in Figure 5.28. It can be seen that the vertical cell walls failed in these specimens as well. However, in HHSD No. 11 the vertical cell walls near the

support plates failed rather the middle ones. In HHSD No. 12 the vertical cell walls at the center failed under cyclic loading. It can thus be concluded that the HHSD performance on both axes was similar. However, the hexagonal-rhombic combination increased the stiffness but tolerated comparatively less displacement and was less efficient in absorbing energy under cyclic loading.

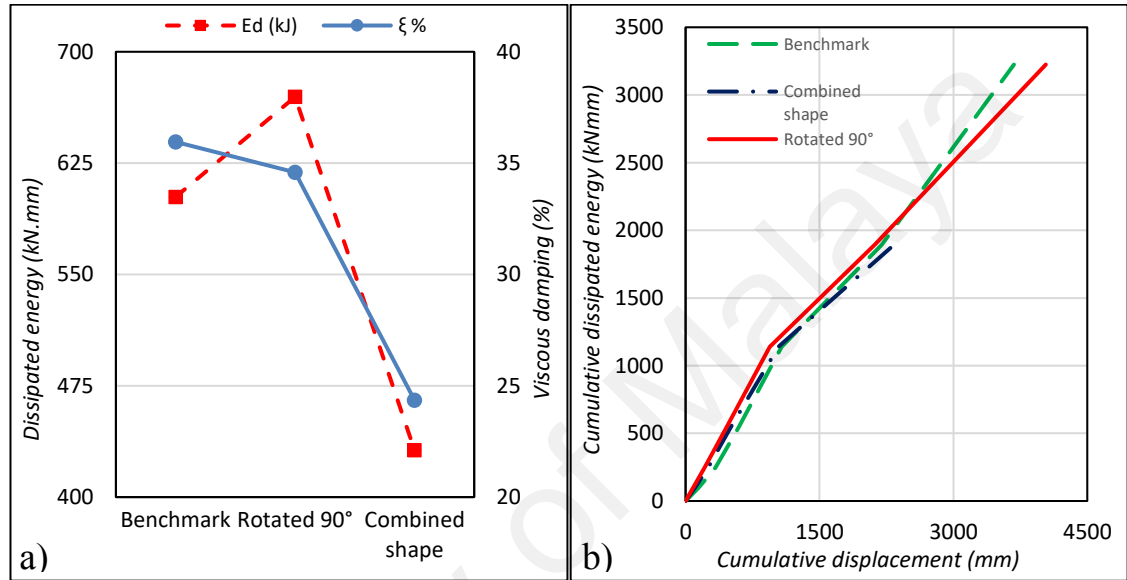


Figure 5.27: a) Dissipated energy and viscous damping ratio, b) cumulative energy dissipated by HHSD No. 1, 11 and 12

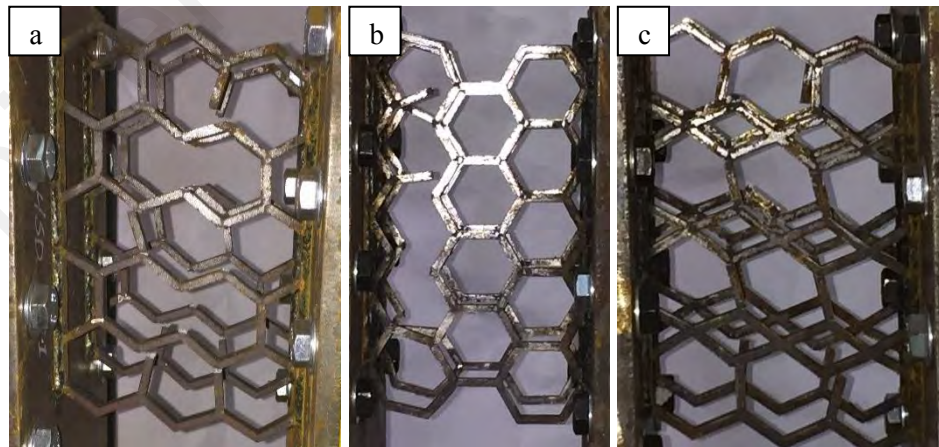


Figure 5.28: Failed specimens at maximum load: a) HHSD No. 1, b) HHSD No. 11 and c) HHSD No. 12

5.4 Numerical analysis

5.4.1 Finite element modeling

Other HHSD behaviors were investigated through Finite Element Analysis (FEA). A Finite Element Model (FEM) was developed and verified with the experimental results. Abaqus (Abaqus Inc., 2014) commercial software was used to perform FEA. Based on the theoretical approach and experiment results, only HHSDs with regular unit cells were considered for FEA. Therefore, HHSD No. 1 to 8 with the same dimensions as illustrated in Table 5.2 were modeled in Abaqus software. The HHSD parts were modeled as 3-dimensional solid elements and meshed as C3D8R type elements, where C is continuum stress/displacement, 3D is 3-dimensional, 8 is the number of nodes in the element and R is the reduced integration procedure. For consistency of the FEA results, the mesh size was the same for all the HHSD models. Figure 5.29 shows the HHSD model and mesh detailing in Abaqus software.

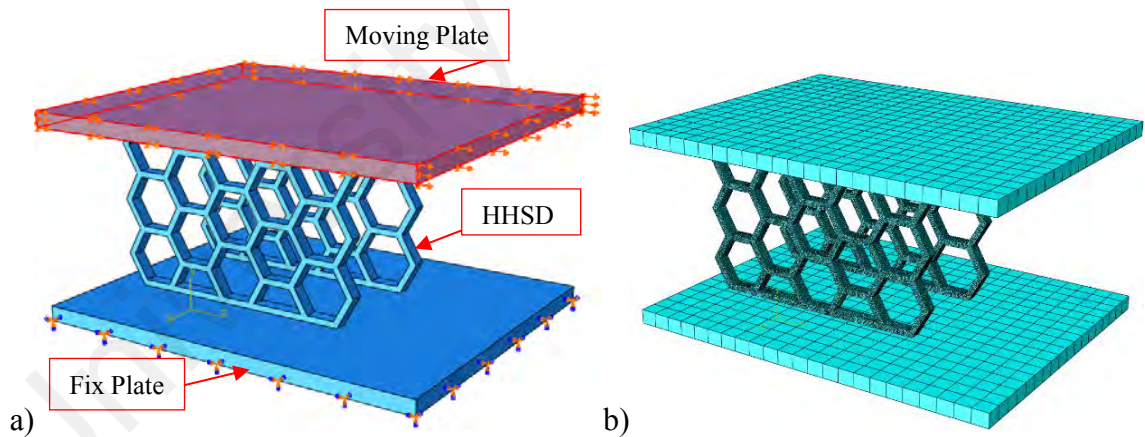


Figure 5.29: a) FE model and b) HHSD mesh detailing in Abaqus software

The material properties were defined in the property module of Abaqus software. Different properties can be defined for different materials based on analysis type and required results. This enables the user to accurately simulate realistic material behavior. The steel material mechanical properties are tabulated in Table 5.5. The kinematic-isotropic hardening of true stress-strain data based on the coupon test results were adopted

for steel material. A ductile damage model is used for ductile materials like steel and is defined by the relationship between fracture strain and stress triaxiality as follows:

$$\eta = \frac{\sigma_m}{\bar{\sigma}} \quad (5-18)$$

Where σ_m is the mean stress and $\bar{\sigma}$ is the equivalent stress, which are:

$$\sigma_m = \frac{1}{3}(\sigma_1 + \sigma_2 + \sigma_3) \quad (5-19)$$

$$\bar{\sigma} = \sqrt{\frac{1}{2}[(\sigma_1 - \sigma_2)^2 + (\sigma_1 - \sigma_3)^2 + (\sigma_2 - \sigma_3)^2]} \quad (5-20)$$

The ductile damage parameters were determined from the coupon test results. The use of damage evolution reduced the mesh dependency in Abaqus. Displacement-based damage evolution is used for steel materials. The damage parameter is zero and starts to increase with strain increment. Once the damage parameter of an element reaches one, it is considered totally damaged and the element will be eliminated from the model. The FEA thus continues without the damaged elements.

Table 5.5: Material properties used in FE modeling

Parameter	Value
Mass density (kg/m ³)	7800
Young's modules (MPa)	200
Poisson ratio	0.3

In the experiment, one HHSD anchorage plate was fixed and another anchorage plate was subjected to cyclic loading. Similarly, in the FE model, the bottom plate was fixed while the top plate was subjected to cyclic displacement in the U1 direction. The same loading protocol as in the experiment test was used in FE modeling (Figure 5.7 (b)). Figure 5.29 (a) shows the boundary condition and loading position employed in FE modeling.

5.4.2 FEA results

According to the experimental results, the maximum positive and negative ultimate strength values of the HHSD specimens were different. This may be due to uncertainties, such as bolt slippage and actuator head rotation during pull loading. To verify the numerical model with the experimental results, the maximum positive and negative force differences were adjusted for the experimental results. Figure 5.30 shows superimposed force-displacement hysteresis curves from the experiment and FEA. It is clear in this figure that there is a good agreement between the FEA and experimental hysteresis curves. The ultimate positive and negative force values of the 8 specimens in FEA also reached the same drift ratio as the experiment. The key results for yield displacement (Δ_y), yield force (P_y), elastic stiffness (K_d), maximum and minimum ultimate displacement (Δ_u), maximum and minimum ultimate force (P_u), plastic stiffness (K_p), ductility (μ) and damping ratio (ζ) from the FEA hysteresis curves are summarized in Table 5.6. It is noted that all HHSD models yielded at low displacement. The HHSD yield displacement was constant with depth (D) changes. The yield displacement of the damper decreased with increments in thickness (T). On the other hand, the yield displacement increased with increments in height and cell wall dimensions. The elastic stiffness of the dampers increased with incrementing depth and thickness, while with increasing height and cell wall dimensions the elastic stiffness decreased. When the HHSD depth, thickness and cell wall dimensions increased, the plastic stiffness also increased. On the contrary, the elastic stiffness decreased as the HHSD height increased. The HHSD ductility ranged from 8 to 28. The specimen with smaller cell walls (HHSD No. 8) had higher ductility. However, the ductility increased significantly with increasing thickness.

Table 5.6: FEA result summary

HHSD No.	Δ_y	P_y	K_d	$\Delta_{u,max}$	$P_{u,max}$	$\Delta_{u,min}$	$P_{u,min}$	K_p	μ	E_d (kJ)	E_s (kJ)	ξ %
No.1	1.19	19.62	16.5	9.97	30.7	-9.80	-31.2	3.1	8.4	705.6	153.1	36.7
No.2	1.19	15.57	13.1	9.94	24.6	-9.61	-24.5	2.5	8.4	568.7	122.1	37.1
No.3	1.19	23.71	20.0	13.92	37.9	-13.99	-38.5	3.2	11.7	1208.6	263.9	36.5
No.4	1.00	48.60	48.6	9.60	71.0	-9.30	-72.7	7.4	9.6	1596.1	340.9	37.3
No.5	0.50	69.70	139.4	13.99	116.5	-13.79	-115.0	8.3	28.0	4668.1	814.9	45.6
No.6	0.63	18.52	29.6	7.11	34.3	-7.28	-34.0	4.8	11.4	560.8	121.9	36.6
No.7	1.75	19.25	11.0	13.93	29.3	-13.66	-29.2	2.1	8.0	933.4	203.9	36.5
No.8	0.63	70.89	113.4	9.93	116.4	-9.72	-114.8	11.7	15.9	2766.3	577.9	38.1

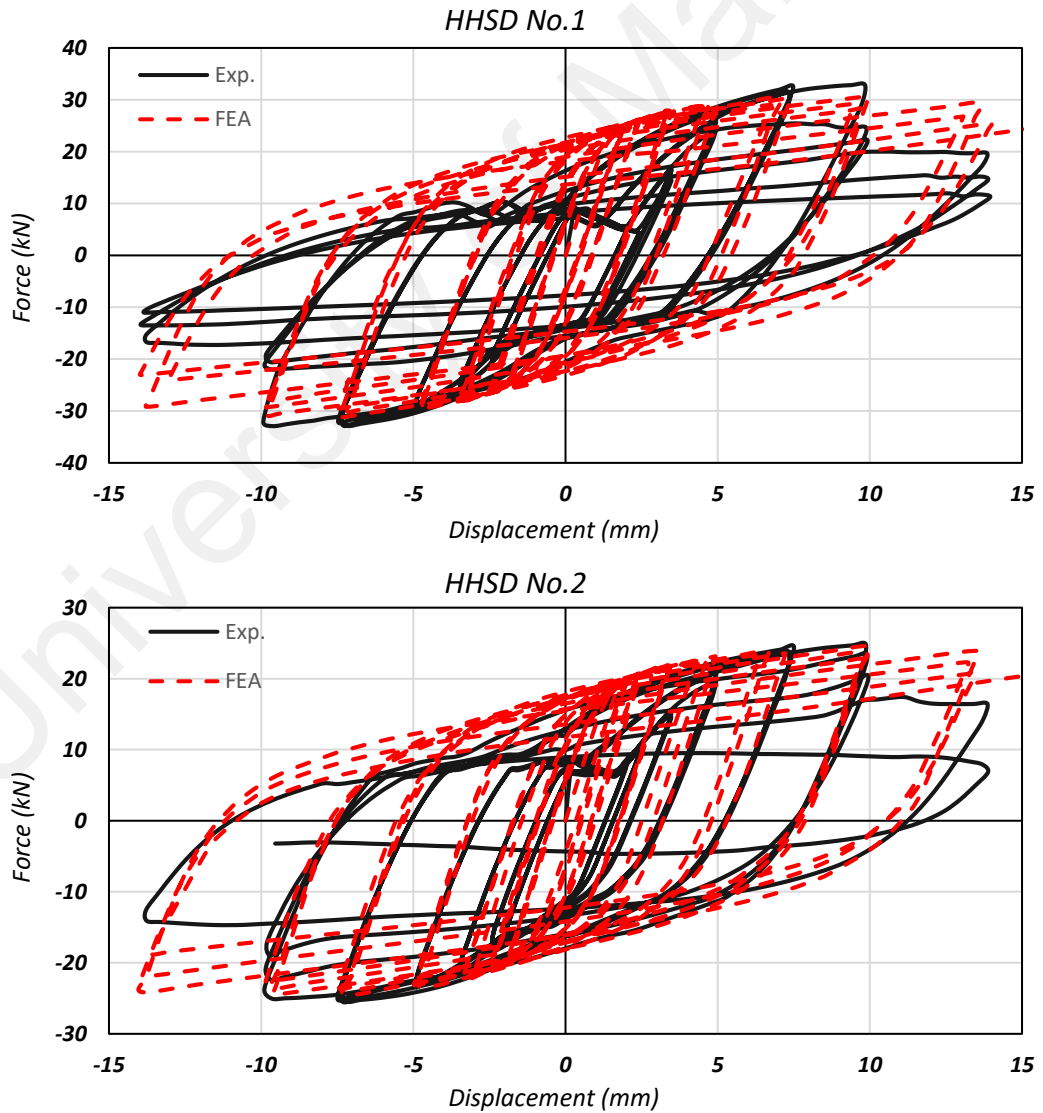


Figure 5.30: Experimental and FEA result comparison

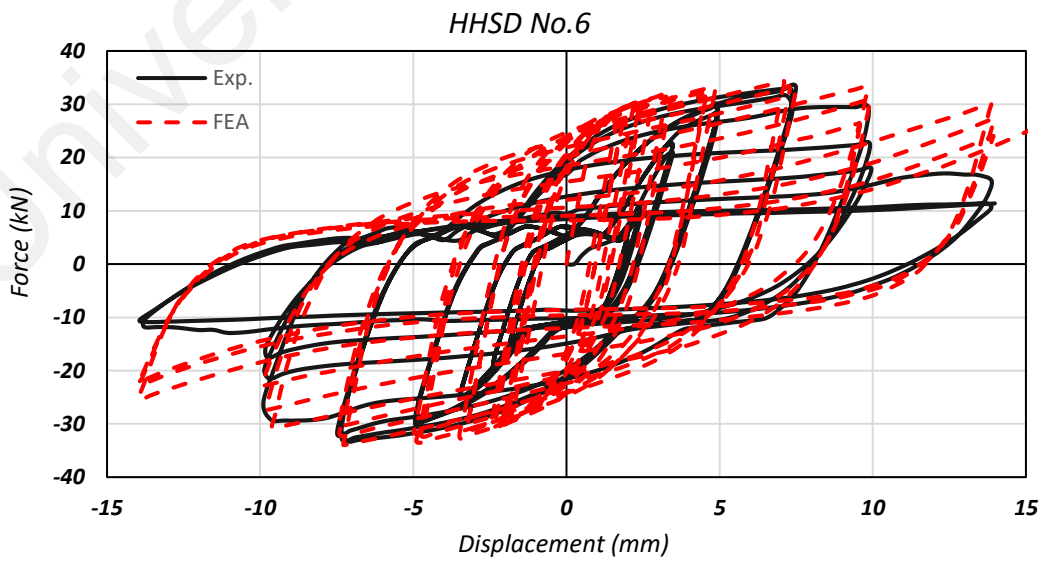
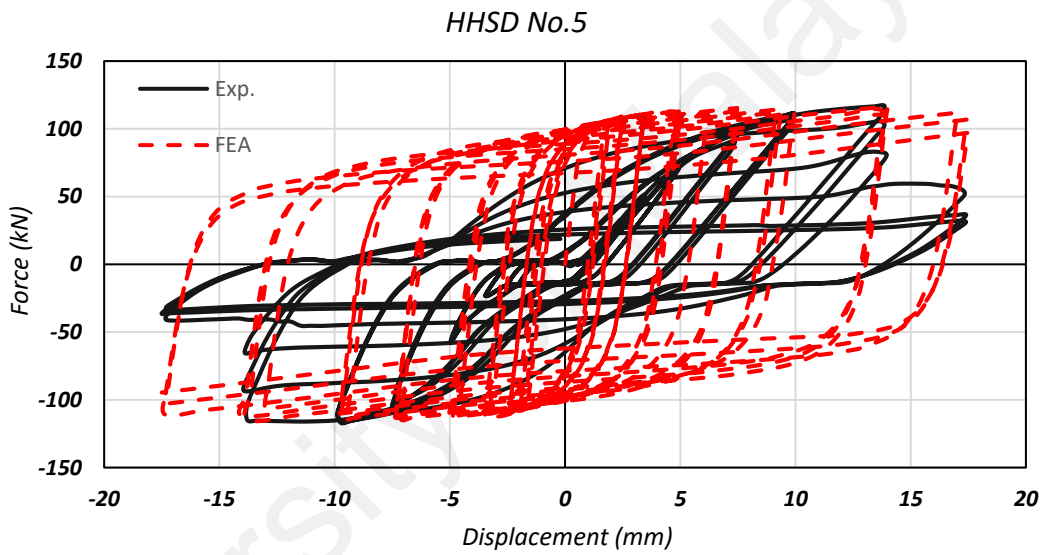
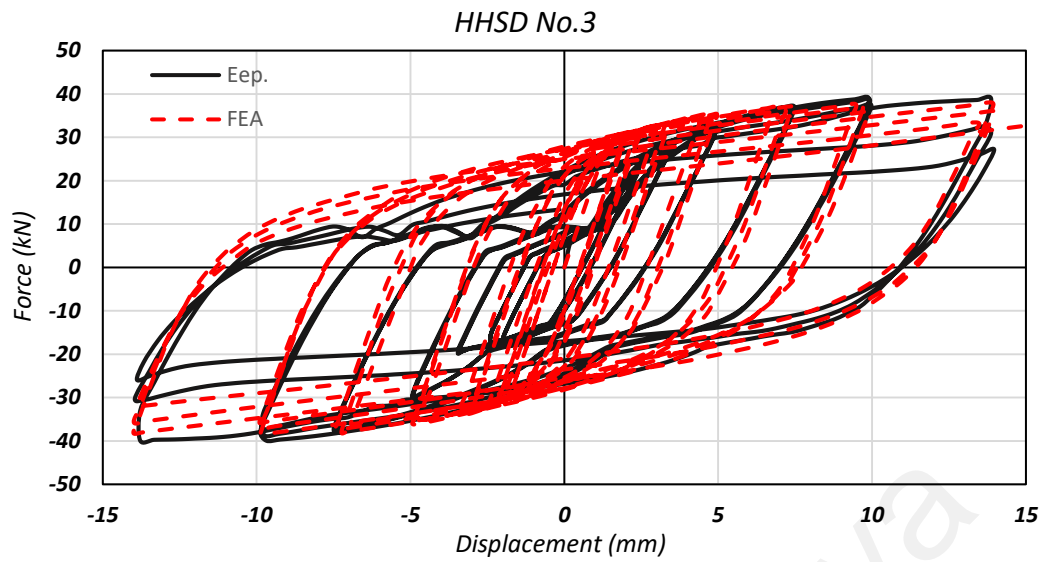


Figure 5.30, Continued

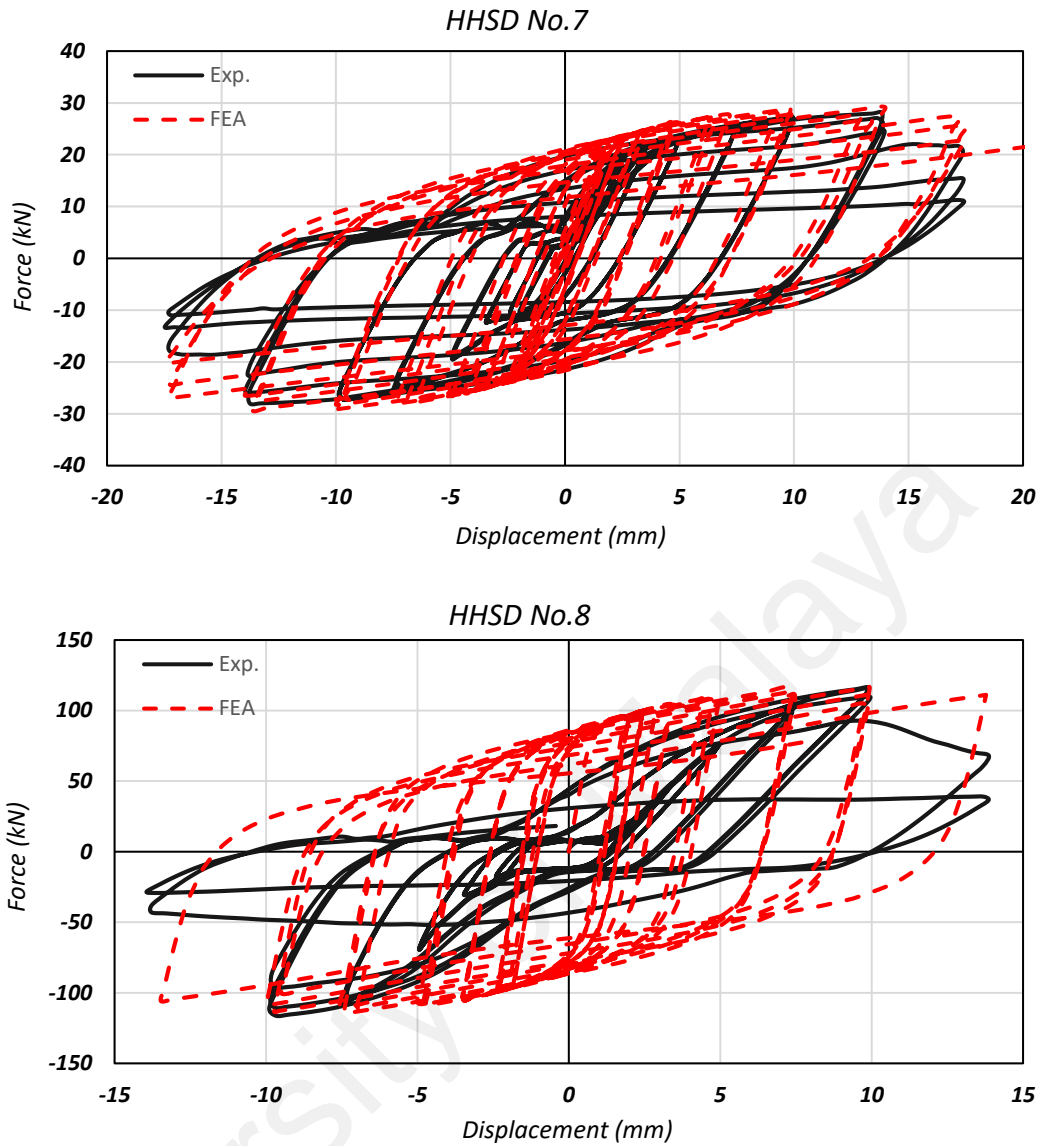


Figure 5.30, Continued

Figure 5.31 illustrates the relationship between the equivalent damping and normalized stiffness. This figure and Table 5.6 indicate that the HHSD damping ratio ranged from 36.5% to 45.6%. Once again, the thicker specimen had the highest damping ratio. It can be concluded that although all parameters directly influenced ductility and damping ratio, the governing parameter was HHSD thickness.

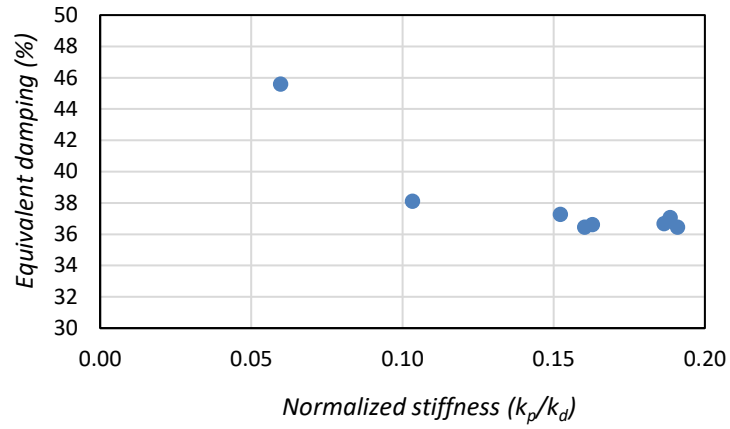


Figure 5.31: Equivalent damping ratio vs normalized stiffness for the HHSD models

The failure mechanism identified with FEA was similar to the experimental results. The stress concentration started at the ends of the vertical walls under cyclic load. Once the specimen reached ultimate strength, the vertical walls failed at the ends as shown in Figure 5.32.

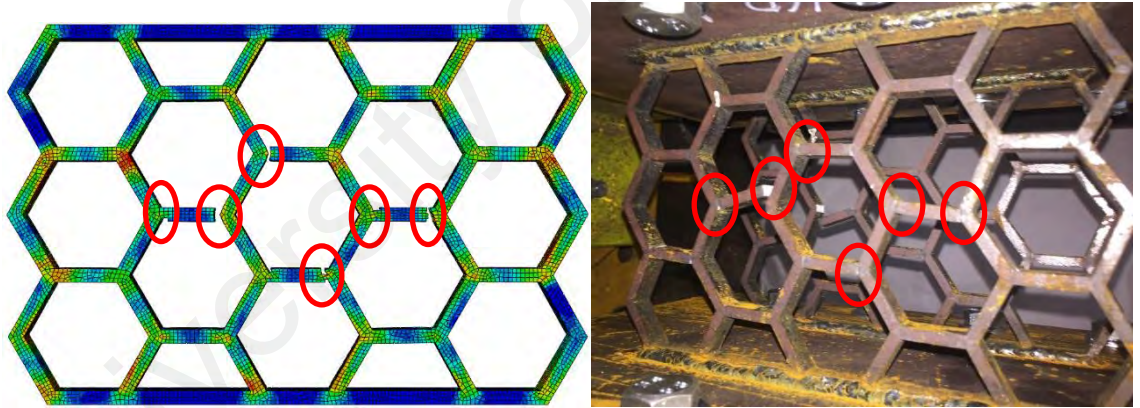


Figure 5.32: Comparison of the failure mechanism in HHSD No. 1 according to FEA and the experiment

The accuracy of the theoretical approach was further checked by comparing the yield displacement and yield force computed by Equations. 5-8 and 5-5 with the FEA results. Table 5.7 provides a comparison of the yield displacement and force obtained with these equations and FEA. The ratio of theoretical to FEA yield displacement was close to unity for most specimens. The theoretical yield force was slightly overestimated compared to FEA. It was also found that the theoretical elastic stiffness was slightly underestimated.

Table 5.7: Comparison of theoretical values with FEA results (units: mm, kN)

Specimen	$\Delta_{y,t}$	$\Delta_{y,FEA}$	Ratio	$P_{y,t}$	$P_{y,FEA}$	Ratio	$K_{d,t}$	$K_{d,FEA}$	Ratio
No.	$\Delta_{y,t}/\Delta_{y,FEA}$			$P_{y,t}/P_{y,FEA}$			$K_{d,t}/K_{d,FEA}$		
HHSD No.1	1.11	1.19	0.94	24.33	19.62	1.24	21.84	16.52	1.32
HHSD No.2	1.11	1.19	0.94	19.47	15.57	1.25	17.47	13.11	0.75
HHSD No.3	1.11	1.19	0.94	29.20	23.71	1.23	26.21	19.96	0.76
HHSD No.4	0.74	1.00	0.74	51.18	48.60	1.05	68.89	48.60	0.71
HHSD No.5	0.42	0.50	0.84	78.91	69.70	1.13	187.09	139.40	0.75
HHSD No.6	0.67	0.63	1.07	24.33	18.52	1.31	36.40	29.63	0.81
HHSD No.7	1.56	1.75	0.89	24.33	19.25	1.26	15.60	11.00	0.71
HHSD No.8	0.50	0.63	0.80	63.47	70.89	0.90	126.46	113.43	0.90

So far, the proposed HHSD exhibited good hysteretic performance under in-plane loading. In this section, the out-of-plane behavior of the HHSD is compared with its in-plane behavior. Figure 5.33 shows the hysteretic behavior of the benchmark specimen subjected to in-plane and out-of-plane loading. The loading protocol was the same for both directions. According to the figure, the HHSD was more flexible and had less bearing capacity when subjected to out-of-plane loading. The HHSD reached 14.6 kN at 14 mm displacement, which is almost half of the in-plane loading capacity, and showed no sign of failure. Another significant observation about the HHSD in this direction is that the force-displacement of the HHSD was linear in the first few loading cycles (yield started at 3 mm displacement). The HHSD was also able to dissipate energy when subjected to out-of-plane loading, but it dissipated less energy compared to its in-plane dissipation capacity.

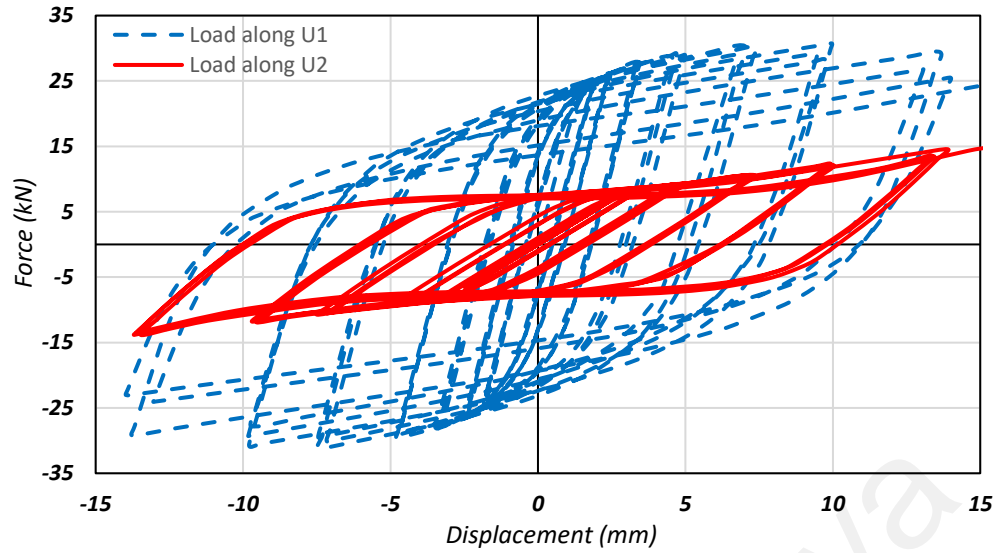


Figure 5.33: In-plane and out-of-plane hysteretic behavior of HHSDs

5.5 HHSD characteristic formula

Based on the results obtained from the experiment and FEA of the parametric study, the key structural characteristic formula of the HHSD is developed in this section. With the theoretical approach, the yield force and yield displacement equations for the HHSD were derived. Consequently, the theoretical elastic stiffness can also be computed. The ultimate HHSD force is calculated from the yield force according to the equation below:

$$P_U = 1.6381 P_y - 0.9428 \quad (5-21)$$

The HHSD plastic stiffness can be computed from the elastic stiffness with the following equation:

$$k_p = 0.0465 k_d + 2.6364 \quad (5-22)$$

Based on parameters such as elastic and plastic stiffness, the equivalent damping ratio of the HHSD can be calculated with the following equation:

$$\xi = 847.65 \left(\frac{k_p}{k_d} \right)^2 - 274.72 \left(\frac{k_p}{k_d} \right) + 58.584 \quad (5-23)$$

5.6 Conclusions

Based on the experimental and FEA results of HHSD, the following conclusions can be drawn:

- The HHSD load-displacement hysteresis curves were uniform, symmetric and stable. The HHSD exhibited low yield displacement and its ultimate strength was 1.6 times greater than its yield strength due to its shape. In addition, The HHSD cumulative displacement was relatively high.
- The HHSD tolerated large deformation and promoted a good range of ductility. The damper was able to dissipate a large amount of energy. The equivalent viscous damping ratio of the HHSD was in the 36%-46% range, which demonstrates the efficiency of the HHSD in absorbing induced energy.
- The HHSD failure mechanism is such how, after it reached its ultimate strength, its stiffness gradually decrease. This feature of HHSD helps in reducing the damages to the primary structure due to aftershock events.
- All studied parameters directly influenced HHSD performance; however, HHSD thickness was the dominant parameter. The characteristic formulas derived can predict HHSD behavior, which is useful for damper implementation in any commercial structural software.
- It is worth mentioning that the HHSD has low initial cost, is lightweight, acts as a fuse for primary structures and can be easily replaced after earthquake events. The HHSD has several design parameters that facilitate adaption to different design criteria imposed by the mechanical and geometrical requirements of new and/or existing structures in which it is to be implemented.

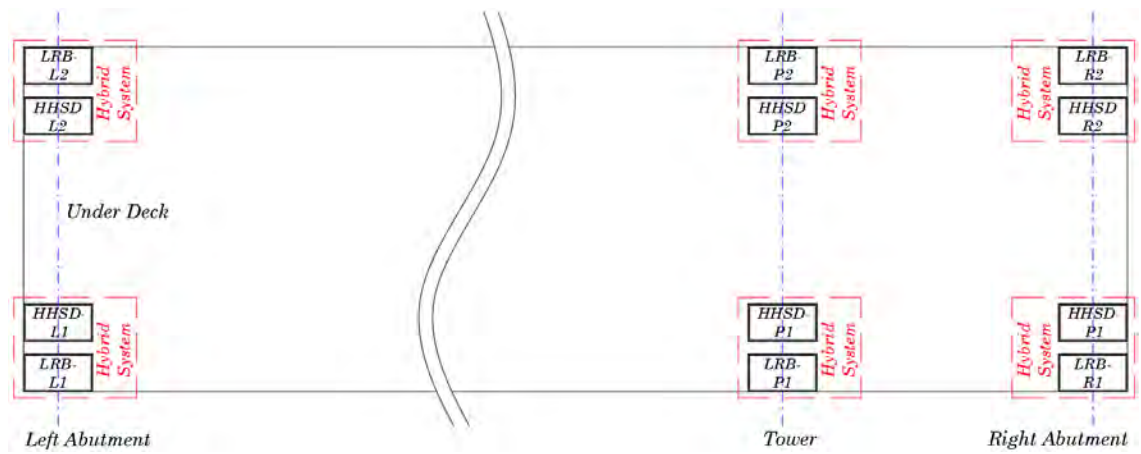
CHAPTER 6: SEISMIC RESPONSE OF THE CABLE-STAYED BRIDGE EQUIPPED WITH HYBRID PASSIVE CONTROL SYSTEMS

6.1 Introduction

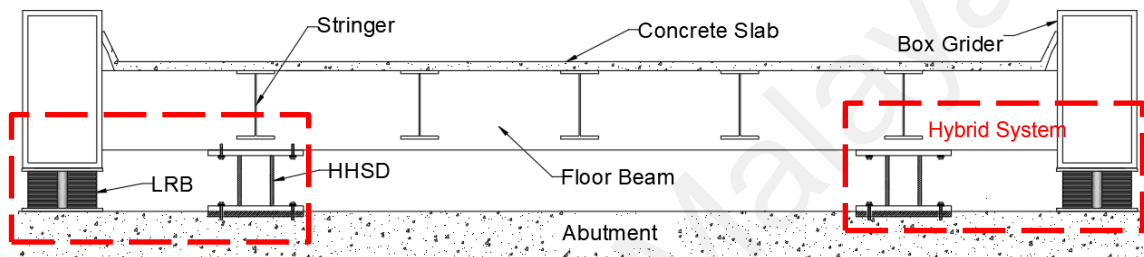
This chapter presents the seismic response of the cable-stayed bridge with hybrid passive control systems. An investigation of all major earthquakes reveals that earthquake-induced pounding is one of the main causes of damage or catastrophic failure in colliding structures. Earthquake-induced pounding occurs when the separation gap between adjacent structures is smaller than the inelastic deformation of the structures. The prediction of uncertainties involved in the occurrence of earthquakes and aftershock events makes the study of the earthquake-induced pounding effect on structures in earthquake-prone areas obligatory (Ghaedi & Ibrahim, 2017). Earthquake-induced pounding damage to structures was reported in the 1971 San Fernando earthquake (Wood & Jennings, 1971), the 1989 Loma Prieta earthquake (Kasai & Maison, 1997), the 1999 Chi-Chi earthquake (Uzarski & Arnold, 2001) and the 2011 Christchurch earthquake (Cole et al., 2011). Earthquake-induced pounding occurs in bridges when the seismic displacement exceeds the gap of the adjacent spans or the bridge's clear distance from the abutments (Bruneau, 1998; Li et al., 2013; Li & Chouw, 2014). Pounding damage was observed in the Chi-Lu cable-stayed bridge during the 1999 Chi-Chi earthquake (Chadwell, 2003). Pounding between the tower and girder of the Yokohama-Bay cable-stayed bridge was reported during the 2011 Tohoku earthquake (Siringoringo et al., 2013). In addition, inspectors reported pounding of the Shipshaw Bridge with abutments in the longitudinal direction due to the Saguenay earthquake in 1988. It is worth mentioning that longitudinal vibration is the dominating mode in some of cable-stayed bridges, which increases the likelihood of earthquake-induced pounding phenomenon on such structures.

Furthermore, the seismic analysis of the isolated bridge in previous chapters indicates that the isolation system increased the longitudinal seismic displacement of the bridge. In other words, after isolation system implementation, the longitudinal flexibility of the bridge increased. Therefore, the likelihood of earthquake-pounding phenomenon occurrence in the fully isolated bridge is higher than the non-isolated bridge.

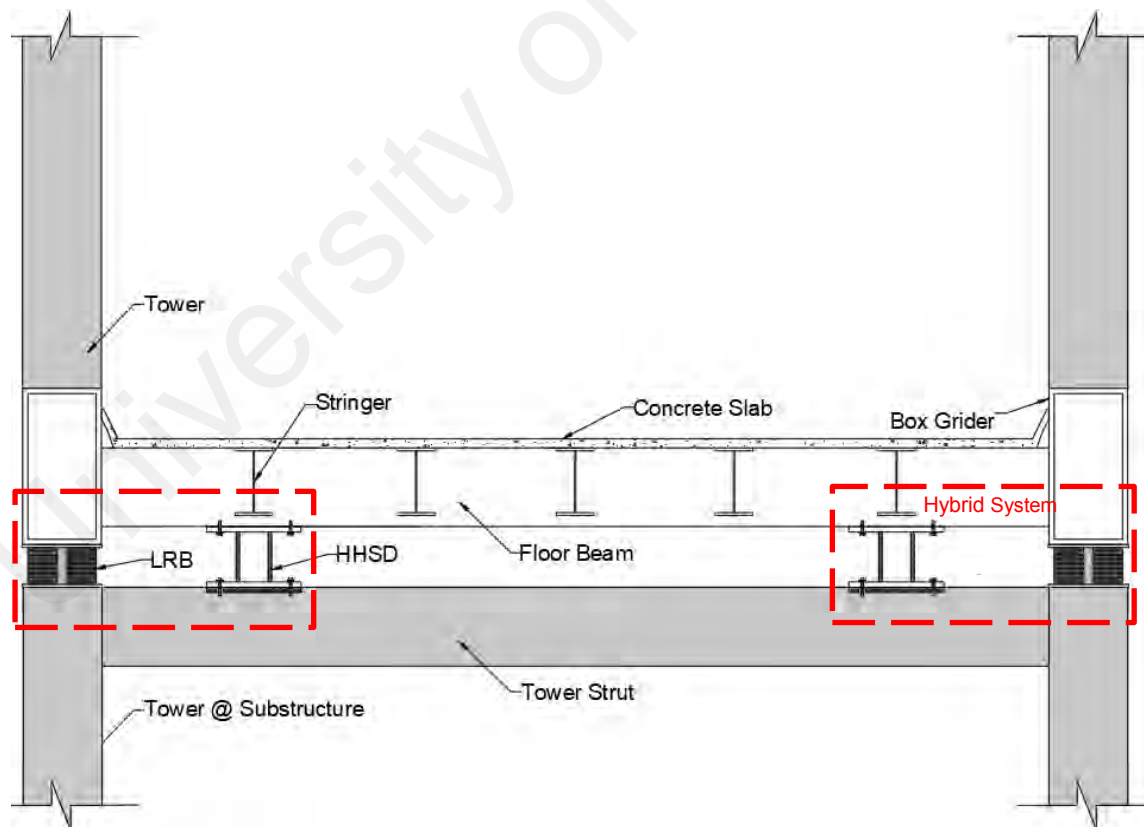
To tackle this problem, the HHSD is proposed to be installed in parallel with a seismic isolation system in the longitudinal direction of the bridge as shown in Figure 6.1. It is worth noting that cable-stayed bridges have an inherent self-centering capability due to the restoring forces from the cables; therefore, implementing metallic dampers without self-centering capability has insignificant influence on their serviceability after earthquake events. The HHSD has a good range of ductility and high energy dissipation capability, as described in Chapter 5. At the abutments, HHSDs are installed between the floor beam and abutments, while at the tower, HHSDs are placed between the floor beam and lower strut of the tower. The top and bottom anchorage plates of HHSDs are installed with bolts to the primary structure. The HHSDs are placed at a close distance from the LRB, such that the dead load from the superstructure does not transfer to the HHSDs. In other words, the HHSDs are placed near the supports where the vertical deflection of the bridge is almost negligible. As shown in Figure 6.1, in the combination of these two passive control systems (hybrid passive control) the seismic isolator mostly contributes in reducing the seismic demand on the superstructure, while the metallic damper helps control the excessive seismic displacement of the bridge and mitigates the earthquake-induced pounding. To evaluate the efficiency of the proposed hybrid control system on the seismic performance of the bridge, a comparative study is done for four cases: 1) non-isolated bridge, 2) isolated bridge, 3) bridge with HHSDs and 4) bridge retrofitted with hybrid devices.



a) Plan view



b) At bridge ends



c) At the deck-tower connection

Figure 6.1: Schematic configuration of the passive hybrid control system in the cable-stayed bridge

6.2 Methodology

The methodology explained in Chapter 3 was used to design the seismic isolation system for the bridge. The thermal movement of the bridge and stiffness of the abutments are calculated in this section to account for the pounding effect in the fully isolated bridge. The HHSD design procedure for the isolated bridge is also proposed and explained briefly.

6.2.1 Thermal movement of the bridge

According to article 3.12 in LRFD (AASHTO, 2012), the design thermal movement of a bridge is dependent on the extreme temperature at the bridge site and is determined by:

$$\Delta_T = \alpha \times L(T_{Max} - T_{Min}) \quad (6-1)$$

Where L is the span length, α is the coefficient of thermal expansion of the steel sections, and T_{Max} and T_{Min} are the average maximum and minimum designed temperatures for the bridge site. From Equation 6-1, the minimum required thermal movement of the bridge at the expansion joints is calculated as 0.030 m.

6.2.2 Abutment stiffness

According to Caltrans (2014), the longitudinal stiffness of the abutments can be obtained with the following equation:

$$k = 47000 \times W_{abut.} \times h \quad (6-2)$$

Where $W_{abut.}$ is the width of the abutment and h is the seating height of the abutment.

6.2.3 HHSD design procedure

The HHSD constitutive formula is derived in Chapter 5. The yield displacement, strength and ultimate strength of the dampers are functions of the HHSD material properties and dimensions. To design the HHSD, three constraints must be considered: (i)

the HHSD height is limited to the space between the floor beam and abutment or tower strut, (ii) the HHSD target displacement is obtained through a simplified analysis of the base-isolated bridge and (iii) the HHSD yield strength should be larger than the LRB yield strength, which leads to a decrease in bridge flexibility. The primary goal of the hybrid system is to minimize the longitudinal seismic displacement of the bridge. Therefore, the simplified or direct displacement method is used for isolated bridges to find the target displacement (Golzan et al., 2016). The isolated bridge has a stiffness of K_1 and effective damping of ζ_{eq1} and the HHSD has a stiffness of K_2 and effective damping of ζ_{eq2} . The HHSD provides additional stiffness and damping to the isolated bridge, which leads to a decrease in the natural period of the bridge and hence, the base shear reduction may be insignificant. It should be noted that the HHSD should not be too stiff at the tower section, as it may increase the seismic demand on the tower section in the substructure. Based on the given explanation, the procedure of designing a metallic damper for isolated bridges is as follows:

Step 1: Set a target displacement for the isolated bridge and find the corresponding effective stiffness and damping ratio values for the dampers from a simplified analysis of the isolated bridge (Buckle et al., 2011).

Step 2: Set the total height (H) of the HHSD as the clear spacing between the floor beam and abutments and tower struts. Assume a suitable value for the horizontal HHSD length (L).

Step 3: Determine the hexagonal numbers in the horizontal and vertical directions based on H and L .

Step 4: Design the HHSD based on depth and thickness. Subsequently, calculate the bridge displacement and verify it with the initial target displacement. This may be achieved through an iterative process in a spreadsheet to find the optimum values.

The results from the previous chapter indicate that the governing factors for higher ductility ratio are depth (D) and thickness (T). Therefore, the HHSD is designed based on variations in these two parameters. The HHSD design flow chart for the isolated bridge is illustrated in Figure 6.2.

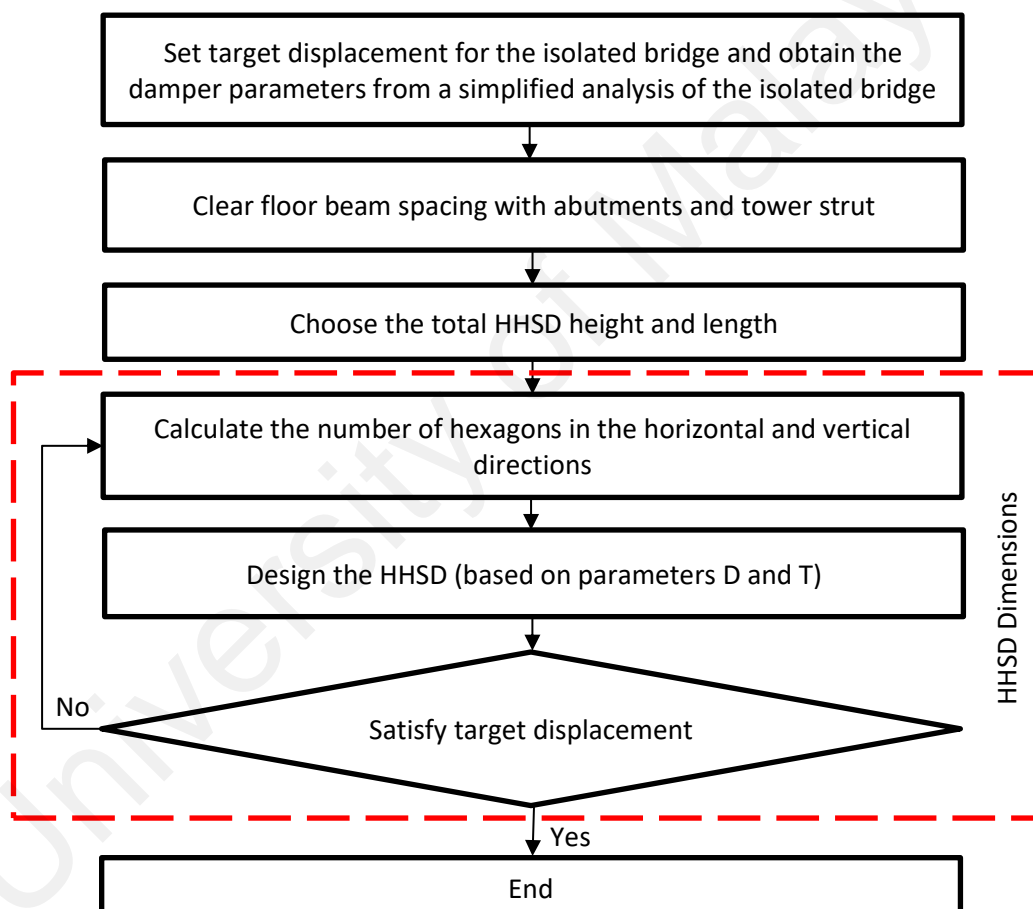


Figure 6.2: HHSD design flow chart for isolated cable-stayed bridges

The HHSD dimensions are obtained based on the explained HHSD design procedure for the fully isolated cable-stayed bridge. The details of the HHSD designed for the isolated bridge are outlined in Table 6.1. It is assumed that two HHSDs are implemented at each location in the bridge near the LRBs (Figure 6.1). Furthermore, the designed

bilinear force-displacement relationship of the HHSDs at different locations of the cable-stayed bridge is shown in Figure 6.3.

Table 6.1: Designed HHSD dimensions for the isolated cable-stayed bridge

HHSD location in the bridge	Height	Length	Depth	Thickness	Cell dimensions		n_x	n_y
	H (mm)	L (mm)	D (mm)	T (mm)	l (mm)	h (mm)		
At left end	285	334	12	10	23.09	23.09	7	5.5
At pylon	272	190	10	8	23.09	23.09	4	5.5
At right end	279	239	10	9	23.09	23.09	5	5.5

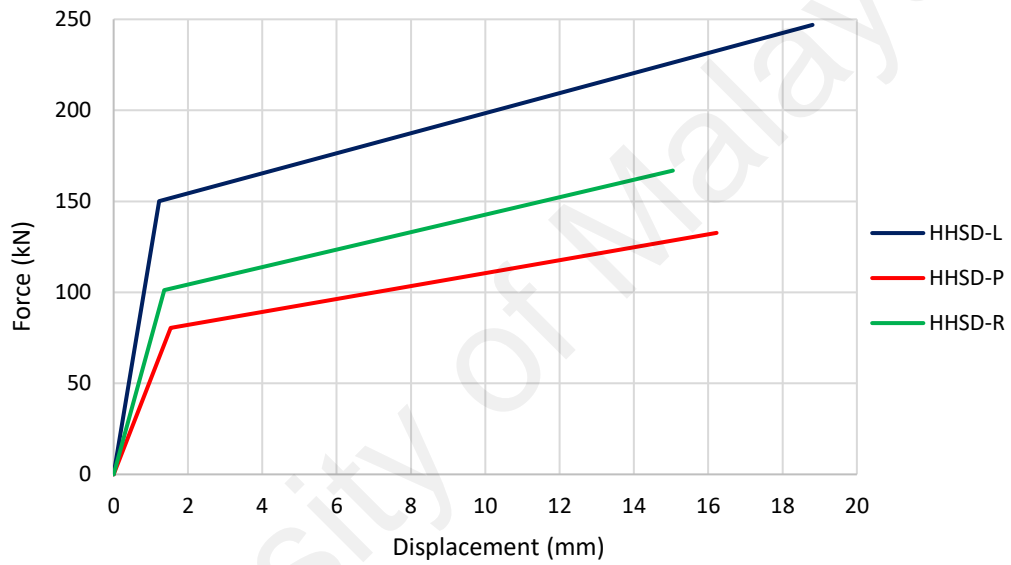


Figure 6.3: Bilinear force-displacement curves of the designed HHSDs

6.2.4 Constitutive model

The total effective stiffness of an isolated bridge equipped with dampers is a combination of the effective stiffness of the damper and isolator, which may be placed in parallel or series. In this study, the isolator and damper are placed in parallel, as shown in Figure 6.4. The combined stiffness of the metallic damper (K_d) and isolator (K_{isol}) in a parallel system gives the stiffness of the hybrid passive system:

$$K_{hybrid} = K_{isol} + K_d \quad (6-3)$$

Similarly, the total equivalent damping of the hybrid system with isolators and dampers in parallel is calculated from the following equation (Golzan et al., 2016; Jara & Casas, 2006; Roesset et al., 1973):

$$\xi_{eq(hybrid)} = \frac{K_{isol}}{K_{(isol+d)}} \xi_{isol} + \frac{K_d}{K_{(isol+d)}} \xi_d \quad (6-4)$$

Where K_{isol} and K_d are the stiffness of the isolator and damper, respectively, and ξ_{isol} and ξ_d are the damping ratio of the isolator and damper, respectively.

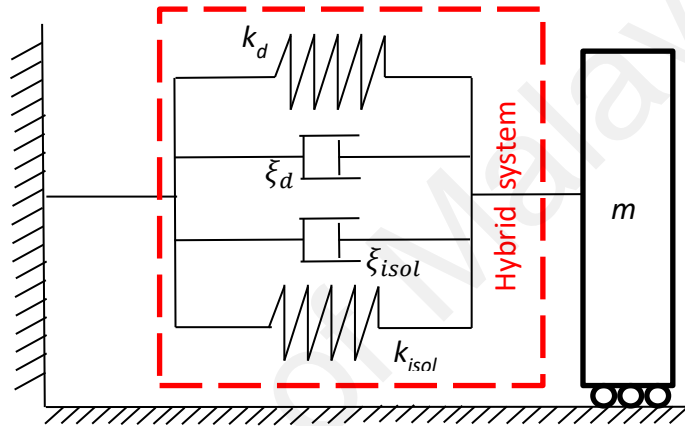


Figure 6.4: Mathematical model of hybrid passive control system in a single-degree-freedom system

Consequently, the equation of motion for a cable-stayed bridge equipped with a hybrid passive control system is modified as follows:

$$[M] \{\ddot{u}\} + [C] \{\dot{u}\} + [K] \{u\} + [D] \{F\} = -[M] [\eta] \{\ddot{x}_g\} \quad (6-5)$$

$$\{u\} = \{x_1, x_2, \dots, x_N\}^T \quad (6-6)$$

Where $[M]$, $[C]$ and $[K]$ are the mass, damping and stiffness matrices of the bridge, respectively; $[D]$ is the location matrix for the restoring forces of the hybrid system; $\{\ddot{u}\}$, $\{\dot{u}\}$ and $\{u\}$ are the bridge acceleration, velocity and displacement vectors, respectively; $\{F\}$ is the restoring force vector of the hybrid system; parameter $[\eta]$ is the earthquake

coefficient matrix and $\{\ddot{x}_g\}$ is the earthquake acceleration vector in the longitudinal direction.

6.2.5 Modeling in SAP2000

The bridge model described in Chapter 3 is used in this chapter for further investigation. In addition to the same bridge model, the link elements representing the abutments and dampers are added to the model to investigate the effect of the passive hybrid control system on earthquake-induced pounding.

6.2.5.1 Gap element

One of the main damage to the Shipshaw Bridge was due to earthquake-induced pounding between the bridge ends and abutments, therefore, the gap element is used to measure the pounding forces of the bridge with abutments. The expansion gap between the bridge and abutments is represented by the nonlinear link element in SAP2000 as shown in Figure 6.5. The link element property is selected as Gap, which is able to undertake only compression force. The force-deformation relationship of the gap element is expressed as following:

$$f = \begin{cases} \text{if } d + \text{open} < 0 & k_G(d + \text{open}) \\ \text{otherwise} & 0 \end{cases} \quad (6-7)$$

Where d is the displacement, open is the initial gap opening that is set to be zero or positive and k_G is the spring stiffness.

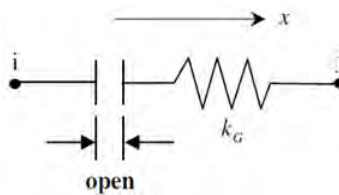


Figure 6.5: Link element with the gap property in SAP2000

In this study, the abutments are assumed to be rigid. Therefore, the abutments are represented by rigid link elements of the same width as the bridge width. The abutments are also in rock bed soil. At the end of each abutment, a gap element is connected to the bridge. The gap opening size of 0.03 m calculated from Equation 6-1 is assigned to the gap element; however, this is a minimum requirement for the gap opening size. In addition, the abutment stiffness obtained from Equation 6-2 is assigned as the gap element stiffness, which represents the abutment stiffness at the bridge ends. It should be noted that the gap elements' stiffness has zero contribution to the overall bridge stiffness.

6.2.5.2 Damper element

The HHSD is modelled in SAP2000 as a nonlinear link element with multilinear plastic properties. The link element has 6 degrees-of-freedom, which are internal to the link, including shear, axial, torsion and pure bending. Shear deformation happens within the shear spring as shown in Figure 6.6. More details of the link element and its behavior are available in the CSI Analysis Reference Manual (Computers and Structures Inc., 2015).

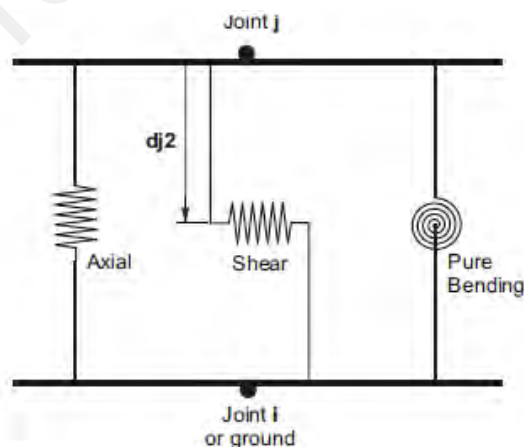


Figure 6.6: Nonlinear link element representing the HHSD in SAP2000

The force-displacement bilinear values obtained from the HHSD design procedure in the previous section used as input for the multi-linear force-deformation definition

symmetrically in the positive and negative regions. The updated model of the bridge with all elements is shown in Figure 6.7. It is worth mentioning that the HHSD has reasonable energy dissipation capability in the transverse direction, which can also be simulated by the nonlinear link element; however, it is neglected in the modelling.

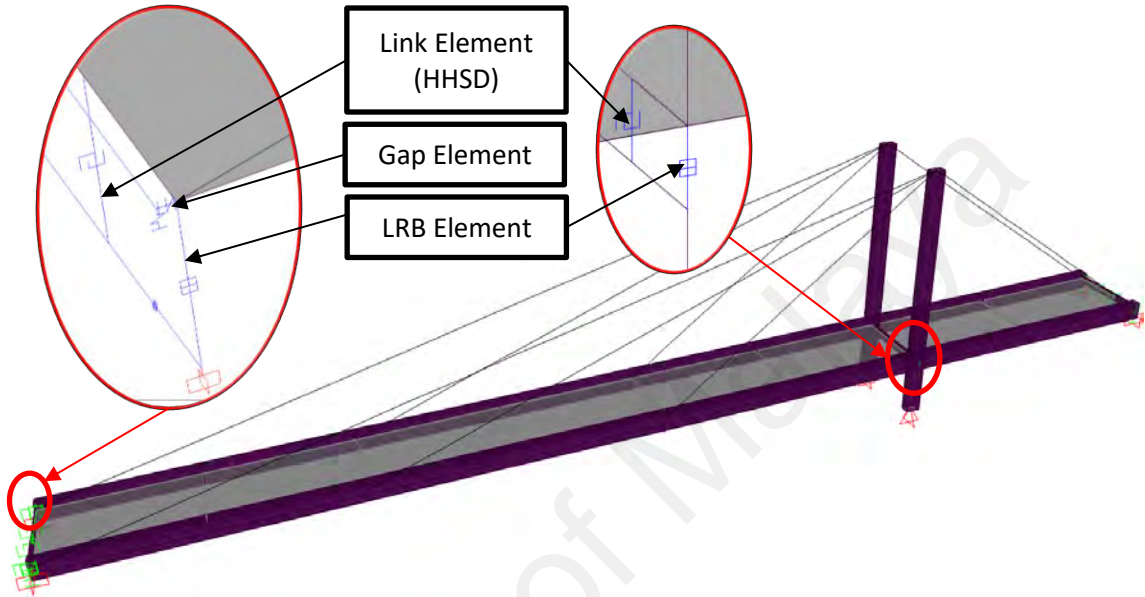


Figure 6.7: Finite element model of the bridge equipped with hybrid passive control systems

6.2.6 Ground motion selection

The effectiveness of the passive hybrid system on the seismic response of the cable-stayed bridge is investigated through nonlinear time-history analysis. The site's seismic hazard values are determined for 2% probability of exceedance in 50 years (on firm soil) from the Natural Resource Canada (NBCC, 2017) and used to plot the standard design spectrum of the bridge based on the NBCC 2017 specification. A set of 14 ground motions with magnitude ranging from 4.5 to 6 are selected from the Pacific Earthquake Engineering Center (PEER, 2017). Details of the selected ground motions are presented in Table 6.2. The 1988 Saguenay earthquake recorded at US.ISFL station, which caused damage to the bridge, is also included among the selected ground motions. The MSE

method (computed weighted mean squared error) is used to scale the selected records to the calculated NBCC design spectrum with 5% structural damping. The standard design spectra of the bridge site and response spectra of the scaled ground motion records for 5% structural damping with the average scaled median are shown in Figure 6.8. In addition, the scaled acceleration time-history of earthquake No. 1 and 5 is presented in Figure 6.9. It should be noted that the earthquakes were only applied in the longitudinal direction of the bridge. A total time size of 40 seconds with step size of 0.01 sec is used for the nonlinear time-history analysis.

Table 6.2: Characteristics of ground motions selected from PEER (2017)

No.	Earthquake	Date	Station	Magnitude	PGA (g)	PGV (cm/sec)
1	Saguenay	1988	US.ISFL	5.85	0.0054	0.448
2	AuSableForks	2002	Belchertown	4.99	0.0047	0.225
3	Mineral	2011	Basking Ridge_ NJ	5.74	0.0048	0.343
4	Mineral	2011	Central Park_ NY City	5.74	0.0023	0.203
5	Mineral	2011	Franklin and Marshall College_ PA	5.74	0.0262	0.592
6	Mineral	2011	Fordham University_ the Bronx_ NYC	5.74	0.0032	0.301
7	Mineral	2011	Keystone College_ La Plume_ PA	5.74	0.0020	0.139
8	Mineral	2011	Temple University_ PA	5.74	0.0101	0.798
9	Sparks	2011	Smith Ranch_ Marlow_ OK	4.73	0.0077	0.258
10	Sparks	2011	Jones High School	5.68	0.0336	0.730
11	Sparks	2011	Wilshire Boulevard; Harrah	5.68	0.0277	1.229
12	Sparks	2011	Luther Middle School	5.68	0.0270	1.594
13	Sparks	2011	GS.OK009	5.68	0.0220	0.832
14	Sparks	2011	GS.OK010	5.68	0.0421	1.405

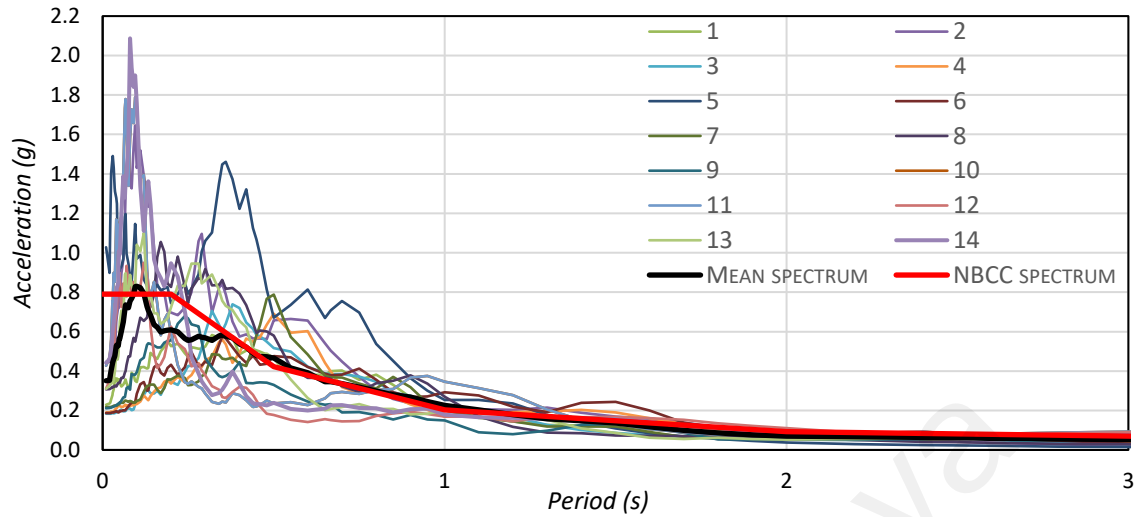


Figure 6.8: Scaled acceleration response spectra of ground motions adopted for analysis

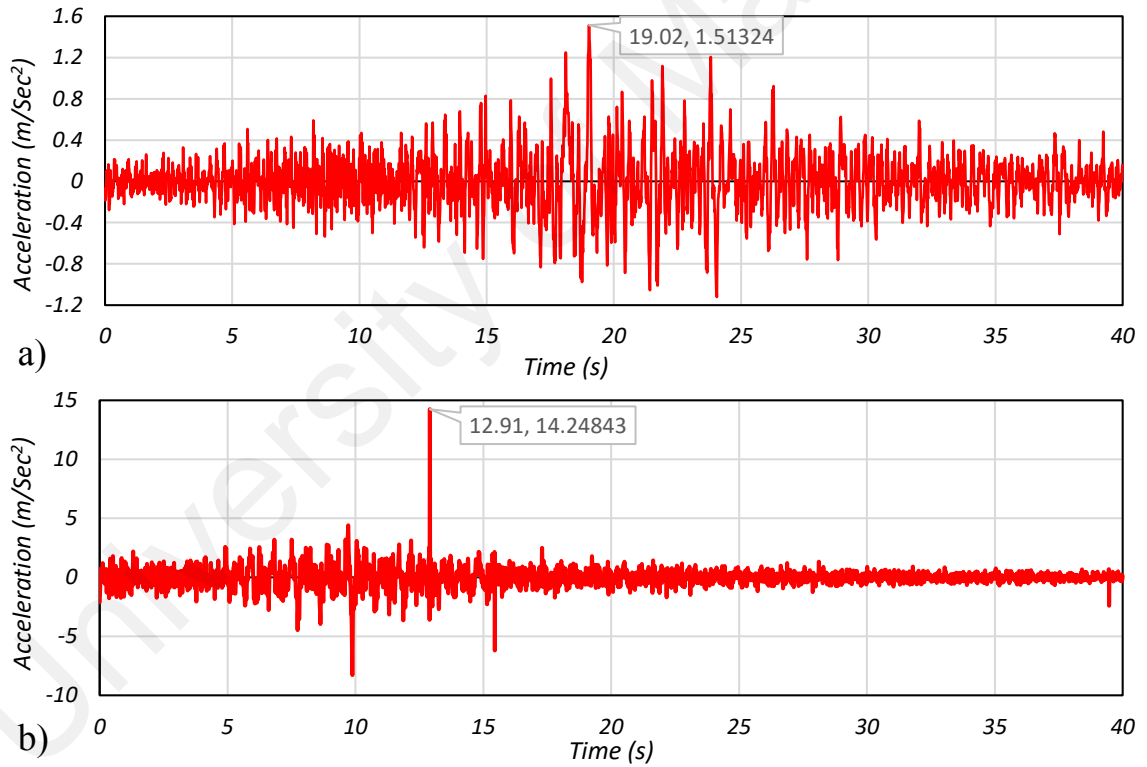


Figure 6.9: Scaled time-history accelerogram of a) earthquake No. 1 and b) earthquake No. 5

6.3 Results and discussion

The major findings from Chapters 3 and 4 prove that the seismic isolation system significantly enhanced the seismic performance of the cable-stayed bridge. However, the

bridge displacement increased due to the seismic isolation system, which can potentially increase the chance of seismic pounding in the bridge. Javanmardi et al. (2018) showed that metallic dampers had insignificant influence on the global seismic response of bridges. Hence, to avoid result repetition in this chapter, the results of deck displacement, base shear and bridge pounding response as well as the hysteretic behavior of the adopted control system are presented.

6.3.1 Displacement and velocity

The peak response of bridge displacement at the deck-tower connection under selected earthquakes is shown in Figure 6.10. It is clear that the displacement of the isolated bridge is the highest among other bridge cases. As discussed in the previous chapter, the isolation system increases the flexibility of the bridge in the longitudinal direction (by changing the boundary condition and also removing the rigid connection between the deck and towers), causing a significant increment in bridge displacement. The isolated bridge displacement enlarged up to 200% compared with the non-isolated bridge. On the other hand, the displacement of the bridge equipped with HHSDs decreased by 7% to 52%, as the HHSDs limited the displacement of the bridge ends due to their stiffness. The displacement of the bridge retrofitted with the hybrid control system also increased compared with the non-isolated and HHSD bridges. Nonetheless, the bridge displacement in this case reduced compared with the isolated bridge. A maximum of 55% reduction in displacement was observed in the case of the bridge equipped with the hybrid control system compared with the isolated bridge. It should be mentioned that HHSDs were able to reduce the displacement of the hybrid bridge, which eventually reduced the likelihood of bridge pounding with the abutments.

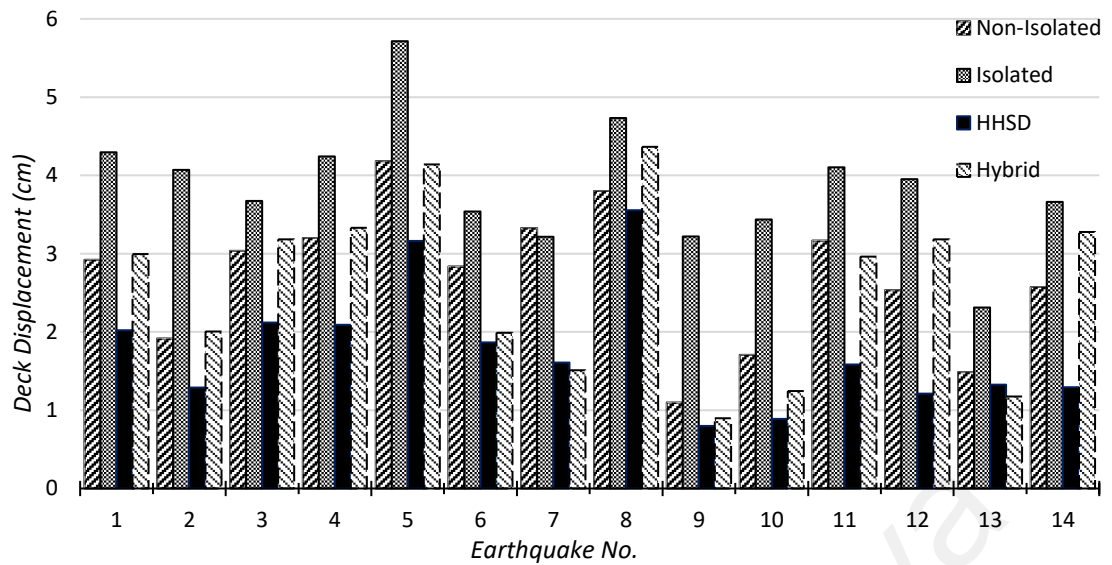


Figure 6.10: Maximum seismic displacement of the bridge at the deck-tower connection

Figure 6.11 shows the displacement time-history response of the bridge at the deck-tower connection due to earthquake No. 1. It is observed in this figure that the time-history trend of displacement for each bridge case is different. The isolated bridge had higher oscillations after reaching to its peak due to bridge pounding with the abutments. The bridge with the hybrid control system had a pulse-type oscillation near the peak ground acceleration of the selected earthquake. In addition, the displacement peak response of the isolated bridge increased, while for the bridge equipped with HHSDs it reduced. On the other hand, the non-isolated bridge and bridge retrofitted with the hybrid control system had the same peak response of displacement. The peak of displacement response for the non-isolated bridge and bridge with the hybrid control system was 0.03 m, which increased to 0.04 m in the isolated bridge and decreased to 0.02 m in the bridge retrofitted with HHSDs.

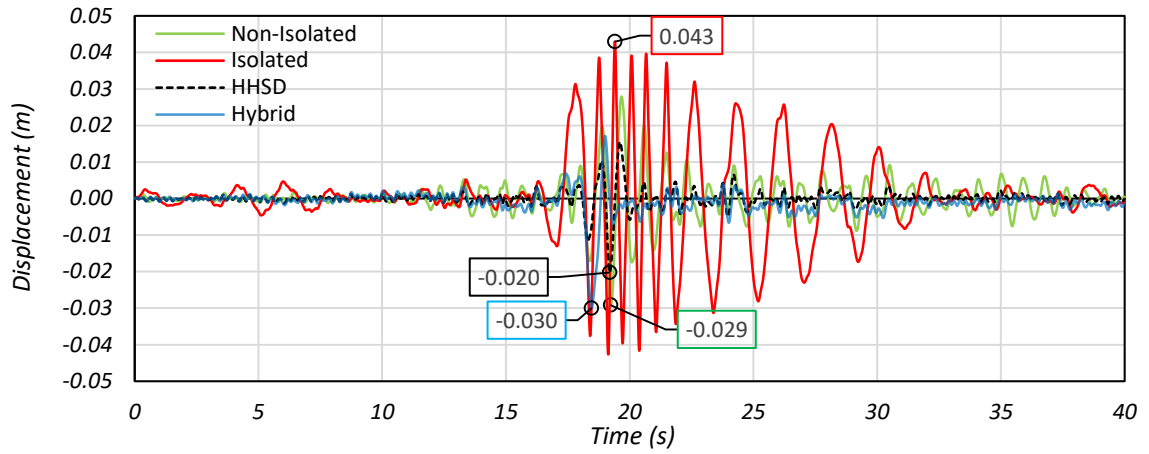


Figure 6.11: Displacement time-history response of the bridge at the deck-tower connection under earthquake No. 1

The velocity time-history response at top of the tower under earthquake No. 1 is shown in Figure 6.12. The tower velocity oscillation in the isolated bridge reduced significantly. The velocity peak of the tower decreased from 0.93 m/sec to 0.12 m/sec. The velocity time-history trends of the tower in the original bridge configuration and the bridge retrofitted with HHSDs were similar, except the peak velocity response reduced by 25%. In the bridge retrofitted with the hybrid control system, the tower oscillation and amplitude enhanced remarkably. The peak response of velocity in this case reduced by 96%, 94.2% and 66.7% compared with the non-isolated bridge, the bridge with HHSDs and isolated bridge, respectively.

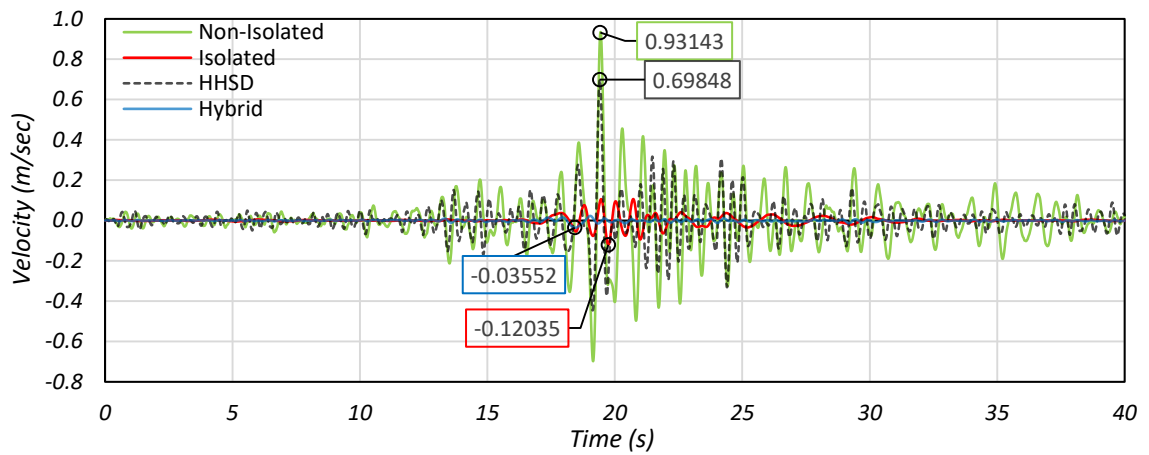


Figure 6.12: Velocity time-history response at the top of the tower under earthquake

No. 1

6.3.2 Base shear

A comparison of the base shear in the original bridge and the bridge with different control systems is illustrated in Figure 6.13. As the results from previous chapters indicated, the isolation system led to a significant reduction in base shear. Subsequently, the isolated bridge base shear reduced in the range of 58% to 86%. The base shear of the bridge equipped with HHSDs under different earthquakes mostly improved compared with the original bridge. However, the base shear was affected by earthquake frequency content, as it either reduced significantly by 52.4% for earthquake No. 7, or only reduced by 1% for earthquake No. 8. Moreover, the bridge retrofitted with the hybrid control system exhibited maximum reduction in base shear compared with other control systems. However, the base shear in this case was quite close to the isolated case under a few earthquakes, as the metallic damper is part of the hybrid control system and its hysteretic behavior is affected by earthquake characteristics. Furthermore, the hybrid control system reduced the base shear from 79% to 93% compared to the isolated system.

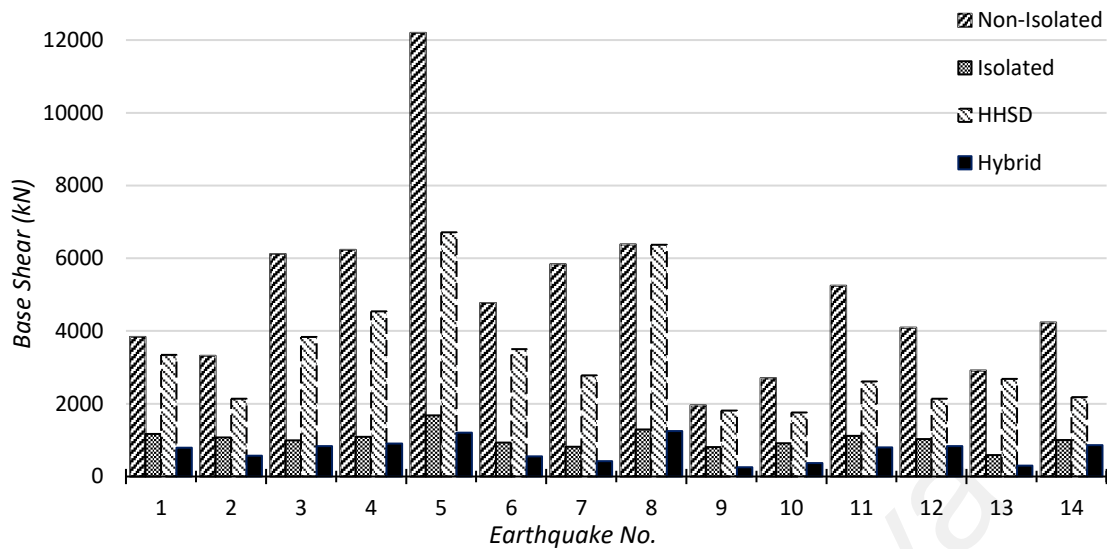


Figure 6.13: Maximum base shear of the bridge with different control systems

The base shear time-history response of the original bridge and the bridges with different control systems under earthquake No. 1 is shown in Figure 6.14. The base shear of the original bridge reached a peak at the same time as the peak ground acceleration. Similarly, the base shear trend for the bridge with metallic dampers was the same as the original bridge; however, the base shear peak response occurred at the same time but reduced from 4424 kN to 3346 kN. The base shear oscillation over time reduced for the isolated bridge and the base shear peak occurrence time shifted slightly right after the peak ground acceleration occurred. Finally, the base shear of the bridge with the hybrid system had the lowest oscillation and the peak response was 795 kN, which was the lowest among other cases. In conclusion, the hybrid system benefits from the advantages of the seismic isolator and HHSD in reducing the peak oscillation of base shear in the bridge time-history response.

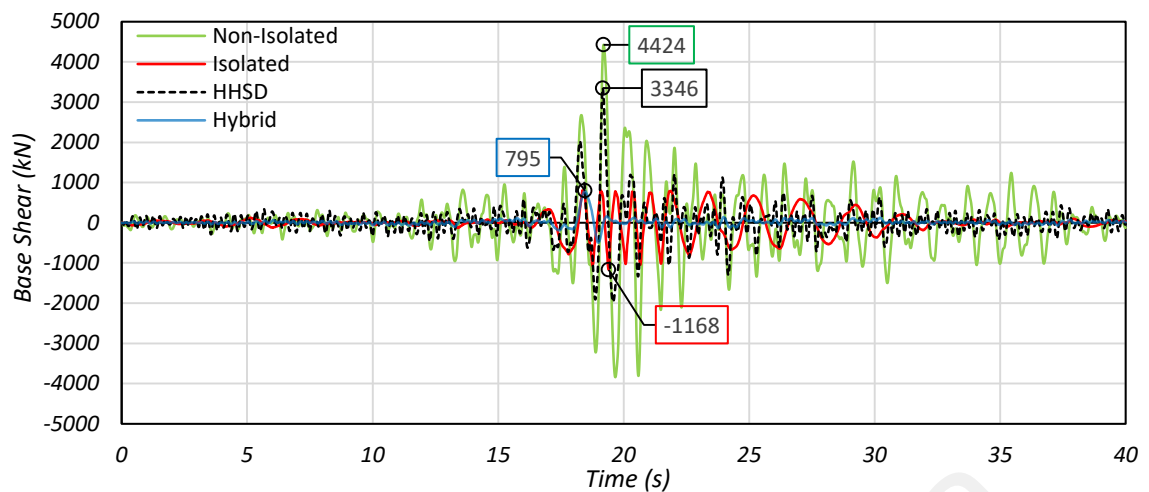


Figure 6.14: Base shear time-history response of the bridge under earthquake No. 1

6.3.3 Pounding force

Figures 6.14 and 6.15 show the maximum pounding force at the left and right bridge ends with the abutments, respectively. It can be seen in these figures that the pounding force at the left and right ends of the bridge was not the same owing to the asymmetric shape and 4% longitudinal slope of the bridge. Pounding in the original bridge occurred during 7 out of 14 earthquakes. The maximum pounding forces of the non-isolated bridge at the left and right abutments were 12596 kN and 8337 kN during earthquakes No. 5 and 8, respectively. It should be noted that the deck-tower connection of the non-isolated bridge was rigid, which limited the longitudinal displacement of the bridge and consequently reduced the likelihood of earthquake-induced pounding. The seismic displacement of the bridge increased after the isolation system was implemented, which also increased the chance of earthquake-induced pounding in the bridge. In the isolated bridge case, the pounding force increased significantly at both abutments under most earthquakes except No. 13. In this bridge case, the maximum pounding force at the left and right abutments reached 27037 kN and 26190 kN, respectively, during earthquake No. 5. The bridge retrofitted with HHSDs had the lowest pounding forces. This is due to the fact that the dampers at the bridge ends controlled the longitudinal seismic movement

of the roller supports and also dissipated seismic energy through the hysteresis of the dampers. Moreover, the rigid connection between the tower and deck also limited the longitudinal displacement of the bridge, which eventually caused a significant reduction in earthquake pounding in the bridge with the abutments in this case. Figures 6.14 and 6.15 indicate that for the bridge equipped with the hybrid system the pounding force was mitigated 100% during most earthquakes. During earthquakes No. 4, 5, 8, 12 and 14, the pounding force reduced significantly compared to the isolated bridge. It worth to mention that the earthquake with the largest base shear also had the largest pounding force.

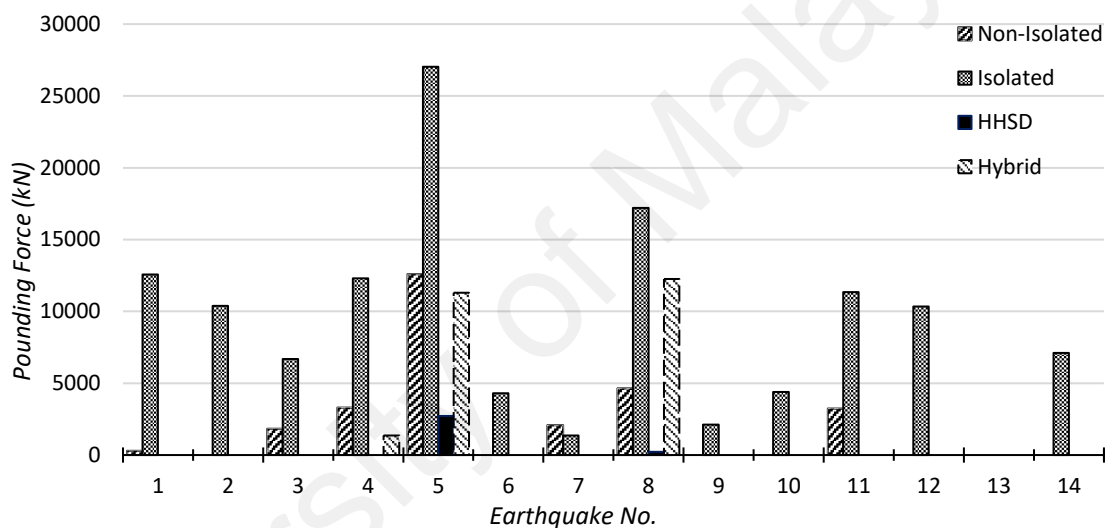


Figure 6.15: Maximum pounding force on the bridge at the left abutment

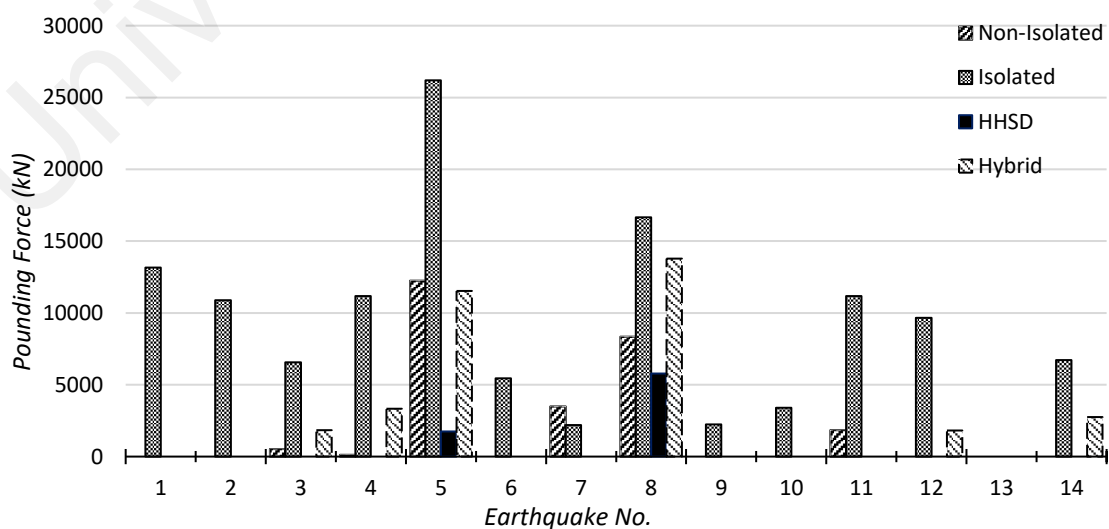


Figure 6.16: Maximum pounding force on the bridge at the right abutment

The pounding effect can be seen clearly from the pounding time-history response of the bridge with abutments. Figure 6.17 shows the time-history response of pounding at the left ends of the bridge during earthquake No. 5. Pounding occurred a few times in the non-isolated bridge, while in the isolated bridge, the pounding force and frequency increased dramatically. In the case of the bridge retrofitted with HHSDs, pounding only happened once with a very small magnitude. Finally, the pounding force and occurrence reduced significantly for the bridge with the hybrid system compared to the isolated bridge. The maximum pounding force at the left abutment was 12600 kN and occurred at 9.8 sec in the original bridge, while in the isolated bridge the maximum pounding force of 27037 kN happened at 10.2 sec. For the bridge equipped with HHSDs, the maximum pounding force reduced to 2720 kN at 9.9 sec. Lastly, the maximum pounding force of 11295 kN at 11.2 sec was observed for the bridge retrofitted with the hybrid control system.

The pounding time-history response of the bridge with the right abutment is shown in Figure 6.18. At the right side of the non-isolated bridge, pounding happened 4 times during earthquake No. 5, while at the left side it happened 5 times under the same earthquake. Again, this was due to the asymmetric geometry of the bridge. The maximum pounding was 12235 kN for the non-isolated bridge and this increased to 26190 kN in the isolated bridge at the same pounding occurrence time. Pounding only happened 2 times for the bridge retrofitted with HHSDs at a maximum value of 1759 kN. For the bridge with the hybrid control system, the maximum pounding force reached 11516 kN. It can be concluded that the bridge retrofitted with HHSDs had the lowest pounding force during earthquake No 5, which was followed by the bridge with the hybrid control system.

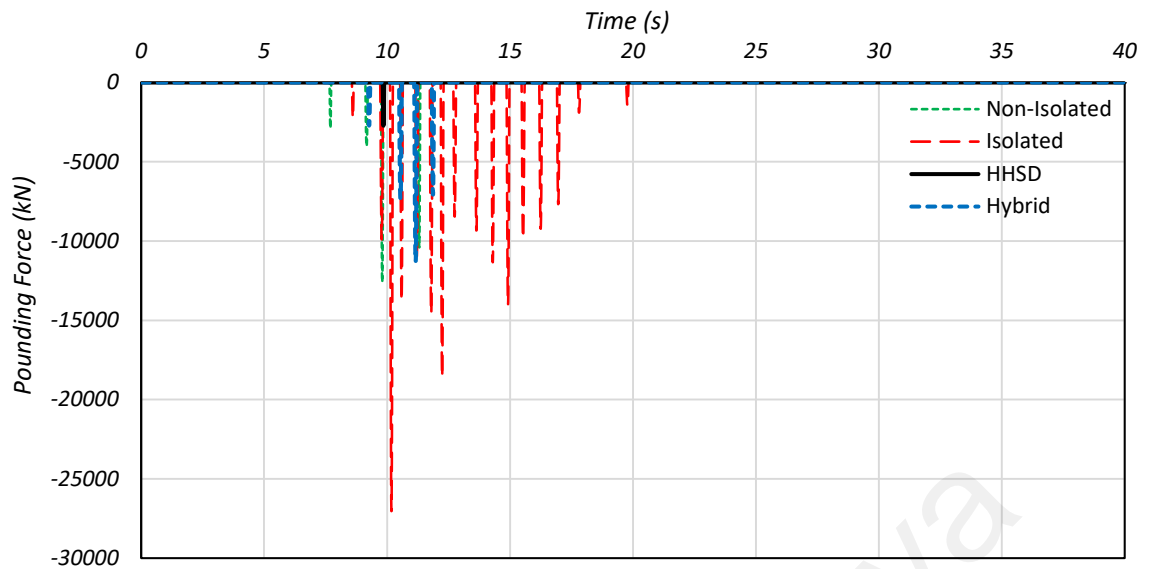


Figure 6.17: Pounding time-history response of the bridge at the left abutment subjected to earthquake No. 5

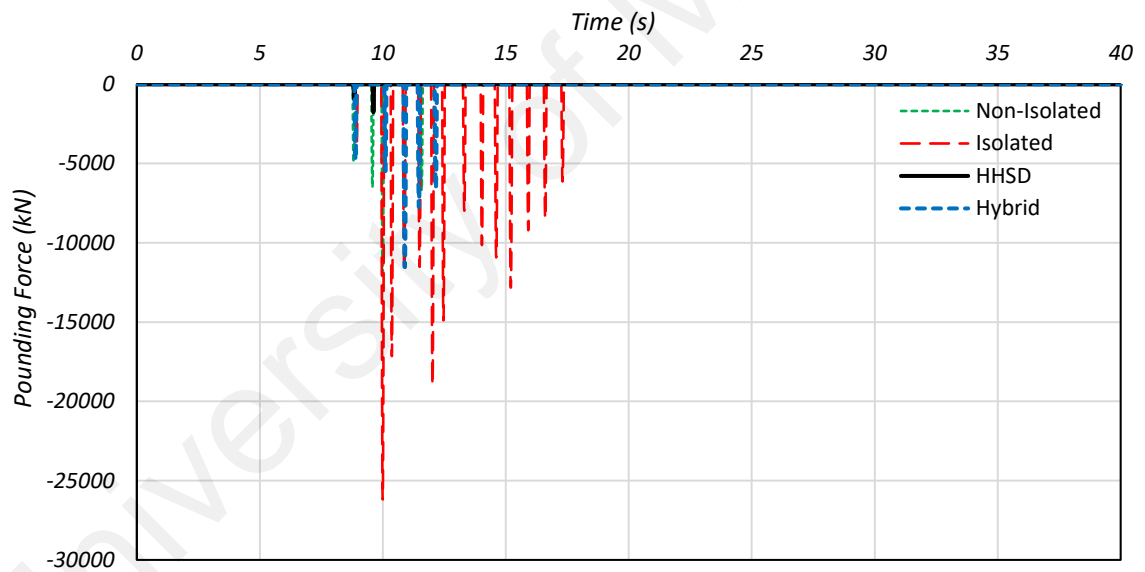


Figure 6.18: Pounding time-history response of the bridge at the right abutment subjected to earthquake No. 5

6.3.4 Hysteresis curves of energy dissipaters

Figure 6.19 displays the force-displacement curves of various control systems at the left and right ends of the bridge during earthquake No. 1. This figure shows that the LRBs in the isolated bridge dissipated huge amounts of energy with repeated numbers of plastic cycles. The HHSDs also dissipated large amounts of energy in the bridge equipped with

HHSDs. The maximum displacement of the metallic dampers was smaller in the bridge with HHSDs than the bridge with the hybrid system. This was due to the fact that the deck-tower connection of the bridge was rigid in this retrofitting case, which limited the seismic displacement of the bridge. For the bridge with the hybrid control system, the LRB plastic formations were significantly small (compared with the isolated bridge), while the HHSDs experienced large plastic deformation and undertook most of the seismic energy. In addition, the maximum LRB displacement in the hybrid control system reduced compared to the LRBs in the isolated bridge. It is worth mentioning that the HHSDs at the abutments had higher seismic dissipation capacity with higher stiffness than the LRBs, as the HHSDs were designed to limit the bridge end displacement.

The force-displacement curves of the various control systems at the tower in different bridge cases during earthquake No. 1 are presented in Figure 6.20. In general, the LRBs in the tower section had higher seismic dissipation capacity than the HHSDs as shown in this figure. It is observed that the HHSDs behaved linearly in the bridge retrofitted with HHSDs because the tower and deck were connected rigidly with each other in this case. As a result, the HHSD movement was very small and the energy dissipation less significant for the HHSDs in this bridge case. In the bridge retrofitted with the hybrid control system, the LRB hysteresis loops reduced notably and the HHSDs experienced quite a large number of plastic formation cycles. However, in this case, the ultimate strength of the HHSDs was lower than the ultimate strength of the LRBs. The LRB displacement reduced remarkably due to the implementation of the HHSDs in parallel with the LRBs in the bridge.

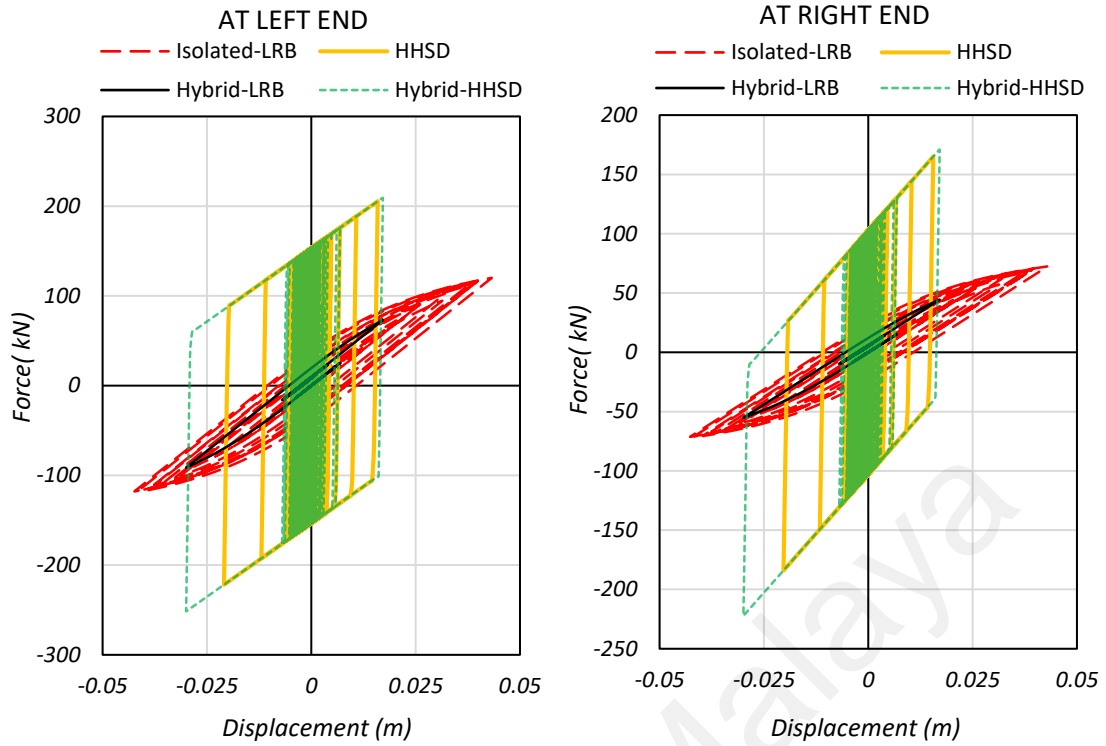


Figure 6.19: Hysteresis loops of control systems at the bridge ends in different cases

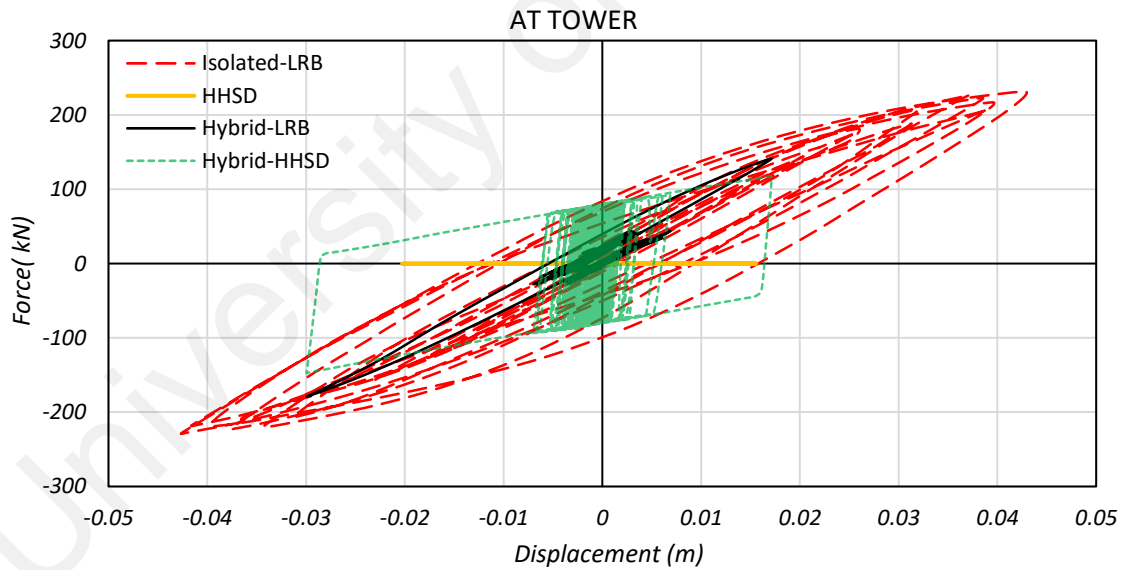


Figure 6.20: Hysteresis loops of control systems at the tower in different bridge cases

6.4 Conclusions

Based on the numerical results of the cable-stayed bridge with different seismic control system, the following conclusions can be drawn:

- The hybrid passive control system remarkably reduced the seismic displacement of the cable-stayed bridge compared to the isolated bridge.
- Less base shear reduction was observed for the bridge retrofitted with HHSDs, while for the isolated bridge, a higher base shear reduction was observed. The base shear of the bridge retrofitted with the hybrid control system reduced further than the isolated bridge.
- The seismic pounding of the bridge with abutments was either eliminated or significantly reduced in the bridge retrofitted with the hybrid control system.
- The seismic isolation system mostly contributed to reducing the global seismic demand of the cable-stayed bridge, while the HHSDs reduced the longitudinal seismic displacement and mitigated the likelihood of bridge pounding with the abutments.
- The energy dissipating capability of the bridge with the hybrid control system was found to be higher than the other bridge cases.
- Finally, it can be concluded that the hybrid passive system is a reliable, efficient and inexpensive control system that reduces seismic demand and prevents seismic damages to the primary structure.

CHAPTER 7: CONCLUSIONS

7.1 Concluding remarks

Based on the nonlinear time-history analysis of cable-stayed bridges retrofitted with different seismic control systems and HHSD development through quasi-static cyclic testing, the following major conclusions can be drawn:

1. Utilizing seismic isolators at the deck-tower connection or the tower base increased bridge flexibility in the longitudinal direction, while utilizing seismic isolators at the bridge end supports increased bridge flexibility in the transverse direction, hence minimizing the seismic demand on the bridge in the longitudinal and transverse directions, respectively. Partial seismic isolation of the cable-stayed bridge only led to enhanced bridge seismic performance in one direction. Moreover, to maximize the isolation system benefits for overall improvement in the seismic response of the bridge in the longitudinal and transverse directions, it was necessary to use an isolation system along the end supports and deck-tower connection or tower base of the cable-stayed bridge simultaneously.
2. Most seismic responses, including the base shear, base moment, cable force variations, bending moment, shear and axial forces of the tower in the fully isolated bridge significantly enhanced, on the other hand, the seismic displacement of the bridge increased. The isolation systems induced torsional deformation at the deck level due to the transverse earthquake component that increased the tower axial force in the substructure. Furthermore, the seismic zone of the bridge found to be an important parameter in the design of seismic isolators for cable-stayed bridges.
3. The HHSDs demonstrated uniform and stable hysteretic behavior, a good range of ductility and high energy dissipation capability. The HHSD constitutive formulas were able to predict the HHSD behavior well. Furthermore, HHSDs are inexpensive, lightweight, rate independent, resistant to ambient temperature and

can be easily replaced after earthquake events. HHSDs are found to be suitable for new structures or for seismic retrofitting of existing structures.

4. Implementing the hybrid passive control system in the cable-stayed bridge caused a significant reduction in the seismic demand on the bridge, especially the seismic displacement of the superstructure. The hybrid control system mitigated the earthquake-induced pounding effect on the bridge with adjacent abutments. In addition, the energy dissipation capability of the cable-stayed bridge with the hybrid passive control system increased remarkably. Consequently, the combination of the seismic isolation and metallic damper known as the hybrid passive control system was found to be a reliable seismic retrofitting alternative to protect existing cable-stayed bridges from earthquake excitations.

7.2 Recommendations of future works

Based on the results and conclusions obtained in each stage of this research, several recommendations for further research are made as follows:

1. The seismic performance of cable-stayed bridges (medium to long-span) with and without control systems should be investigated under spatially varying ground motions.
2. The HHSD consists of two parallel steel plates. Hence, a further study can be performed to examine the behavior of HHSDs with more ductile steel material and the number of parallel plates could be increased to three or four.
3. In this study, the potential locations of HHSDs in other structures were presented; therefore, experimental and analytical studies can be carried out to investigate the HHSD effects on the seismic performance of such structures.

4. A shaking table test should be carried out on a structure equipped with the proposed control system to investigate the realistic performance of the hybrid passive control system.
5. The effectiveness of the hybrid control system in mitigating earthquake-induced pounding in other types of bridges can be studied further.

University of Malaya

REFERENCES

- AASHTO. (2010). *Guide Specifications for Seismic Isolation Design* (Third). Washington DC: American Association of State Highway and Transportation Officials.
- AASHTO. (2012). *LRFD Bridge Design Specifications*. Washington DC: American Association of State Highway and Transportation Officials.
- Abaqus Inc. (2014). Abaqus theory Abaqus theory manual, Version 6.14. *Abaqus Inc.*
- Abdel-Ghaffar. (1991). Cable-stayed bridges under seismic action. In *Cable-stayed bridges; Recent Development and their Future*, (pp. 171–192). yokohama (japan): Elsevier Science Ltd.
- Abdel-Ghaffar, & Khalifa, M. A. (1992). Importance of cable vibration in dynamics of cable-stayed bridges. *Journal of Engineering Mechan*, 117(11), 2571–2589.
- Abdel-Raheem, S. E., & Hayashikawa, T. (2003). *Tower nonlinear dynamic response of cable-stayed bridge under great earthquake ground motion*. 北海道大学.
- Abebe, D. Y., Jeong, S. J., Getahun, B. M., Segu, D. Z., & Choi, J. H. (2015). Hysteretic characteristics of shear panel damper made of low yield point steel. *Materials Research Innovations*, 19, 902–910.
- Aghlara, R., & Tahir, M. M. (2018). A passive metallic damper with replaceable steel bar components for earthquake protection of structures. *Engineering Structures*, 159(July 2017), 185–197.
- Aghlara, R., Tahir, M. M., & Adnan, A. Bin. (2018). Experimental study of Pipe-Fuse Damper for passive energy dissipation in structures. *Journal of Constructional Steel Research*, 148, 351–360.
- Alfredo Cámara Casado. (2011). *Seismic Behaviour of Cable-Stayed Bridges: Design, Analysis and Seismic Devices*. Universidad Politécnica de Madrid.
- Ali, H. M., & Abdel-Ghaffar. (1995). Modeling the nonlinear seismic behavior of cable-stayed bridges with passive control bearings. *Computers and Structures*, 54(3), 461–492.
- Ali, H. M., & Abdel-ghaffar, A. M. (1994). Seismic energy dissipation for cable-stayed bridges using passive devices. *Earthquake Engineering & Structural Dynamics*, 23(December 1991), 877–893.
- Ali, H. M., & Abdel-ghaffar, A. M. (1995). Seismic Passive Control of Cable-Stayed Bridges. *Shock and Vibration*, 2(4), 259–272.
- ASTM-E8. (2015). *Standard Test Methods for Tension Testing of Metallic Materials*. <https://doi.org/10.1520/E0008>
- ATC-40. (1996). *Seismic evaluation and retrofit of concrete buildings*. California seismic

safety commission.

- Au, F. T. K., Cheng, Y. S., Cheung, Y. K., & Zheng, D. Y. (2001). On the determination of natural frequencies and mode shapes of cable-stayed bridges. *Applied Mathematical Modelling*, 25(12), 1099–1115.
- Azevedo, J., & Calado, L. (1994). Hysteretic behaviour of steel members: Analytical models and experimental tests. *Journal of Constructional Steel Research*, 29(1–3), 71–94.
- Bannantine, J. A., Comer, J. J., & Handrock, J. L. (1990). *Fundamental of metal fatigue analysis*. Englewood Cliffs, NJ: Prentice hall.
- Benavent-Climent, A. (2010). A brace-type seismic damper based on yielding the walls of hollow structural sections. *Engineering Structures*, 32(4), 1113–1122.
- Benavent-Climent, A., Morillas, L., & Vico, J. M. (2015). A study on using wide-flange section web under out-of-plane flexure for passive energy dissipation. *Earthquake Engineering and Structural Dynamics*, 44(July 2010), 657–675.
- Bergman, D. M. (1987). *Evaluation of Cyclic Testing of Steel-plate Devices for Added Damping and Stiffness*. Department of Civil Engineering, University of Michigan.
- Black, C., Makris, N., & Aiken, I. D. (2002). *Component testing, stability analysis and characterization of buckling-restrained Unbonded Braces*. Pacific Earthquake Engineering Research Center.
- Black, C., Makris, N., & Aiken, I. D. (2004). Component Testing, Seismic Evaluation and Characterization of Buckling-Restrained Braces. *Journal of Structural Engineering*, 130(6), 880–894.
- Bommer, J. J., & Ruggeri, C. (2002). The specification of acceleration time-histories in seismic design codes. *European Earthquake Engineering*, 16(1), 3–17.
- Branco, F. A., Mendes, P. M., & Guerreiro, L. M. C. (2000). Special studies for Vasco Da Gama Bridge. *Journal of Bridge Engineering*, 254(August), 233–239.
- Briones, B., & Llera, J. C. de la. (2014). Analysis, design and testing of an hourglass-shaped ETP-copper energy dissipation device. *Engineering Structures*, 79, 309–321.
- Bruneau, M. (1998). Performance of steel bridges during the 1995 Hyogoken–Nanbu (Kobe, Japan) earthquake—a North American perspective. *Engineering Structures*, 20(12), 1063–1078.
- Bruno, D., & Leonardi, A. (1997). Natural Periods of Long-Span Cable-Stayed Bridges. *Journal of Bridge Engineering*, 2(3), 105–115.
- Buckle, I. G., Al-Ani, M., & Monzon, E. (2011). Seismic Isolation Design Examples of Highway Bridges. In *NCHRP* (Vol. 262, p. 382).
- Built, S. M. (1982). *Lead rubber dissipators for the base isolation of bridge structures*. University of Auckland.

- Caetano, E. (2007). Cable vibration in cable-stayed bridges. *IABSE*, 9.
- Caetano, E., Cunha, A., & Taylor, C. A. (2000a). Investigation of Dynamic Cable–Deck Interaction in a Physical Model of a Cable-Stayed Bridge. Part I: Modal Analysis. *Journal of Earthquake Engineering and Structural Dynamics*, 29(4), 481–498.
- Caetano, E., Cunha, A., & Taylor, C. A. (2000b). Investigation of Dynamic Cable–Deck Interaction in a Physical Model of a Cable-Stayed Bridge. Part II: Seismic Response. *Journal of Earthquake Engineering and Structural Dynamics*, 29(4), 481–498.
- Caltrans. (2014). *California Amendments to AASHTO LRFD Bridge Design Specifications*. (6, Ed.). Sacramento, CA: California Department of Transportation.
- Calvi, G. M., Sullivan, T. J., & Villani, a. (2010). Conceptual Seismic Design of Cable-Stayed Bridges. *Journal of Earthquake Engineering*, 14(8), 1139–1171.
- Casado, A. C. (2011). *Seismic Behaviour of Cable-Stayed Bridges: Design, Analysis and Seismic Devices*. Universidad Politécnica de Madrid.
- Casciati, F., Faravelli, L., & Petrini, L. (1998). Energy dissipation in shape memory alloy devices. *Computer-Aided Civil and Infrastructure Engineering*, 13(6), 433–442.
- Chadwell, C. B. (2003). *Seismic Response of a Single Tower Cable-Stayed Bridges*. University of California, Berkeley.
- Chan, R. W. K., & Albermani, F. (2008). Experimental study of steel slit damper for passive energy dissipation. *Engineering Structures*, 30(4), 1058–1066.
- Chan, R. W. K., Albermani, F., & Kitipornchai, S. (2008). Evaluation of yielding shear panel device for passive energy dissipation. *Journal of Constructional Steel Research*, 91(2), 14–25.
- Chan, R. W. K., Albermani, F., & Kitipornchai, S. (2013). Experimental study of perforated yielding shear panel device for passive energy dissipation. *Journal of Constructional Steel Research*, 91, 14–25.
- Chang, C.-M., & Loh, C.-H. (2006). Seismic Response Control of Cable-Stayed Bridge Using Different Control Strategies. *Journal of Earthquake Engineering*, 10(4), 481–508.
- Chang, Mo, Y., Chen, C., & Lai, L. (2004). Lessons learned from the damaged Chi-Lu cable-stayed bridge. *Journal of Bridge*, (2012), 343–352.
- Chen, Z., Dai, Z., Huang, Y., & Bian, G. (2013). Numerical simulation of large deformation in shear panel dampers using smoothed particle hydrodynamics. *Engineering Structures*, 48, 245–254.
- Chen, Z., Ge, H., & Usami, T. (2005). Hysteretic performance of shear panel dampers. *Advances in Steel Structures*, 2, 1223–1228.
- Chen, Z., Ge, H., & Usami, T. (2006). Hysteretic Model of Stiffened Shear Panel Dampers. *Journal of Structural Engineering*, 132(3), 478–483.

- Chen, Z. Q., Wang, X. Y., Ko, J. M., Ni, Y. Q., Spencer, B. F., & Yang, G. (2003). MR damping system on Dongting Lake cable-stayed bridge. In *Smart Structures and Materials 2003: Smart Systems and Nondestructive Evaluation for Civil Infrastructures*.
- Cheng, S., Du, S., Yan, X., Guo, Q., & Xin, Y. (2017). Experimental study and numerical simulation of clapboard lead damper. *Proceedings of the Institution of Mechanical Engineers, Part C: Journal of Mechanical Engineering Science*, 231(9), 1688–1698.
- Chopra, A. K. (2014). *Dynamics of structure, theory and applications to earthquake engineering* (4th ed.). Pearson.
- Christopoulos, C., & Filiatrault, a. (2006). *Principles of passive supplemental damping and seismic isolation*. (C. C & F. A., Eds.). Pavia (Italy): IUSS Press.
- Clough, R. W., & Penzien, J. (1993). *Dynamics of structures* (2nd ed.). McGraw-Hill.
- Cole, G., Chouw, N., & Dhakal, R. (2011). Building and bridge pounding damage observed in the 2011 Christchurch earthquake. *Bulletin of the New Zealand Society for Earthquake Engineering*, 44(4), 334–341.
- Computers and Structures Inc. (2015). *CSI Analysis Reference Manual*. Berkeley, CA.
- Curadelli, R. O., & Riera, J. D. (2007). Design and testing of a lead damper for seismic applications. *Proceedings of the Institution of Mechanical Engineers, Part C: Journal of Mechanical Engineering Science*, 221(2), 159–164.
- Deng, K., Pan, P., Li, W., & Xue, Y. (2015). Development of a buckling restrained shear panel damper. *Journal of Constructional Steel Research*, 106, 311–321.
- Deng, K., Pan, P., Sun, J., Liu, J., & Xue, Y. (2014). Shape optimization design of steel shear panel dampers. *Journal of Constructional Steel Research*, 99, 187–193.
- Deng, K., Pan, P., & Wang, C. (2013). Development of crawler steel damper for bridges. *Journal of Constructional Steel Research*, 85, 140–150.
- DesRoches, R., & Delemont, M. (2002). Seismic retrofit of simply supported bridges using shape memory alloys. *Engineering Structures*, 24(3), 325–332.
- Dezfuli, H., & Alam, M. S. (2013). Multi-criteria optimization and seismic performance assessment of carbon FRP-based elastomeric isolator. *Engineering Structures*, 49, 525–540.
- Dolce, M., Cardone, D., & Marnetto, R. (2000). Implementation and testing of passive control devices based on shape memory alloys. *Earthquake Engineering & Structural Dynamics*, 29(v), 945–968.
- Dolce, M., Cardone, D., Ponzo, F. C., & Valente, C. (2005). Shaking table tests on reinforced concrete frames without and with passive control systems. *Earthquake Engineering & Structural Dynamics*, 34(14), 1687–1717.
- Dongbin, Z., Xin, N., Peng, P., Mengzi, W., Kailai, D., & Yabin, C. (2016). Experimental

study and finite element analysis of a buckling-restrained brace consisting of three steel tubes with slotted holes in the middle tube. *Journal of Constructional Steel Research*, 124, 1–11.

Dyke, S. J., Caicedo, J. M., Turan, G., Bergman, L. a., & Hague, S. (2003). Phase I Benchmark Control Problem for Seismic Response of Cable-Stayed Bridges. *Journal of Structural Engineering*, 129(7), 857–872.

Engelen, N. C. Van, Osgoode, P. M., Tait, M. J., & Konstantinidis, D. (2011). Partially bonded fiber-reinforced elastomeric isolators (PB-FREIs). *Structural Control and Health Monitoring*, (May 2011).

Eurocode8. Design of structures for earthquake resistance. Part1: General rules, seismic actions and rules for buildings. (2004).

Eurocode8. Design of structures for earthquake resistance. Part2: Bridges (2005).

Fan, L., Hu, S., & Yuan, W. (1994). Seismic response analysis for long-span bridges considering pile/soil-structure interaction and travelling seismic wave effects. In *In Cable-Stayed and Suspension Bridges; IABSE/FIP International Conference* (pp. 429–435). Deauville (France).

Fan, S., Ding, Z., Du, L., Shang, C., & Liu, M. (2016). Nonlinear finite element modeling of two-stage energy dissipation device with low-yield-point steel. *International Journal of Steel Structures*, 16(4), 1107–1122.

Federal Emergency Management Agency. (2007). *Interim protocols for determining seismic performance characteristics of structural and nonstructural components*. Washington, DC, USA.

Felber, A. J., & Stiemer, S. F. (1992). An object oriented programming approach to ambient vibration data analysis for bridges. In *Can. Soc. for Civ. Engrg. Annu. Conf.* (pp. 375–384). Quebec City, Canada.

FEMA-273. (1997). *NEHRP guidelines for seismic rehabilitation of buildings*. Washington DC.

FEMA-356. (2000). *Prestandard and commentary for the seismic rehabilitation of buildings*. Washington DC.

FEMA-440. (2005). *Improvements of nonlinear static seismic analysis procedures*. Washington DC.

Filiatrault, A., Tinawai, R., & Massicotte, B. (1993a). Damage to cable-stayed bridge during 1988 Saguenay earthquake. I: Pseudostatic analysis. *Journal of Structural Engineering*, 119(5), 1432–1449.

Filiatrault, A., Tinawai, R., & Massicotte, B. (1993b). Damage to cable-stayed bridge during 1988 Saguenay earthquake. II: Dynamic analysis. *Journal of Structural Engineering*, 119(5), 1450–1463.

Fleming, J. F., & Egeseli, E. A. (1980). Dynamic behaviour of a cable-stayed bridge.

- Franco, J. M., Cahís, X., Gracia, L., & López, F. (2010). Experimental testing of a new anti-seismic dissipator energy device based on the plasticity of metals. *Engineering Structures*, 32(9), 2672–2682.
- Garivani, S., Aghakouchak, A. A., & Shahbeyk, S. (2016). Numerical and experimental study of comb-teeth metallic yielding dampers. *International Journal of Steel Structures*, 16(1), 177–196.
- Ge, H., Chen, X., & Matsui, N. (2011). Seismic Demand on Shear Panel Dampers Installed in Steel-Framed Bridge Pier Structures. *Journal of Earthquake Engineering*, 15(3), 339–361.
- Ghabraie, K., Chan, R., Huang, X., & Xie, Y. M. (2010). Shape optimization of metallic yielding devices for passive mitigation of seismic energy. *Engineering Structures*, 32(8), 2258–2267.
- Ghaedi, K., & Ibrahim, Z. (2017). Earthquake Prediction. In T. Zouaghi (Ed.), *Earthquakes - Tectonics, Hazard and Risk Mitigation* (pp. 205–227). InTech.
- Ghaedi, K., Ibrahim, Z., Adeli, H., & Javanmardi, A. (2017). Invited Review: Recent developments in vibration control of building and bridge structures. *Journal of Vibroengineering*, 19(5), 3564–3580.
- Gibson, L. J., & Ashby, M. F. (1997). *Cellular Solids: Structure and Properties* (second). Cambridge/New York: Cambridge University Press.
- Gibson, L. J., Ashby, M. F., Schajer, G. S., & Robertson, C. I. (1982). The mechanics of two-dimensional cellular materials. In *Proceedings of the Royal Society of London* (pp. 25–42).
- Gimsing, N. J. (1998). *Cable supported bridges: concept and design* (Second). John Wiley and Sons.
- Golzan, S. B., Langlois, S., & Legeron, F. P. (2016). Implementation of a Simplified Method in Design of Hysteretic Dampers for Isolated Highway Bridges. *Journal of Bridge Engineering*, 1–14.
- Guan, Z., You, H., & Li, J. (2017). Lateral Isolation System of a Long-Span Cable-Stayed Bridge with Heavyweight Concrete Girder in a High Seismic Region, 1–15.
- Han, Q., Jia, J., Xu, Z., Bai, Y., & Song, N. (2014). Experimental evaluation of hysteretic behavior of rhombic steel plate dampers. *Advances in Mechanical Engineering*, 2014.
- Hao, W., Rui, Z., Zhouhong, Z., Chen, W., & AiQun, L. (2012). Study on seismic response control of a single-tower self-anchored suspension bridge with elastic-plastic steel damper. *Science China Technological Sciences*, 55(6), 1496–1502.
- Hao, X.-Y., Li, H.-N., Li, G., & Makino, T. (2014). Experimental investigation of steel structure with innovative H-type steel unbuckling braces. *The Structural Design of*

- Hassan, M. M., Nassef, A. O., & El Damatty, A. A. (2012). Determination of optimum post-tensioning cable forces of cable-stayed bridges. *Engineering Structures*, 44, 248–259.
- He, M., Hu, R., Chen, L., Chen, C., & Wang, J. (2015). Intelligent active control of a benchmark cable-stayed bridge. *Structures and Buildings*, 168(168), 890–901.
- He, W. L., & Agrawal, A. K. (2007). Passive and hybrid control systems for seismic protection of a benchmark cable-stayed bridge. *Structural Control and Health Monitoring*, 14(1), 1–26.
- He, W. L., Agrawal, A. K., & Mahmoud, K. (2001). Control of Seismically Excited Cable-Stayed Bridge Using Resetting Semiactive Stiffness Dampers. *Journal of Bridge Engineering*, 6(6), 376–384.
- Hedayat, A. A. (2015). Prediction of the force displacement capacity boundary of an unbuckled steel slit damper. *Journal of Constructional Steel Research*, 114, 30–50.
- Hilber, H. M., Hughes, T. J. R., & Taylor, R. L. (1977). Improved numerical dissipation for time integration algorithms in structural dynamics. *Earthquake Engineering & Structural Dynamics*, 5(3), 283–292.
- Housner, G. W., Bergman, L. A., Caughey, T. K., Chassiakos, A. G., Claus, R. O., Masri, S. F., ... Yao, J. T. P. (1997). Structural Control: Past, Present, and Future. *Journal of Engineering Mechanics*, (September), 897–971.
- Hsu, H. L., & Halim, H. (2017). Improving seismic performance of framed structures with steel curved dampers. *Engineering Structures*, 130, 99–111.
- Huber, P., & Medeot, R. (2005). New design approaches and related devices to reduce seismic risk. In *IABSE symposium*. Lisbon.
- Iemura, H., & Pradono, M. H. (2002). Passive and semi-active seismic response control of a cable-stayed bridge. *Journal of Structural Control*, 9(3), 189–204.
- Iemura, H., & Pradono, M. H. (2003). Application of pseudo-negative stiffness control to the benchmark cable-stayed bridge. *Journal of Structural Control*, 10(3–4), 187–203.
- Ismail, M., & Casas, J. R. (2014). Novel Isolation Device for Protection of Cable-Stayed Bridges against Near-Fault Earthquakes. *Journal of Bridge Engineering*, 1–12.
- Ismail, M., Rodellar, J., & Ikhoulane, F. (2010). An innovative isolation device for aseismic design. *Engineering Structures*, 32(4), 1168–1183.
- Janjic, D., Pircher, M., & Pircher, H. (2003). Optimization of Cable Tensioning in Cable-Stayed Bridges. *Journal of Bridge Engineering*, 8(June), 131–137.
- Jara, M., & Casas, J. R. (2006). A direct displacement-based method for the seismic design of bridges on bi-linear isolation devices. *Engineering Structures*, 28(6), 869–

- Javanmardi, A., Ghaedi, K., Ibrahim, Z., & Muthu, K. U. (2018). Seismic Pounding Mitigation of an Existing Cable-Stayed Bridge Using Metallic Dampers. In *IABSE Conference – Engineering the Developing World* (pp. 617–623). Kuala Lumpur, Malaysia: International Association for Bridge and Structural Engineering.
- Javanmardi, A., Ibrahim, Z., Ghaedi, K., & Khatibi, H. (2017). Numerical analysis of vertical pipe damper. In *IABSE SYMPOSIUM; Engineering the Future* (pp. 2974–2980). VANCOUVER: International Association for Bridge and Structural Engineering.
- Jie, Z., Li, A., & Tong, G. (2015). Analytical and experimental study on mild steel dampers with non-uniform vertical slits. *Earthquake Engineering and Engineering Vibration*, 14(1), 111–123.
- Karavasilis, T. L., Krawalla, S., & Hale, E. (2012). Hysteretic model for steel energy dissipation devices and evaluation of a minimal-damage seismic design approach for steel buildings. *Journal of Constructional Steel Research*, 70, 358–367.
- Karoumi, R. (1998). *Response of cable-stayed and suspension bridges to moving vehicles: Analysis methods and practical modeling techniques*. KTH Royal Institute of Technology, Stockholm.
- Kasai, K., & Maison, B. F. (1997). Building pounding damage during the 1989 Loma Prieta earthquake. *Engineering Structures*, 19(3), 195–207.
- Kato, S., Kim, Y. B., Nakazawa, S., & Ohya, T. (2005). Simulation of the cyclic behavior of J-shaped steel hysteresis devices and study on the efficiency for reducing earthquake responses of space structures. *Journal of Constructional Steel Research*, 61(10), 1457–1473.
- Kawashima, K., & Unjoh, S. (1991). Seismic behavior of cable-stayed bridges. In *Cable-stayed bridges; recent developments and their future* (pp. 193–212). Yokohoma (Japan): Elsevier Science Ltd.
- Kawashima, Unjoh, S., & Tsunomot, M. (1993). Estimation of damping ratio of cable-stayed bridges for seismic design. *Journal of Wind Engineering and Industrial Aerodynamics*, 27(1), 254–257.
- Kelly, J. M., Skinner, R. I., & Heine, A. J. (1972). Mechanisms of energy absorption in special devices for use in earthquake resistant structures. *Bulletin of the New Zealand National Society for Earthquake Engineering*, 5(3), 63–88.
- Kitazawa, M., Naganuma, T., Noguchi, J., & Adachi, Y. (2000). Seismic Design and Behavior of the Higashi-Kobe Bridge and Restoration After the 1995 Kobe Earthquake. *Proc. 12th World Conference on Earthquake Engineering, Auckland, New Zealand, Paper No.*, 1–6.
- Kiureghian, A. Der. (1980). A response spectrum method for random vibrations analysis of MDF systems. *Earthquake Engineering and Structural Dynamics*, 9(November 1980).

- Ko, J. M., Ni, Y. Q., & He, G. J. (2001). Applied seismic response characteristics of multi-span cable-stayed bridges with stabilizing cables. In *Key Engineering Materials* (pp. 737–742). Trans Tech Publications.
- Krawinkler, H., & Seneviratna, G. D. P. . (1998). Pros and cons of a pushover analysis of seismic performance evaluation. *Engineering Structures*, 20, 425–464.
- Leonhardt, F., & Zellner, W. (1980). Cable-stayed bridges. In *IABSE surveys* (p. S-13/80).
- Li, B., Bi, K., Chouw, N., Butterworth, J. W., & Hao, H. (2013). Effect of abutment excitation on bridge pounding. *Engineering Structures*, 54, 57–68.
- Li, B., & Chouw, N. (2014). Experimental investigation of inelastic bridge response under spatially varying excitations with pounding. *Engineering Structures*, 79, 106–116.
- Li, H., & Li, G. (2007). Experimental study of structure with “dual function” metallic dampers. *Engineering Structures*, 29(8), 1917–1928.
- Li, H., Liu, J., & Ou, J. (2009). Investigation of seismic damage of cable-stayed bridges with different connection configuration. *Journal of Earthquake and Tsunami*, 3(3), 227–247.
- Li, X. Z., Cai, J., & Qiang, S. H. (2001). Active control of long span cable-stayed bridges under seismic loads. In *International symposium on traffic induced vibrations and controls* (pp. 39–46). Beijing.
- Llera, J. C. de la, Esguerra, C., & Almazán, J. L. (2004). Earthquake behavior of structures with copper energy dissipators. *Earthquake Engineering & Structural Dynamics*, 33(3), 329–358.
- Ma, H., & Cho, C. (2008). Feasibility study on a superelastic SMA damper with re-centring capability. *Materials Science and Engineering A*, 473(1–2), 290–296.
- Ma, H., & Yam, M. C. H. (2011). Modelling of a self-centring damper and its application in structural control. *Journal of Constructional Steel Research*, 67(4), 656–666.
- Maleki, S., & Bagheri, S. (2010a). Pipe damper, Part I: Experimental and analytical study. *Journal of Constructional Steel Research*, 66(8–9), 1088–1095.
- Maleki, S., & Bagheri, S. (2010b). Pipe damper, Part II: Application to bridges. *Journal of Constructional Steel Research*, 66(8–9), 1096–1106.
- Maleki, S., & Mahjoubi, S. (2013). Dual-pipe damper. *Journal of Constructional Steel Research*, 85, 81–91.
- Maleki, S., & Mahjoubi, S. (2014). Infilled-pipe damper. *Journal of Constructional Steel Research*, 98, 45–58.
- Martínez-Rodrigo, M. D., & Filiatrault, a. (2015). A case study on the application of passive control and seismic isolation techniques to cable-stayed bridges: A comparative investigation through non-linear dynamic analyses. *Engineering Structures*, 99, 232–252.

- Matteis, G. De, Brando, G., & Mazzolani, F. M. (2011). Hysteretic behaviour of bracing-type pure aluminium shear panels by experimental tests. *Earthquake Engineering and Structural Dynamics*, 40(December 2010), 1143–1162.
- Matteis, G. De, Mazzolani, F. M., & Panico, S. (2007). Pure aluminium shear panels as dissipative devices in moment-resisting steel frames. *International Association for Earthquake Engineering*, 36(January), 841–859.
- Mazzolani, F. M. (2008). Innovative metal systems for seismic upgrading of RC structures. *Journal of Constructional Steel Research*, 64(7–8), 882–895.
- Mazzolani, F. M., Corte, G. Della, & D’Aniello, M. (2009). Experimental analysis of steel dissipative bracing systems for seismic upgrading. *Journal of Civil Engineering and Management*, 15(1), 7–19.
- Miller, D., & Doh, J.-H. (2014). A simple hybrid damping device with energy-dissipating and re-centering characteristics for special structures. *The Structural Design of Tall and Special Buildings*, 24(July 2014), 421–439.
- Morgenthal, G. (1999). *Cable-stayed bridge earthquake response and passive control*. Imperial college of science technology and medicine London UK.
- Motamedi, M., & Nateghi-A., F. (2018). Study on mechanical characteristics of accordion metallic damper. *Journal of Constructional Steel Research*, 142, 68–77.
- Mozos, C. M., & Aparicio, a. C. (2010a). Parametric study on the dynamic response of cable stayed bridges to the sudden failure of a stay, Part II: Bending moment acting on the pylons and stress on the stays. *Engineering Structures*, 32(10), 3301–3312.
- Mozos, C. M., & Aparicio, A. C. (2010b). Parametric study on the dynamic response of cable stayed bridges to the sudden failure of a stay, Part I: Bending moment acting on the deck. *Engineering Structures*, 32(10), 3288–3300.
- Nakashima, M., Iwai, S., Iwata, M., Takeuchi, T., Konomi, S., Akazawa, T., & Saburi, K. (1994). Energy dissipation behaviour of shear panels made of low yield steel. *Earthquake Engineering & Structural Dynamics*, 23(12), 1299–1313.
- Natural Resources of Canada. (2015). Seismic Hazard Map, Geological Survey of Canada. Retrieved from <http://www.seismescanada.nrcan.gc.ca/hazard-alea/simphaz-en.php>
- Nazmy, A. S., & Abdel-Ghaffar, A. M. (1990). Three-dimensional nonlinear static analysis of cable-stayed bridges. *Computers & Structures*, 34(2), 257–271.
- Nazmy, A. S., & Abdel-Ghaffar, A. M. (1992). Effects of Ground Motion Spatial Variability on The Response of Cable-Stayed Bridges. *Journal of Earthquake Engineering and Structural Dynamics*, 21(1), 1–20.
- NBCC. (2017). National Building Code of Canada. Retrieved from <http://www.earthquakescanada.nrcan.gc.ca>
- Ni, Y. Q., Wang, J. Y., & Ko. (2000). Modal interaction in cable-stayed Ting kau bridge.

- Nuzzo, I., Losanno, D., Serino, G., & Rotondo, L. M. B. (2014). A Seismic-resistant Precast R. C. System equipped with Shear Link Dissipators for Residential Buildings. *Second Intl. Conf. on Advances in Civil, Structural and Environmental Engineering*, 2(1), 249–254.
- Oh, S.-H., Kim, Y.-J., & Ryu, H.-S. (2009). Seismic performance of steel structures with slit dampers. *Engineering Structures*, 31(9), 1997–2008.
- Ok, S.-Y., Kim, D.-S., Park, K. S., & Koh, H.-M. (2007). Semi-active fuzzy control of cable-stayed bridges using magneto-rheological dampers. *Engineering Structures*, 29(5), 776–788.
- Okamoto, Y., & Nakamura, S. (2011). Static and seismic studies on steel/concrete hybrid towers for multi-span cable-stayed bridges. *Journal of Constructional Steel Research*, 67(2), 203–210.
- Oliveira Pedro, J. J., & Reis, A. J. (2010). Nonlinear analysis of composite steel-concrete cable-stayed bridges. *Engineering Structures*, 32(9), 2702–2716.
- Özkaynak, H. (2017). Model proposal for steel cushions for use in Reinforced Concrete frames. *KSCE Journal of Civil Engineering*, 1–11.
- Park, K.-S., Jung, H.-J., & Lee, I.-W. (2003). Hybrid control strategy for seismic protection of a benchmark cable-stayed bridge. *Engineering Structures*, 25(4), 405–417.
- Park, K.-S., Lee, I.-W., Jung, H. J., & Park, J.-G. (2003). Integrated Passive-Active System for Seismic Protection of a Cable-Stayed Bridge. *Journal of Earthquake Engineering*, 7(4), 615–633.
- Park, Y. J., Wen, Y. K., & Ang, A. (1986). Random vibration of hysteretic systems under bi-directional ground motions. *Earthquake Engineering & Structural Dynamics*, 14(4), 543–557.
- PEER. (2017). Pacific Earthquake Engineering Center. Retrieved from <http://ngawest2.berkeley.edu/site>
- Pinelli, J. P., Craig, J. I., Goodno, B. J., & Hsu, C.-C. (1993). Passive control of building response using energy dissipating cladding connections. *Earthquake Spectra*. <https://doi.org/10.1193/1.1585728>
- Pinkaew, T., Lukkunapraist, P., & Chatupote, P. (2003). Seismic effectiveness of tuned mass dampers for damage reduction of structures. *Engineering Structures*, 25(1), 39–46.
- Priestley, M. J. N., Sejhle, F., & Calvi, G. M. (1996). *Seismic design and retrofit of bridges*. John Wiley and Sons.
- Rai, D. C., Annam, P. K., & Pradhan, T. (2013). Seismic testing of steel braced frames with aluminum shear yielding dampers. *Engineering Structures*, 46, 737–747.

- Ren, & Obata, M. (1999). Elastic-Plastic Seismic Behavior of Long Span Cable-Stayed Bridges. *Bridge Engineering*, 4(December), 1404–1412.
- Ren, W. X., & Peng, X. L. (2005). Baseline finite element modeling of a large span cable-stayed bridge through field ambient vibration tests. *Computers and Structures*, 83(8–9), 536–550.
- Robinson, W. H., & Greenbank, L. R. (1976). An extrusion energy absorber suitable for the protection of structures during an earthquake. *Earthquake Engineering & Structural Dynamics*, 4(3), 251–259.
- Robinson, W. H., & Tucker, A. G. (1977). A lead-rubber shear damper. *Bulletin of the New Zealand National Society for Earthquake Engineering*, 10(3), 151–153.
- Roesset, J. M., Whitman, R. V., & Dobry, R. (1973). Modal Analysis for Structures with Foundation Interaction. *Journal of the Structural Division*, 99(3), 399–419.
- Saaed, T. E., Nikolakopoulos, G., Jonasson, J.-E., & Hedlund, H. (2013). A state-of-the-art review of structural control systems. *Journal of Vibration and Control*, 21(5), 919–937.
- Saha, P., & Jangid, R. S. (2009). Seismic control of cable-stayed bridge using semi-active hybrid system. *The IES Journal Part A: Civil & Structural Engineering*, 2(1), 1–16.
- Sahoo, D. R., Singhal, T., Taraithia, S. S., & Saini, A. (2015). Cyclic behavior of shear-and-flexural yielding metallic dampers. *Journal of Constructional Steel Research*, 114, 247–257.
- Schemmann, A. G. (1998a). Vibration control of cable-stayed bridges - part 1: modeling issues. *Earthquake Engineering & Structural Dynamics*, 27(8), 811–814.
- Schemmann, A. G. (1998b). Vibration control of cable-stayed bridges - part 2: control analyses. *Earthquake Engineering & Structural Dynamics*, 27(8), 825–843.
- Sepúlveda, J., Boroschek, R., Herrera, R., Moroni, O., & Sarrazin, M. (2008). Steel beam-column connection using copper-based shape memory alloy dampers. *Journal of Constructional Steel Research*, 64(4), 429–435.
- Sharabash, A. M., & Andrawes, B. O. (2009). Application of shape memory alloy dampers in the seismic control of cable-stayed bridges. *Engineering Structures*, 31(2), 607–616.
- Shattarat, N. K., Symans, M. D., McLean, D. I., & Cofer, W. F. (2008). Evaluation of nonlinear static analysis methods and software tools for seismic analysis of highway bridges. *Engineering Structures*, 30(5), 1335–1345.
- Shih, M.-H., Sung, W.-P., & Go, C.-G. (2004). Investigation of newly developed added damping and stiffness device with low yield strength steel. *Journal of Zhejiang University. Science*, 5(3), 326–334.
- Shih, M.-H., & Sung, W. P. (2005). A model for hysteretic behavior of rhombic low yield strength steel added damping and stiffness. *Computers and Structures*, 83(12–13),

- Simo, J. C., & Kelly, J. M. (1984). The Analysis of Multilayer Elastomeric Bearings. *Journal of Applied Mechanics*, 51(2), 256–262.
- Siringoringo, D. M., & Fujino, Y. (2006). Observed dynamic performance of the Yokohama-Bay Bridge from system identification using seismic records. *Structural Control and Health Monitoring*, 13(1), 226–244.
- Siringoringo, D. M., Fujino, Y., & Namikawa, K. (2013). Seismic Responses Analyses of the Yokohama-Bay Cable-Stayed Bridge in the 2011 Great East Japan (Tohoku) Earthquake. *Journal of Bridge Engineering*, 10.1061, 1–17.
- Skinner, R. I., Kelly, J. M., & Heine, a. J. (1974). Hysteretic Dampers for Earthquake-Resistant Structures. *Earthquake Engineering & Structural Dynamics*, 3(September 1974), 287–296.
- Soneji, B. B., & Jangid, R. S. (2007a). Passive hybrid systems for earthquake protection of cable-stayed bridge. *Engineering Structures*, 29(1), 57–70.
- Soneji, B. B., & Jangid, R. S. (2007b). Response of an isolated cable-stayed bridge under bi-directional seismic actions. *Structure and Infrastructure Engineering*, 6(3), 347–363.
- Soong, T. T., & Dargush, G. F. (1997). *Passive energy dissipation systems in structural engineering*. Wiley.
- Soydan, C., Yuksel, E., & Irtem, E. (2014). The Behavior of a Steel Connection Equipped with the Lead Extrusion Damper. *Advances in Structural Engineering*, 17(1), 25–39.
- Soyluk, K., & Dumanoglu, a. a. (2000). Comparison of asynchronous and stochastic dynamic responses of a cable-stayed bridge. *Engineering Structures*, 22(5), 435–445.
- Tagawa, H., Yamanishi, T., Takaki, A., & Chan, R. W. K. (2016). Cyclic behavior of seesaw energy dissipation system with steel slit dampers. *Journal of Constructional Steel Research*, 117, 24–34.
- Takeda, Y., Kimura, Y., Yoshioka, K., Furuya, N., & Takemoto, Y. (1976). An experimental study on braces encased in steel tube and mortar. In *Annual Meeting Architectural Institute of Japan* (pp. 1041–1042).
- Tsai, K.-C., Chen, H.-W., Hong, C.-P., & Su, Y.-F. (1993). Design of steel triangular plate energy absorbers for seismic-resistant construction. *Earthquake Spectra*.
- Tuladhar, R., Dilger, W. H., & Elbadry, M. M. (1995). Influence of Cable Vibration on Seismic Response of Cable-Stayed Bridges. *Canadian Journal of Civil Engineering*, 22(5), 1001–1020.
- Tyler, R. G. (1978a). A tenacious base isolation system using round steel bars. *Bulletin of the New Zealand Society for Earthquake Engineering*, 11(4).

- Tyler, R. G. (1978b). Tapered steel energy dissipators for earthquake resistant structures. *Bulletin of the New Zealand National Society for Earthquake Engineering*, 11(4).
- Uzarski, J., & Arnold, C. (2001). Chi-Chi, Taiwan, earthquake of September 21, 1999 reconnaissance report. *Earthquake Spectra*, 17(A), 37–60.
- Valdebenito, G. E. (2009). *Passive Seismic Protection of Cable-Stayed Bridges Applying Fluid Viscous Dampers under Strong Motion*. Universitat Politècnica de Catalunya.
- Vargas, R., & Bruneau, M. (2007). Effect of Supplemental Viscous Damping on the Seismic Response of Structural Systems with Metallic Dampers. *Journal of Structural Engineering*, 133(10), 1434–1444.
- Vargas, R., & Bruneau, M. (2009). Experimental Response of Buildings Designed with Metallic Structural Fuses. II. *Journal of Structural Engineering*, 135(4), 394–403.
- Vasdravellis, G., Karavasilis, T. L., Uy, B., & Asce, M. (2012). Design Rules, Experimental Evaluation, and Fracture Models for High-Strength and Stainless-Steel Hourglass Shape Energy Dissipation Devices. *Journal of Structural Engineering*, 1–14.
- Villaverde, R. (2009). *Fundamental concepts of earthquake engineering*. CRC Press.
- Virlogeux, M. (1999). Recent evolution of cable-stayed bridges. *Engineering Structures*, 21(8), 737–755.
- Virlogeux, M. (2001). Bridges with Multiple Cable-stayed Spans. *Structural Engineering International*, 11(1), 61–82.
- Wada, A., Saeki, E., Takeuch, T., & Watanabe, A. (1989). Development of unbonded brace. In Column. *A Nippon Steel Publication*, 115(12).
- Walker. (2009). *Modal superposition in the dynamic analysis of cable-stayed bridges*. Imperial college of science technology and medicine London UK.
- Walther, R., Houriet, B., Isler, W., Moia, P., & Klein, J.-F. (1988). *Cable-Stayed Bridges*. Thomas Telford Ltd.
- Wang, Y.-P., & Chien, C.-S. C. (2009). A study on using pre-bent steel strips as seismic energy-dissipative devices. *Earthquake Engineering & Structural Dynamics*, 38, 1009–1026.
- Wang, & Yang, C. G. (1996). Parametric studies on cable-stayed bridges. *Computers and Structures*, 60(2), 243–260.
- Wesolowsky, M. J., & Wilson, J. C. (2003). Seismic isolation of cable-stayed bridges for near-field ground motions. *Earthquake Engineering & Structural Dynamics*, 32(13), 2107–2126.
- Wethyavivorn, B., & Fleming, J. F. (1987). Three dimensional seismic response of a cable-stayed bridge. In *International conference on cable-stayed bridges*. Bangkok Thailand.

- Wood, J., & Jennings, P. (1971). Damage to freeway structures in the San Fernando earthquake. *Bulletin of the New Zealand National Society for Earthquake Engineering*, 4(3), 347–76.
- Wyatt, T. A. (1991). The dynamic behaviour of cable-stayed bridges: fundamentals and parametric studies. *Proc., Cable-Stayed Bridges: Recent Developments and Their Future*, 151–170.
- Yamaguchi, H., & Furukawa, T. (2004). Nonlinear seismic response and a seismic retrofit of a long-span cable-stayed bridge. In *9th National Convention on Civil Engineering*. Petchburi.
- Yamazaki, S., Usami, T., & Nonaka, T. (2016). Developing a new hysteretic type seismic damper (BRRP) for steel bridges. *Engineering Structures*, 124, 286–301.
- Zayas, V. A., Low, S. S., & Mahin, S. A. (1990). A simple pendulum technique for achieving seismic isolation. *Earthquake Spectra*, 6(2), 317–333.
- Zhang, C., Zhang, Z., & Zhang, Q. (2012). Static and dynamic cyclic performance of a low-yield-strength steel shear panel damper. *Journal of Constructional Steel Research*, 79, 195–203.
- Zhang, Y., & Zhu, S. (2007). A shape memory alloy-based reusable hysteretic damper for seismic hazard mitigation. *Smart Materials and Structures*, 16(5), 1603–1613.
- Zhao, J., Wu1, B., & Ou, J. (2011). A novel type of angle steel buckling-restrained brace: Cyclic behavior and failure mechanism. *Earthquake Engineering & Structural Dynamics*, 40, 1083–1102.
- Zheng, J., & Takeda, T. (1995). Effects of soil-structure interaction on seismic response of PC cable-stayed bridge. *Soil Dynamics and Earthquake Engineering*, 14(6), 427–437.
- Zhu, J., Zhang, W., Zheng, K. F., & Li, H. G. (2015). Seismic Design of a Long-Span Cable-Stayed Bridge with Fluid Viscous Dampers. *Practice Periodical on Structural Design and Construction*, 1–11.
- Zong, Z., Zhou, R., Huang, X., & Xia, Z. (2014). Seismic response study on a multi-span cable-stayed bridge scale model under multi-support excitations. Part I: shaking table tests. *Journal of Zhejiang University SCIENCE A*, 15(5), 351–363.

LIST OF PUBLICATIONS AND PAPERS PRESENTED

ISI Published:

1. **Javanmardi, A.**, Ibrahim, Z., Ghaedi, K., Jameel, M., Khatibi, H., & Suhatri, M. (2017). Seismic response characteristics of a base isolated cable-stayed bridge under moderate and strong ground motions. Archives of Civil and Mechanical Engineering, 17(2), 419–432. <https://doi.org/10.1016/j.acme.2016.12.002> (ISI-Indexed-**Q1**).
2. **Javanmardi, A.**, Ibrahim, Z., Ghaedi, K., Khan, N. B., & Ghadim, H. B. (2018). Seismic isolation retrofitting solution for an existing steel cable-stayed bridge. PLOS ONE, 13(7), 1–22. <https://doi.org/10.1371/journal.pone.0200482> (ISI-Indexed-**Q1**).
3. **Javanmardi, A.**, Ibrahim, Z., Ghaedi, K., Ghadim, H. B & Hanif, M,U. State-of-the-art Review of Metallic Dampers: Testing, Development and Implementation. Archives of Computational Methods in Engineering, (ISI- Indexed-**Q1**) (Revision Submitted) 2018.

ISI Under Review:

1. **Javanmardi, A.**, Ibrahim, Z., Ghaedi, K. Development of a new yielding metallic damper for mitigation of seismic demands on the structures. Journal of Constructional Steel Research (ISI-Indexed-**Q2**) (Submitted) 2018.
2. **Javanmardi, A.**, Ibrahim, Z., Ghaedi, K. Seismic response of cable-stayed bridge equipped with hybrid passive control system. (Under writing).

Conference Proceedings:

- 1) **Javanmardi, A.**, Ghaedi, K., Ibrahim, Z., & Muthu, K. U. (2018). Seismic Pounding Mitigation of an Existing Cable-Stayed Bridge Using Metallic Dampers. In IABSE Conference – Engineering the Developing World (pp. 617–623). Kuala Lumpur, Malaysia: International Association for Bridge and Structural Engineering. (Scopus Indexed)
- 2) **Javanmardi, A.**, Ibrahim, Z., Ghaedi, K., & Khatibi, H. (2017). Numerical analysis of vertical pipe damper. In 39th IABSE SYMPOSIUM; Engineering the Future (pp. 2974–2980). Vancouver, Canada: International Association for Bridge and Structural Engineering. (Scopus Indexed)
- 3) **Javanmardi, A.**, Ibrahim, Z., Ghaedi, K., Jameel, M., Usman, H., & Gordan, M. (2016). Seismic response of a base isolated cable-stayed bridge under near-fault ground motion excitations. In 13th International Conference on Concrete Engineering & Technology. Shah Alam, Selangor.
- 4) **Javanmardi, A.**, Ghaedi, K., Ibrahim, Z., & Khatibi, H. (2016). Nonlinear seismic behavior of a based isolated cable-stayed bridge. In S. B. University (Ed.), 4th international congress on Civil engineering, Architecture and Urban Development. Tehran: Civilica. Retrieved from https://www.civilica.com/Paper-ICSAU04-ICSAU04_0204.html